Title
Passive Voltage Boosting Methods for Wireless Energy Harvesting Systems

Author
Duong, Connie

Publication Date
2023

Peer reviewed|Thesis/dissertation

Passive Voltage Boosting Methods for Wireless Energy Harvesting Systems

By

CONNIE DUONG

DISSERTATION

Submitted in partial satisfaction of the requirements for the degree of

DOCTOR OF PHILOSOPHY

in

Electrical and Computer Engineering

in the

OFFICE OF GRADUATE STUDIES

of the

UNIVERSITY OF CALIFORNIA

DAVIS

Approved:

Rajeevan Amirtharajah, Chair

David Horsley

Omeed Momeni

Committee in charge

2023

This dissertation is dedicated to all of the teachers, mentors, and professors who saw the world as it could be and taught me to do the same and to my parents for their vision and sacrifices for me to have a better life and strong faith in God made me who I am today. This dissertation is also dedicated to "the God and Father of our Lord Jesus Christ, who has blessed us in the heavenly realms with every spiritual blessing in Christ." (Ephesians 1:3)

Contents

List of Figures

List of Tables

Connie Duong
2023
Electrical and Computer Engineering

Passive Voltage Boosting Methods for Wireless Energy Harvesting Systems

Abstract

Wireless power transfer has significantly improved the user experience in device charging and is currently an area of active research. Some major limitations of wireless charging systems include size constraints due to low frequency operation, the need for close proximity and tight alignment for efficient power transfer, and limited use of the device while charging. This work proposes several techniques to passively boost the voltage harvested and decrease the size of the power module.

The rectifier and DC-DC converter explored in this dissertation extend technology proposed in existing literature that uses a resonator as the high quality factor component in the antenna matching network and energy storage element, respectively. This project proposes further development of these technologies by multiplexing the resonator between the rectifier and converter to reduce power module size and decrease generated electromagnetic interference by eliminating the need for magnetics. Preliminary testing has shown a resonator is more effective than an inductor (by a maximum of 30 percent) in boosting the rectifier output voltage and can boost the rectifier output voltage by a maximum of 8 times compared to an unmatched rectifier at 18 MHz on a commercial-grade printed circuit board. Initial DC-DC converter simulations with NMOS switches and realistic diodes show a 100 kHz resonator can store energy in a boost DC-DC converter on the order of nanojoules for a 10 V to 14 V step up conversion with 68 percent efficiency. This is similar in performance to a simulated inductor-based converter, which has a 78 percent efficiency when operating with the same step up ratio.

The resonator-based DC-DC converter was built on a printed circuit board (PCB) using

discrete transistors and a 185 kHz ceramic resonator. Simulations and measurements both showed the proposed discrete transistors did not effectively boost a 5 V input voltage by 1.4 times as was shown previously. Different methods to address this issue such as a floating driver and PMOS switches were proposed. An integrated design was also implemented using the open-source SkyWater 130 nm CMOS process design kit (PDK).

A magnetoelectric (ME) antenna is proposed to decrease the size of the antenna by operating at acoustic resonance. Another benefit is more lenient alignment rules, which provide more device usage flexibility while charging. The maximum voltage output from the fabricated ME antenna is 0.3 V with a Qi transmitter producing 0.8 W as the source. The size of the antenna is 2 cm by 1.5 cm, which is smaller than the commercial Qi receiving antennas of 4 cm by 4 cm. When used to harvest vibrational energy, a slightly larger antenna (3 cm by 1.5 cm) could provide a maximum output power of 0.3 μW for an input vibration acceleration of approximately +/- 8 g.

Acknowledgments

I would like give a special thanks to my advisor, Dr. Rajeevan Amirtharajah, for his wisdom and kindness and for always supporting me through any and all educational tangents and wild endeavours. Also, thank you to the past and present members of the MCSG Lab: to Son for his generous help and lab expertise, to Heather for her kindness and companionship, to Sean for his amazing knowledge and for always willing to discuss any bizarre problem, and to Tim, Karthika, Nathan, Nick, Andrew, and Ken for their friendship.

I would also like to thank the many professors I've had the honor of meeting and learning from during my time at UC Davis. Thank you to Dr. Valeria La Saponara for allowing me to use her lab facilities and for her willingness to help and support my research. Thank you to Dr. Stephen Lewis for his passion and commitment to teaching, for his insightful and considerate advice, and for all his time and energy invested into my education; I have learned so much from him both as a student in his class and as a lecturer for his class, and words cannot express how indebted I am for this incredible learning opportunity.

This journey of grad school would not have been possible without the encouragement of my family. Thank you to my parents for their love and support and to my baby niece Ariella, who taught me how to love and how to see the beauty in the world. Thank you to Davis Chinese Christian Church and Living Stones Fellowship, who became my home away from home and whose love and friendship carried me through many storms.

"And we know that in all things God works for the good of those who love him, who have been called according to his purpose." (Romans 8:28)

Chapter 1

Introduction

1.1 Overview

For decades, wireless communication technology has revolutionized how information is processed and sent, and currently, the emerging concept of wireless power transfer has the potential to alter the design of power modules. Figure 1.1 illustrates the block diagram of a general wireless energy harvester. The main components include the antenna to receive wireless signals, a matching network to equalize the impedance, the rectifier that converts a time-varying (AC) signal into a constant (DC) one, and a DC-DC converter to change the voltage to a level acceptable for use. The load for this system is usually a rechargeable battery, which has strict input power requirements. This dissertation explores designs to improve the antenna, matching network of the rectifier, and DC-DC converter. Improvements to the antenna will be made by implementing a magnetoelectric (ME) antenna that aims to decrease the form factor of the power module. The rectifier will be further enhanced with a high quality factor matching network through the use of a resonator, and the DC-DC converter will share the piezoelectric resonator with the matching network for a more compact design. A block diagram of these concepts is illustrated in Fig. 1.2

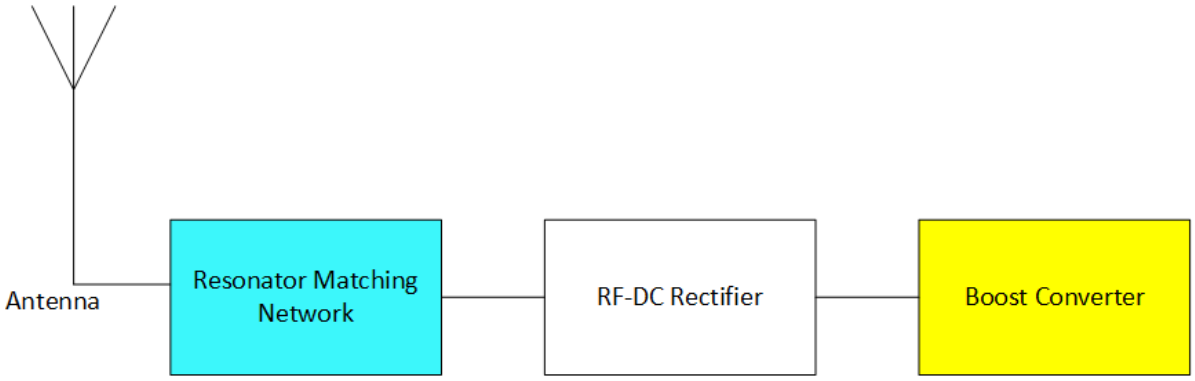

Figure 1.1: General block diagram for power module to harvest wireless energy.

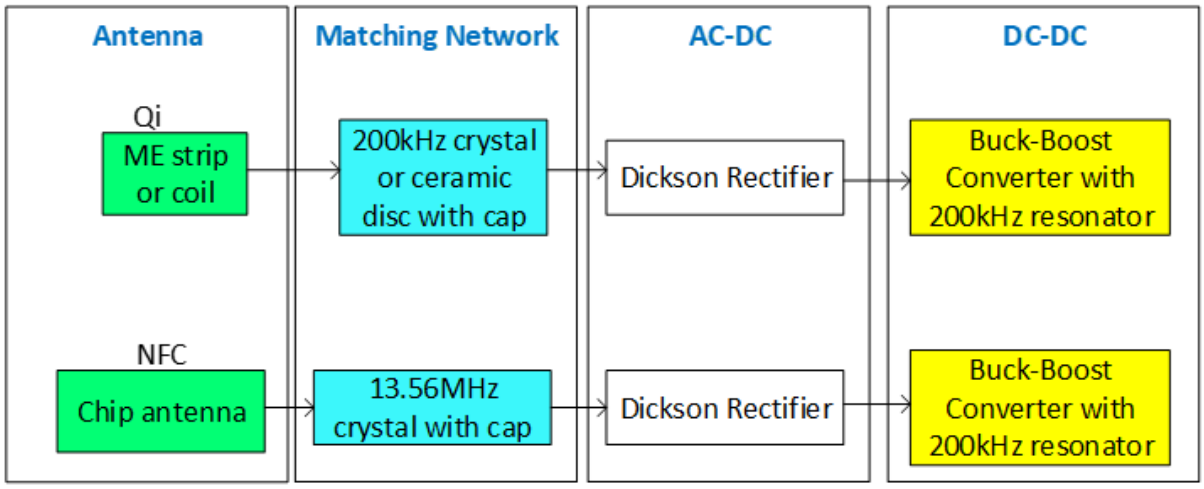

Figure 1.2: Proposed system for wireless power transfer.

1.2 Qi Standard

The current standard for wireless power transfer in commercial products is the Qi standard, named after the Chinese word for air or energy. As of 2020, almost 1000 products ranging from cellular phones to smartwatches to wireless earbud cases have Qi charging capability [1]. With the growing demand for personal electronic devices, wireless power transfer is an increasingly lucrative option to charge personal devices without the need for cumbersome cables. The global market for wireless charging devices is projected to grow 22 percent every year from now until 2027, reaching a value of over $40 billion by 2027 [2].

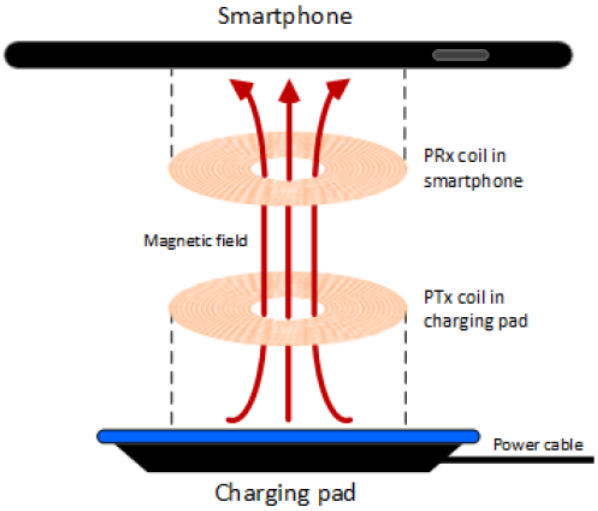

Figure 1.3: Qi charging diagram for a smartphone [3].

The Qi standard operates within the low frequency range, from 87-205 kHz, and can provide 5-15 W of power. A Qi charging system consists of a transmitter that provides the wireless signal and a receiver that uses this signal to charge a device, such as a smartphone. Figure 1.3 illustrates this concept [3] [4].

Due to the low frequency of operation, the coils are much smaller than the wavelength and do not act as antennas. Rather, they interact through magnetic induction and resemble a transformer as shown in Fig. 1.4. The components C_p, R_p, and L_p represent the capacitance, resistance, and inductance of the primary or transmitting coil, while L_s, C_s, and R_s are the corresponding components for the secondary (receiving) coil. The mutual inductance, M, is defined by Eqn 1.1 and determines the coupling factor, k, as shown in Eqn 1.2 [5]. Mutual inductance depends on permeability (μ_0 and μ_r), the number of turns in the primary or transmitting coil (N_p) and secondary or receiving coil (N_s), the area of the coils (A), and the distance between the coils (l). Because the mutual inductance is inversely proportional to the distance between the coils, the coils must be in very close proximity for the most efficient power transfer. Requiring tight coupling has disadvantages such as inefficient power transfer when not properly aligned and not allowing handheld use of the device when charging, since

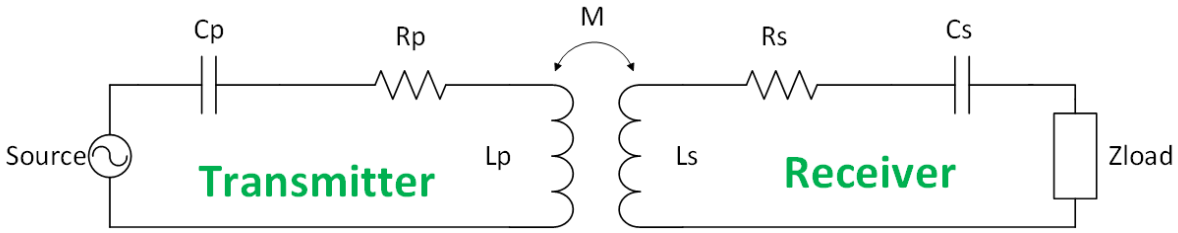

Figure 1.4: Illustrating a Qi charging system as a transformer [4].

the device has to be within 2.5 mm of the transmitter interface as specified by the 2017 Qi standard. The main parameters of this system that determine performance are the coupling factor, as mentioned above, and the quality factor of the coils (Eqn 1.3) which is defined by the operating frequency ω, the inductance, and the resistance [3] [4].

$$M = \frac{\mu_0 \mu_r N_s N_p A}{l} \tag{1.1}$$

$$k = \frac{M}{\sqrt{L_s L_p}} \tag{1.2}$$

$$Q = \frac{\omega L}{R} \tag{1.3}$$

1.3 NFC Charging

A proposed alternative to the Qi standard is near field communication (NFC) wireless charging, which operates at 13.56 MHz. Although the power transferred is lower (only up to 1 W according to the NFC Forum's WLC standard), this emerging standard does not require strict alignment and requires a smaller coil due to the higher frequency. Currently, this wireless charging standard has only been implemented in a few devices including the Huawei smart glasses, Samsung fitband, and Microsoft stylus, but it has the potential to be used in small devices such as wireless earbuds, wrist-worn electronics, and home sensors.

The benefits include loose coupling, integration into smaller devices, and higher data rates compared to the Qi standard [6] [7] [8].

NFC charging is currently not as mainstream as the Qi standard, but there are companies such as NuCurrent and NXP that are working to increase the power transferred at this frequency up to 5 W and to incorporate it into devices like wearables and wristbands that are too small to contain a Qi charging coil [7].

1.4 Vibration

While wireless communication and power transfer relies on electromagnetic waves to propagate energy, vibration carries energy over distances in the form of acoustic waves. Certain materials can convert between vibration and electromagnetic energy such as magnetostrictive (MR) materials, which convert energy between vibration and a magnetic field, and piezoelectric (PE) materials, which transfers energy from vibration to an electric field. The induced vibration due to an electromagnetic signal or the generated electromagnetic signal from an applied vibration can be utilized for energy harvesting in two ways. First, a composite material can be made from layers of MR and PE materials to convert a magnetic field to an electric field with vibration as an intermediate energy form occurring when the magnetic field induces a strain on the MR material. This strain is transferred to the PE material, which produces a voltage. Although this method requires energy to be converted to several different forms, it has certain advantages such as requiring smaller device lengths and no impedance mismatch [9]. Secondly, vibration can be applied directly to a PE material to generate an induced voltage. Since a device containing MR and PE materials to convert magnetic fields into a voltage already has a PE material, the device can also be used to harvest vibration directly and convert it into a voltage.

1.5 Project Motivation and Organization

The main purpose of this project is to design a wireless energy harvesting system compatible with the Qi and NFC charging standards to decrease the size of the power module and increase the time between uses before the device has to be charged. One proposed method is to create a more compact rectifier and DC-DC converter module by using a resonator to create a high quality factor matching network and to act as the energy storage element in the converter. Another method is to design a compact antenna using magnetoelectric materials to continuously harvest ambient energy from wireless sources without tight coupling. By allowing for continuous charging during use, the battery can last longer or be smaller, since it does not need to store as much energy between charges.

A practical application for this project is wearable devices use as watches, fitbands, and earbuds. Since most users are constantly surrounded by electronics, wireless charging pads can be integrated into keyboards, a mouse, or even smartphones, so the user can charge their wearables while using them. Another application can be for implantable devices, which can be charged routinely during a doctor's visit or from charging sources implanted in furniture, so the user does not have to replace the battery or remove it for charging.

The rest of this dissertation is organized as follows: Chapter 2 explains how a resonator can be implemented into the matching network of a rectifier. Chapter 3 shows a DC-DC converter using the resonator as an energy storage element. Chapter 4 provides simulations combining the rectifier and DC-DC converter into a single system. Chapter 5 describes the ME antenna performance in harvesting RF and vibrational signals. Chapter 6 details implementing the rectifier and converter in an integrated design, and Chapter 7 concludes the dissertation with a summary and future work to further enhance the project.

Chapter 2

High Frequency Wireless Energy Harvesting

2.1 Rectifier Overview

A rectifier converts AC power into DC power, most commonly through the use of diodes or diode-connected transistors, which only allow current to flow in one direction, and capacitors, which store the energy of the rectified AC signal. The configuration of the diodes in the circuit invert the negative part of the input signal and allows the capacitors to continuously charge. The goal is to keep the capacitors continuously charged and produce a steady DC output signal. This circuit is commonly used in wireless energy harvesting, in which a rectifier is attached to an antenna that receives the high frequency input signal.

Specifications for a rectifier's performance include efficiency, output voltage, and sensitivity. The efficiency of a rectifier is the ratio of the output power to the input power and depends on many factors such as forward voltage drop of the diodes, parasitics of the rectifier, and the impedance of the rectifier compared to the input source or antenna. The output voltage is affected by the number of stages and the load resistance. The sensitivity of a rectifier is defined by the minimum input power at which the rectifier can function and

is dependent on the forward voltage of the diodes and the losses associated with the circuit (such as impedance mismatch).

This project targets a low frequency range (100-200 kHz) and a high frequency range (10-20 MHz) to correspond to the Qi and NFC standard operating frequency ranges, respectively. Although NFC charging occurs at 13.56 MHz, a frequency in the same range was chosen to allow more flexibility in choosing quartz crystals and other piezoelectric resonators during the prototype stage. After verifying rectifier performance at a frequency in the same order of magnitude of NFC charging, future work will be performed with stricter frequency requirements.

2.2 Literature Review

One method of improving rectifier performance is to decrease the threshold voltage of the transistors or forward voltage drop of the diodes. Doing this will minimize the "dead zone" [10], which is the minimum input for the rectifier to function. Various designs have been proposed to address the threshold voltage in CMOS technologies [11] [12], and Schottky diodes are commonly used in discrete designs because of their small voltage drop [13]. Besides the voltage drop, other specifications of Schottky diodes such as resistance and saturation current also affect output voltage and efficiency as mentioned in [14].

In addition, there is an optimal load resistance where the highest efficiency occurs, and is usually determined by sweeping a range of load impedances [15]. An extremely low load resistance (such as a short) will cause most of the voltage to be dropped across the rest of the circuit instead of at the load; a high load resistance (such as an open circuit) will decrease the output power, which is determined by Equation 2.1, where P is the power of the load resistor and V is the voltage across a resistor with resistance R.

$$P = \frac{V^2}{R} \tag{2.1}$$

Because the input to the diode is an AC signal, there is the problem of impedance mismatch between the source (or antenna) and the rectifier. Impedance mismatch occurs in AC circuits because the impedance is a complex value, consisting of a resistance, which is independent of frequency, and a reactance, which depends on frequency. To enable maximum power transfer between the source and the rectifier, the source and the rectifier impedances should be complex conjugates of each other. This means that the reactances cancel and the resistances are equal. The rectifier is mostly capacitive, so to provide a complex conjugate, the matching network should be mostly inductive [16]. According to the maximum power theorem, the load should have the same resistance as the source for maximum power transfer.

Different methods for matching the rectifier to the source (or antenna) have been proposed. Impedance matching methods can be divided into two categories: distributed and discrete. Distributed methods involve fabricating a matching network through microstrip lines, while discrete methods use off-the-shelf passive components. A common method in impedance matching is to use transmission line segments, which has been simulated in [17]. Although high performance can be achieved, this method only works for the ultra high frequency range and above (greater than several hundred megahertz) because the signals have shorter wavelengths. In addition, the area of the circuit will be increased with additional transmission line sections. Another method of matching is to use an off-center-fed dipole (OCFD) antenna that is the complex conjugate of the rectifier impedance [18].

Discrete inductors and capacitors are often used in common impedance matching configurations, such as L and pi networks [15] [19]. A disadvantage of using discrete inductors is their inductance and equivalent series resistance (ESR) varies with frequency in addition to a low quality factor, which causes loss in the matching network. The quality factor, Q, of the matching network is important because a higher Q means less energy is dissipated in the network, Eqn 2.2.

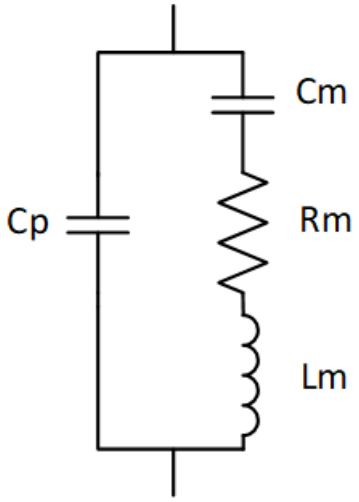

Figure 2.1: Butterworth-Van Dyke model for a resonator.

$$Q = \frac{\text{energy stored per cycle}}{\text{energy dissipated}} = \frac{1}{R}\sqrt{\frac{L}{C}} \tag{2.2}$$

To address this, a crystal resonator can be used as a high Q inductor [19]. A crystal resonator can be modeled with the Butterworth-Van Dyke model [16], which is shown in Fig. 2.1. The components Lm, Cm, and Rm are the motional inductance, capacitance, and resistance, respectively, and Cp is the shunt capacitance. The frequency response of a typical resonator can be seen in Fig. 2.2. At the series resonance frequency (f_r), the impedance of the crystal is minimized; at the parallel resonance or anti-resonance frequency (f_a), the crystal impedance is maximized. These frequencies can be calculated from the model parameters as shown in Eqns 2.3a and 2.3b [20]. In between these two frequencies, the crystal is dominated by its inductance and can be used as the inductive component in the matching network. It is proposed that the small bandwidth of operation for in this method is reasonable for the high Q obtained compared to using discrete inductors.

$$f_r = \frac{1}{2\pi\sqrt{L_m C_m}} \tag{2.3a}$$

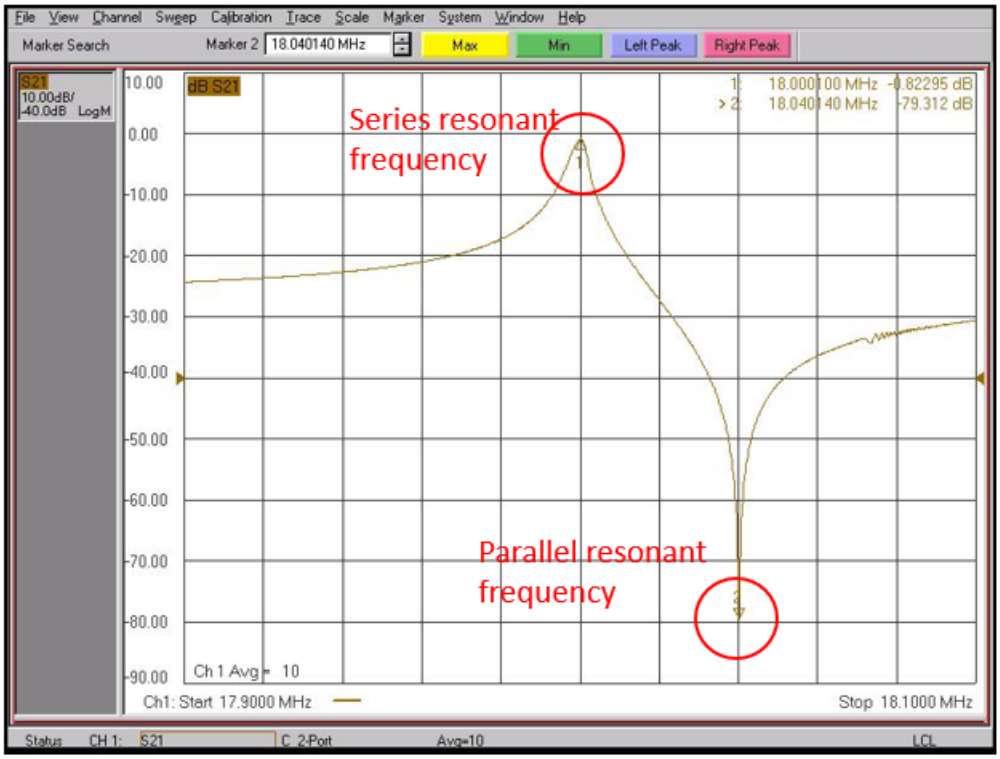

Figure 2.2: Measured frequency response of a 18 MHz crystal resonator.

$$f_a = \frac{1}{2\pi\sqrt{\frac{L_m C_m C_p}{C_p + C_m}}} \tag{2.3b}$$

2.3 Design

One-stage, 2-stage, and 3-stage Dickson rectifiers were fabricated on a printed circuit board (PCB). The rectifying component is the Schottky diode SMS7630 from Skyworks, which was chosen for its low forward voltage drop (0.26-0.32 V) and high quality RF performance. All capacitors besides the matching capacitors are chosen to be 1 nF, and the load resistance is 47 kΩ.

An L matching scheme was used to compare the effects of an inductor compared to a crystal resonator. Figure 2.3 shows the topology of an L match, which was chosen for its

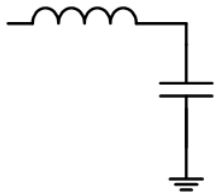

Figure 2.3: L matching network using a series inductor and shunt capacitor.

simplicity and because the crystal parameters were measured in series with rest of the circuit. For each rectifier, the impedance at 18 MHz was measured with and without matching. The results are summarized below in Table 2.1. Discrete surface mount inductors and capacitors and a through-hole 18 MHz crystal were used for matching. The shunt capacitors are used to bring the real part of the impedance to 50 Ω, and the inductor or crystal minimizes the reactance of the rectifier.

Table 2.1: Measured matching information.

	1 Stage LC	**1 Stage Crystal**	**2 Stage LC**	**2 Stage Crystal**	**3 Stage LC**	**3 Stage Crystal**
Frequency (MHz)	18.0073	18.0073	18.0039	18.0039	18.0027	18.0027
Impedance, Unmatched (Ω)	$302 - j1150$	$316 - j1125$	$380 - j610$	$340 - j702$	$340 - j417$	$325 - j480$
Shunt Cap (pF)	15	15	33	33	39	39
Inductance (μH)	3.68	3.51	1.65	1.78	1.47	1.45
ESR (Ω)	41.4	17.9	9.2	24.8	13	20.4
Impedance, Matched (Ω)	$75 + j21$	$54 + j3.8$	$39 - j12$	$48 - j0.53$	$46 + j2$	$48 - j3$
Quality Factor	12	27	24	9.4	15	9.5

2.4 Results

Fabricated Dickson rectifiers with different matching topologies were compared. In all the rectifiers (1, 2, and 3 stages), using a crystal resonator in the matching network produced higher output voltage and higher efficiency than using a coil inductor in the matching network. Figure 2.4 shows the comparison of the efficiency of the various rectifiers with matching networks. Figure 2.5 compares the output voltage.

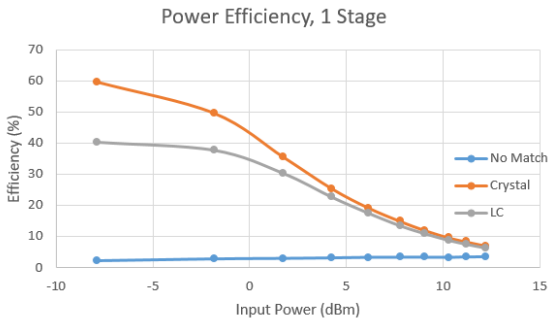

(a) One Stage Rectifier.

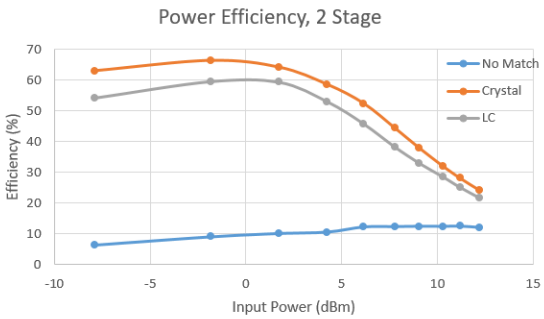

(b) Two Stage Rectifier.

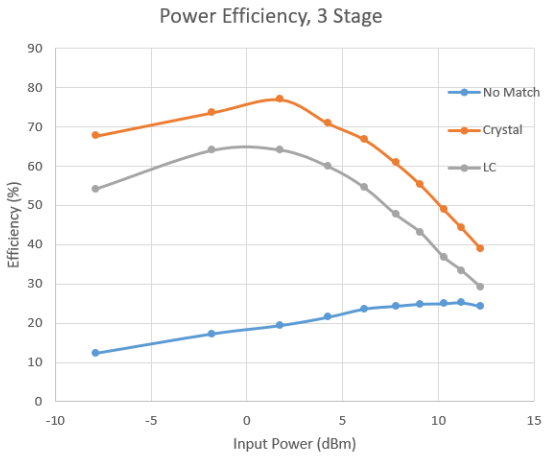

(c) Three Stage Rectifier.

Figure 2.4: Measured Dickson rectifier efficiency with a 47 kΩ load.

In comparison, the same Dickson rectifier was simulated in ADS using the SMS7630 diode model (Fig. 2.6). Both simulation and testing verified that using a crystal resonator as the inductor element in the matching network produced a higher rectifier output voltage and matching the rectifier to the antenna produced higher output than no matching at all. However, the simulated values differed from the measured values, which is most likely due to the simulation program's treatment of the diode's breakdown voltage. As seen in Fig. 2.6, the output voltage saturates at 5 V, which is the breakdown voltage used in the model (and was increased from the datasheet value of 2 V for better observation), but in reality, in Fig.

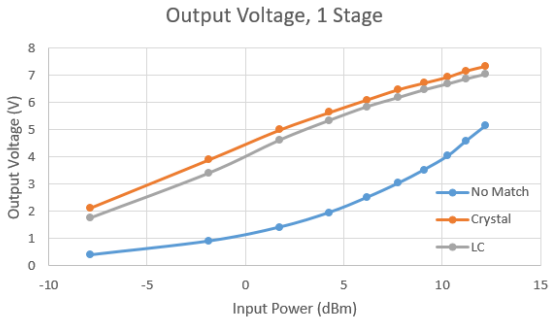

(a) One Stage Rectifier.

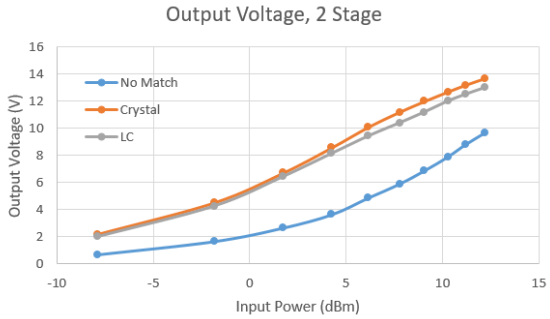

(b) Two Stage Rectifier.

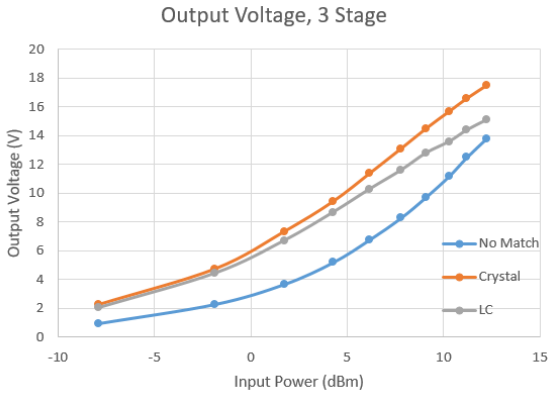

(c) Three Stage Rectifier.

Figure 2.5: Measured Dickson rectifier output voltage with a 47kΩ load.

2.5, it can be seen that the output voltage can reach higher than the breakdown voltage. This is because of the time varying nature of the input signal, which prevents the diode from experiencing a constant voltage above the breakdown voltage, so the diode does not actually break down. The ADS software does not seem to take this into account and limits the output voltage with the breakdown voltage as the highest absolute voltage, so there is a discrepancy between the simulation and measurements.

This was resolved by operating the diode rectifiers at a lower input power range that had a lower voltage than the breakdown voltage of the SMS7630 diodes. This eliminated the contradiction between the breakdown voltage of the actual diode and that implemented

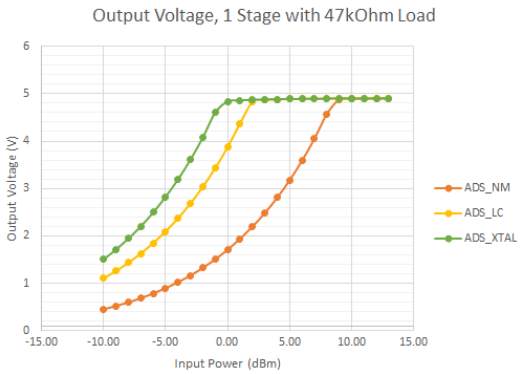

(a) One Stage Rectifier in ADS.

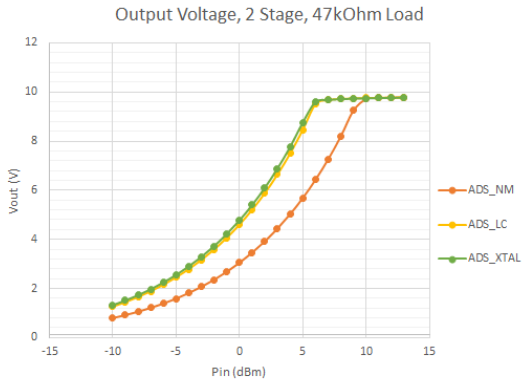

(b) Two Stage Rectifier in ADS.

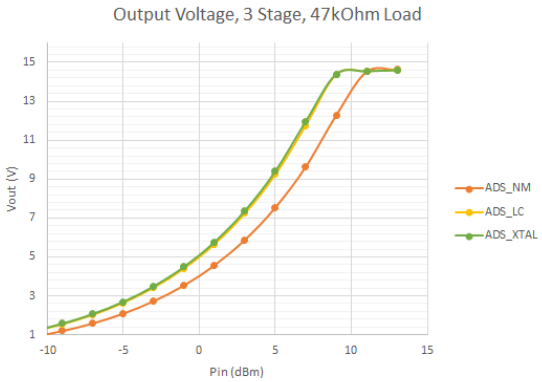

(c) Three Stage Rectifier in ADS.

Figure 2.6: ADS simulation of Dickson rectifier with various numbers of stages and matching networks.

in the diode Spice model. Figure 2.7 shows the simulated output power compared to the measured at an input power range of -20 dBm to 1 dBm. The simulations are consistent with measured results at this input power range.

The methods mentioned previously in Section 2.2 and their performance are summarized in Table 2.2 below in comparison to the results from this work.

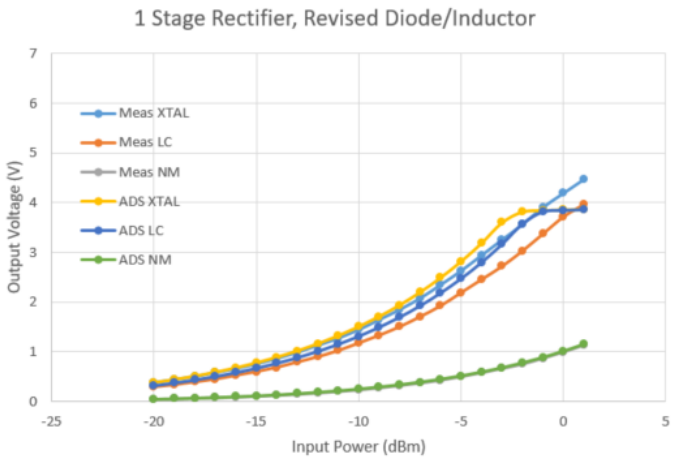

(a)

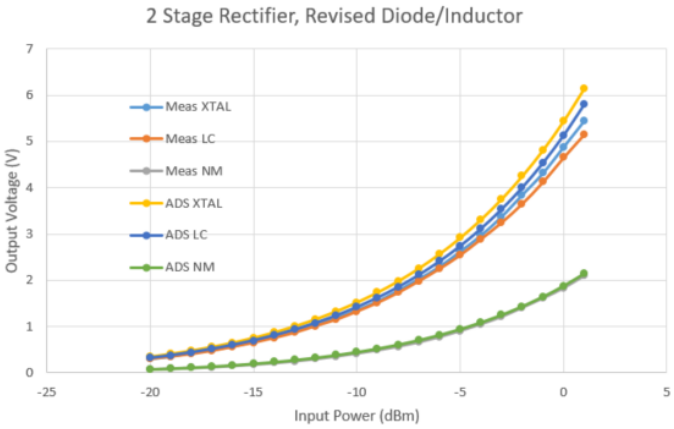

(b)

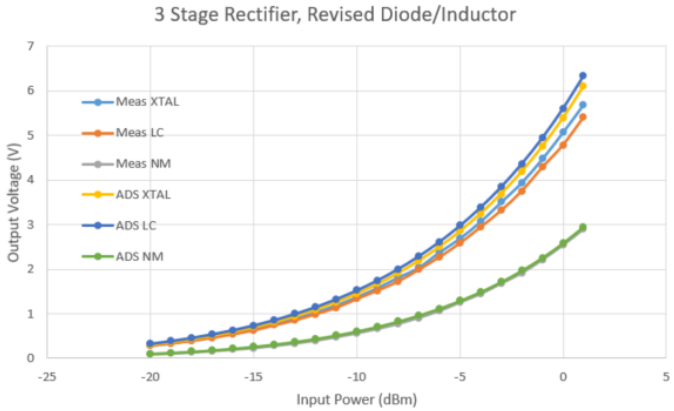

(c)

Figure 2.7: Simulated and measured output voltage for various stage rectifiers at a lowered input power.

Table 2.2: Rectifier performance comparison table.

Work	Diode	Matching Scheme	Frequency	Pin Range	Max Efficiency	Vout, Load
[17]	SMS7630, single	Transmission line	700 MHz	-15 to 10 dBm	76% at -5 dBm	–
[18]	HSMS2820, single	OCFD antenna	0.9-1.1 GHz, 1.8-2.5 GHz	-25 to 25 dBm	75% at 20 dBm	–
[15]	HSMS285C, doubler	Discrete LC	434 MHz	-35 to 0 dBm	55% at 0 dBm	1 V, 20 kΩ
[15]	HSMS285C, Delon 2 stage	Discrete LC	434 MHz	-30 to 0 dBm	50% at 0 dBm	2.9 V, 16 kΩ
[19]	HSMS286C, doubler	Crystal	13.56 MHz	-35 to -20 dBm	68% at -20 dBm	4.72 V, open
This work	SMS7630, doubler	LC	18.007 MHz	-20 to 12 dBm	40% at -8 dBm	1.8 V, 47 kΩ
This work	SMS7630, doubler	Crystal	18.007 MHz	-20 to 12 dBm	60% at -8 dBm	2.1 V, 47 kΩ
This work	SMS7630, Dickson 2 stage	LC	18.003 MHz	-20 to 12 dBm	60% at -2 dBm	4.3 V, 47 kΩ
This work	SMS7630, Dickson 2 stage	Crystal	18.003 MHz	-20 to 12 dBm	66% at -2 dBm	4.5 V, 47 kΩ

Table 2.2: Rectifier performance comparison table (continued).

Work	Diode	Matching Scheme	Frequency	Pin Range	Max Efficiency	Vout, Load
This work	SMS7630, Dickson 3 stage	LC	18.002 MHz	-20 to 12 dBm	64% at 2 dBm	6.7 V, 47 kΩ
This work	SMS7630, Dickson 3 stage	Crystal	18.002 MHz	-20 to 12 dBm	77% at 2 dBm	7.4 V, 47 kΩ

2.5 Further Implementation

Proof that a rectifier can benefit from a matching network between the antenna and the rectifier and that the use of a high quality factor inductor-like element greatly improves performance provides the basis for applying this concept in a practical application. Currently, measurements and simulations were done at 18 MHz, which is on the same order of magnitude of 13.56 MHz. In addition, preliminary simulations have been done at approximately 200 kHz, which is in the range of the Qi standard for wireless power transfer. The results can be seen in Fig. 2.8. LC1 uses an ideal inductor (0.3 mH, no ESR) in the matching network, while LC2 uses a discrete inductor with the closest value (0.27 mH, 34 Ω ESR). The resonator model used has a series resonance frequency of 185 kHz and is based off the specifications provided from Fuji for a ceramic disc resonator used in Section 3.6 in a resonator-based DC-DC converter.

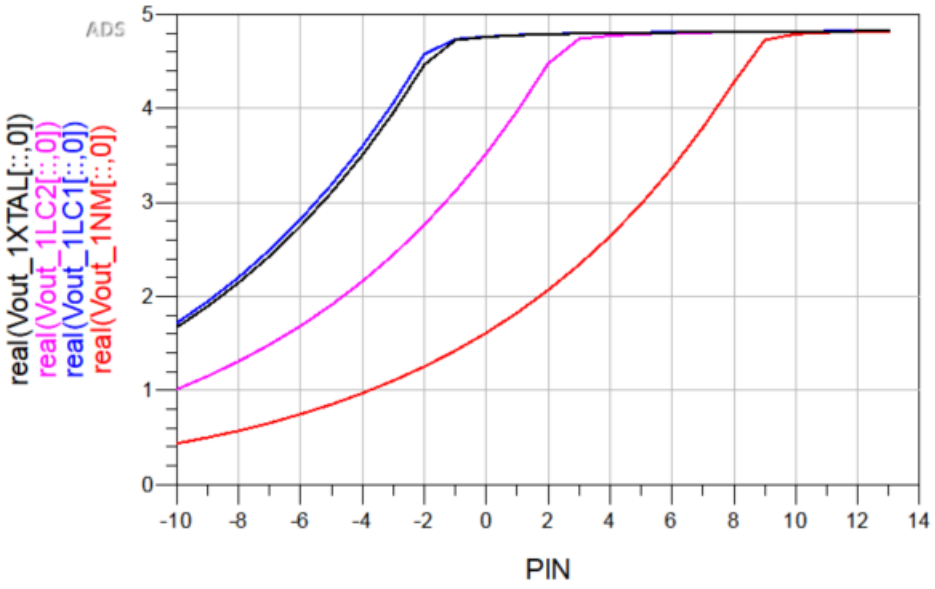

Figure 2.8: Simulated output voltage for 1 stage rectifier at 200 kHz for various matching networks. XTAL is matching with resonator; LC1 is matching with ideal inductor; LC2 is matching with realistic inductor; NM is no matching.

Chapter 3

DC-DC Converter Using Piezoelectric Resonator as Energy Storage Element

3.1 Overview

Although rectifiers can regulate the output voltage through the use of a variable number of stages, any change in output voltage will require a change in the rectifier topology, which is inefficient and undesirable in terms of board space and performance. A solution to this problem is to use a switching DC-DC converter, which regulates the output rectifier voltage to the desired output voltage needed through adjusting the pulse width modulating (PWM) signals controlling switches in its power stage. A DC-DC converter uses an energy storage element, such as an inductor, and a series of switches to manipulate the input voltage to the desired output voltage by controlling the duty cycle of switches' driving PWM signals. While an external control module is needed, a DC-DC converter avoids the disadvantages of solely relying on the rectifier to control the output voltage by producing a large range of output values with a single circuit.

3.2 Literature Review

A basic buck-boost converter is shown in Fig. 3.1, where the inductor is the energy storage element for adjusting the output voltage, the load capacitor is chosen for the desired output ripple, and the load determines the output power. When switch K1 is on continuously, the circuit functions as a boost converter, with a PWM signal controlling switch K2 and the output voltage. Diode D1 is off in this mode of operation. To use this circuit as a buck converter, switch K2 is always off, diode D2 is always on, and a PWM signal controls switch K1 and the output voltage [21].

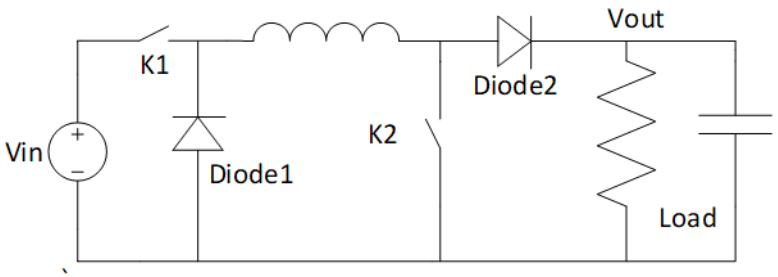

Figure 3.1: Noninverting buck-boost converter.

In addition to using an inductor to store energy in a magnetic field, energy in the DC-DC converter can be stored in vibrations through the use of piezoelectric materials. [22] uses a piezoelectric transformer, which consists of two piezoelectric materials: one that converts a voltage to vibration and another that converts the vibration back into a voltage. The voltage gain of this depends on the size of the materials and the number of layers of piezoelectric material used [23]. In addition, piezoelectric resonators can be used in DC-DC converters by taking advantage of the sinusoidal current generated when the resonator is excited at the resonant frequency. This concept has been shown in [24], [25], [26], and [27].

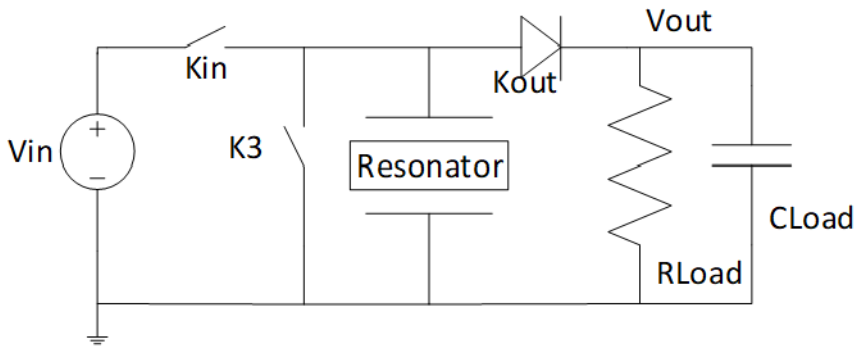

Figure 3.2: DC-DC converter with piezoelectric resonator.

3.3 Design

The following DC-DC converter utilizing a piezoelectric resonator follows the topology presented in [26] and is compared to the classic noninverting buck-boost converter (Fig. 3.1) using simulation in LTSpice. The basic schematic is shown in Fig. 3.2. In comparison to the inductor-based converter, the piezoelectric-based converter has replaced D1 with switch K3 and eliminated switch K2.

Because a main concern in wireless energy harvesting is limited access to sufficient input power, this section focuses on the boost mode of [26]'s converter. The voltage waveforms can be seen in Fig. 3.3(a), where V_p is the voltage at the top of the resonator (Fig. 3.3(b)).

As can be seen, the piezoelectric current is sinusoidal, suggesting resonant behavior. In reality, the switching occurs at slightly higher than resonance to avoid interruptions in the current and mechanical deformation. The converter's six phases can be grouped into two sections: charge transfer when the resonator is connected to an external source or load and voltage variation when the resonator is isolated. Charge conservation and energy conservation govern the converter's behavior and is defined by Eqns 3.1 and 3.2. V_{in}, V_3, V_{out} are the voltages across the resonator when Kin, K3, and Kout are on, respectively. This leads to the simplification shown in the second line of Eqn 3.1, since V_p is 0 V when K3 is

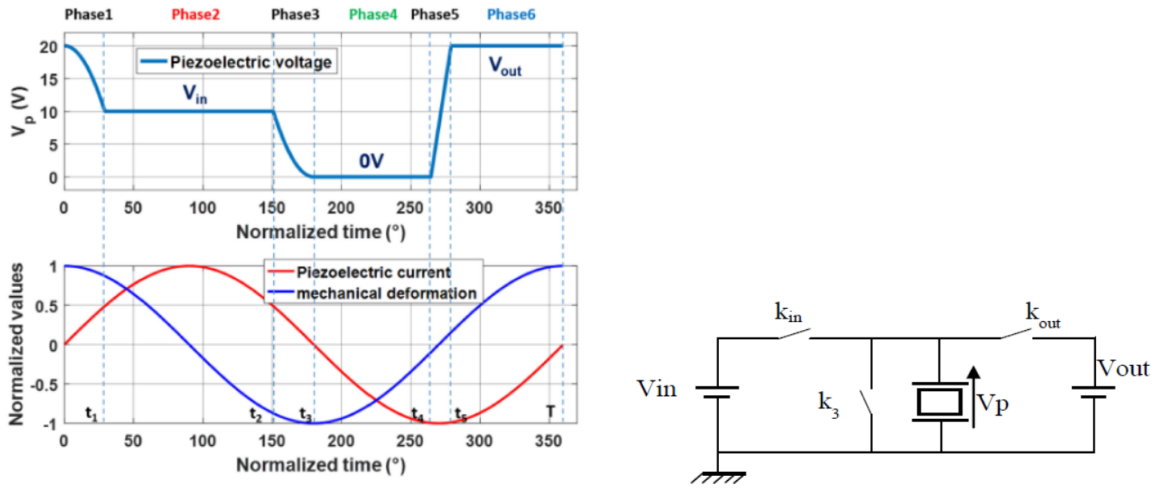

(a) Voltage and current waveforms.

(b) DC-DC converter with electromechanical resonator schematic.

Figure 3.3: DC-DC converter with resonator [26].

on.

$$V_{in}Q_{in} + V_3Q_3 + V_{out}Q_{out} = 0 \tag{3.1}$$

$$V_{in}Q_{in} + V_{out}Q_{out} = 0$$

$$Q_{in} + Q_3 + Q_{out} = 0 \tag{3.2}$$

Implementing zero voltage switching, the output to input voltage ratio for the boost converter can be defined by Eqn 3.3.

$$\frac{V_{out}}{V_{in}} = \frac{2 + R_L C_0 \omega (1 + \cos \omega t_4)/(2\pi)}{1 - \cos \omega t_4} \tag{3.3}$$

where R_L is the load resistance, C_0 is the shunt capacitance of the resonator, ω is the resonant frequency, and t_4 is the time when K3 opens and Phase 5 begins. Intuitively, the load resistance is proportional to the gain, since an infinite load would theoretically produce

the highest gain. The voltage waveform in Fig. 3.3(a) shows the switching times are governed by the zero voltage switching principle except for t_4, which controls the output voltage of the converter and is the degree of freedom. Therefore, the voltage gain only depends on the parameter t_4 and not the other switching times. Because of the sinusoidal nature of the resonator current, the voltage is dependent on a cosine function. However, only values of ωt_4 in the second half of the switching period are valid, since the converter always needs to use the first half of the period to store and discharge energy. This is reflected in the nature of the gain equation that follows the format of $\frac{1+x}{1-x}$,which comes from solving the charge and energy equations and is symmetrical around ωt_4 equal to π.

3.4 Simulations

Because the conventional boost converter connects the inductor to the input source at all times, but the resonator boost converter connects the input to the energy storage element for only one out of the six phases, it is predicted that the resonator boost converter will have lower losses, leading to higher efficiency. The following simulations in LTSpice explore whether this idea is true. Figure 3.4 shows the schematics of the two circuits implemented with ideal diodes and switches, while Fig. 3.5 shows the schematics implemented with off-the-shelf diodes (SMS7630) and NMOS (CSD17585F5) switches. The resonator model used is based off the piezoelectric disc resonator in [26]. Simulations show the converter operating in boost mode at a switching frequency of 83 kHz with a target output voltage around double the input voltage (10 V).

Note that in Fig. 3.5(b) an additional NMOS is required for the input switch. This is to prevent backflow of current through the source to drain diode when the NMOS is off. The simulation results are summarized below in Table 3.1, and the steady-state waveforms are shown in Fig. 3.6 and Fig. 3.7. The output voltage in the ideal circuit is 18 V, but large voltage drops across the parasitic resistances of the SMS7630 diodes limit the output voltage

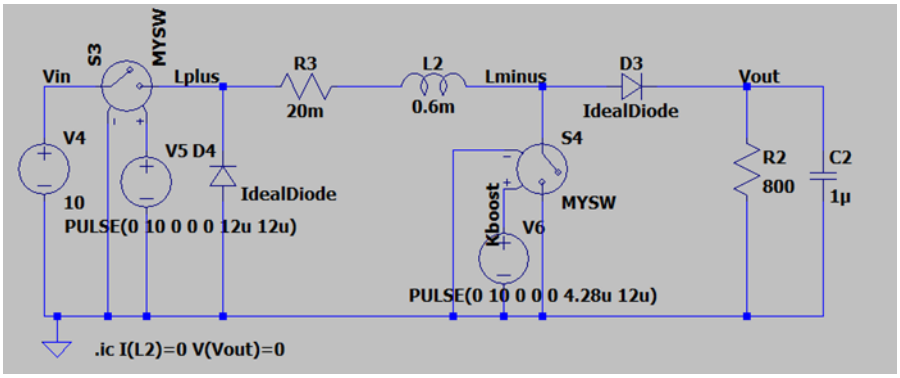

(a) Inductor-based converter.

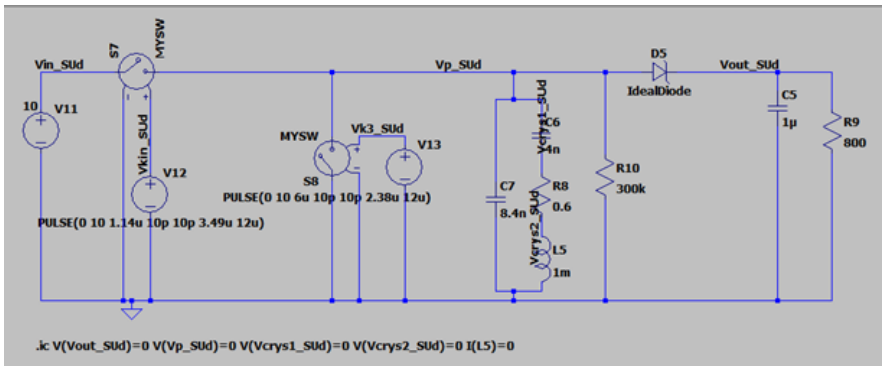

(b) Resonator-based converter.

Figure 3.4: Schematic of buck-boost converter with ideal diodes and switches.

to around 14 V in the non-ideal case. A comparison of these results to those in existing literature is shown in Table 3.2.

Contrary to predictions, the efficiency of the resonator-based converter is comparable to that of the inductor-based converter but not higher. Upon closer inspection, there are current spikes in the current drawn from the voltage source, which degrade the efficiency by increasing power draw (Fig. 3.8). However, the value of the current spikes is so high (several amps compared to the resonator current of around 200 mA) that this is most likely attributed to simulation computations and is not guaranteed to occur in the actual circuit. If this did occur in a prototype implementation, a different MOSFET can be used as the switching device. The results of these simulations show a boost converter with a piezoelectric

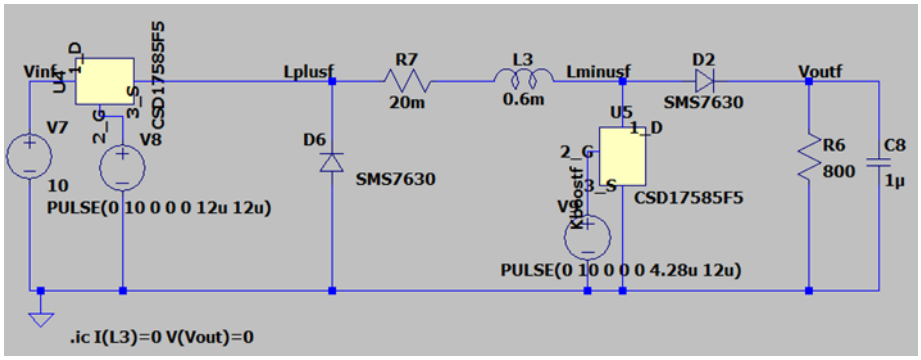

(a) Inductor-based converter.

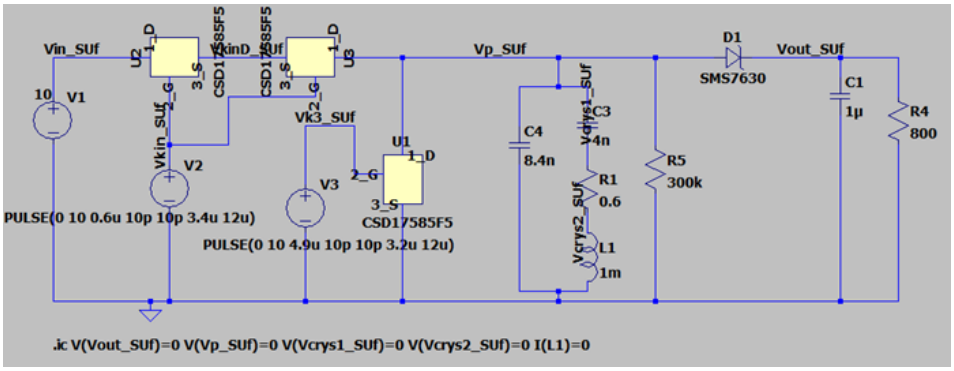

(b) Resonator-based converter.

Figure 3.5: Schematic of buck-boost converter with realistic diodes and transistor-based switches.

resonator is a potential candidate to replace conventional inductor-based DC-DC converters.

3.5 Further Implementation

Future steps after showing a piezoelectric resonator can be used to store energy in a DC-DC converter include combining this converter with the rectifier and choosing a different disc resonator that operates in the Qi standard frequency range. The proposed resonator resonates at 100 kHz in the radial mode, with a thickness mode resonant frequency in the megahertz range. This could have potential applications in NFC charging, which operates at 13.56 MHz. The results of a preliminary simulation operating at a switching frequency

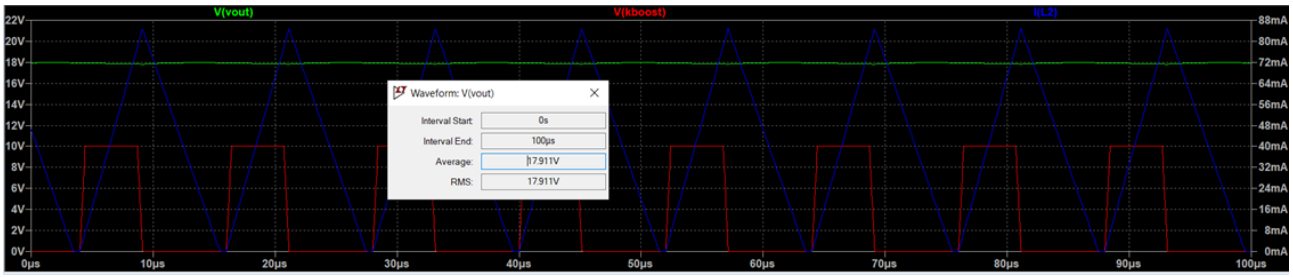

(a) Inductor-based converter voltage waveforms.

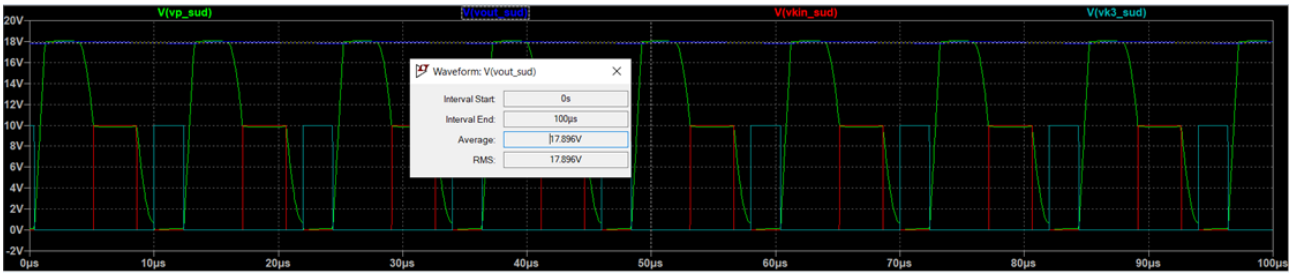

(b) Resonator-based converter voltage waveforms.

Figure 3.6: Simulated voltage waveforms for boost converter using ideal switches and diodes for a 12 μs switching period.

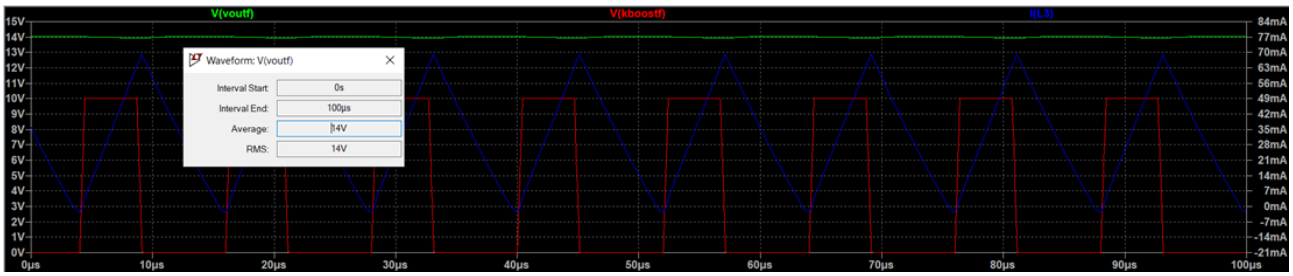

(a) Inductor-based converter voltage waveforms.

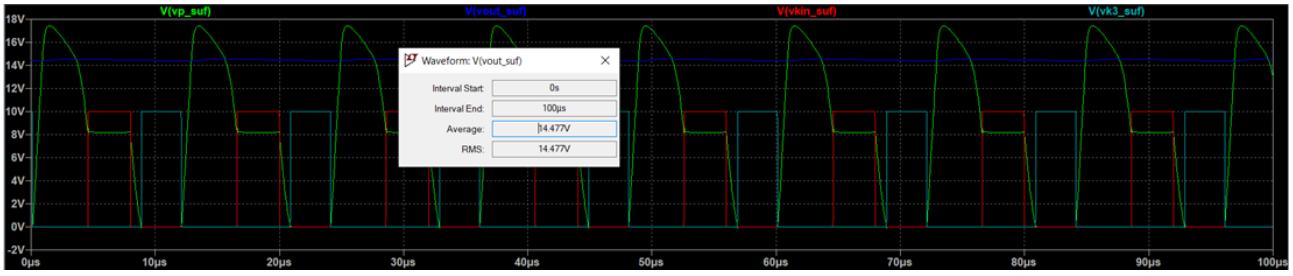

(b) Resonator-based converter voltage waveforms.

Figure 3.7: Simulated voltage waveforms for buck-boost converter with realistic diodes and switches for a 12 μs switching period.

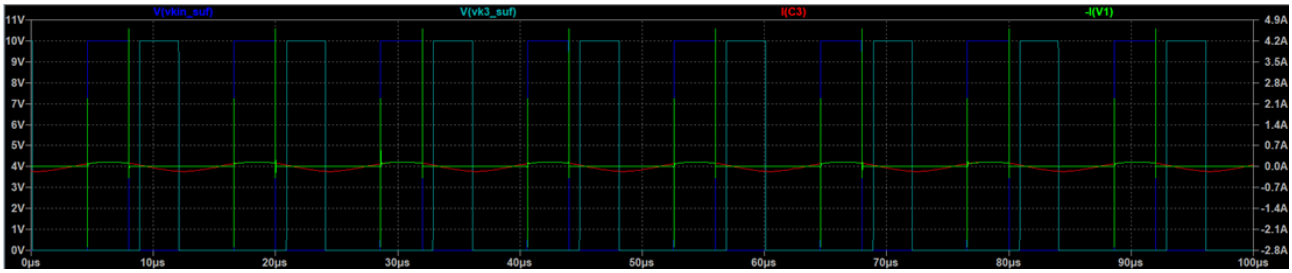

Figure 3.8: Simulated current waveforms of resonator converter with respect to switching waveforms. Current of input voltage source V1 is inverted to show current leaving voltage source.

Table 3.1: Output values for boost converter for various energy storage and switching elements.

Energy storage, switch	**Output Voltage (V)**	**Output Ripple (mV)**	**Efficiency (%)**
Inductor, Ideal	17.9	144	98.75
Resonator, Ideal	17.9	210	95.07
Inductor, NMOS	14.0	114	76.94
Resonator, NMOS	14.5	171	67.93

of approximately 110 kHz is shown in Fig. 3.9. The resonator model for this schematic was altered from the previous model to have a resonant frequency of 100 kHz. Usually, the switching frequency is slightly higher than the resonant frequency of the resonator to ensure all the energy transfer stages can be completed within a resonant period. Figure 3.10 shows boost converters operating at 110 kHz with various energy storage and switching elements. Table 3.3 summarizes the performance of the ideal resonator-based DC-DC converter shown in Fig. 3.9(a), the ideal inductor-based, nonideal resonator-based, and nonideal inductor-based DC-DC converter shown in Fig. 3.10(a), Fig. 3.10(b), and Fig. 3.10(c), respectively.

Table 3.2: Comparison of various parameters for DC-DC Converters.

	Energy Storage	Mode	Vin (V)	Vout (V)	Pout (W)	Efficiency (%)	Freq (kHz)	Method
This work	Piezo Resonator	boost	10	14.5	0.262	68	83	LTSpice
This work	Inductor	boost	10	14	0.245	77	83	LTSpice
[27]	Piezo Resonator	boost	10	20	0.1-0.2	98	90, 190	–
[26]	Piezo Resonator	boost	10	20	0.150	98-99	89	Analytical Model
[26]	Piezo Resonator	boost	10	15	0.160	98	89	PCB
[24]	Piezo Resonator	buck	100	90	2	99	114	PCB
[25]	Piezo Resonator	boost	100	220	10	98	114	LTSpice
[28]	Inductor	boost	15	17.5	26	95.3	600	0.18um BCD
[29]	Piezo Resonator	buck	50	30	8	95	6300	PCB

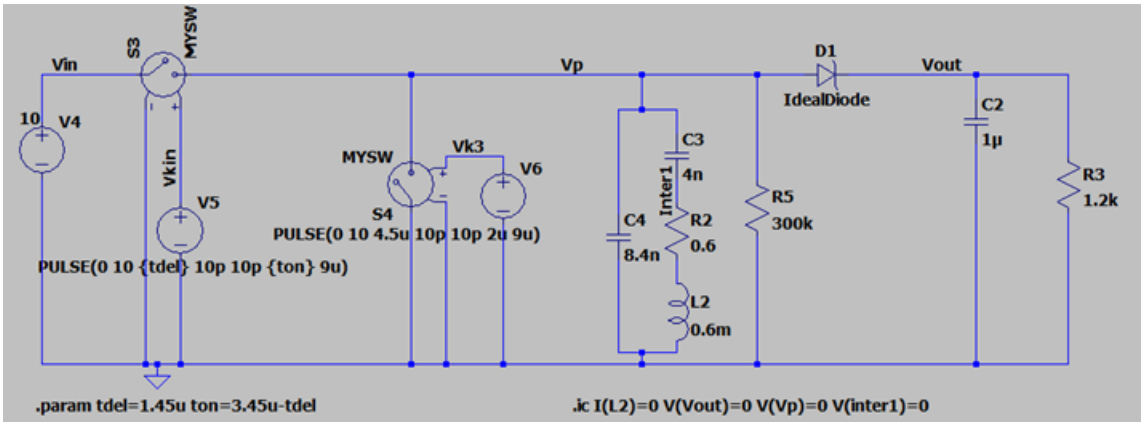

(a) Schematic of converter with 100 kHz resonator and ideal switches and diodes.

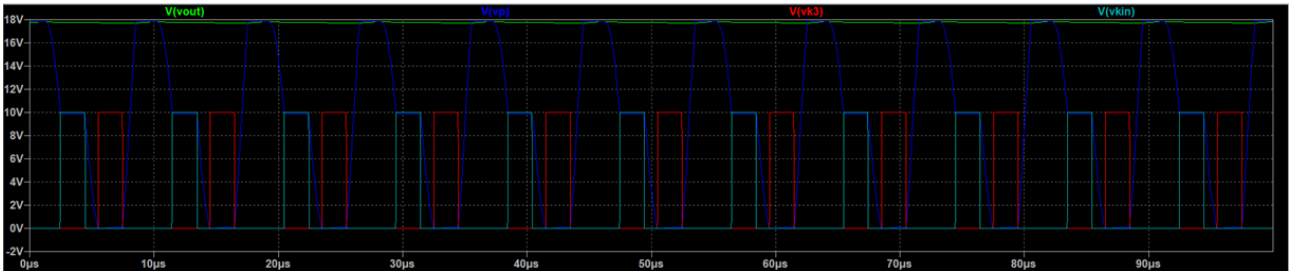

(b) Simulated voltage waveforms.

Figure 3.9: Boost converter with 100 kHz resonator operating with a switching frequency of 110 kHz.

3.6 PCB Prototype Testing

The resonator based DC-DC converter was implemented on a printed circuit board (PCB) with a ceramic resonator manufactured by Fuji as shown in Fig. 3.11. The ceramic resonator used has the frequency response shown in Fig. 3.12 while operating in the radial mode, which means it resonates along its radius. Table 3.4 summarizes the parameters of the ceramic resonator calculated from the measured frequency response and from the factory provided specifications. The largest difference is in the equivalent resistance, which measurements show to be two orders of magnitude higher than what was estimated from the mechanical Q in the datasheet. This is expected: looking at the measured frequency response in Fig. 3.12, the resolution bandwidth is 1 kHz and could be limiting what can be measured as the

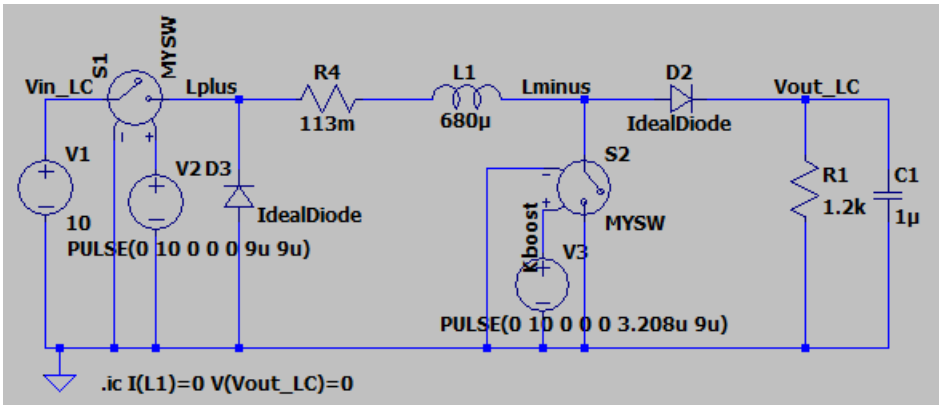

(a) Schematic of converter with inductor. ideal switches, and ideal diodes.

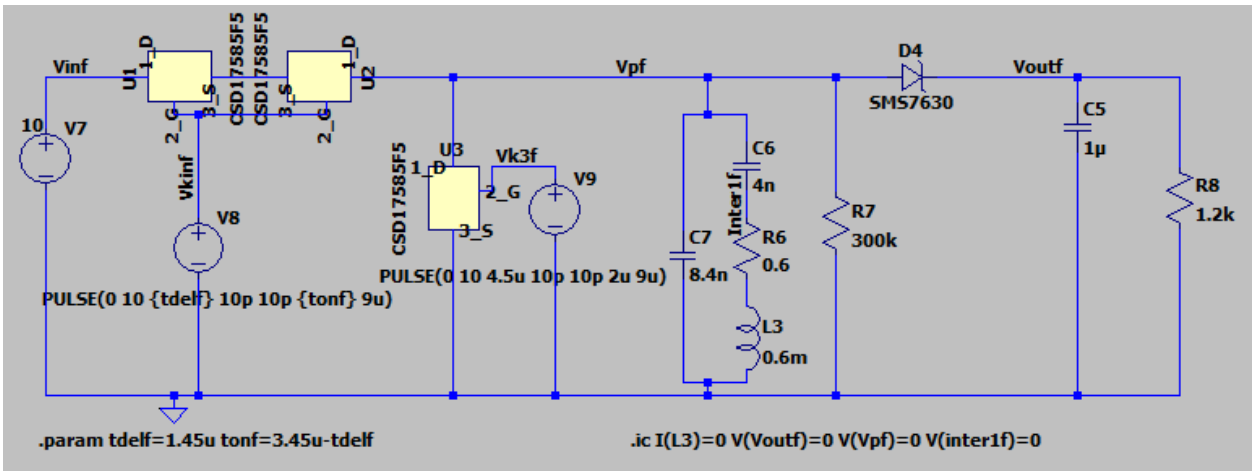

(b) Schematic of converter with resonator, transistor-based switches, and realistic diodes (nonideal).

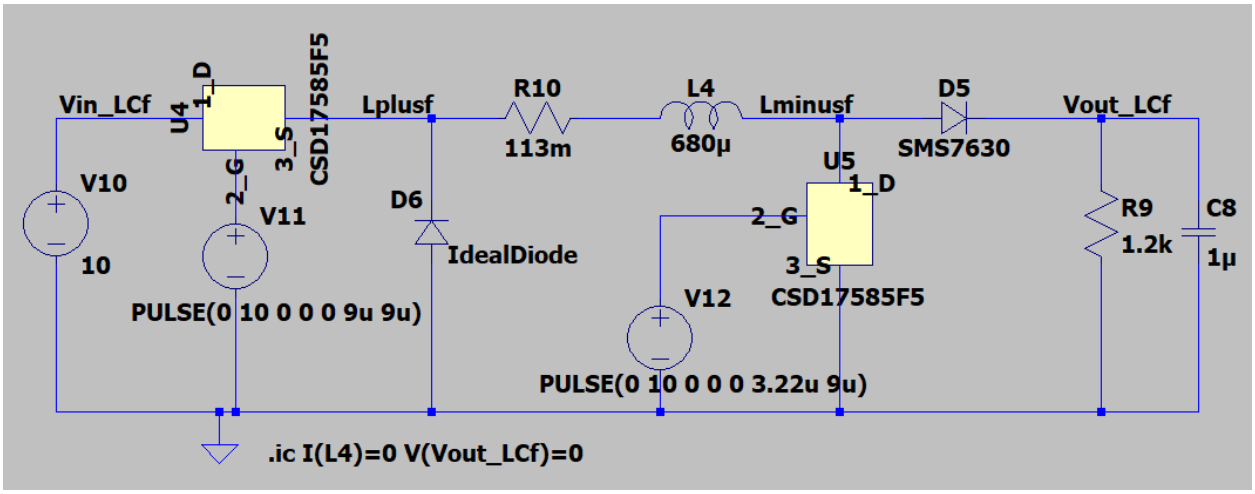

(c) Schematic of converter with inductor, transistor-based switches, and realistic diodes (nonideal).

Figure 3.10: Additional boost converter schematics with a switching frequency of 110 kHz.

Table 3.3: Performance of DC-DC converters with a switching frequency of 110 kHz. Ideal or non-ideal refers to the switches and diodes used.

	Input Voltage (V)	Output Voltage (V)	Output Power (mW)	Efficiency (%)	Energy Stored (nJ)
Resonator, Ideal	10	17.8	265	95	38
Inductor, Ideal	10	17.9	267	99	1.2
Resonator, Non-ideal	10	14.3	170	68	66
Inductor, Non-ideal	10	14.1	165	78	0.63

resonant frequency and bandwidth. Because the bandwidth is related to the quality factor by Eqn. 3.4, a wider bandwidth would produce a lower quality factor. A lower quality factor is reflected in a higher resistance, and future measurements should be done with a lower resolution bandwidth to verify the exact bandwidth. The DC-DC converter is driven by either by a microcontroller or stimulus system as shown in Fig. 3.13.

$$Bandwidth = \frac{2\pi f_0}{Q} \tag{3.4}$$

The previous simulations from Section 3.4 were modified to incorporate the NMOS transistors (RE1C002) and diode (MMBD452) used in the PCB implementation. The diode model was modified from the previous SMS7630 diode one due to lack of an available Spice model, so some parameters not provided in the MMBD datasheet were borrowed from the SMS7630 diode. Figure 3.14 shows the circuit schematic. The input is 5 V, and the switching frequency is 200 kHz. The output was measured with switching signals of 3.3 V and 5 V to observe the different behavior between using the TI MSP432 microcontroller, which has

an output voltage of 3.3 V, and the Tektronix HFS9003 stimulus system, which was used to output 5 V switching signals. Figure 3.15 shows the difference in output and resonator voltage due to use of different switching signal amplitude. However, both cases produced a lower boost ratio than 1.4, which was achieved in Sections 3.4 and 3.5, and the converter operating with 3.3 V switching signals did not even boost the input with an output to input voltage ratio of only 0.63. This was resolved using a floating driver for the input NMOS switch as shown in Fig. 3.16. Because the negative terminal is connected to the source of the transistors, the potential difference between the gate and source terminal is driven to what the voltage source is supplying. Figure 3.17 shows the output and resonator waveforms for 3.3 V switching signals. These results are summarized in Table 3.5.

The measured output of the resonator-based converter is shown in Fig. 3.18(a) and 3.18(b) in comparison with the resonator voltage and the gate signals, which are pulses with magnitudes of 3.3 V and 5 V, respectively. The 3.3 V switching signals does not completely turn on or off the NMOS switches. In both cases, the output voltage is lower than the applied input voltage of 5 V and the max resonator voltage, which suggest that the diode voltage drop from the forward voltage (approximately 0.5 V) and series resistance (not provided in datasheet but estimated in simulation to be 20 Ω based off the SMS7630 Spice model) is too high to sufficiently boost the output voltage. In addition, the discrete NMOS transistors have a high threshold voltage, so the resonator voltage when connected to the input voltage is only 4.3 V in the PCB implementation. The simulation predicts that the maximum resonator voltage should be approximately 6 V, but in the PCB implementation the maximum resonator voltage is only 4.6 V, which suggests either additional parasitics not modeled or incomplete switching in the transistors that is no longer accounted for in the Spice models. Table 3.5 summarizes these voltages for the simulated and measured results. The input voltage was lowered compared with a switching signal of 5.1 V to see when the incomplete switching starts to occur. The boost ratio and output voltage are plotted in

Fig. 3.19 as a function of input voltage. It can be seen that without a floating driver, the converter cannot boost any voltage higher than 100 mV. Figure 3.20 shows the voltage waveforms for a 100 mV input. Although voltage boost occurs, the resonator voltage is quite distorted compared to what is expected. All of these issues make a discrete implementation of the resonator-based DC-DC converter with only NMOS transistors and diodes difficult and impractical. An integrated solution is considered in Chapter 6, where additional changes to the design are also implemented such as changing the NMOS switch at the input and the output diode to a PMOS switch.

Table 3.4: Calculated parameters from frequency response or estimated from datasheet specifications of Fuji ceramic resonator.(*Note: these values should be re-calculated from a frequency response measured with a smaller resolution bandwidth.)

Parameter	From measurements	From datasheet	Percent error
Diameter (mm)	11.94	11.99	0.42%
Thickness (mm)	0.72	0.75	4.00%
C_p (nF)	1.92	2	4.00%
C_m (nF)	0.63	0.71	11.27%
L_m (mH)	1.16	1.04	11.54%
R_m (Ω)	*13.37	0.48	2685%
Q	*101	2500	95.96 %
Resonant frequency, f_0 (kHz)	184.67	185.83	0.62%

3.7 Conclusion and Future Work

Simulations at 89 kHz proved consistent with literature and were modified to operate at 110 kHz, which is in the Qi frequency range. Then, a PCB prototype was built using a ceramic disc resonator with a resonant frequency of 185 kHz and a switching frequency of 200 kHz. Although the switching and voltage waveform shapes were consistent with simulations,

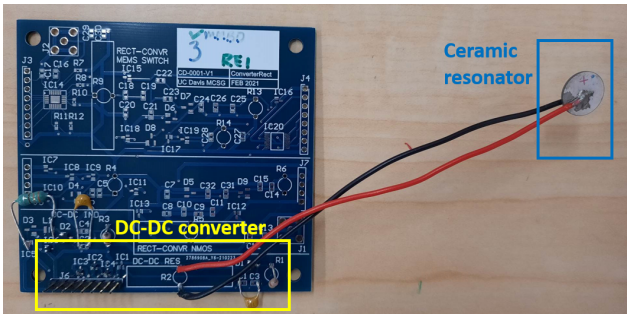

Figure 3.11: Resonator-based DC-DC converter on a printed circuit board.

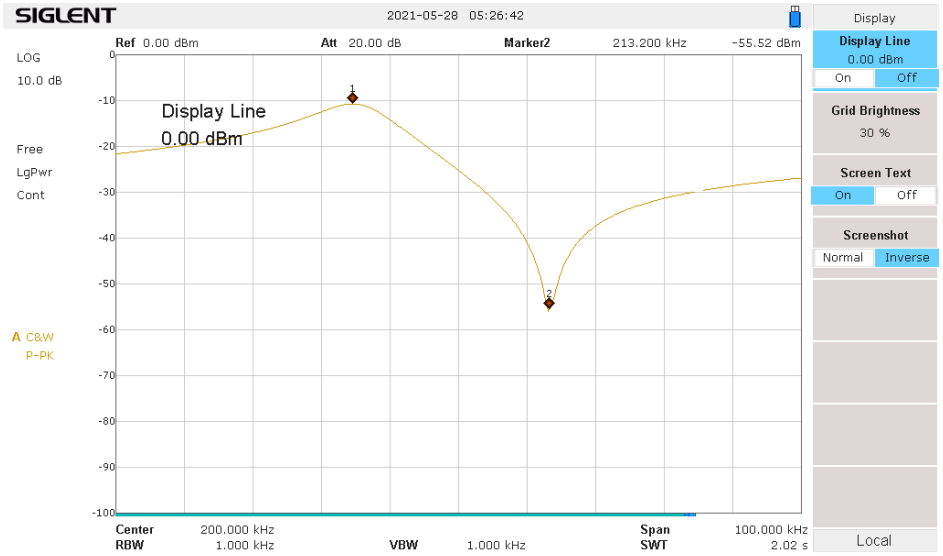

Figure 3.12: Measured frequency response of Fuji ceramic resonator.

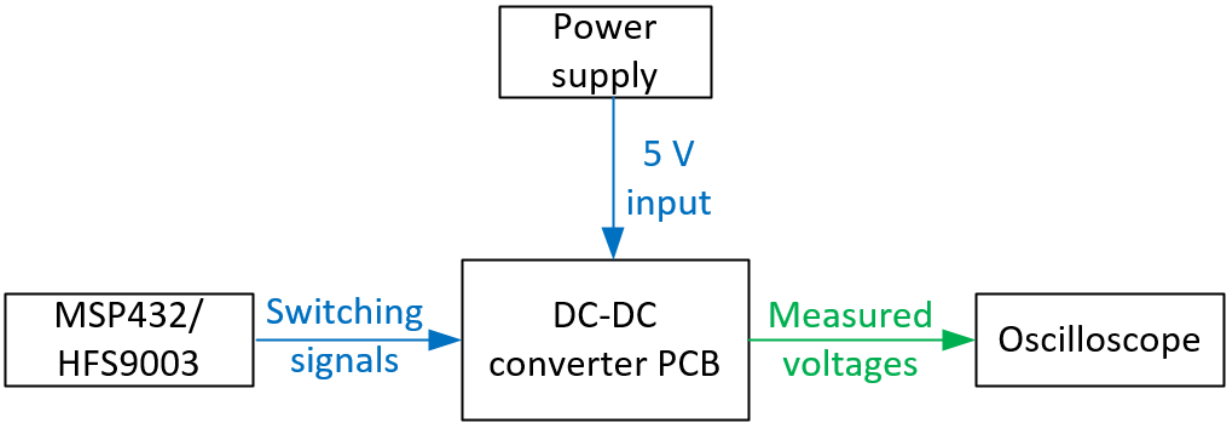

Figure 3.13: Test setup for PCB implementation of resonator-based DC-DC converter.

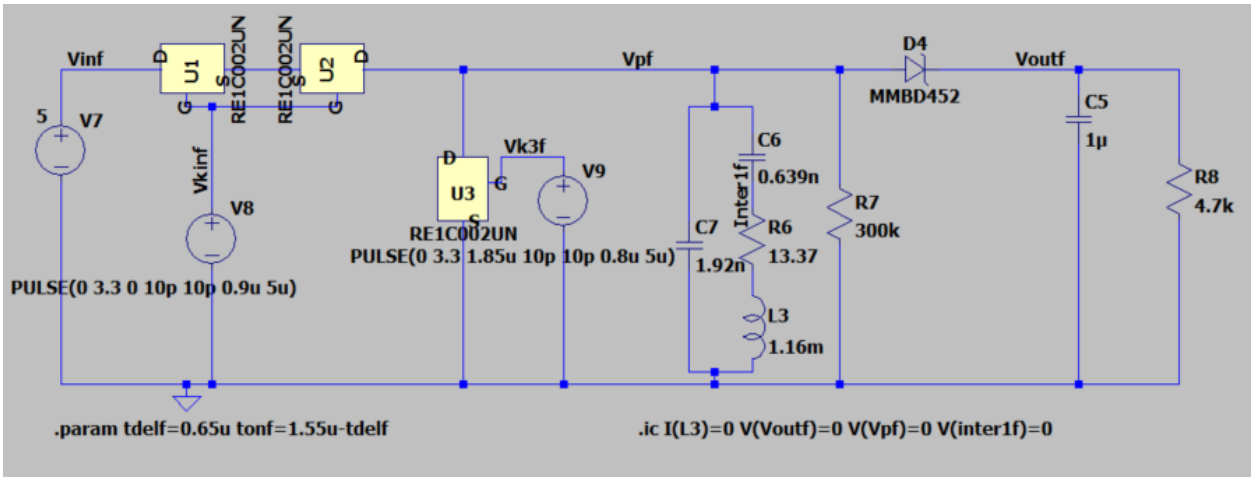

Figure 3.14: Simulation schematic with models of discrete NMOS switches and diodes used in PCB.

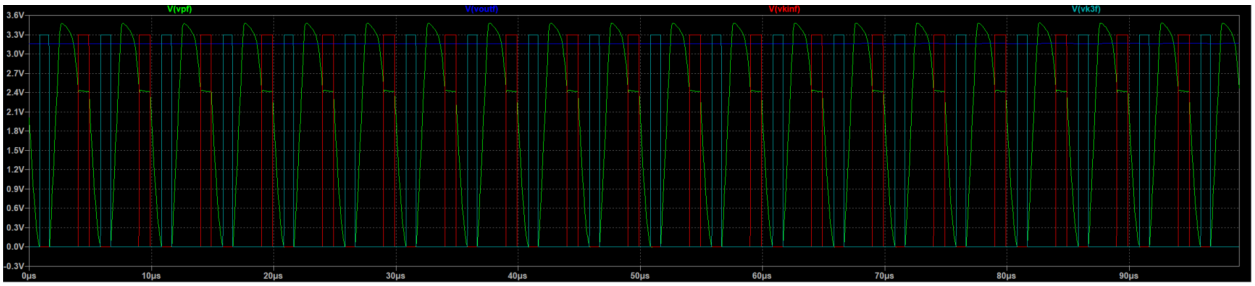

(a) Simulated voltage response of DC-DC converter driven with 3.3 V switching signals.

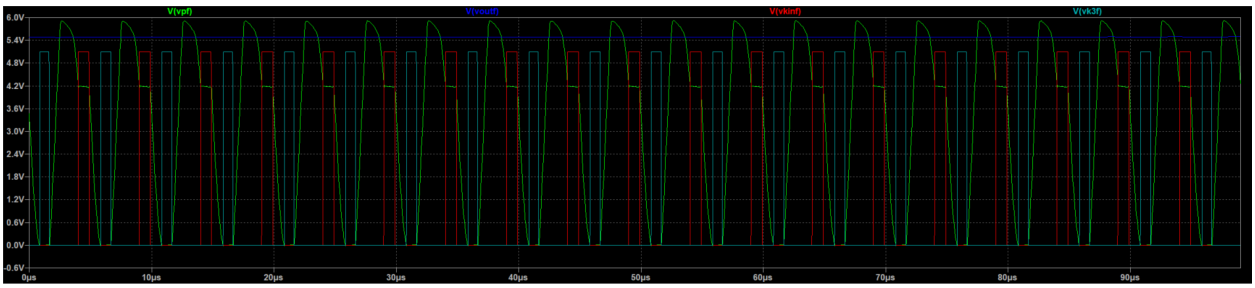

(b) Simulated voltage response of DC-DC converter driven with 5.0 V switching signals.

Figure 3.15: Simulated resonator and output voltage waveforms with different switching signal amplitudes.

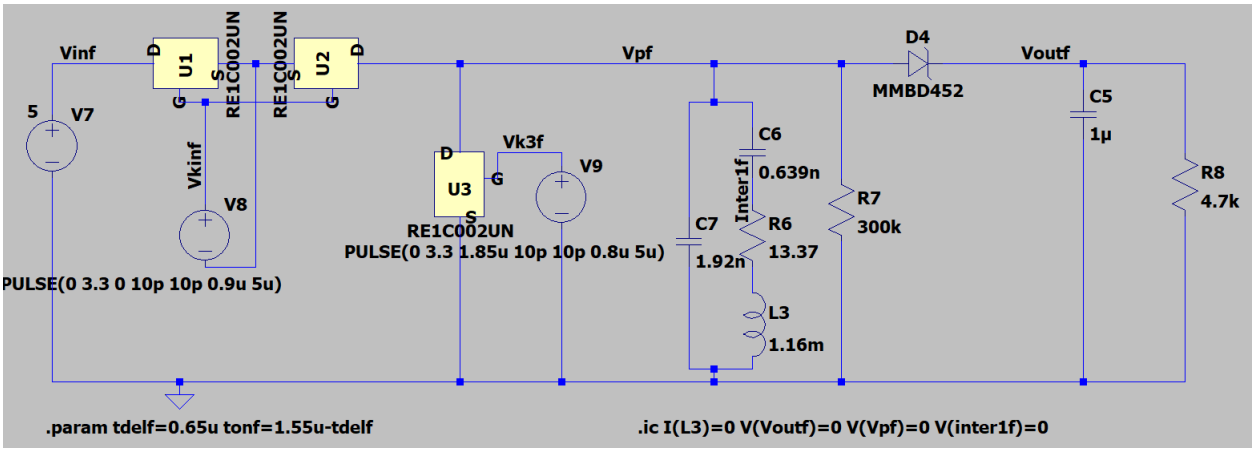

Figure 3.16: Simulation schematic with floating driver for input NMOS transistor switches.

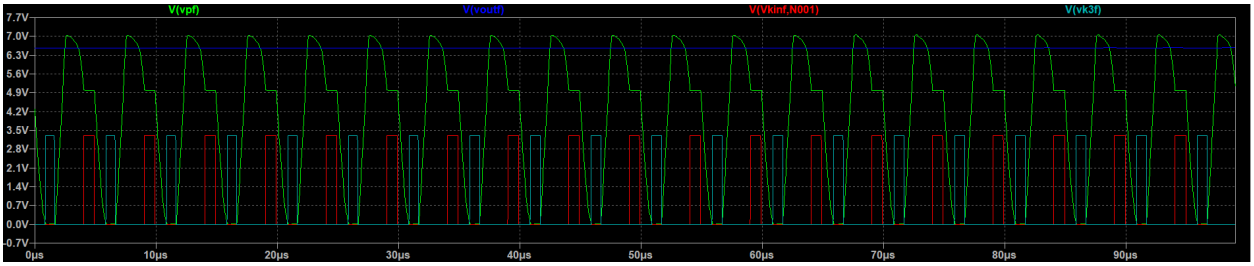

Figure 3.17: Simulated voltage response for DC-DC converter with 3.3 V switching signals and a floating driver for the input switch.

Table 3.5: Summary of simulated and measured resonator voltage when connected to the input ($V_{p,input}$), at maximum ($V_{p,max}$), input (V_{in}) and output voltage (V_{out}), and switching voltage (V_{sw}).

Type	$V_{p,input}$ (V)	$V_{p,max}$ (V)	V_{out} (V)	V_{in} (V)	V_{sw} (V)	Boost Ratio
simulated	2.42	3.47	3.15	5	3.30	0.65
simulated	4.18	5.91	5.49	5	5.10	1.10
simulated, floating	4.98	7.02	6.57	5	3.30	1.31
simulated, floating	4.98	7.03	6.57	5	5.10	1.31
measured	2.50	3.50	3.10	5	3.30	0.62
measured	4.28	4.64	4.10	5	5.10	0.82

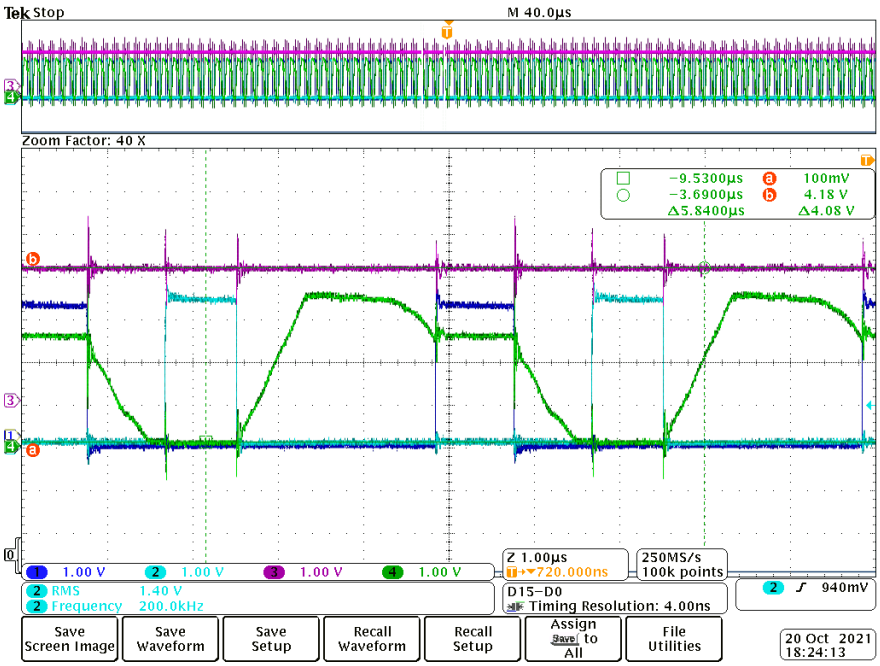

(a) Measured voltage response of DC-DC converter driven with 3.3 V switching signals.

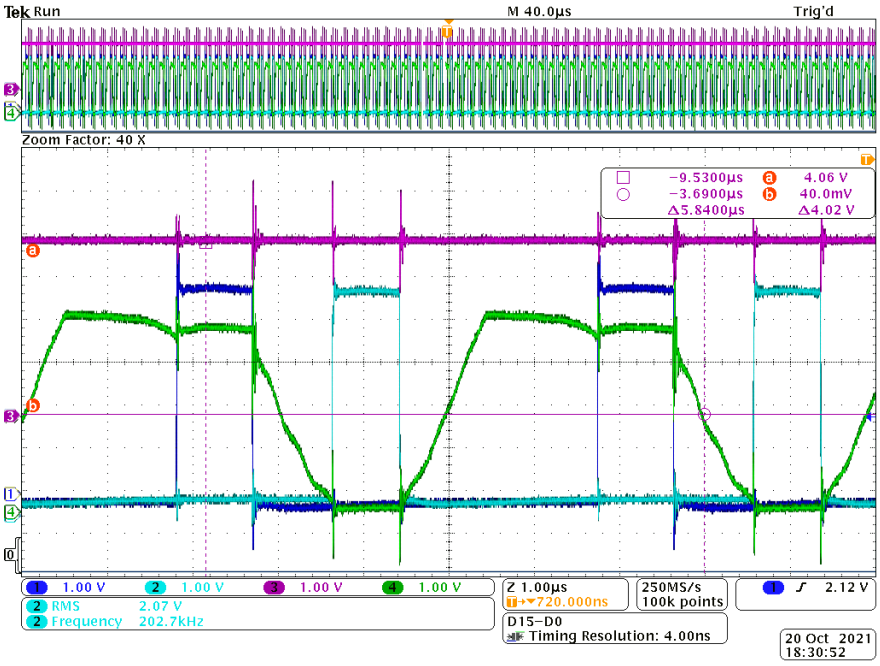

(b) Measured voltage response of DC-DC converter driven with 5.0 V switching signals.

Figure 3.18: Resonator voltage (green), output voltage (magenta), and input switching (blue) and k3 (switch parallel with resonator) switching (cyan) signals for PCB DC-DC converter.

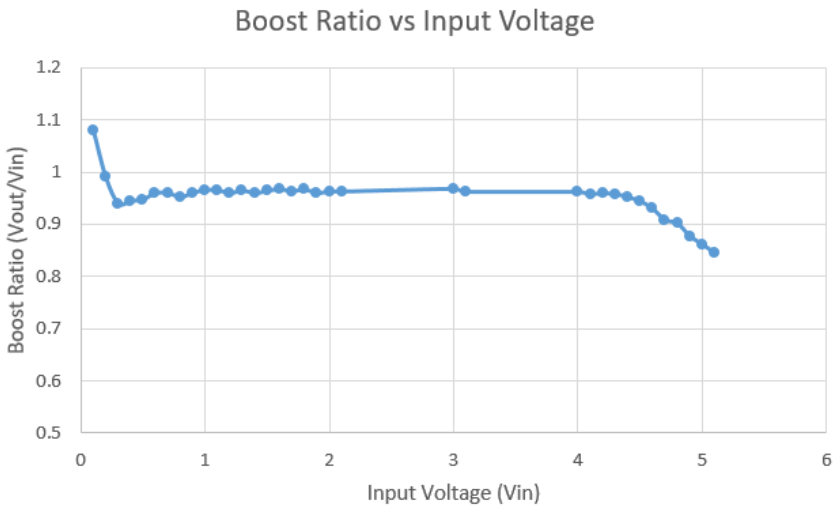

(a) Measured output boost ratio as a function of input voltage.

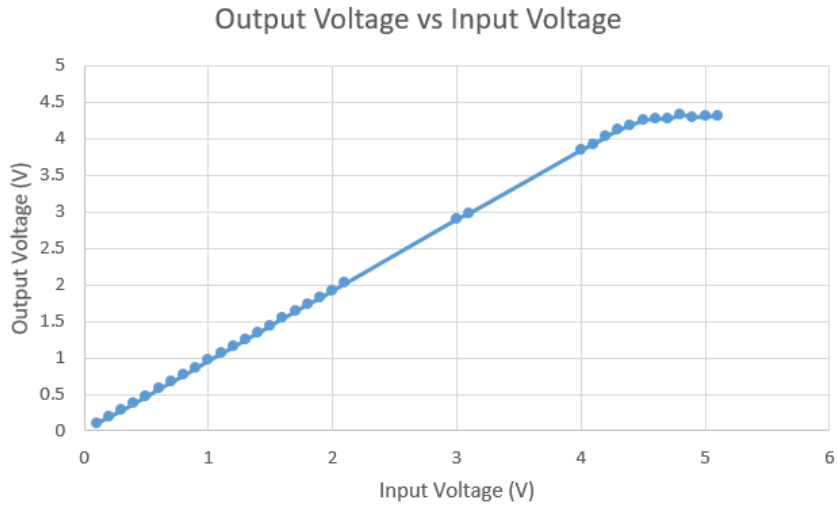

(b) Measured output voltage as a function of input voltage.

Figure 3.19: Measured output boost ratio (a) and output voltage (b) plotted at various input voltages.

Figure 3.20: Measured output voltage (green), resonator voltage (magenta), and switching signals (yellow and blue) for resonator-based converter with a 100 mV input.

the output voltage was much lower than expected due to the large parasitics of discrete transistors. In PCB testing, the input voltage was lowered to find a value that allowed the NMOS transistors to switch on and off sufficiently to boost the input voltage, which turned out to be 100 mV. This showed that in order to maintain converter boost performance, the input voltage would have to be low, the input NMOS switches would need to use a floating driver (which was shown in simulation), or the input NMOS switches would need to be replaced with PMOS transistors (shown in Chapter 6).

Chapter 4

Rectifier and DC-DC Converter Combined System

4.1 Resonator Switching Network

A block diagram of the proposed combined rectifier and DC-DC converter is shown below in Fig. 4.1. The output of the rectifier is the input of the DC-DC converter (V_{in}). The main advantage of this design is sharing the piezoelectric resonator between the matching network of the rectifier and the DC-DC converter. This can be accomplished through two proposed methods:

1. In the 100 kHz-200 kHz range, the resonator is used for matching in the rectifier as long as a Qi transmitter is detected. The rectifier will store the energy in a supercapacitor or other component that does not require a regulated voltage input. When there is no wireless energy source detected or the input RF signal is too low, the resonator will be used as the energy storage element in the DC-DC converter. Because the Qi standard for wireless charging produces higher power than NFC charging, it can be assumed that when the Qi rectifier is used, there is no need for a DC-DC converter. When there is no Qi transmitter present, the resonator used in the matching network (in the range of 100-200 kHz) can be

Table 4.1: Condition of switches for using the resonator in the rectifier or DC-DC converter.

Resonator Circuit	**DC1**	**DC2**	**DC3**
Rectifier	ON	OFF	OFF
DC-DC Converter	OFF	ON	ON

utilized in the DC-DC converter connected to the NFC rectifier.

2. The crystal will be periodically used as either a component in the matching network or as an energy storage element. The time that the crystal spends in each can be determined by a fixed duty cycle or by the voltage of the supercapacitor used to the store the rectifier output.

Sharing the resonator between the rectifier and converter requires the use of additional switches labeled DC1, DC2, and DC3. Although DC2 can replace the diode, using an additional diode eliminates one PWM signal. DC2 can be controlled by the same waveform as DC3, and the diode requires no PWM signal. The operation of the switches are summarized in Table 4.1. Switches Kin and K3 are open when the rectifier is operating and switching during DC-DC converter operation.

A concern with the introduction of the switches DC1-DC3 is the effect on the matching network of the rectifier. Switch DC1 would contribute additional on-resistance, and DC3 would contribute additional shunt capacitance when off. Using the rectifier previously matched at 190 kHz (Fig. 4.2), the effects of the switches can be seen in Fig. 4.3. Figure 4.3(b) shows that the addition of DC1 does not affect the performance, while the addition of DC3 lowers the output voltage because it affects the shunt capacitor in the matching network, as seen in Fig. 4.3(a). This can be remedied by decreasing the shunt capacitance that was originally used in the matching to take into account the contribution from DC3.

However, when the same topology is applied at a higher frequency (18 MHz), the results vary drastically. Figure 4.4 shows the schematics used, and Fig. 4.5 shows the effects of the switches on the output voltage. When both DC1 and DC3 are employed, the rectifier has

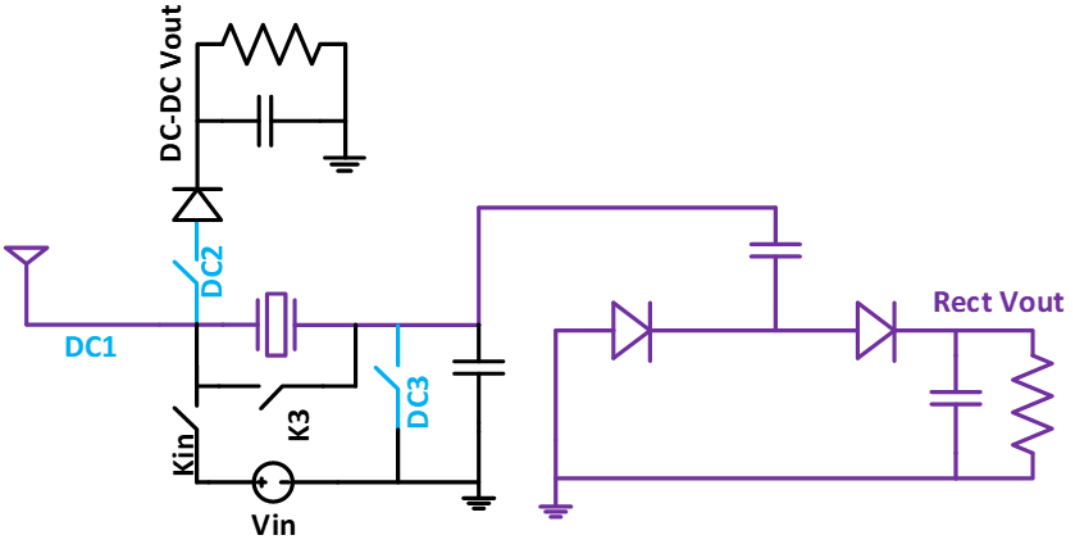

(a) Rectifier (purple) using the resonator in the matching network.

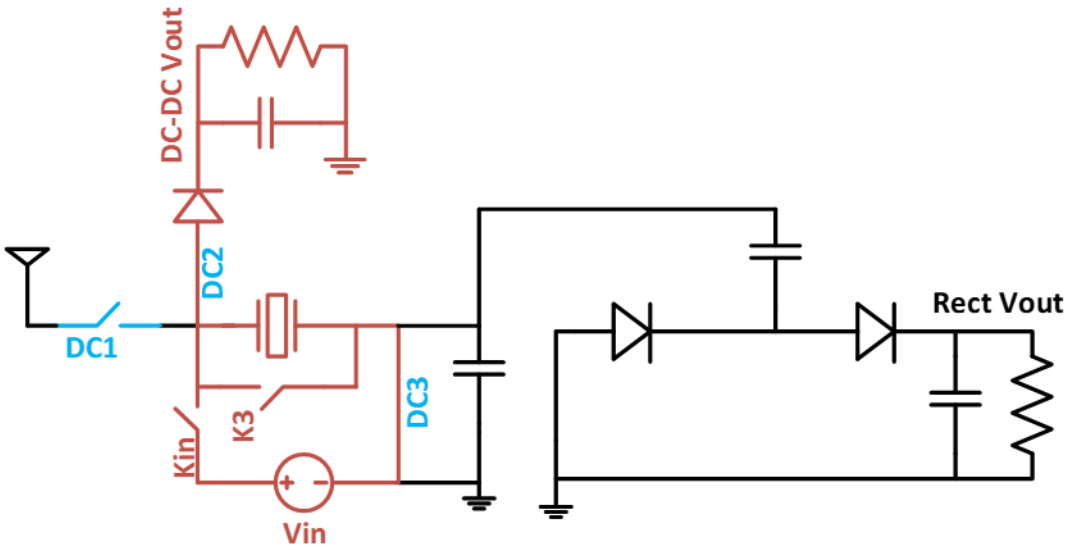

(b) DC-DC converter (red) using the resonator as the energy storage element.

Figure 4.1: Proposed circuits for rectifier and DC-DC converter sharing piezoelectric resonator.

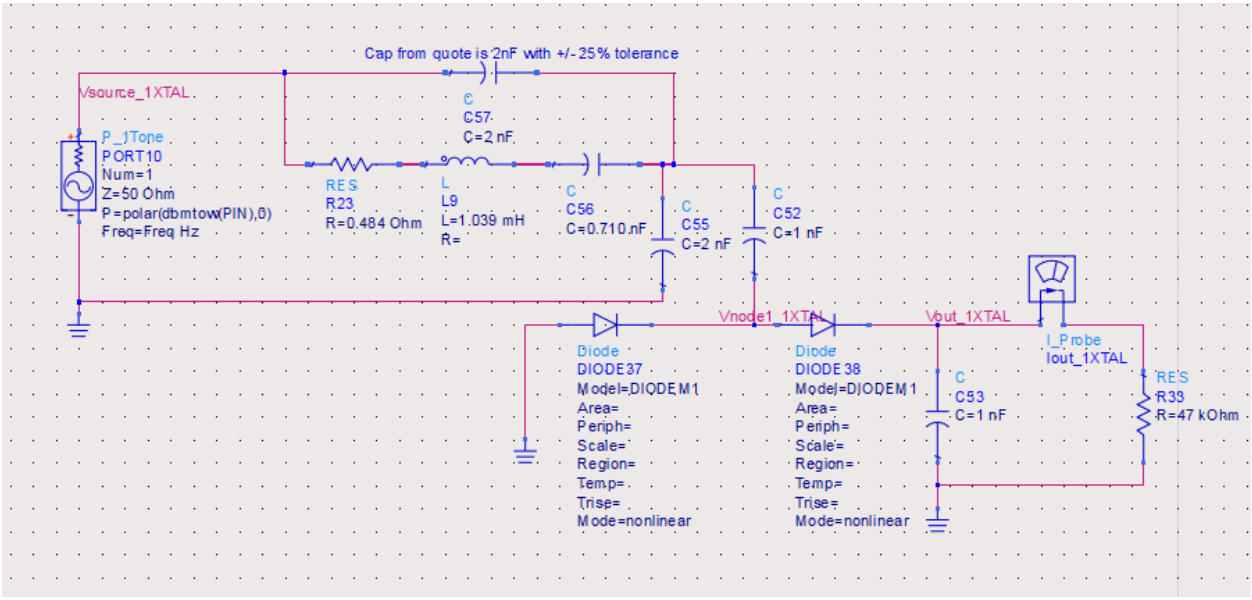

(a) Rectifier with no switches.

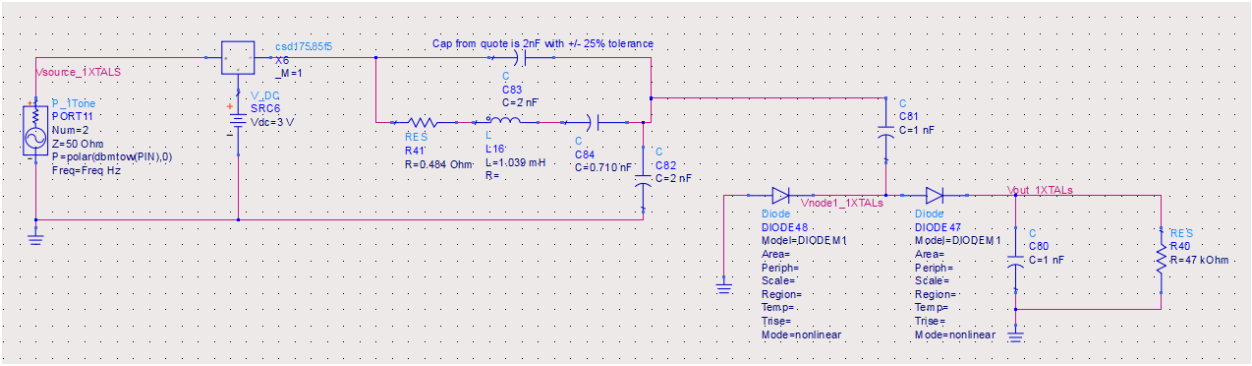

(b) Rectifier with one switch, DC1.

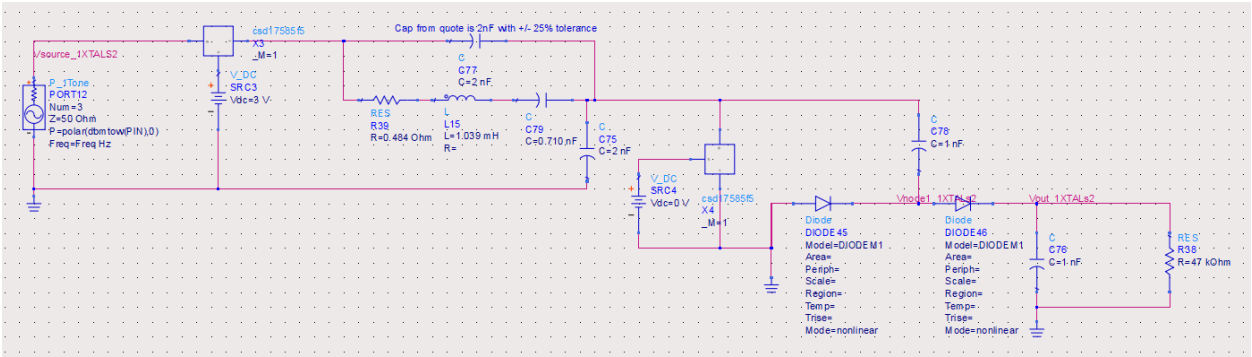

(c) Rectifier with two switches, DC1 and DC3.

Figure 4.2: Schematic diagram with switches in matching network with 190 kHz resonator.

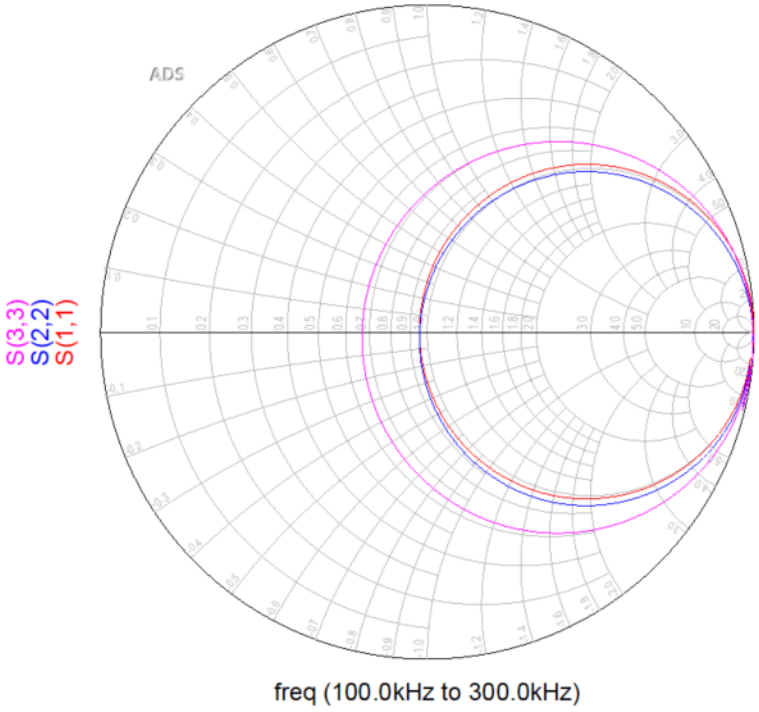

(a) Simulated impedance of rectifier. S(1,1) is the reflection coefficient of Fig. 4.2(a); S(2,2) is that of Fig. 4.2(b); S(3,3) is of Fig. 4.2(c).

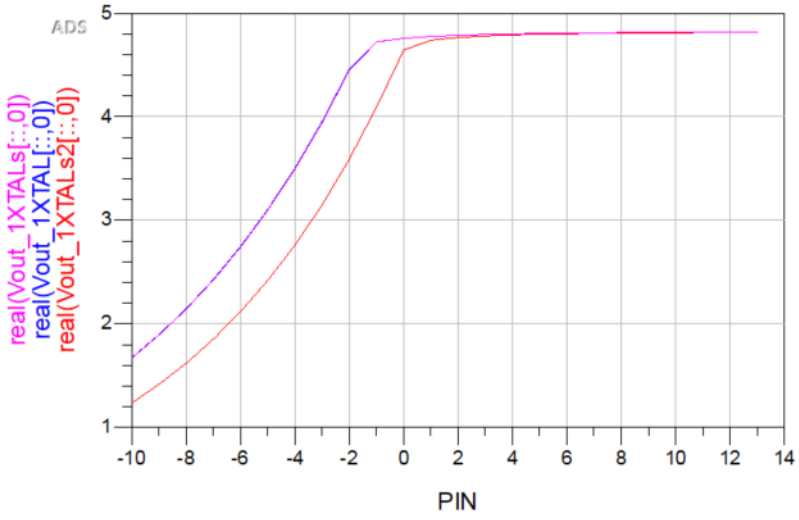

(b) Simulated output voltage of rectifier. XTAL shows response with no extra switches; XTALs shows response with DC1; XTALs2 shows response with DC1 and DC3.

Figure 4.3: Impedance and output voltage of 1 stage rectifier with resonator matching network at 190 kHz and additional switches.

even worse performance than if the rectifier was not matched at all. The rectifier employing only DC1 also has a lower output voltage than the matched rectifier with no extra switches. This is expected, since the effect of the switches and their parasitics is more pronounced at higher frequencies. This simulation shows the impedance contributions of the switches need to be taken into account before designing the matching network.

4.2 Combined Performance

In addition, preliminary simulations were done to combine the rectifier and DC-DC converter. The following simulations combine the 18 MHz rectifier with a DC-DC converter operating at 83 kHz. The DC-DC converter was replaced with a lossy transformer to simplify the ADS simulation. Figure 4.6 shows the schematics used to replace the converter with a transformer in LTSpice, while Fig. 4.7 shows the ADS schematic using this transformer model. Figure 4.8 shows the output voltage of the transformer being supplied by the rectifier. The input sinusoid amplitude is 13 V to create a rectifier output of around 10 V, which was the input voltage for the converter used in the previous chapter. Simulations show replacing a DC-DC converter with a lossy transformer produces the same output voltage magnitude, although the output voltage of the lossy transformer cannot replicate the output ripple of the converter.

As seen in Fig. 4.8, the output voltage is greatly reduced at the final DC output due to the crystal and inductor matching network when the rectifier is combined with the DC-DC converter. This is caused by the load of the DC-DC converter being too small, and the principle of voltage division dominates over the the benefits obtained from a matched circuit. The high impedance of the rectifier consumes most of the power, so little is delivered to the output. The addition of the matching network only introduces more resistance that consumes the available power. This is verified by sweeping the load values and observing the simulated efficiency of the rectifier (Fig. 4.9). As expected, the optimal load for the matched

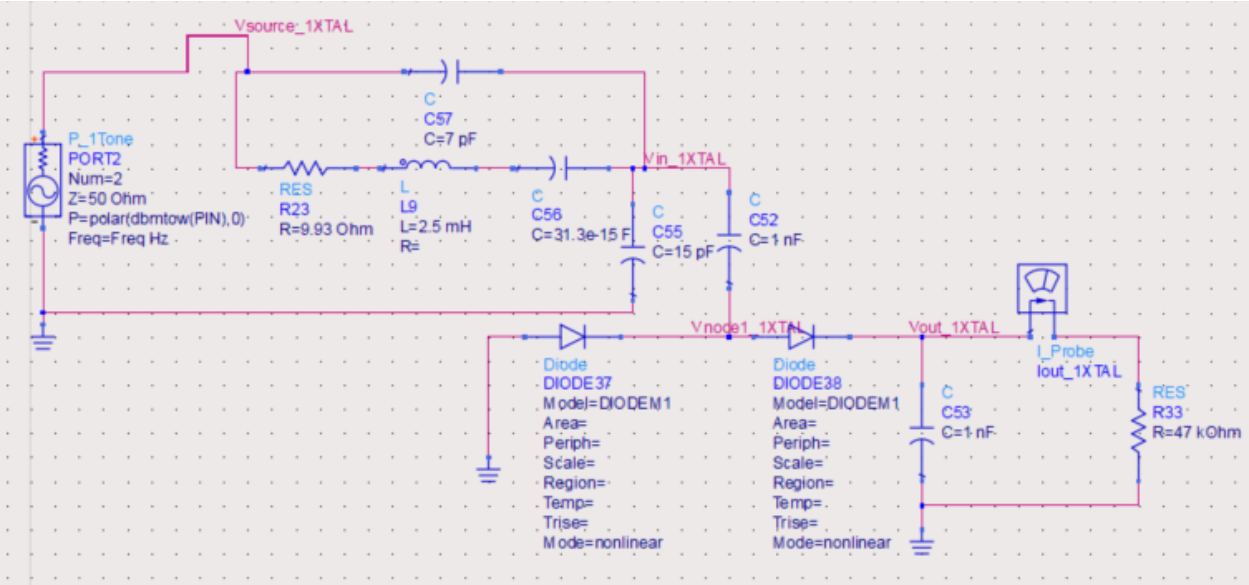

(a) Rectifier with matching network and no switches.

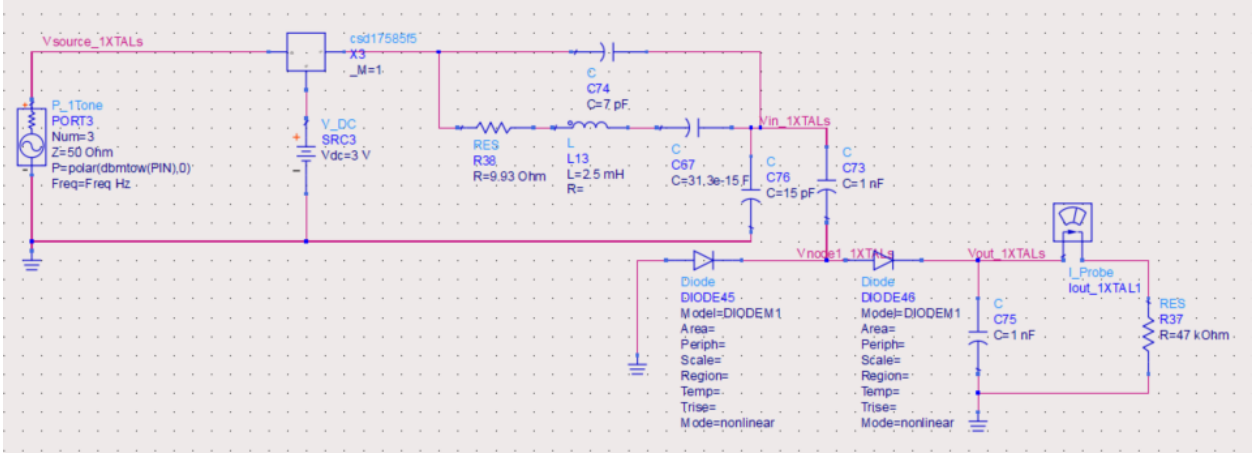

(b) Rectifier with matching network and one switch.

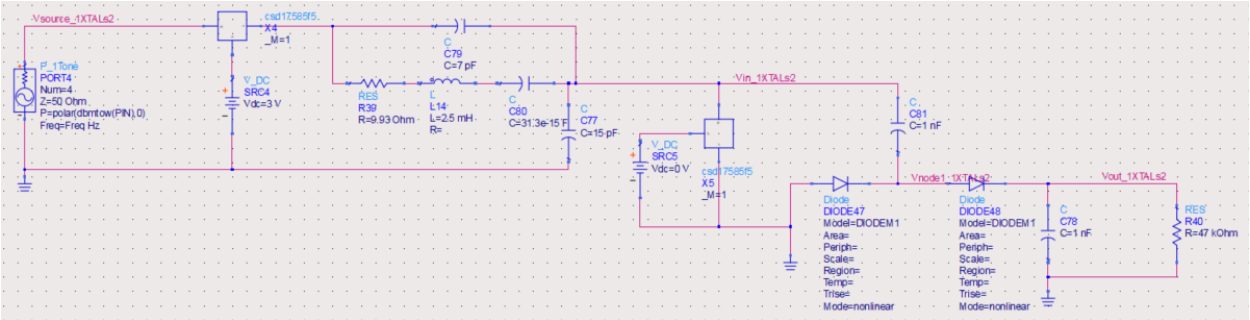

(c) Rectifier with matching network and two switches.

Figure 4.4: Schematics of rectifiers and their matching networks with a 18 MHz crystal resonator.

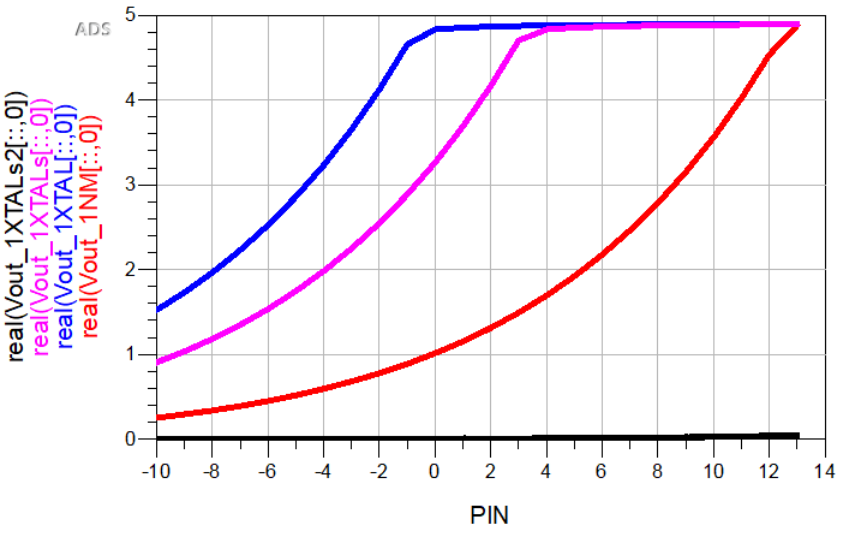

(a) Simulated output voltage of various rectifiers.

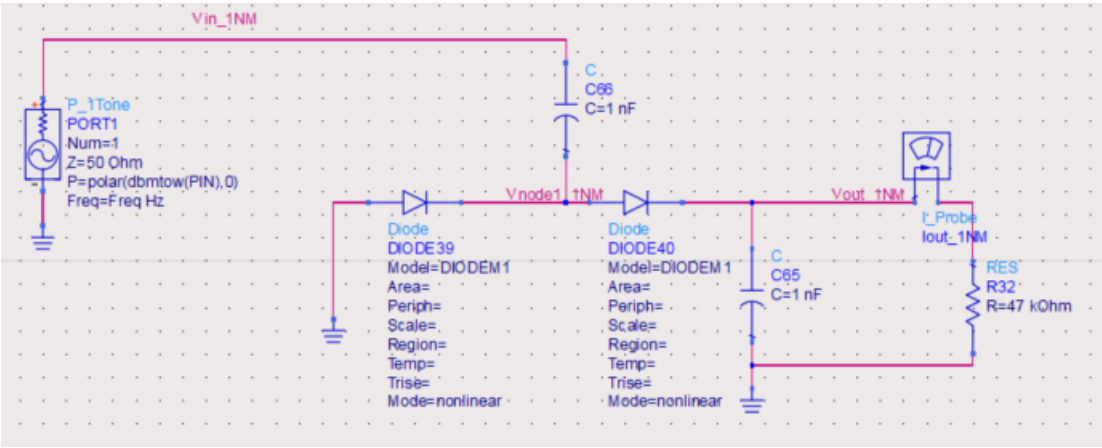

(b) Rectifier with no matching.

Figure 4.5: Simulated output voltage of rectifiers with switches and rectifier with no matching shown for comparison.

rectifiers occur between 5 kΩ and 50 kΩ, so the DC-DC converter with a load of 800 Ω is insufficient to use with the matching networks. From Fig. 4.9, it is also apparent the rectifier with a resonator-based matching network has a higher efficiency than both the unmatched rectifier and the rectifier with an inductor-based matching network. Therefore, future designs will use the optimal load resistance values of the rectifier with a resonator-based matching

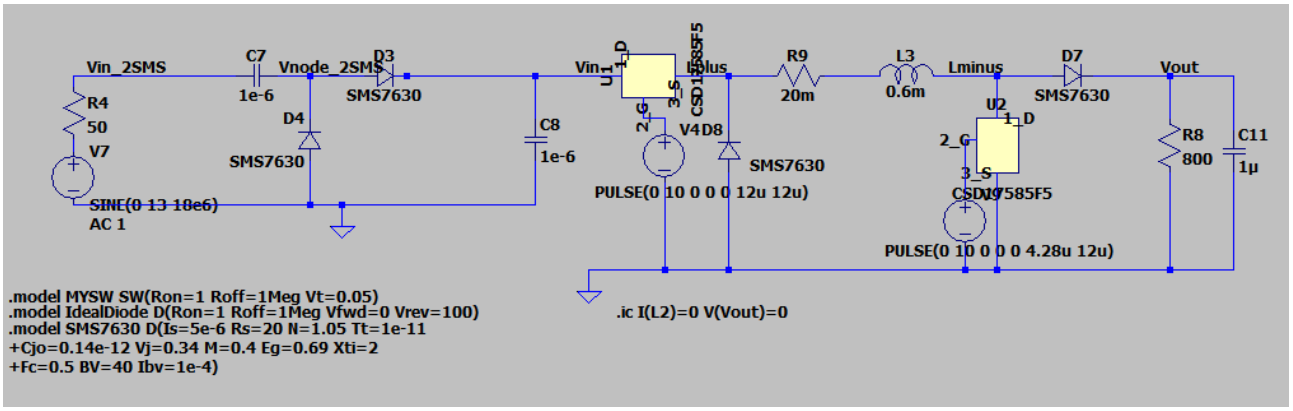

(a) Rectifier and DC-DC converter with inductor.

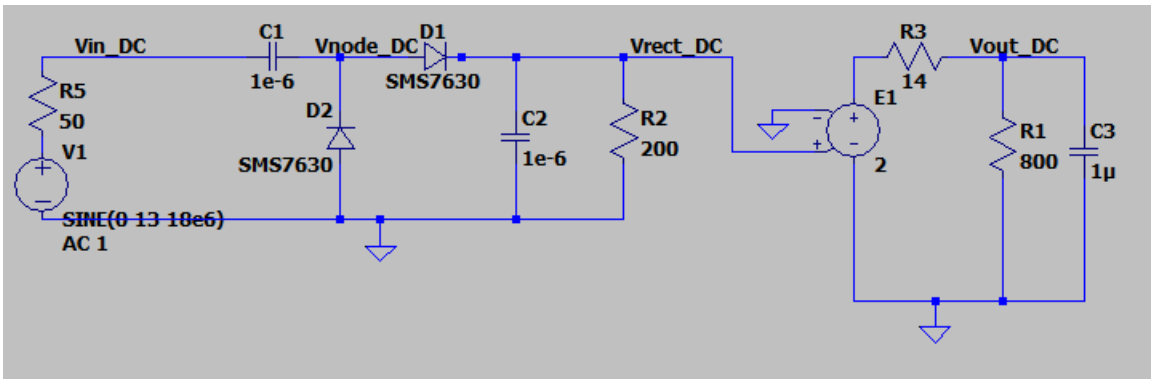

(b) Rectifier with lossy transformer E1-R3 to replace converter in (a).

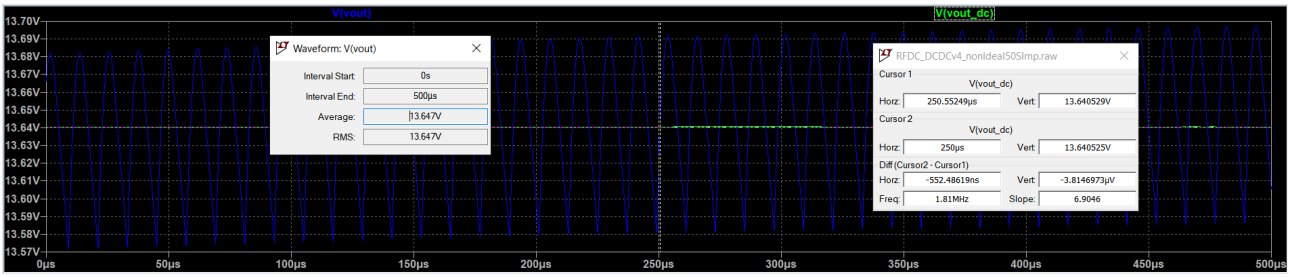

(c) Output voltage of both schematics. Vout_DC is output of converter in (a); Vout is output of transformer in (b).

Figure 4.6: Schematics and simulated output voltage of rectifier and DC-DC converter and the lossy transformer used to replace it.

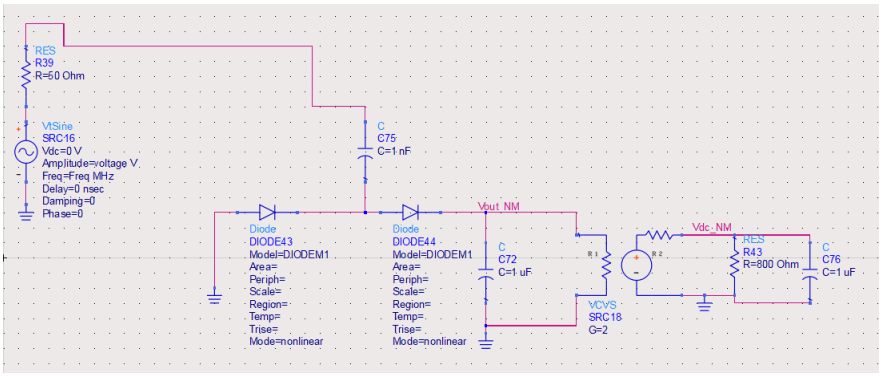

(a) Rectifier with no matching and lossy transformer.

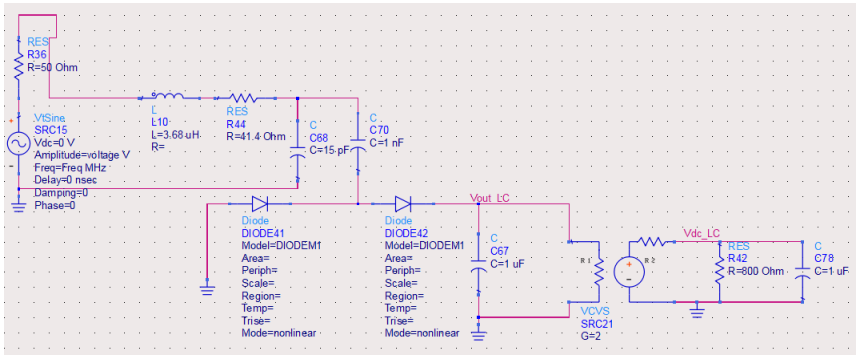

(b) Rectifier with LC matching and lossy transformer.

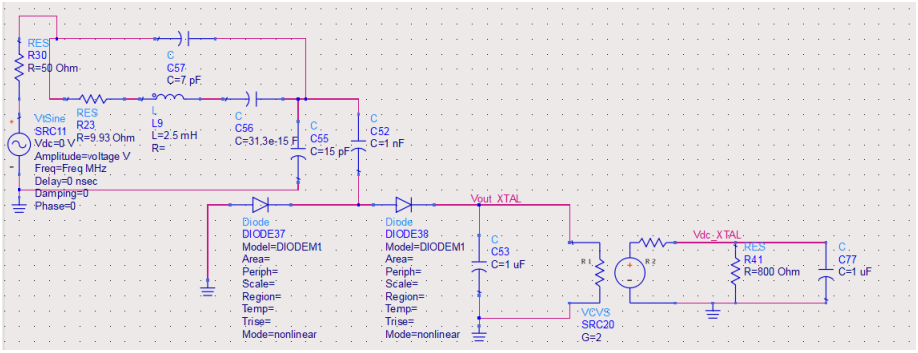

(c) Rectifier with crystal in matching network and lossy transformer.

Figure 4.7: Schematics and output voltage of rectifier and DC-DC converter and the lossy transformer used to replace it. R1 is 200 Ω; R2 is 14 Ω.

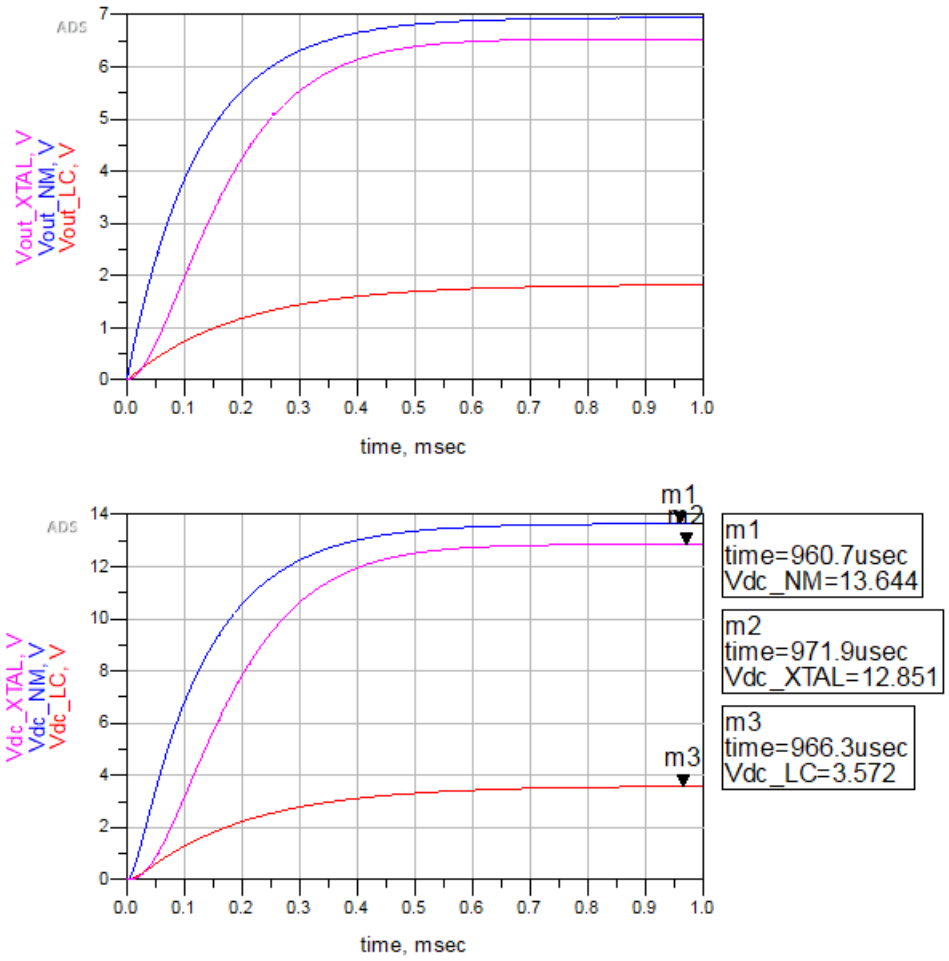

Figure 4.8: Simulated output voltage of rectifier (top) and of transformer model of DC-DC converter (bottom).

network for the best performance and highest efficiency.

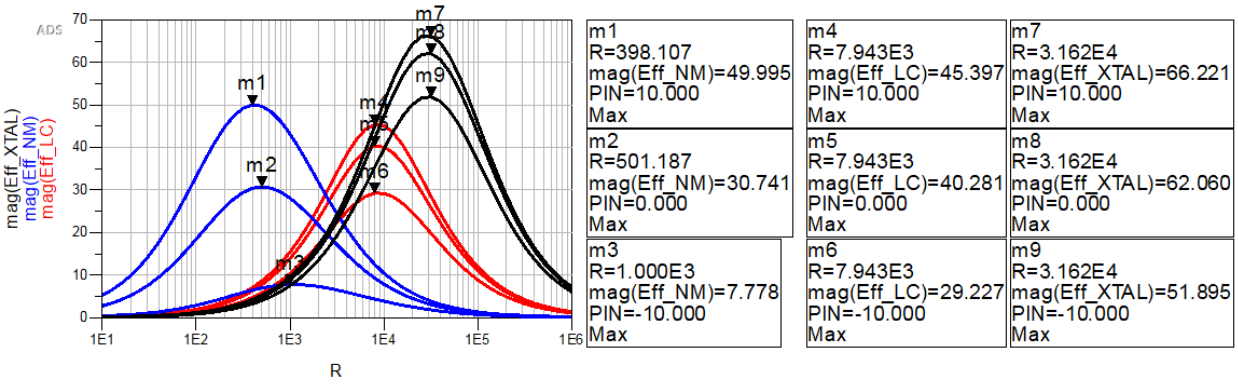

Figure 4.9: Simulated efficiency curves with respect to various loads.

Chapter 5

Magnetoelectric Antenna

5.1 Motivation

After proposing methods to improve the performance of the rectifier and the DC-DC converter, what remains to be addressed is the front end of the wireless energy harvesting system, which is the antenna. In many consumer wearable electronics, the size is restricted by the antenna, which can be reduced to one-tenth of the wavelength used [30]. However, since the wavelength (λ) is inversely proportional to the frequency (f) as seen in Eqn 5.1, in cases of lower frequencies such as those used in the Qi standard charging, even using an antenna that is one tenth of the wavelength would still be hundreds of meters long! Clearly that is not the case for any phone or smart watch currently on the market because Qi charging uses the concept of transformers rather than antenna theory as described in the first chapter. However, a transformer transfers energy through magnetic induction and requires a close proximity and tight coupling between the receiver and the transmitter. Equation 5.1 shows that the wavelength (and therefore, the antenna length) can be decreased by either increasing the frequency or by decreasing the velocity of propagation, v_p, through using a different medium or different kind of wave.

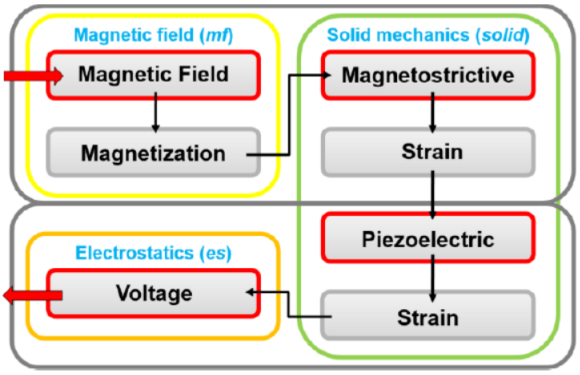

Figure 5.1: Diagram of the operation of an ME antenna [34].

$$\lambda = \frac{v_p}{f} \tag{5.1}$$

For instance, electromagnetic waves propagate in air at the speed of light (3×10^{10} cm/s), while acoustic waves travel in air at the speed of sound (3.4×10^4 cm/s). A proposed solution is to use a different type of antenna that relies on vibrations rather than electromagnetic waves. This means acoustic wavelengths will be smaller than electromagnetic wavelengths for the same frequency. A magnetoelectric (ME) antenna converts a detected magnetic field into vibrations through a magnetostrictive material, and the vibrations are converted back to an electrical signal through a piezoelectric material, as seen in Fig. 5.1. This concept is explored in [30], [31], and [32], while [33] has measured the amount of power that can be harvested with a rectifier connected to this type of antenna.

Figure 5.2 shows how the ME antenna will fit into the overall wireless energy harvester. Table 5.1 proposes the targeted specifications of the system in comparison with that of existing literature. The proposed ME antenna dimensions range from 1 to 2 cm long by 2 mm wide, while smart watches (which are currently some of the smallest commercial devices with Qi charging) have a case size of around 4 cm by 4 cm [35] [36].

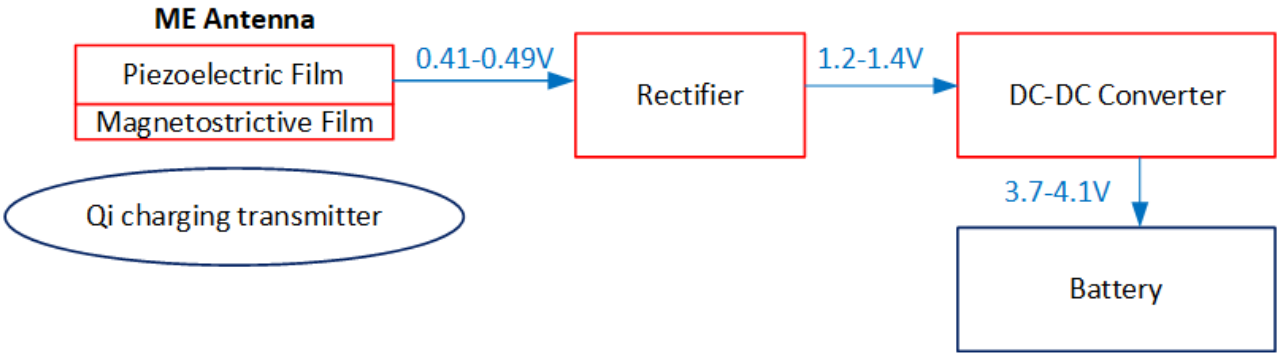

Figure 5.2: Block diagram of energy harvesting system with ME antenna.

Table 5.1: Targeted specifications for proposed system compared to existing literature. PVDF is polyvinylidene fluoride.

	Proposed System	[33]	[31]
Magnetostrictive material	Metglas 2605 SA1 FeBSiC	$Fe_{64}Co_{17}Si_7B_{12}$	Metglas 2605 SA1 FeBSiC
Piezoelectric material	PVDF	PVDF	PVDF
Dimensions, Length × Width × Height (mm)	9.8-13 × 1.6 × 0.06	5-30 × 5 × 0.09	0.05 height
Frequency (kHz)	150-200	47-337	50
ME voltage coefficient (V/cm-Oe)	45-58	3-146	238-310
Power density (mW/cm^3)	0.3-1	0.065-1.5	N/A
Output power(μW)	0.1-5	0.04-6.4	N/A
Output voltage(V)	3.7-4.2	0.14-1.3	N/A

5.2 Magnetoelectric Antenna Overview

Magnetoelectric (ME) antennas are attractive replacements for conventional antennas due to their size advantage. ME antennas resonant acoustically through vibrations, meaning their

resonant wavelength is proportional to the speed of sound, while traditional electromagnetic (EM) antennas depend on an EM resonance with a wavelength proportional to the speed of light. This means the wavelength of an EM wave at the same frequency of an acoustic wave will be 6 orders of magnitude longer, translating to the need for a longer antenna [30].

A magnetoelectric device is often composed of several laminate layers instead of being made from a single material. Epoxy is used to glue a piezoelectric (PE) sheet between two magnetostrictive (MR) material layers. When the magnetostrictive material deforms due to a magnetic field, the strain induced is coupled to the piezoelectric layer, producing a voltage. If the applied magnetic field is perpendicular to the magnetostrictive material, the strain will occur along the thickness of the material (transverse strain). If the applied magnetic field is along the length of the material, a longitudinal strain occurs. However in both cases, a longitudinal strain can be produced in the piezoelectric layer if the length of the device is much larger than the thickness [37], as seen in Fig. 5.3. In an alternating current (AC) magnetic field, vibrations are produced in the device, so a direct current (DC) magnetic field is usually needed to bias the device for strain in both positive and negative directions. From [37], for an input magnetic field, H, applied along the length of the ME device, the strain, S_m, and magnetic flux density, B, in a magnetostrictive material can be defined in terms of the stress, T_m, and magnetic field applied (Eqn. 5.2). The stress is scaled by the elastic compliance, s^H, of the MR material and magnetic field by the piezomagnetic constant, d_m, to produce the strain. Similarly, the stress is related to the magnetic flux density through the piezomagnetic constant and the magnetic field is related through the permeability of the MR material under stress, μ^T. Analogously, the strain, S_p, and electric field, E, produced in a piezoelectric material are dependent on the applied stress, T_p, and dielectric displacement, D (Eqn. 5.3). The strain in the PE material is related to the stress and dielectric displacement through the elastic compliance, s^D, and piezoelectric constant, g_p, respectively, while the electric field induced can be found as the sum of the negative

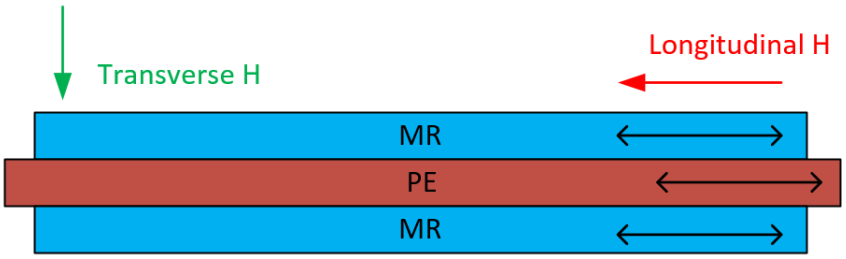

Figure 5.3: Cross sectional view of magnetoelectric antenna showing longitudinal strain with transverse or longitudinal applied magnetic field.

stress scaled by the PE constant and the dielectric displacement scaled by the stiffness, β^T. A detailed proof of these equations and extension into the transverse case is presented in [37]

$$S_m = s^H T_m + d_m H \tag{5.2a}$$

$$B = d_m T_m + \mu^T H \tag{5.2b}$$

$$S = s^D T_p + g_p D \tag{5.3a}$$

$$E = -g_p T_p + \beta^T D \tag{5.3b}$$

In addition, the energy transfer in the ME laminate from magnetic field to electric potential can be modeled as an electrical circuit as shown in Fig. 5.4. The equivalent stress to produce certain strain from an applied magnetic field is related to the magnetic field through the magneto-elastic coupling factor, ϕ_m, defined by Eqn. 5.4, which depends on the cross-sectional area of the MR material (A_2), the piezomagnetic constant ($d_{33,m}$), and the elastic compliance under a certain applied magnetic field ($s^H_{33,m}$). The subscripts 3 or 1 refer to the longitudinal (along the length of the ME antenna) or the transverse (along the width of the antenna), respectively. The conversion to voltage produced from the piezoelectric layer is defined by the elastic-electric coupling factor, ϕ_p (Eqn. 5.5). The elastic-electric coupling factor is determined by the dimensions of the PE material, the piezoelectric voltage coefficient ($g_{31,p}$), the elastic compliance under a constant electric field (s^D_{33}), and the inverse

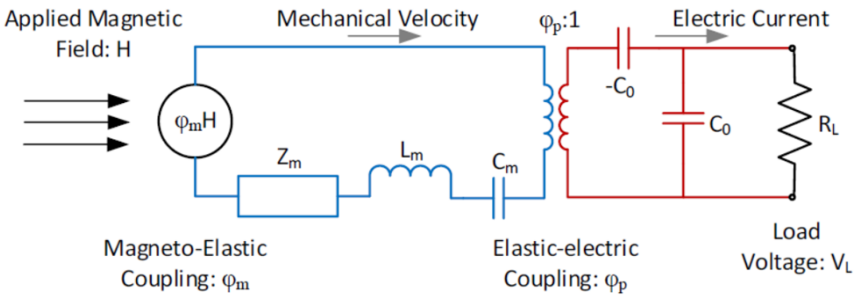

Figure 5.4: Electrical model of ME device, reproduced from [38].

dielectric constant ($\bar{\beta}_p$). The piezoelectric voltage coefficient with the 1 and 3 subscripts means it is the transverse coefficient for a longitudinal applied input. From these two coupling factors, the magnetoelectric coefficient, α_{ME}, can be calculated (Eqn. 5.6) for an ME device with no load by referring the left hand side of the transformer in Fig. 5.4, which represents the magneto-mechanical domain, to the right hand side of the transformer, which is the electrical domain, and by assuming the loss due to the mechanical impedances of Z_m, L_m, and C_m are insignificant and can be accounted in β, a loss factor with a value less than or equal to one. C_o is the capacitance of the piezoelectric film defined in Appendix F, and ω is the operating frequency. The most commonly used ME coefficient in literature for comparison is the voltage produced from 1 oersted of magnetic field and 1 cm of piezoelectric thickness, t_p. Another figure of merit for ME devices, M_o, shows the amount of coupling between the material layers (Eqn. 5.7). Figures and equations are adapted from [37], [38], and [39].

$$\phi_m = \frac{A_2 d_{33,m}}{s_{33}^H} \tag{5.4}$$

$$\phi_p = \frac{wl\ g_{13,p}}{t_p\ s_{33}^D\ \bar{\beta}_p} \tag{5.5}$$

$$\alpha_{ME} = \frac{\beta \phi_p \phi_m}{4\pi \times 10^{-3}\ t_p\ \omega C_o} \left[\frac{\text{V}}{\text{cm-Oe}}\right] \tag{5.6}$$

$$M_o = \frac{\beta \phi_p^2}{\omega C_o} \tag{5.7}$$

Applications for a magnetoelectric device can vary from communications to power transfer. In [40], two ME devices are used: one as an antenna for energy harvesting and another for magnetic field sensing. [41] and [33] use an ME antenna for energy harvesting, while [42] looks at the effect of device shape on the performance. Other work in signal processing measures the resolution [31], signal improvement with a modulation frequency [43], and noise and sensitivity [44] of magnetoelectric devices. In addition to laminates, further work has been done on the nanoscale to create ME devices using integrated circuit fabrication techniques [30].

This chapter compares the energy harvesting capacity of a magnetoelectric antenna compared to similarly-sized copper coil. A voltage multiplier is used to convert the harvested AC voltage into DC, and power and voltage density is evaluated. Section 5.3 describes the design and setup of the experiment, while Section 5.4 shows the results. Section 5.5 compares these results to current literature. Section 5.6 and Section 5.7 details use of the ME antennas to harvest vibrational energy.

5.3 Design

As mentioned previously, a main advantage of utilizing an ME device is its small size dependent on an acoustic wavelength rather than an electromagnetic one. The resonant frequency and length of a magnetostrictive (MR) material is defined in Eqn 5.8 [33], where f_r is the resonant frequency, L is the length, E is the Young's modulus, and ρ is the density of the magnetostrictive material. In addition, with the measured output voltage (V_{ME}) of the magnetoelectric device, the piezoelectric material thickness (t_p), and the input magnetic field (H_{ac}), the ME coefficient can be easily calculated from experimental results according to Eqn 5.9 [33]. The coefficient in Eqn. 5.9 is the experimentally derived version of Eqn.

5.6.

$$f_r = \frac{1}{2L}\sqrt{\frac{E}{\rho}} \tag{5.8}$$

$$\alpha_{ME} = \frac{V_{ME}}{t_p H_{ac}} \tag{5.9}$$

Although the resonant frequency of the MR material is commonly used as the main design parameter to match the frequency of the input magnetic field, the piezoelectric material also has a resonance, which depends on the mass of the piezoelectric material, m_{film} and its stiffness, k. An important note is the equivalent tip mass of the piezoelectric film is used to determine the resonant frequency. [45] calculates the tip mass, m and piezoelectric resonant frequency, f_{rp}, as shown in Eqn 5.10 and Eqn 5.11, respectively.

$$m = \frac{33}{140} m_{film} \tag{5.10}$$

$$f_{rp} = \frac{1}{2\pi}\sqrt{\frac{k}{m}} \tag{5.11}$$

The ME devices were fabricated using epoxy (Young's modulus of 3.34 GPa) and cyanoacrylate or superglue (Young's modulus of 1.26 GPa). Because the Young's modulus of PVDF is around 1.56 GPa, different adhesives were used to observe the effect of different levels of stress on the PVDF on the magnetoelectric coefficient. Appendix F shows how materials with different Young's modulus values can experience different stress. All values of Young's modulus can be referenced on [46]. Two different methods were used to fabricate the ME devices. Initially, the antennas were fabricated by manually applying the epoxy and compressing the layers with weights to create a uniform layer of epoxy between the MR and PE layers. However, vacuum bagging was also used for fabrication to provide a more direct comparison to [33], which also follows this method, and to be consistent with what is commonly used in literature ([47], [48], [49]). Figure 5.5 shows the layout of the Metglas layer

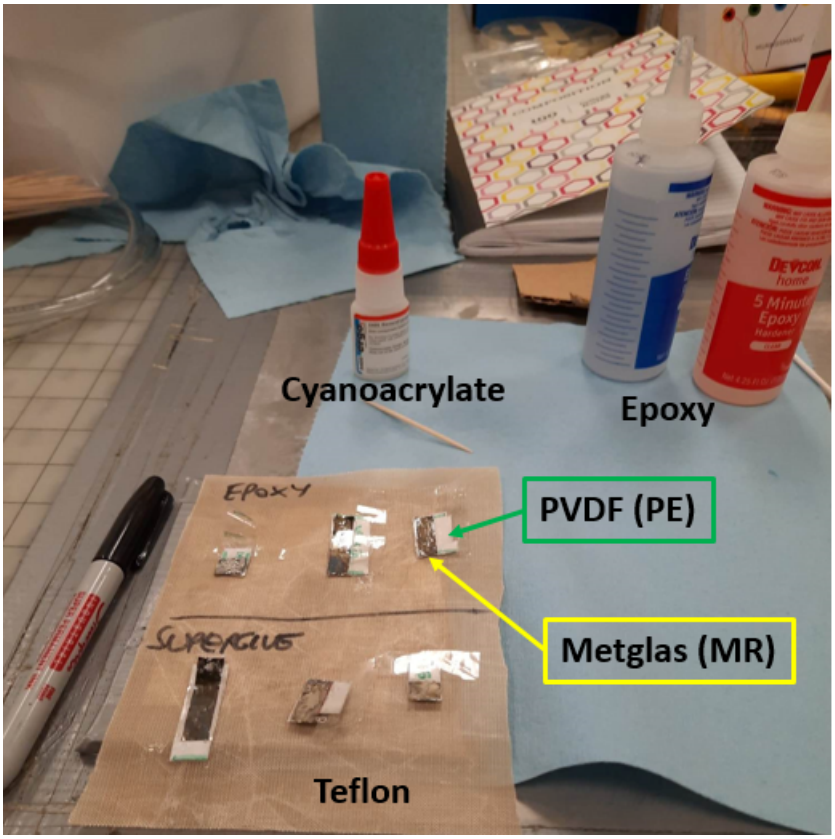

Figure 5.5: Magnetoelectric samples prepared with epoxy and cyanoacrylate for the vacuum bag.

(MR material) on the PVDF material (PE material) with tape to cover the silver electrode coating on the PVDF to protect it from the adhesive. The samples were placed on a Teflon-based fabric so excess epoxy would not adhere to anything besides the Metglas and PVDF, and this cloth containing the samples was placed between two metal plates to create a flat surface for the samples while the adhesive cured. Figure 5.6 shows the vacuum bag setup to fabricate the ME samples. The vacuum bag was created using a two-ply plastic sheet that was sealed with sealant tape on the top and bottom. A vacuum pump provided between 15-20 psi of pressure to the vacuum bag while the adhesive cured.

The magnetic field coil setup is shown in Fig. 5.7. For measuring the voltage coefficient, two coils were used to generate the AC field for a spatially larger and more consistent AC magnetic field (Fig. 5.7(a)). For energy harvesting measurements, only one coil was used

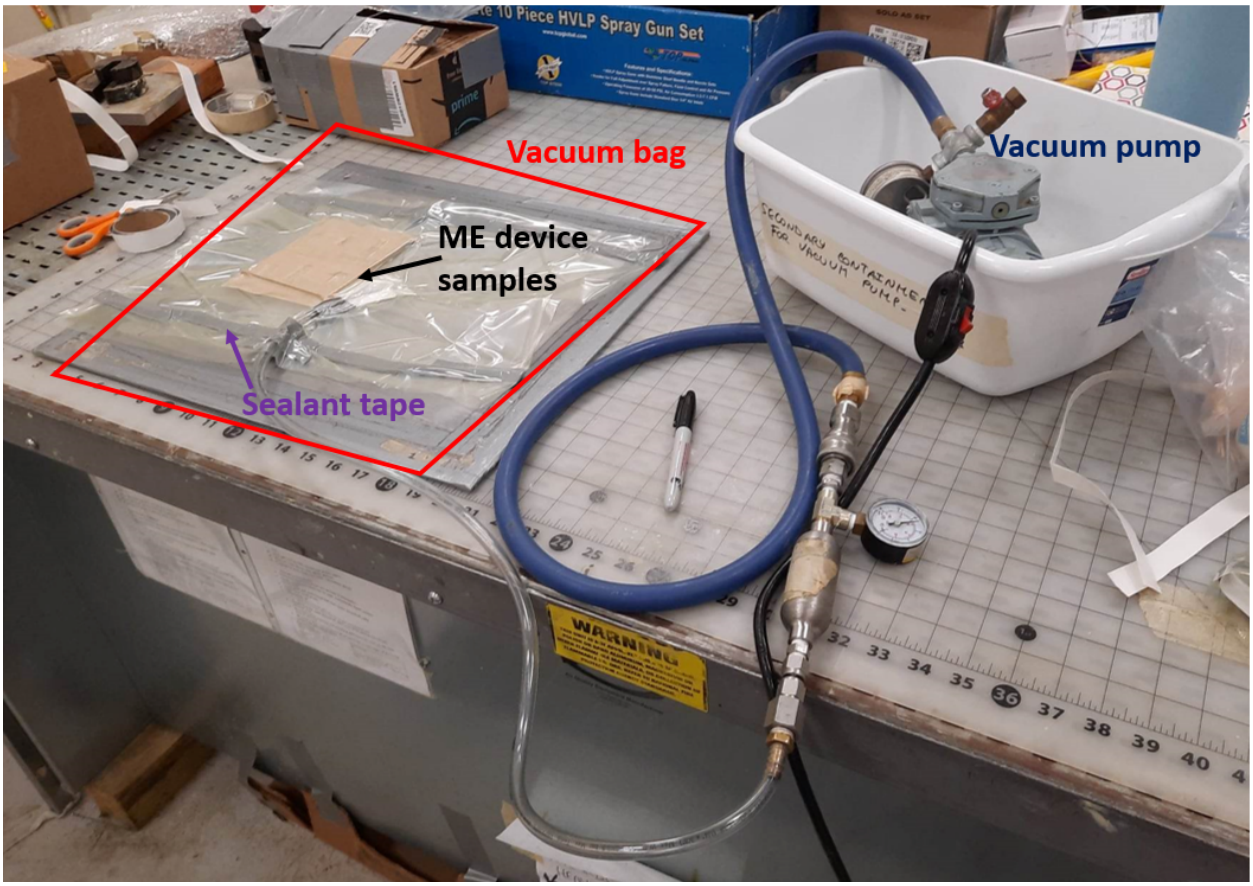

Figure 5.6: Vacuum bag setup to provide uniform pressure for adhesive to cure in ME devices.

for AC magnetic field generation (Fig. 5.7(b)) because the copper coil measurements only need one AC coil for energy harvesting, so using one input coil for both experiments made the results more comparable.

The magnetic flux density, B, can be calculated using the Biot-Savart law for a current carrying wire, and for a pair of coils. Equation 5.12 [50] was used to calculate the DC magnetic field from the current drawn by the Helmholtz coils (I), permeability (μ), number of coils (N), spacing between the two coils (c), and the radius of the coils (a). The magnetic flux contribution adds up to a larger field in the center of the two coils; Fig. 5.8 shows the calculated magnetic field strength at various distances, x, from the coils and the net magnetic field resulting from the Helmholtz coil pair. The DC bias point was determined experimentally to be the DC magnetic field where the output voltage of the ME antenna was

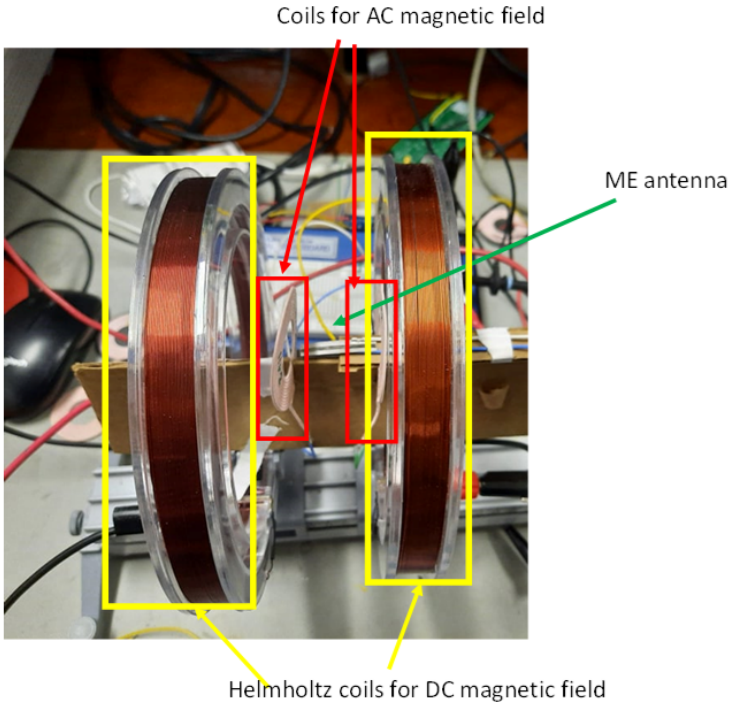

(a) Setup for ME antenna characterization.

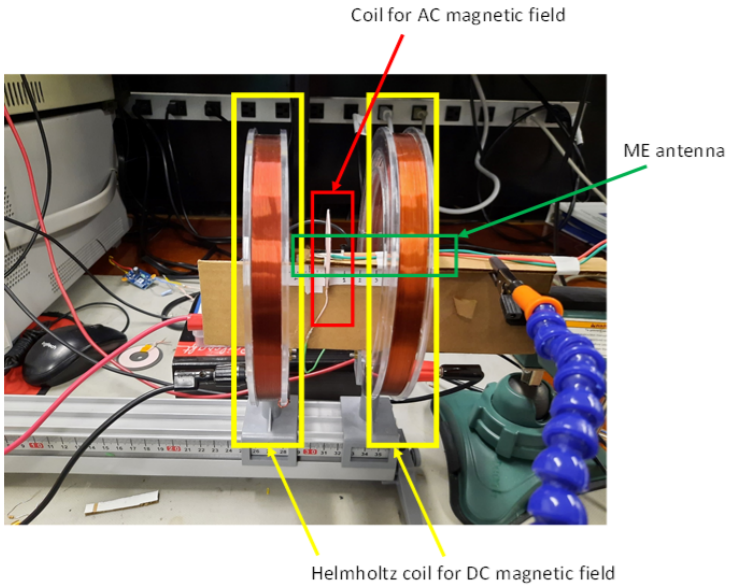

(b) Setup for ME antenna energy harvesting measurement.

Figure 5.7: Coil placement for AC and DC magnetic field.

the highest. The magnetic flux density, B, calculated from Eqn 5.12 has units of gauss and can be converted to magnetic field strength, H, with units of oersted using Eqn 5.13 if the field is propagating in air. A similar exercise can be performed for the AC coils to determine the AC magnetic field supplied. Due to the difficulty in measuring AC current, a 1 Ω resistor can be used in series with the coils to measure the AC voltage instead. Figure 5.9 shows the schematic of the circuit used to generate the AC magnetic field. For frequencies in the 80 kHz to 100 kHz range, 470 nF capacitors were used with a 5.2 μH coil to generate the magnetic field. The voltage, v_{in}, is the input, while the inductor voltage, v_L, and the resistor voltage, v_R, are used to calculate the power in the inductor as shown in Eqn. 5.14.

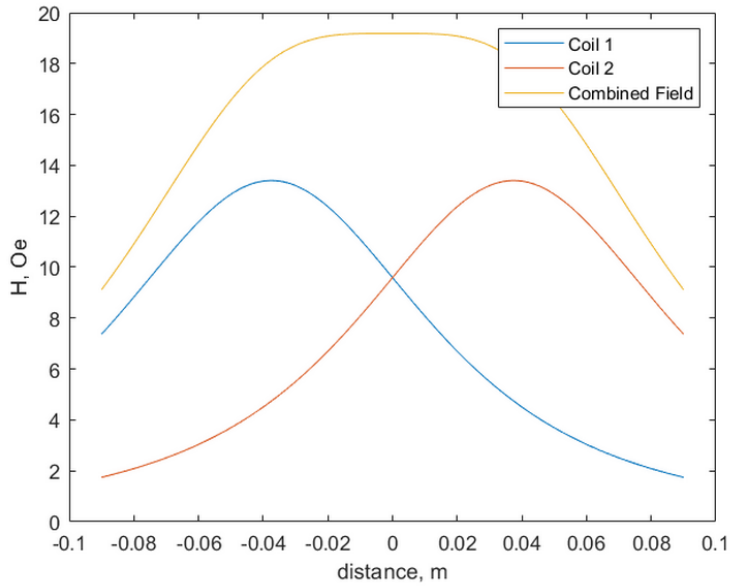

Figure 5.8: Calculated magnetic field of a pair of Helmholtz coils as a function of position.

$$B = \frac{\mu N I a^2}{2}\left(\frac{1}{(a^2+(c-x)^2)^{3/2}} + \frac{1}{(a^2+(c+x)^2)^{3/2}}\right) \tag{5.12}$$

$$H = \frac{4\pi}{1000} \times \frac{B}{\mu} \tag{5.13}$$

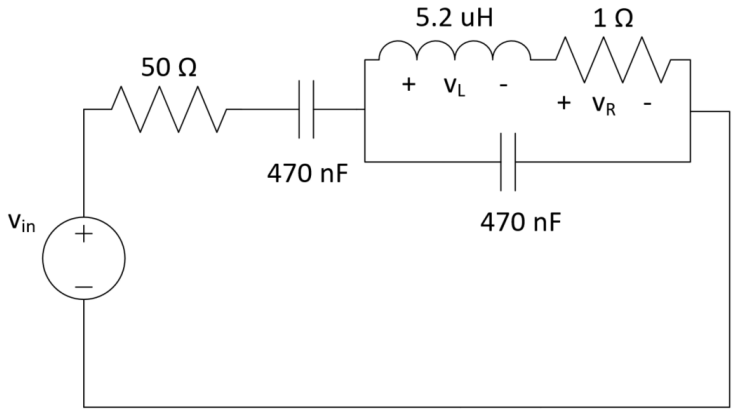

Figure 5.9: Schematic of coil circuit used to generate AC magnetic field [51].

$$P = V_{rms} \times I_{rms} = v_L \times \frac{v_R}{1} = v_L \times v_R \tag{5.14}$$

Table 5.2 details the MR and PE materials used and their conversion coefficients that can be calculated from Eqn 5.4- 5.5 and from the material properties provided in [38]. The piezoelectric material thickness includes the thickness of the silver ink metallization for mass calculations, but is not included in the area calculation for the coupling factor. This is because the metallization should be accounted for in the mass and stiffness but is assumed rigid and lossless in the transfer of vibration energy. Likewise, the full surface area of the piezoelectric material is used to calculate the elastic-electric coupling, but only the area in contact with the magnetostrictive material is used for density calculations later in the paper because the conversion from vibration to electric field utilizes the entire piezoelectric material, but the transfer for magnetic energy to vibration in the PE sheet only depends on the area touching the MR material. Figure 5.10(a) and 5.10(b) show the voltage multiplier used with the ME and antenna and coil for energy harvesting. The ME coefficient was calculated for the resonant frequency calculated from Eqn.5.8 (97.9 kHz) and the experimentally determined resonant frequency (89 kHz), which was the frequency with the highest output voltage from the ME device. Rectifier measurements were taken with a single coil as mentioned before at

89 kHz with 1.86 V across and 0.86 A through the inductor, transmitting about 0.8 W for the ME antenna.

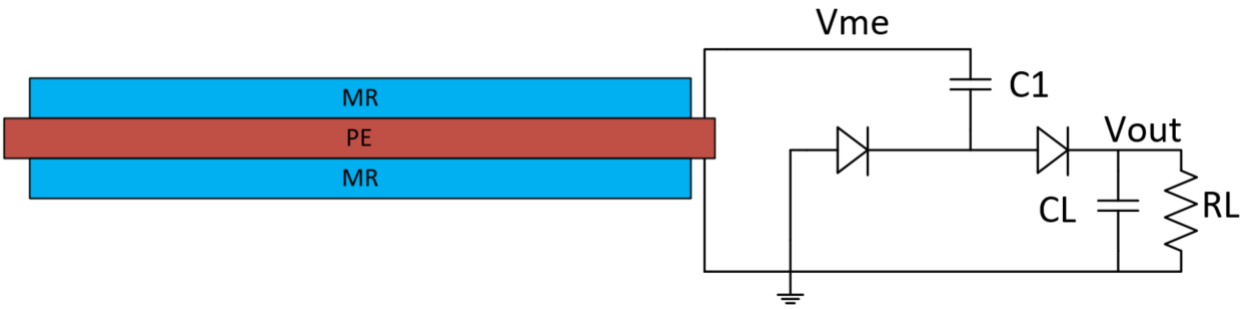

(a)

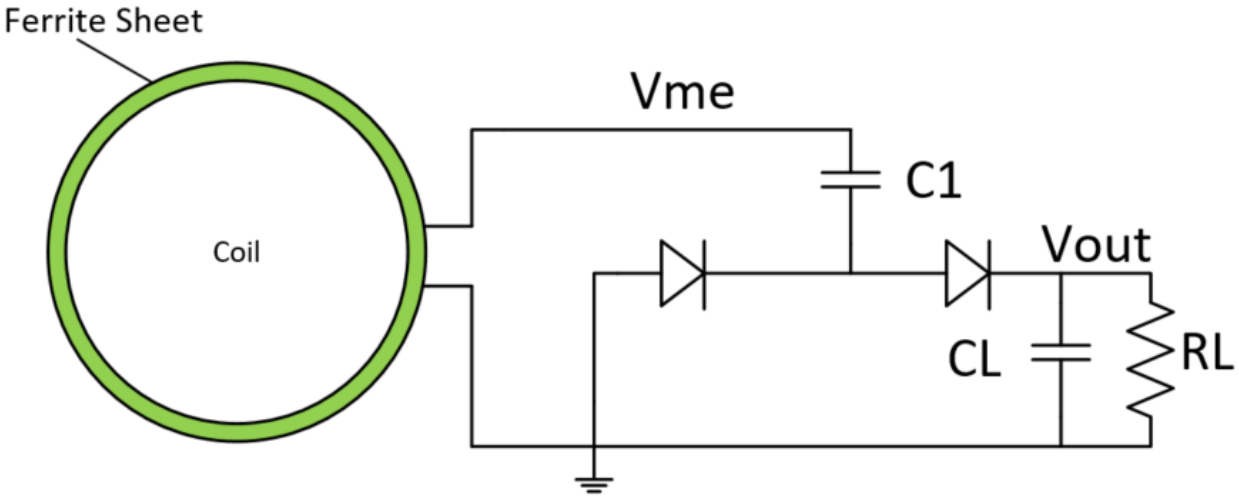

(b)

Figure 5.10: Schematic of voltage multiplier used for energy harvesting.

5.4 Measured Results

A main difference between the ME device and coil in energy harvesting is the ME device has a higher load resistance at the maximum power point (MPP) when connected to a voltage multiplier (Fig. 5.11). The MPP for the ME antenna occurs at a load of 10 kΩ, which is an order of magnitude higher than the MPP load of the coil (around 200 Ω). This is useful in

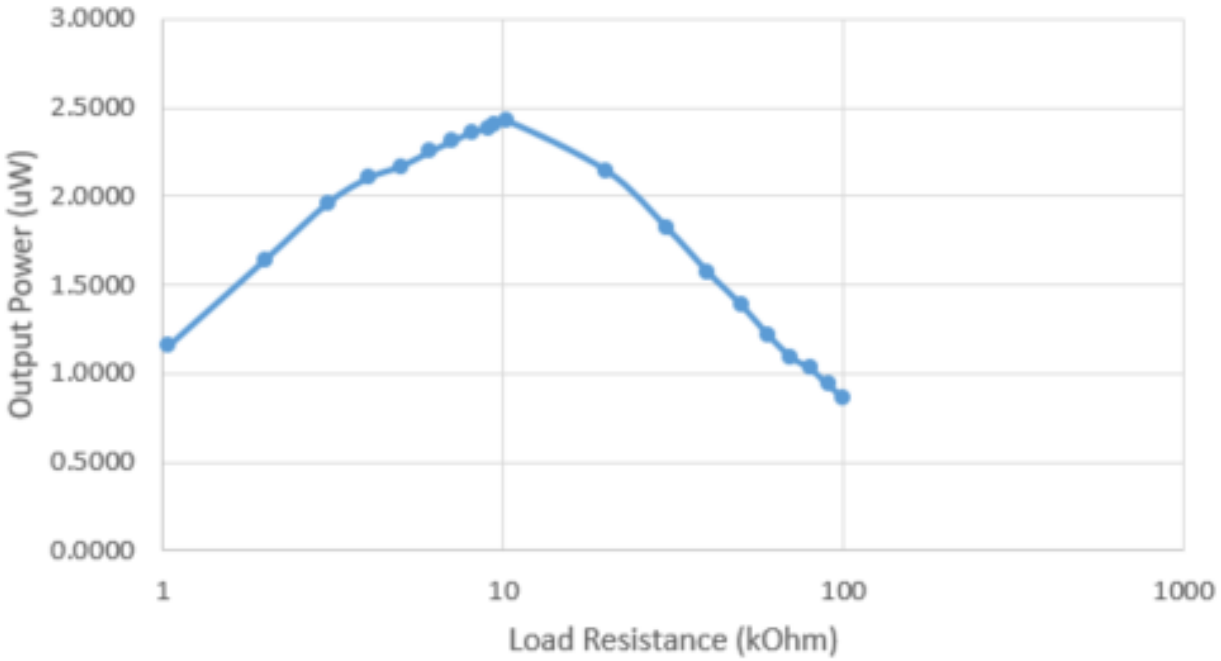

(a)

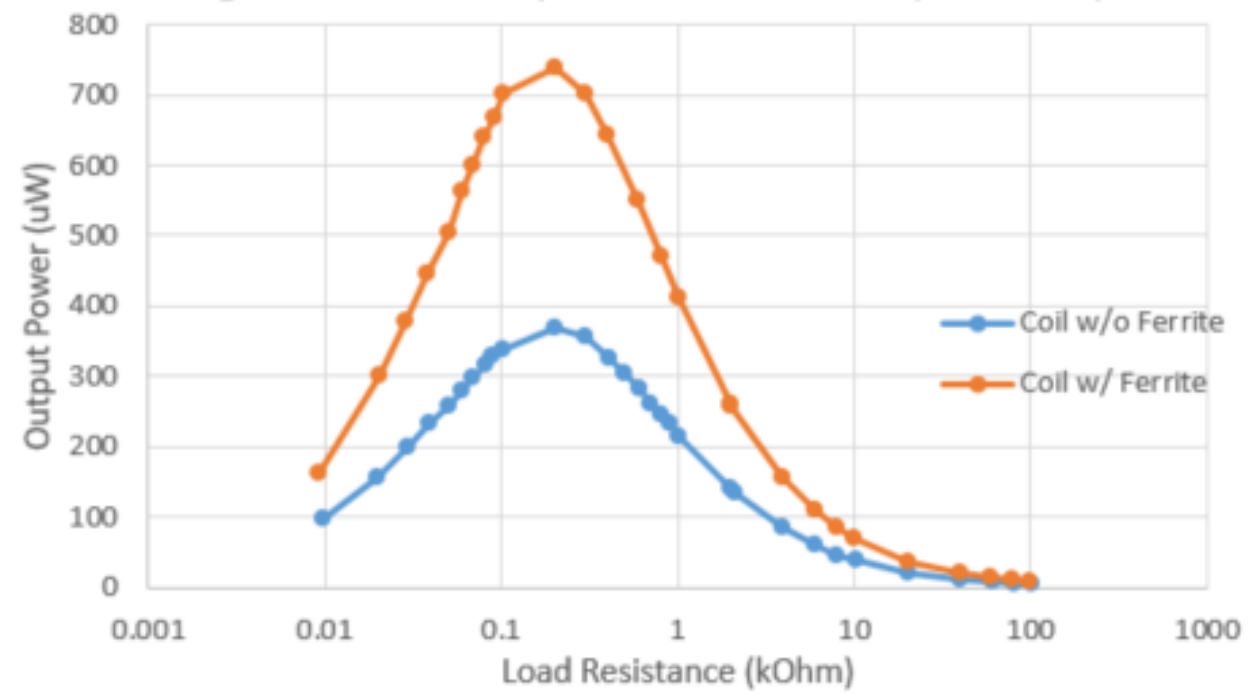

(b)

Figure 5.11: Measured maximum power point for ME antenna (a) and coil (b) with a 1-stage rectifier at 89 kHz.

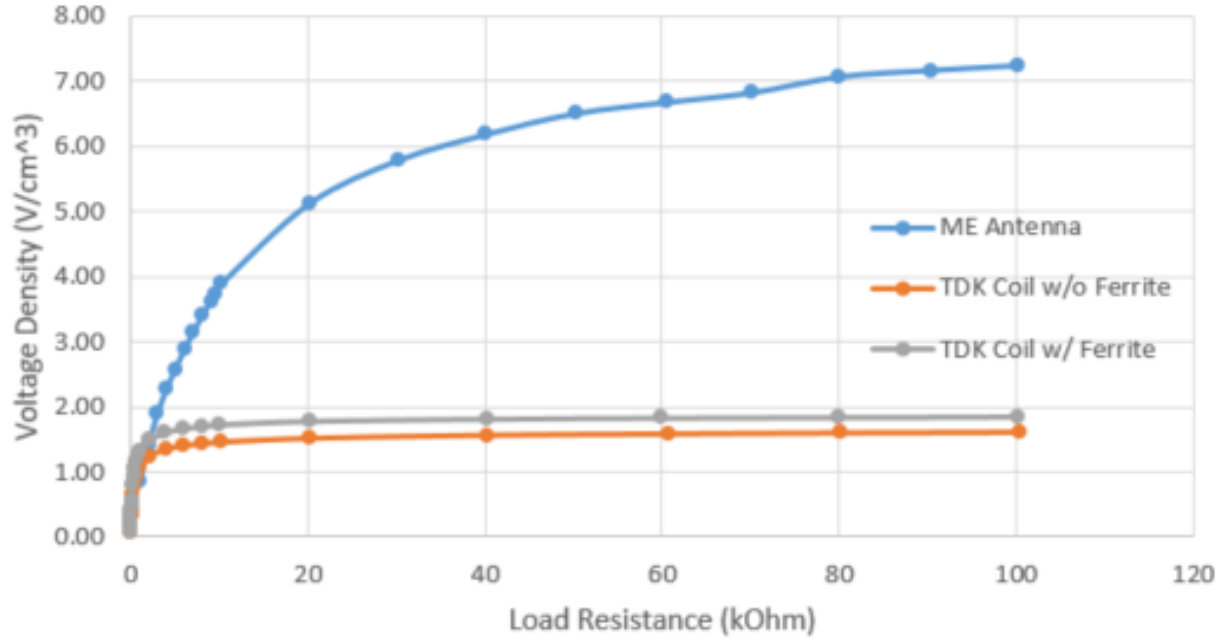

(a)

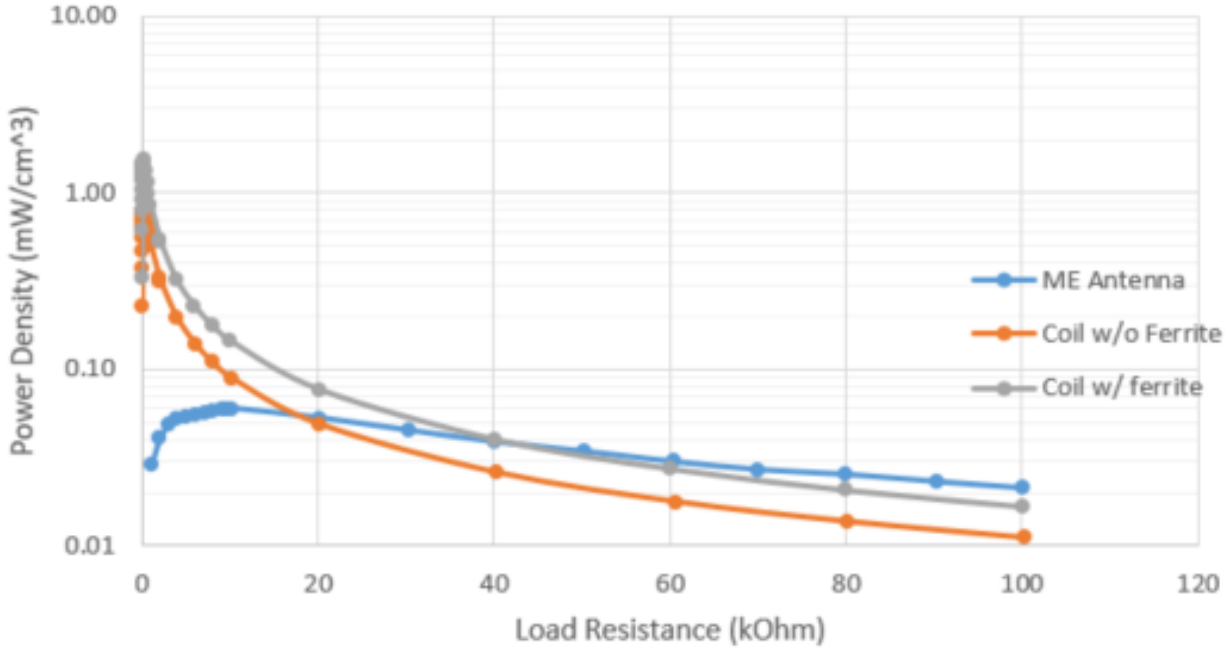

(b)

Figure 5.12: Measured voltage per unit volume (a) and power density (b) for constant input current.

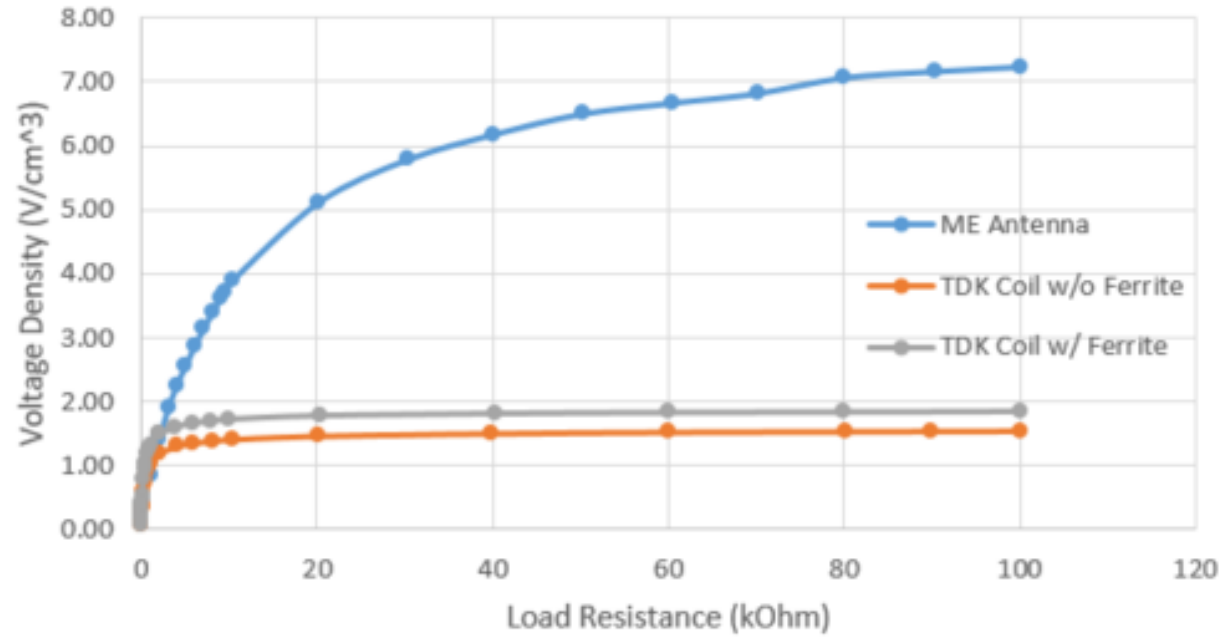

(a)

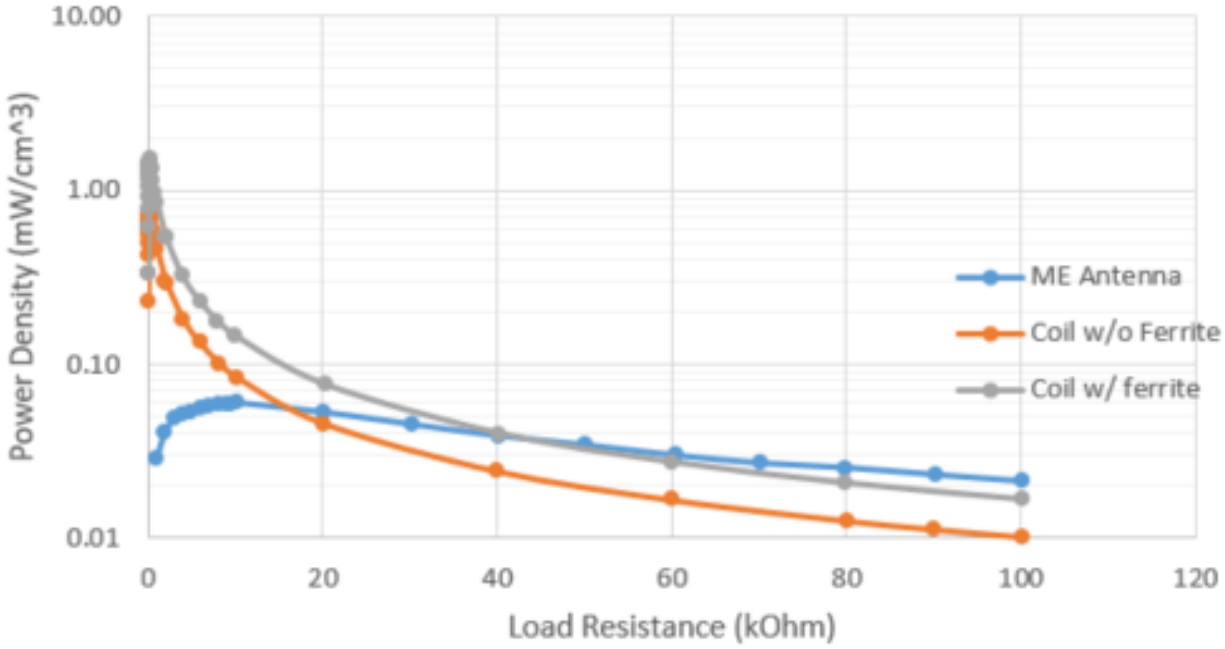

(b)

Figure 5.13: Measured voltage per unit volume (a) and power density (b) for similar input power.

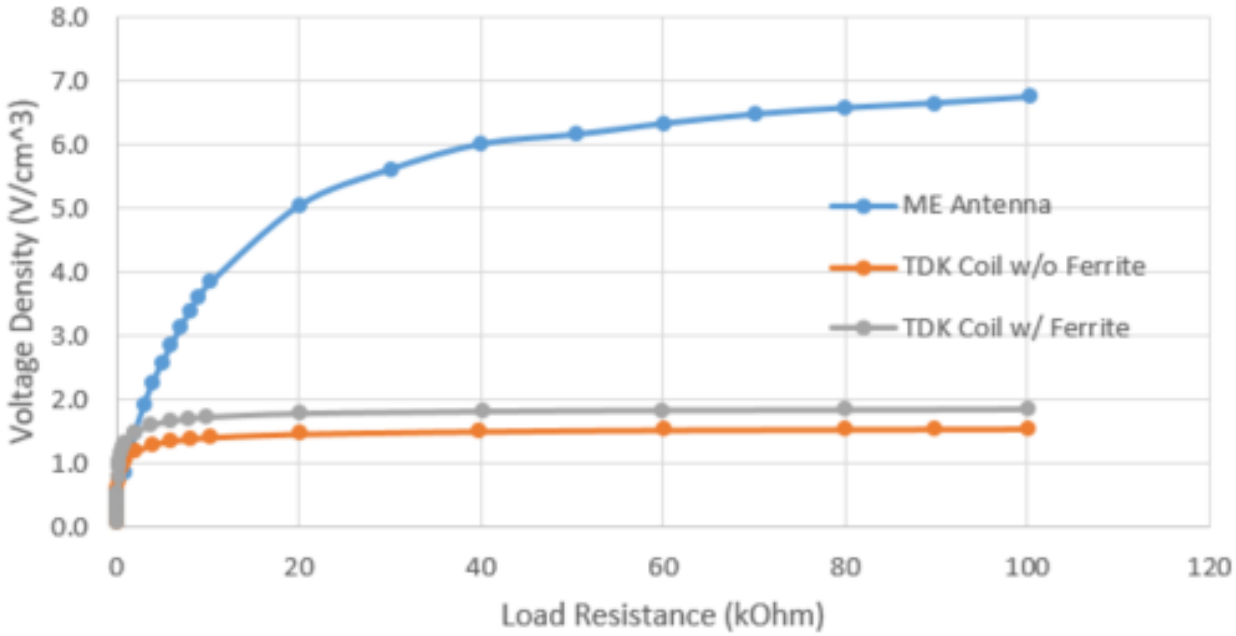

(a)

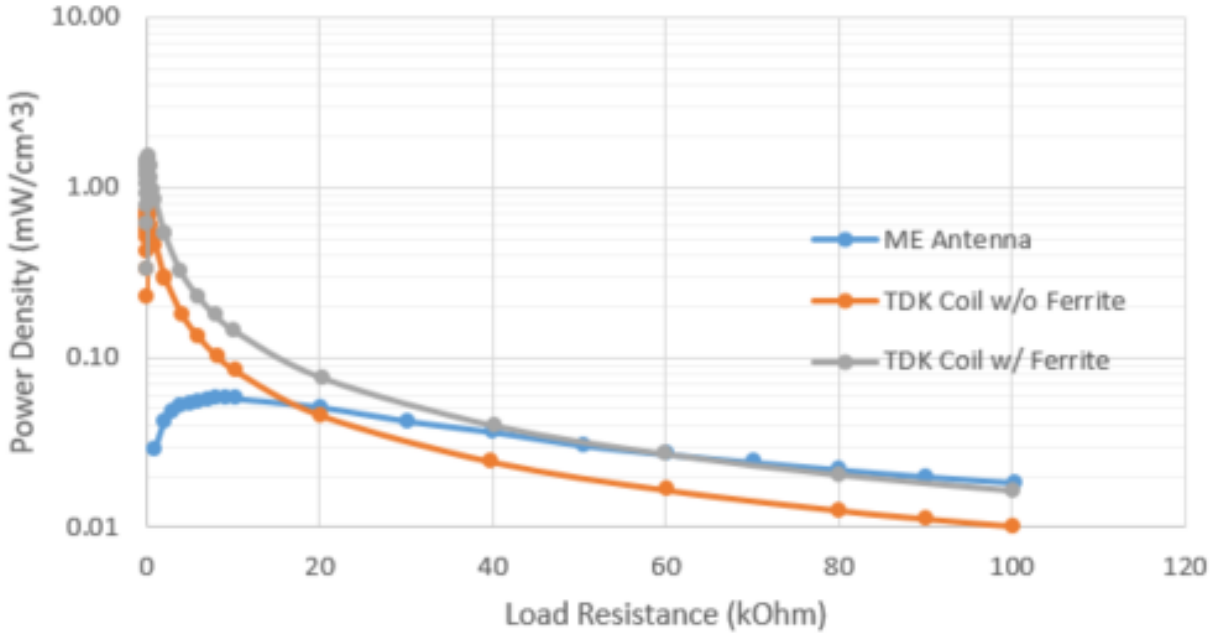

(b)

Figure 5.14: Measured voltage per unit volume (a) and power density (b) for constant input voltage.

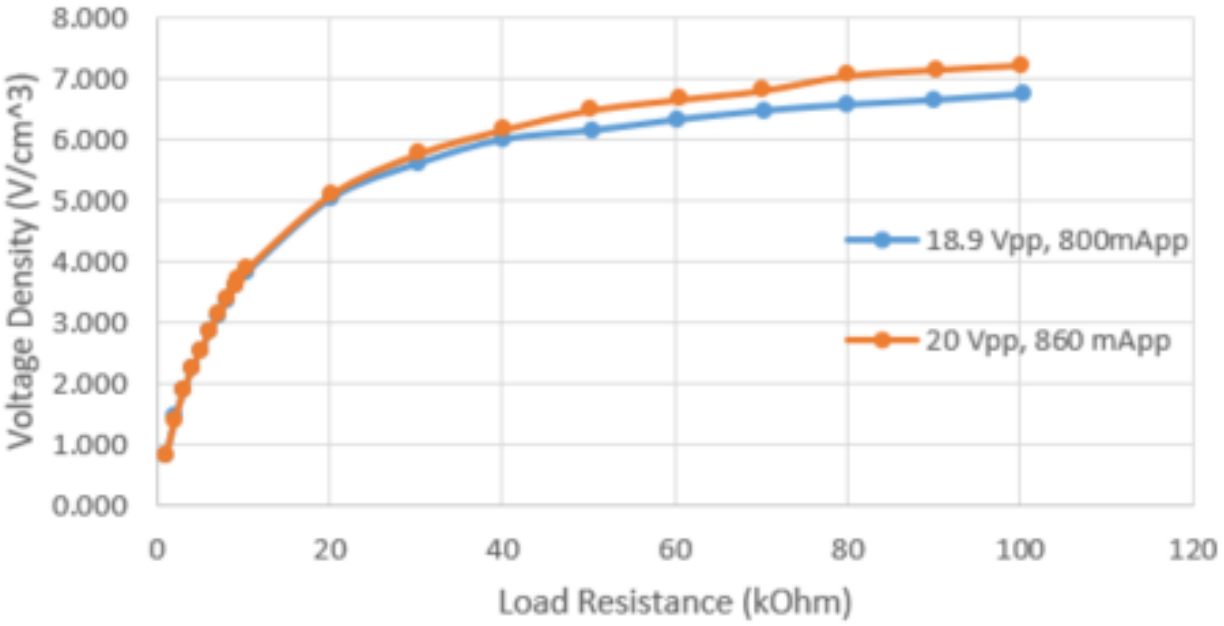

(a)

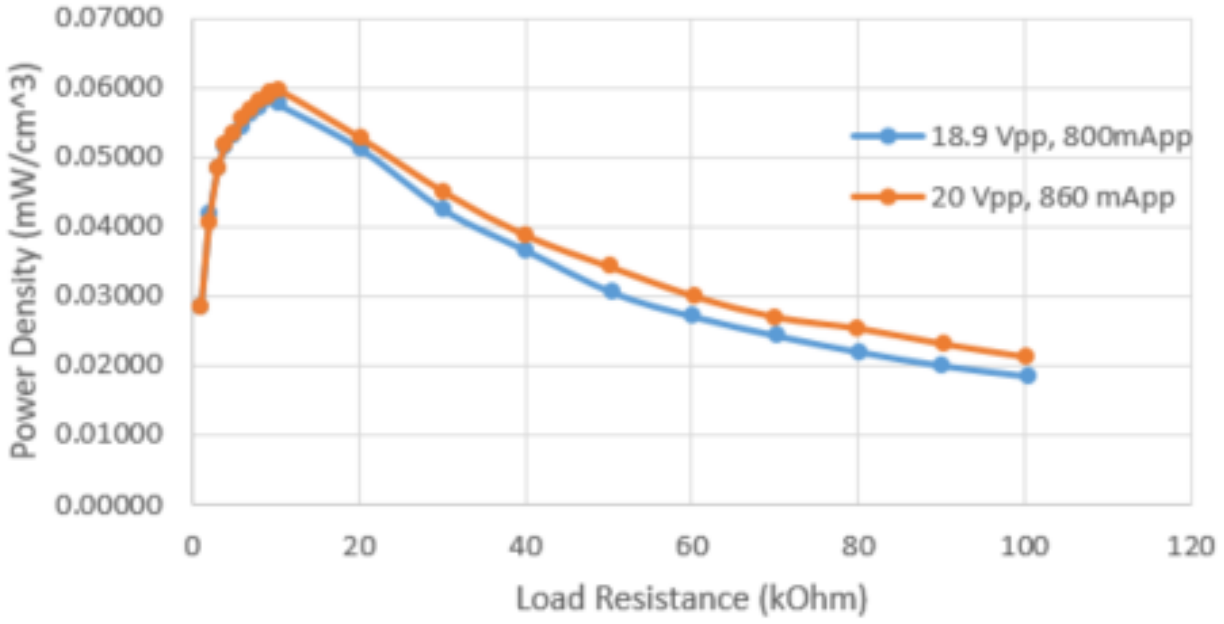

(b)

Figure 5.15: Comparison of ME antenna voltage per unit volume (a) and power density (b) for two different input voltages and currents.

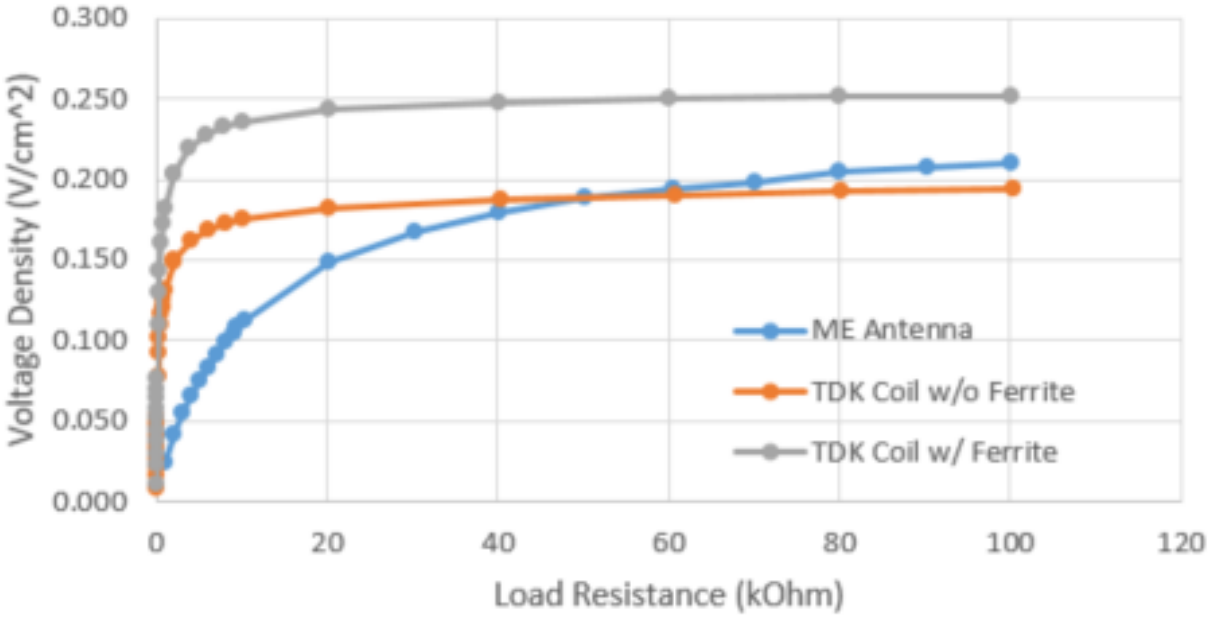

(a)

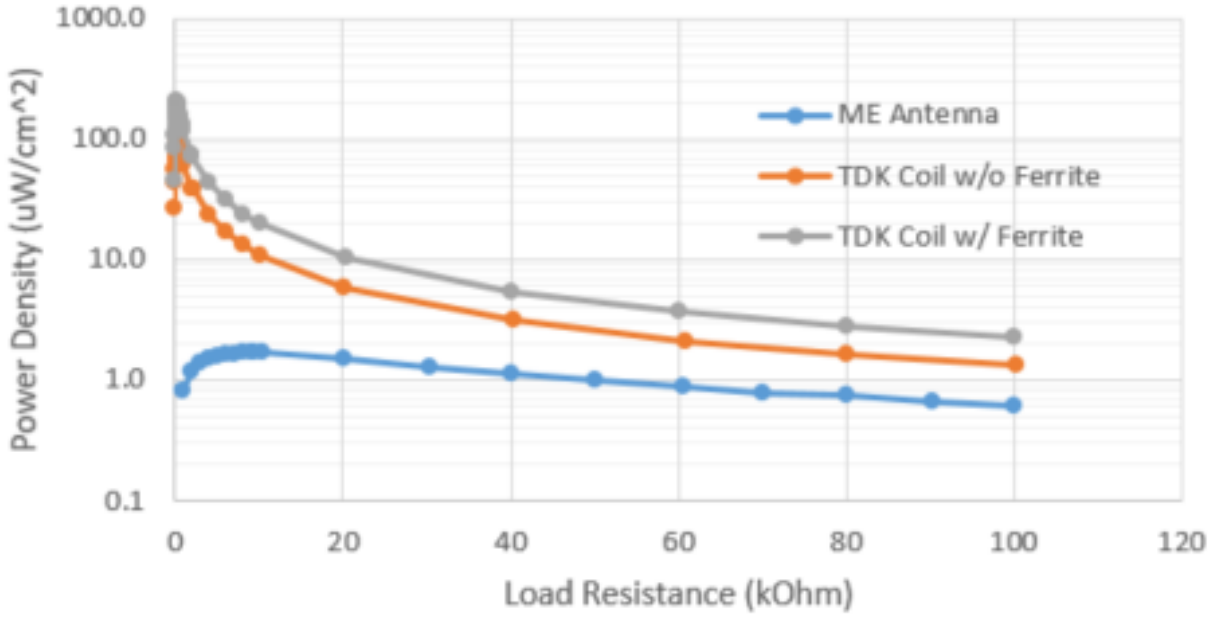

(b)

Figure 5.16: Measured voltage (a) and power (b) density with respect to area.

Table 5.2: Material and calculated system parameters.

MR material: Metglas 2065SA1	
Dimensions	7 mm × 20 mm × 0.025 mm
Density, ρ_m [38]	7180 kg/m^3
Resonant frequency, calculated	97.9 kHz
PE material TE Silver Ink PVDF 1-1004347-0	
Dimensions	15 mm × 20 mm × 0.040 mm
Piezoelectric thickness	0.028 mm
Density, ρ_p [38]	1780 kg/m^3
Mass, m_{film}	2.136×10^{-5} kg
Mass, m	5.03×10^{-6} kg
Capacitance, C_o	1.12 nF
Receiving coil: TDK WT242490-30F2-G	
Ferrite sheet: Wurith 354004	
Magneto-elastic coupling, ϕ_m	9.626×10^{-4} N-m/A
Elastic-electric coupling, ϕ_p	0.656 N/V
Average density, $\bar{\rho}$	5241.5 kg/m^3
ME coefficient at 97.9 kHz, α_{ME}	25,964 V/cm-Oe ($\beta = 1$)
ME coefficient at 89 kHz, α_{ME}	28,560 V/cm-Oe ($\beta = 1$)

charging batteries, which have a higher impedance when their state of charge is low. The MPP for the coil with and without a ferrite sheet is the same, as expected. The ferrite sheet on the back of the coil serves to better contain the magnetic field for coupling to the coil and allows a higher output power, but it does not alter the electrical properties (such as impedance) of the coil.

In addition, the power and voltage density between the coil and ME antenna were compared. The volume and area used in these calculations are a function of the surface area of the magnetostrictive material and the total thickness. Although the entire device size is determined by the piezoelectric material (which is wider than the magnetostrictive material), part of the piezoelectric material is used for contact with the leads and is not considered part of the antenna capable of harvesting magnetic energy, so the device size used for these density calculations do not include the extra piece of piezoelectric material not in direct contact with the magnetostrictive material. The voltage density per volume of the ME antenna can be up to four times larger than that of the coil with and without the ferrite layer. Although the power density per volume benefit is not as significant, the ME device still shows a larger power density at large load resistances (above 60 kΩ). Figures 5.12, 5.13, and 5.14 show measured power and voltage density comparisons for the same input current, similar input power, and same input voltage, respectively. An important observation is that all of the trends mentioned in voltage and power density remained consistent throughout these three trials, meaning keeping either of the input parameters consistent is sufficient for a direct comparison between the three antennas. Input power was kept similar but not exact because from the coupling interaction between the transmitting coils and receiving antennas, the input voltage and current varied between the setups. The variation between inputs for the ME antenna is plotted in Fig. 5.15, showing that slight variations in input voltage (5 percent) and input current (7 percent) does not affect the voltage or power density below the MPP and only causes slight deviation at higher output load resistances.

Table 5.3: Measured output voltage ripple compared to output DC voltage.

Antenna	Output DC Voltage (V)	Output Ripple (V)	Ripple as a Percentage of Output (%)
ME, MPP	0.160	0	0
Coil with ferrite, MPP	0.389	0.088	23
Coil no ferrite, MPP	0.273	0.084	31

However, when comparing the power and voltage density per area, the coil antenna with a ferrite layer has a higher density for all loads (Fig. 5.16). The ME antenna has a slightly higher voltage density per area than the coil without a ferrite layer for load resistances higher than 60 kΩ. This is because the output power and voltage for the ME antenna is lower than the coil, but the thickness of the device gives it an advantage in terms of volume density. Because area density only takes into account surface area and not the thickness, the coil antenna outperforms the ME antenna. Another difference worth mentioning is the output voltage ripple. Whereas there is some leakage from the input AC signal through the copper coil that is made worse at low resistance loads or with a ferrite sheet (Fig. 5.18 and 5.19), the ME antenna has virtually no output voltage ripple due to the energy transfer between magnetic to mechanical to electrical domains (Fig. 5.17.) Table 5.3 summarizes the measured voltage ripple and compares it to the DC output voltage.

Table 5.4 summarizes the differences in performance between the ME antenna and the coil. The ME voltage coefficient was measured at an input AC magnetic field of 0.7 Oe. In addition, the output voltage for the voltage multiplier with an ME antenna input at 89 kHz was plotted as function of position in Fig. 5.20. Consistent with expectations, the output voltage decreases symmetrically as the ME antenna is moved further away from the AC coil. Results are shown with an open circuit load and at the MPP of 10.1 kΩ. The polynomial fit equation for these measured curves is consistent with expectations, with the voltage inversely proportional to the distance from the coil and decreasing in a symmetrical

fashion as the distance increases. The R^2 values both being higher than 95 percent also shows a high accuracy between the measured data and the polynomial fit curve. Because the ME antenna is operating in the near field region of the generated magnetic field, the far field relationships, such as antenna power being inversely proportional to the square of the distance, do not apply here.

5.5 Literature Comparison

Table 5.5 compares the ME antenna performance in this work with that in existing literature. [30] used an integrated circuit fabrication process to produce a nanoplate resonator (NPR), which allows for a higher operating frequency due to the sub-millimeter dimensions. [34] also uses a similar structure and method. The work in this paper is most closely related to [33], which produces similar results. [39] also had a similar ME coefficient as what was measured in this work. [31] and [40] use similar material as this work and also operate at a similar frequency. Figure 5.21 compares the ME coefficient from various antennas measured in this work with those in existing literature, which shows an ME coefficient of 94 V/cm-Oe is a reasonable value for a 20 cm long antenna. Comparing with what was calculated from Eqn. 5.6, the loss factor, β, is 3.29×10^{-3}. Vacuum bagging compared to manual weight compression to make the ME antenna laminates did not have a significant advantage, mainly because the fast set time of epoxy and cyanoacrylate (on the order of several minutes) fixed the adhesive layer thickness before the vacuum bag could be sealed properly. Sealing the vacuum bag required at least 10 to 20 minutes, so the vacuum bagging method, though able to provide higher pressure, did not help in decreasing the adhesive thickness or making the adhesive layer more uniform. This can be seen in Fig. 5.21, where the coefficient of antennas fabricated with the vacuum bagging method did not have a significant difference from the other ones that were manually compressed. In addition, the type of adhesive did not have a noticeable effect on the ME antenna performance either. Both the epoxy and

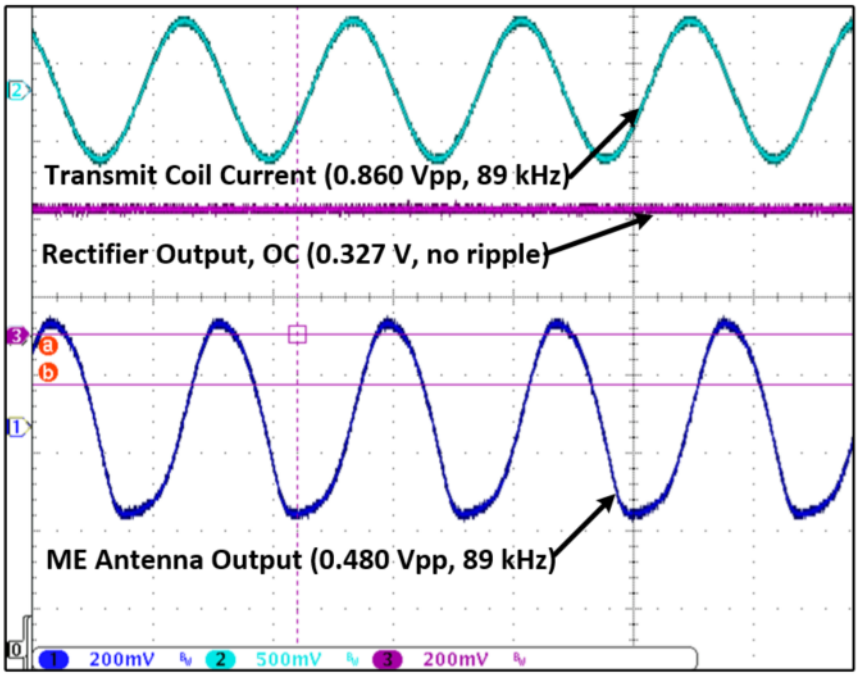

(a)

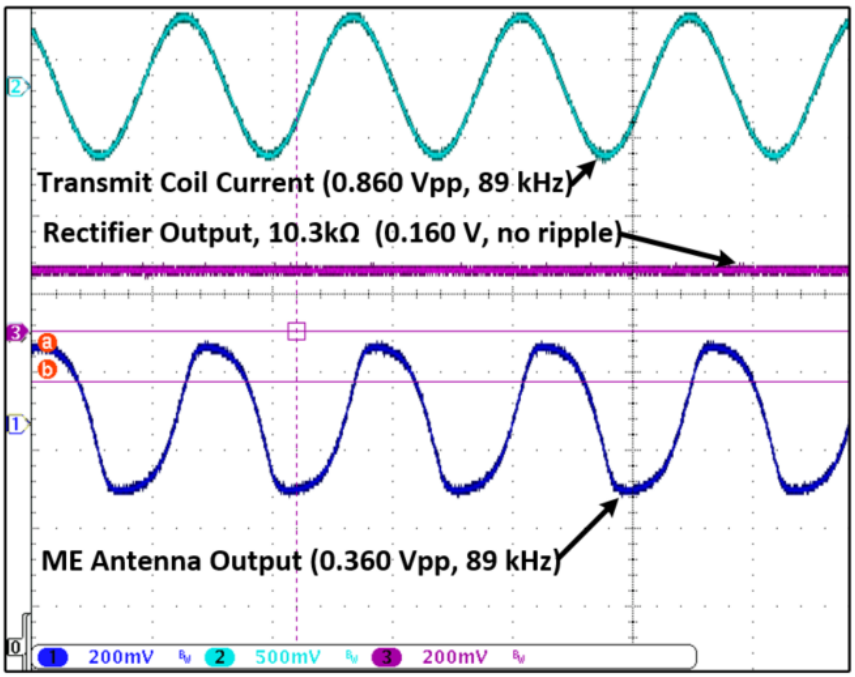

(b)

Figure 5.17: Measured rectifier output ripple with no load (a) and at MPP (b) for ME antenna input.

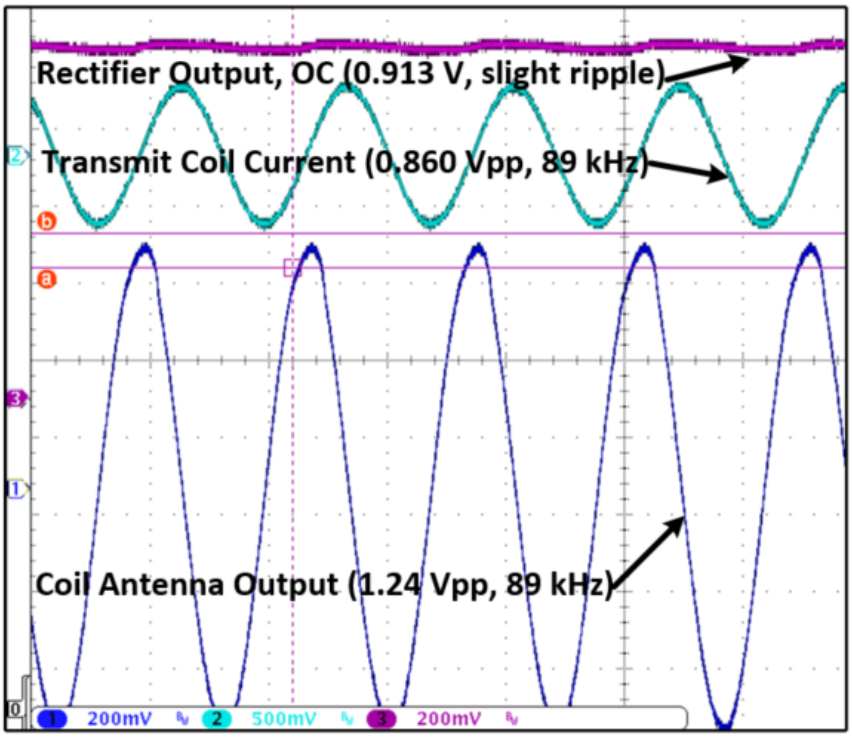

(a)

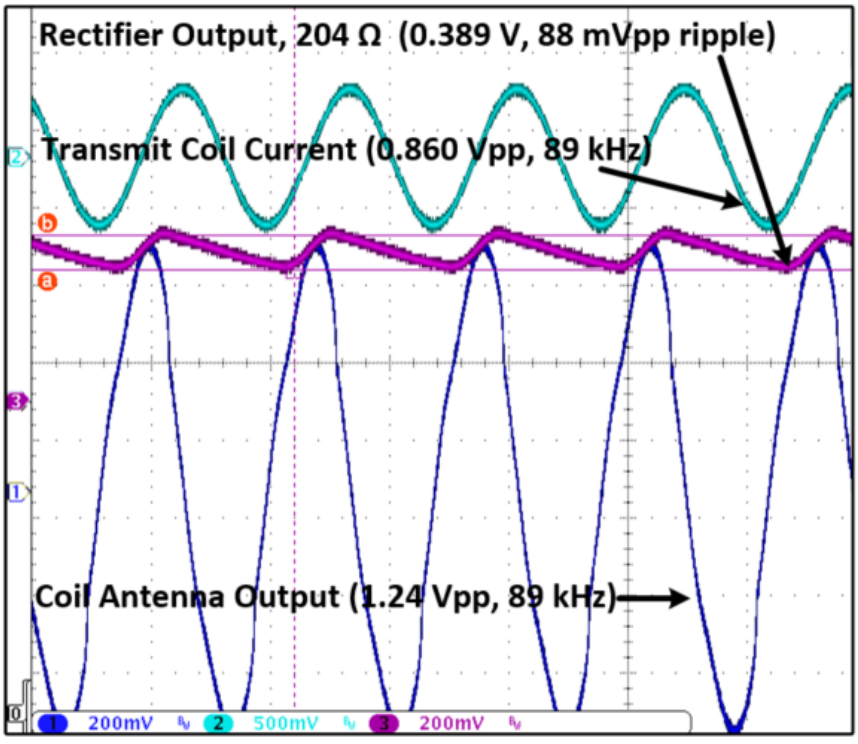

(b)

Figure 5.18: Measured rectifier output ripple with no load (a) and at MPP (b) for coil input with ferrite sheet.

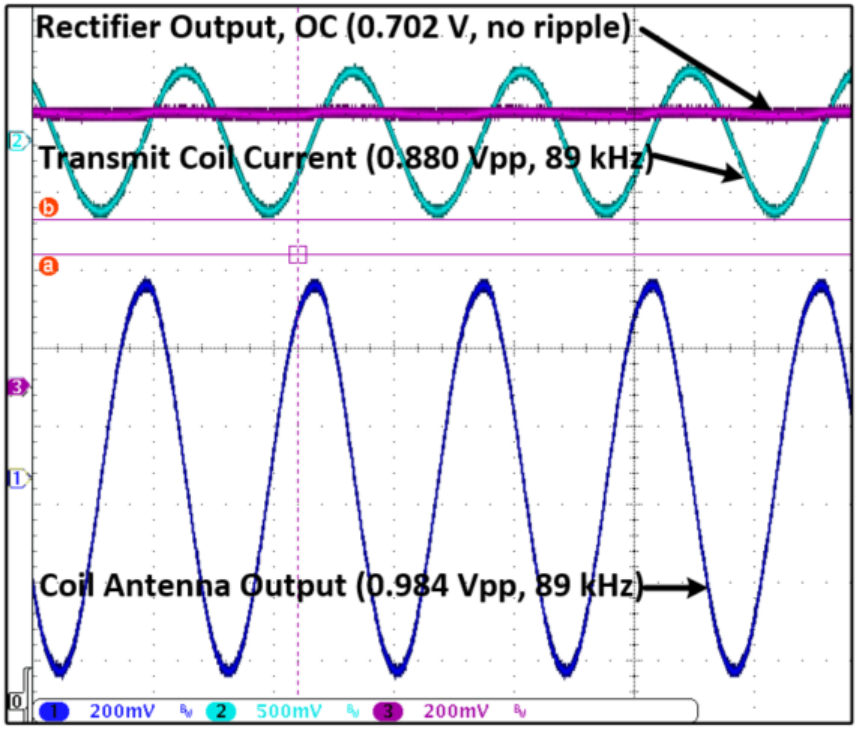

(a)

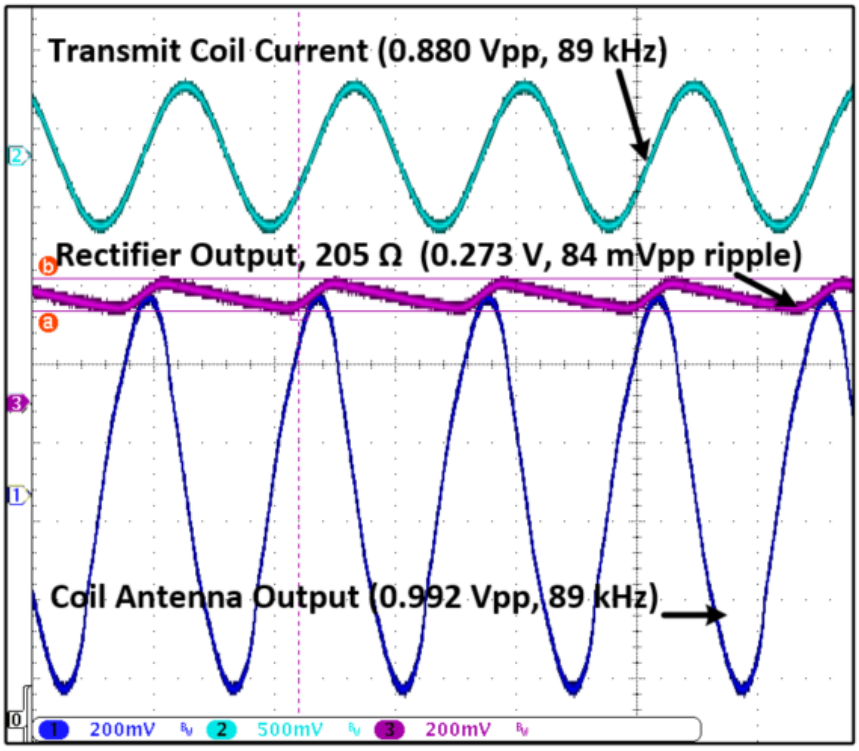

(b)

Figure 5.19: Measured rectifier output ripple with no load (a) and at MPP (b) for coil input without ferrite sheet.

Table 5.4: Result summary of ME device and coil antenna for constant input current (magnetic field).

	ME antenna	Coil without ferrite	Coil with ferrite
Dimensions (mm)	15 × 20	21.3 (diam)	21.3 (diam)
Thickness (mm)	0.29	1.2	1.4
Area (cm^2)	1.4	3.56	3.56
Volume (cm^3)	0.041	0.43	0.48
Frequency (kHz)	89	89	89
OC input voltage (Vpp)	0.480	0.984	1.24
OC output voltage (V)	0.324	0.709	0.914
DC Magnetic Field (Oe)	19.1	–	–
AC Magnetic Field (Oe)	0.85	0.85	0.85
Max Power Density (volume) (mW/cm^3)	0.0597	0.864	1.53
Max Voltage Density (volume) (V/cm^3)	7.24	1.61	1.85
Max Power Density (area) (mW/cm^2)	1.73	103.7	207
Max Voltage Density (area) (V/cm^2)	0.21	0.19	0.25

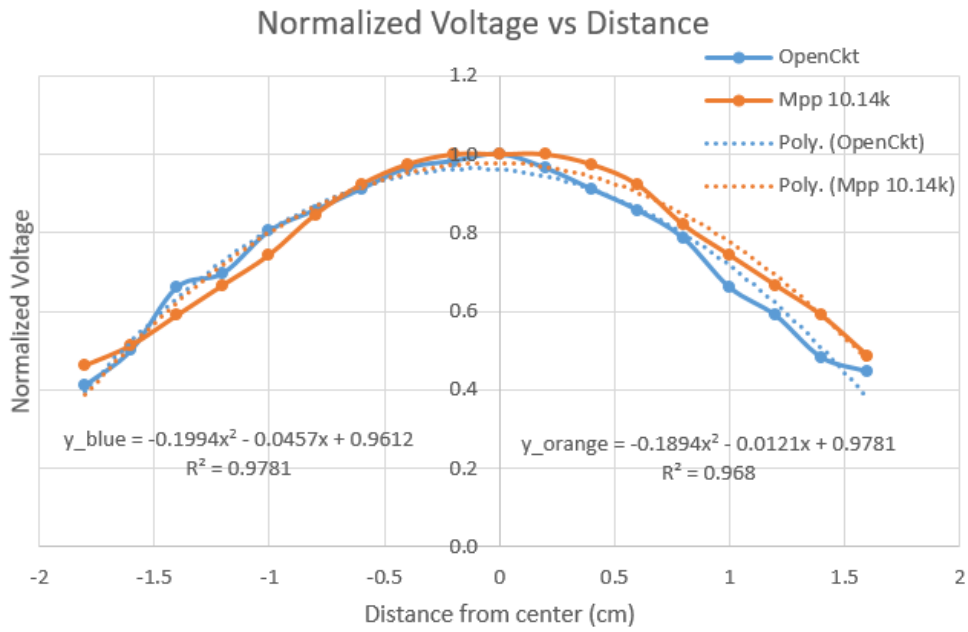

Figure 5.20: Measured output voltage of rectifier and ME antenna as a function of position from AC coil.

cyanoacrylate adhesive antennas had similar magnetoelectric coefficients for a given length. However, the proposed system in Table 5.1 proved to be too small to manually fabricate with consistent performance and will need to be verified with alternate fabrication methods. Figure 5.22 compares the ME coefficients measured to their lengths. Consistent with Fig. 5.21, the higher frequency antennas (with lengths shorter than 15 mm) have a lower ME coefficient. However, antennas longer than 25 mm had a similar or lower coefficients than the 20 cm antennas. This could be caused by the test setup (in which the coil supplying the AC magnetic field was not wide enough to produce uniform field across the entire antenna) or by a saturation in energy conversion, where the loss in a larger piece of material negates the larger amount of energy harvested.

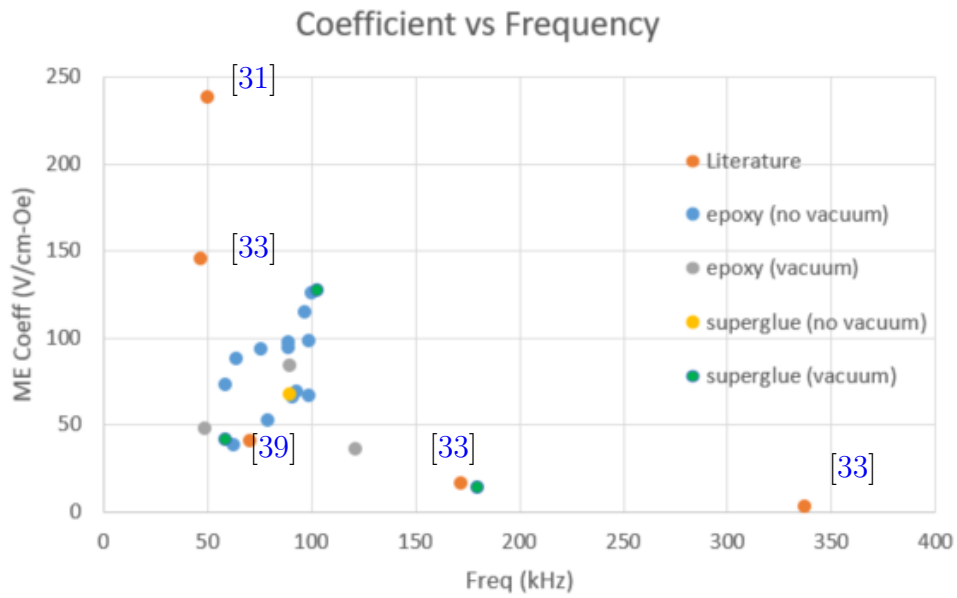

Figure 5.21: Comparison of measured ME coefficient for several antennas at different frequencies.

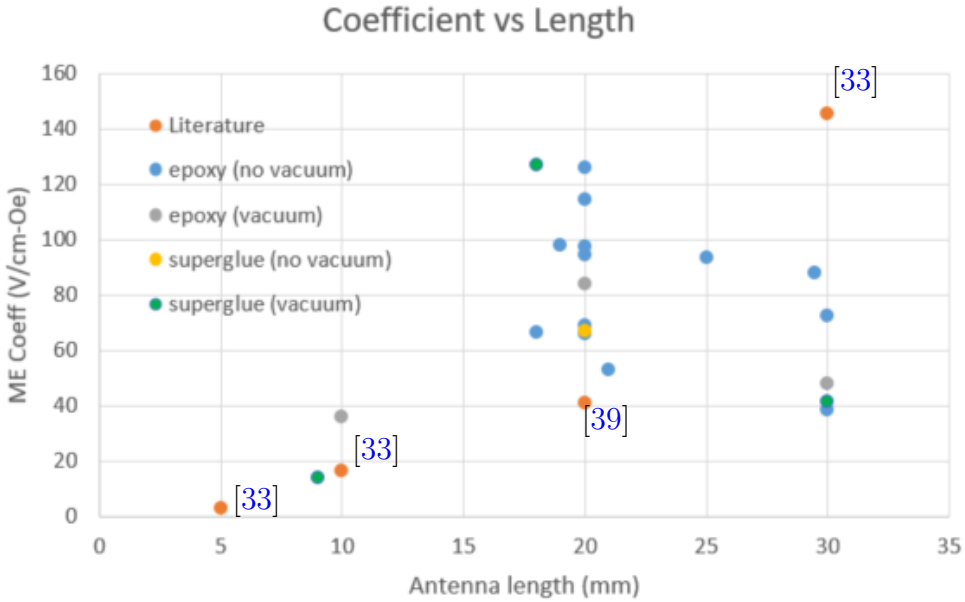

Figure 5.22: Comparison of measured ME coefficient for several antennas at different lengths.

Table 5.5: Comparison of current work with literature.

	This work	[33]	[31]	[30]	[39]	[40]	[34]
Year	2022	2015	2006	2017	2020	2022	2018
MR material	Metglas 2605 SA1	$Fe_{64}Co_{17}Si_7B_{12}$	Metglas 2605 SA1	FeGaB	TdVib	Metglas	FeGaB
PE material	PVDF	PVDF	PVDF	AlN	PZT	PMN-PT	AlN
Dimensions (mm)	15 × 20	5 × 5-30	NA	0.05 × 0.2	10 × 20	20 × 140	0.1 × 0.2
Thickness (μm)	290	90	NA	0.5	1760	250	1
Frequency	89 kHz	47-337 kHz	50 kHz	60.7 MHz	70.5 kHz	15 kHz	27 MHz
ME coefficient (V/cm-Oe)	94	3-146	238-310	6000	41	350 nC/Oe	NA
Coupling FOM, M_o	2.25	NA	NA	NA	2.95	NA	NA
Power density (mW/cm^3)	0.0597	0.065-1.5	NA	NA	28.4	49 mW/Oe	NA

Table 5.5: Rectifier performance comparison table (continued).

	This work	[33]	[31]	[30]	[39]	[40]	[34]
Output power (μW)	2.42	0.04-6.4	NA	NA	10,000	NA	NA
Output voltage (V)	0.324	0.14-1.3	NA	180e-6	7-15	NA	0.3-1.2

5.6 Vibration: Setup and Characterization

In addition to harvesting energy from magnetic fields, the PVDF layer of the ME antenna can convert vibration into voltage. In a similar fashion to the Metglas material, a certain length of PVDF material will have a resonant frequency that produces the highest output voltage with an applied vibration. To characterize the ME antennas' vibration performance, the resonance frequency was determined before measuring its output power. The setup for measuring the resonance frequency is shown in Fig. 5.23 and Fig. 5.24. In Fig. 5.23 [45], National Instrument's portable data acquisition unit (myDAQ) was used to control the amplitude and frequency of vibration supplied by the shaker. LabVIEW was used with the myDAQ unit to generate the input signal, which could be a chirp signal that swept through a range of frequencies, and to measure the vibration and ME antenna voltage and provide the frequency spectrum of each. Figure 5.25 shows an example of the LabVIEW display that allows the user to adjust the input and view the desired signals. Several complications arise using the setup in Fig. 5.23. First, when sweeping through a range of frequencies, a 60 Hz tone is coupled to the ME antenna output from the power supply. This can be resolved by applying a single tone frequency, which does not have this leak-through (Fig.

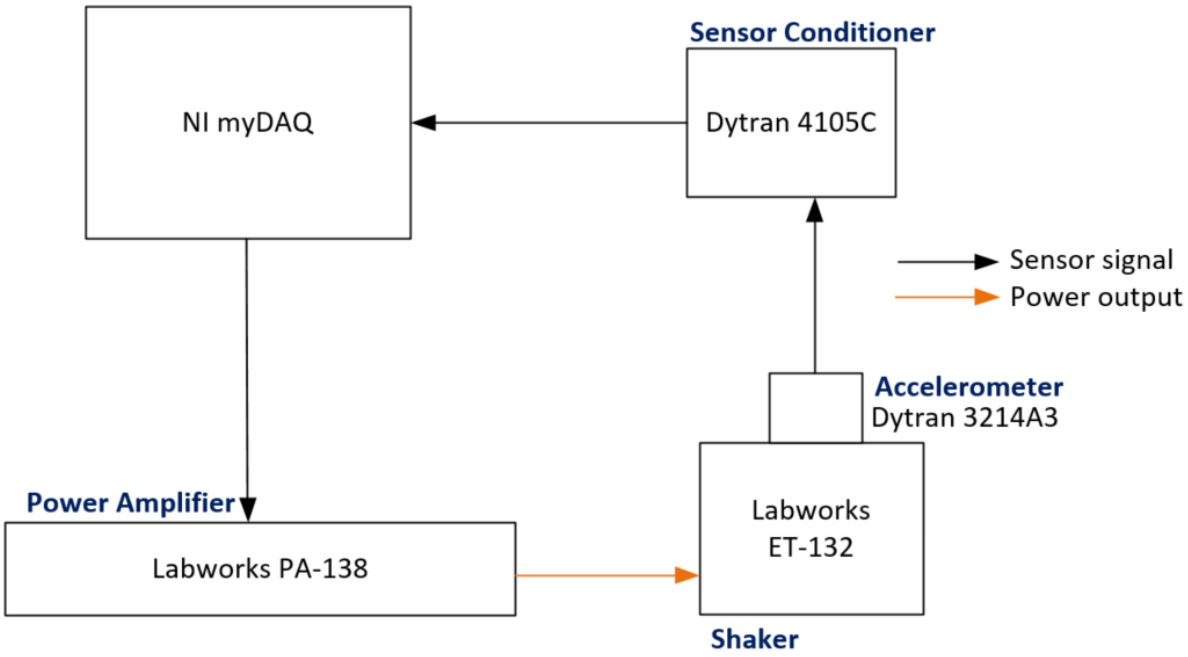

Figure 5.23: Test setup to measure ME device voltage output and adjust vibration frequency and amplitude with LabVIEW and NI myDAQ.

5.26). Secondly, the input impedance of the myDAQ channel is comparable to the impedance of the ME antenna, since PVDF materials are capacitive and have high impedance. This required the use of an op-amp buffer (TL062CP) at the output of the ME antenna. Because oscilloscope probes usually have about 1 MΩ of input impedance, the setup in Fig. 5.24 does not require this buffer.

The measured resonant frequencies of ME antennas of various lengths are summarized in Fig. 5.27. As expected, the lower the resonant frequency, the longer the length of an ME antenna. The main dimension of importance is the length that is protruding and free to move. Therefore, even though the entire length of an ME antenna could be 20 mm, the length used is how much is protruding from the clamp on top of the shaker, which could be 18 mm, or 2 mm shorter than the entire length. Figure 5.28 shows several examples of how the ME antennas are secured to the shaker. In some cases, a thin layer of padding is added around the wire leads to provide a more secure contact between the metal clamp and ME

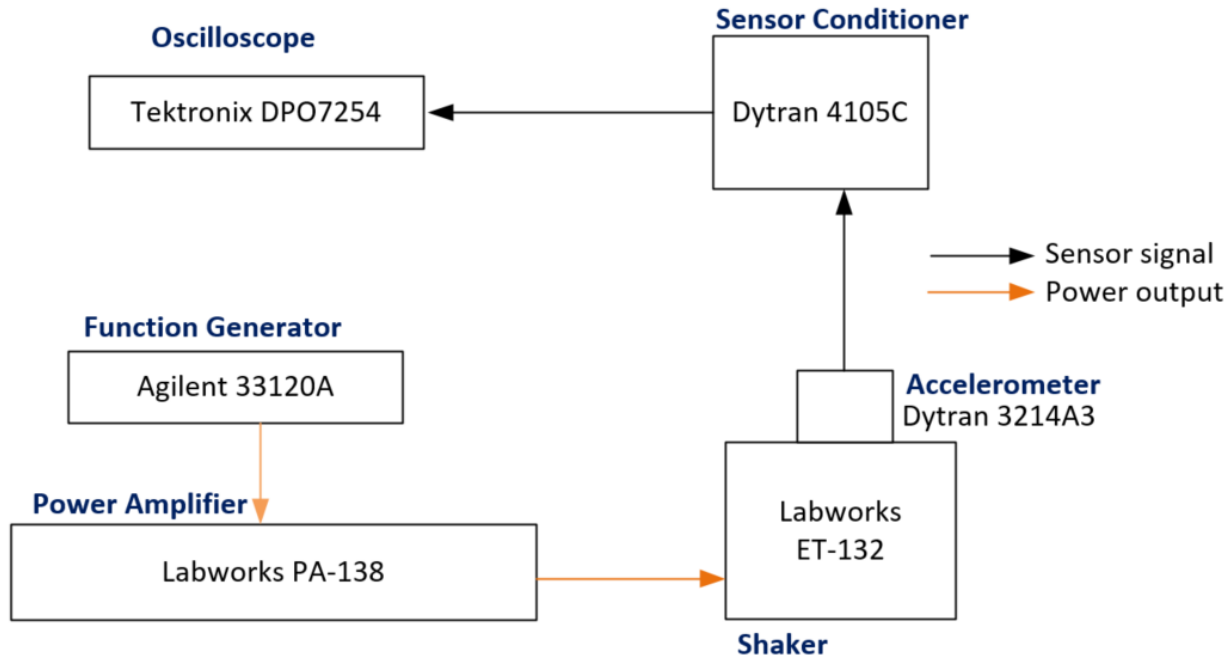

Figure 5.24: Test setup to measure ME antenna voltage and vibration controlled with function generator.

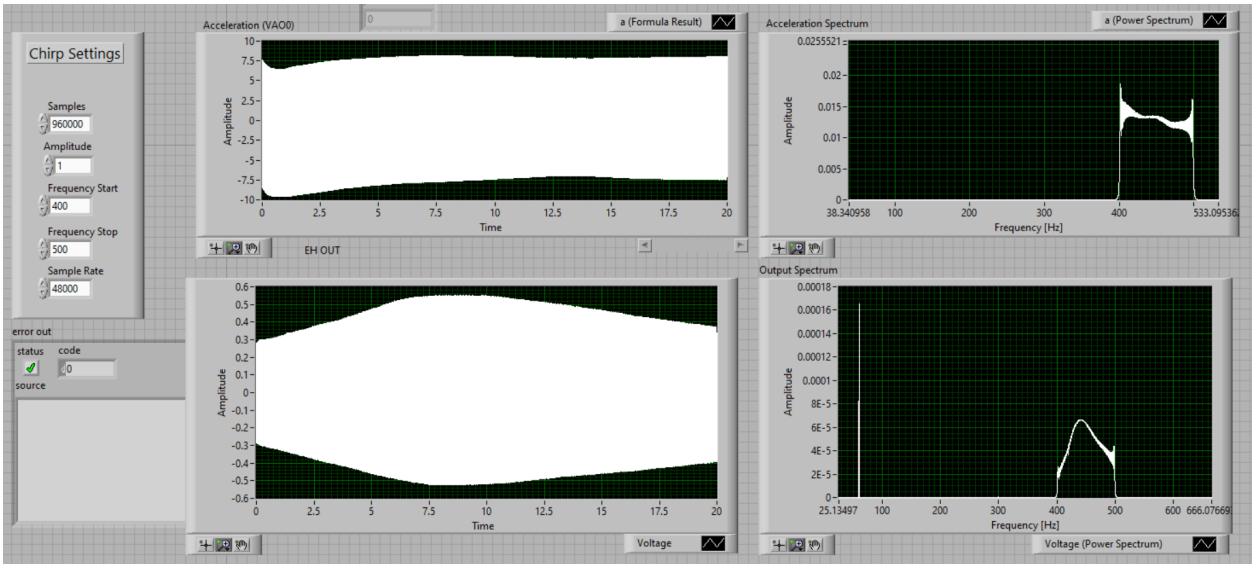

Figure 5.25: LabVIEW user interface showing frequency sweep of vibration to determine resonance frequency of ME antenna.

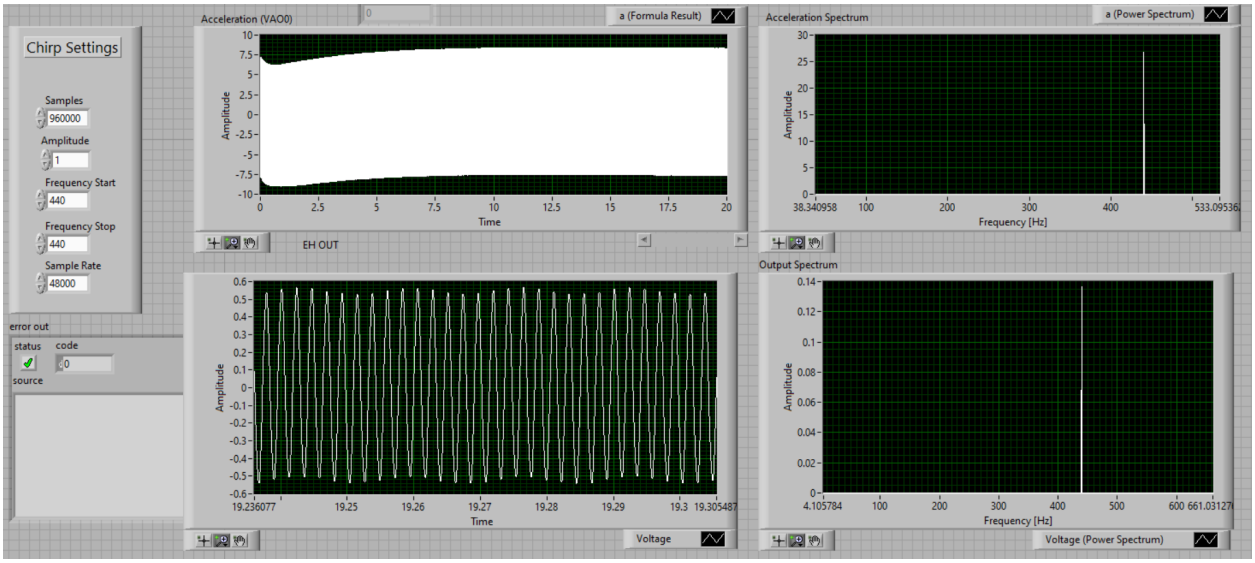

Figure 5.26: LabVIEW user interface showing measured vibration and ME device output at a single frequency.

antenna, which allows for better vibration transfer.

From the vibration resonant frequency, the stiffness of the ME antenna can be calculated and is summarized in Table 5.6 for the 29 mm long antenna used in later measurements shown in Fig. 5.31 through Fig. 5.33. Some nonidealities exist in this calculation. First, the leads being attached on the side of the ME antenna causes the device to not be a true cantilever with one fixed end. Because of this, the effective length would be shorter than the measured length. It can be seen in Fig. 5.27 that as the antenna increases in length, the antenna with the smaller 28 AWG leads has a lower frequency than the antenna with the thicker 22 AWG leads, suggesting the thinner wires have a weaker effect on the effective length and, therefore, the frequency. Another nonideality is the width of the ME devices are 15 mm, which is comparable to the length, which ranged from 18 mm to 30 mm. This was also not accounted for in the frequency calculations, which assumed an ideal cantilever model.

In addition to measuring the resonant frequency, the voltage normalized to vibration (Fig.5.29(a)) and the voltage density per unit area was also compared (Fig.5.29(b)). Mea-

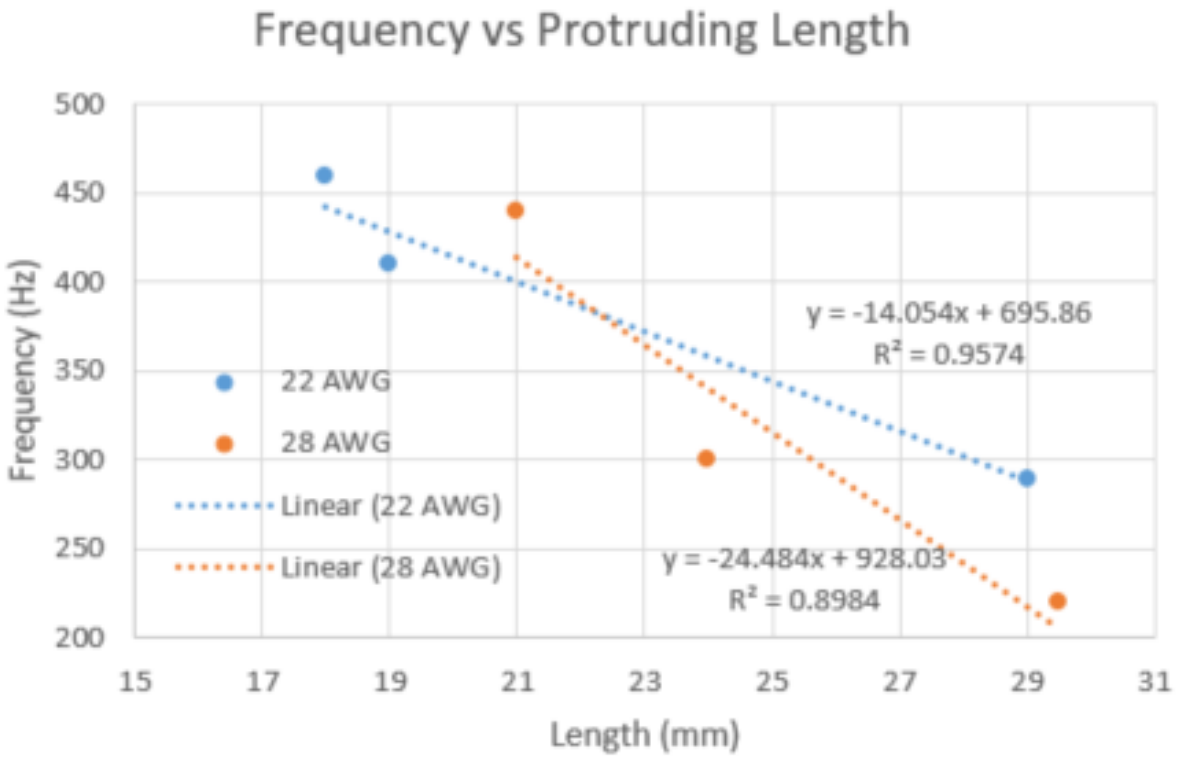

Figure 5.27: Measured vibration and ME device output at a single frequency.

Table 5.6: Measured and calculated parameters for 29 mm long ME antenna.

Parameter	Value
Dimensions (measured)	30 mm × 15 mm × 0.04 mm
Mass, m_{film} (calculated)	3.20×10^{-5} kg
Mass, m (calculated)	7.55×10^{-6} kg
Resonant frequency, f_0 (measured)	290 Hz
Stiffness, k (calculated)	25.07 Pa

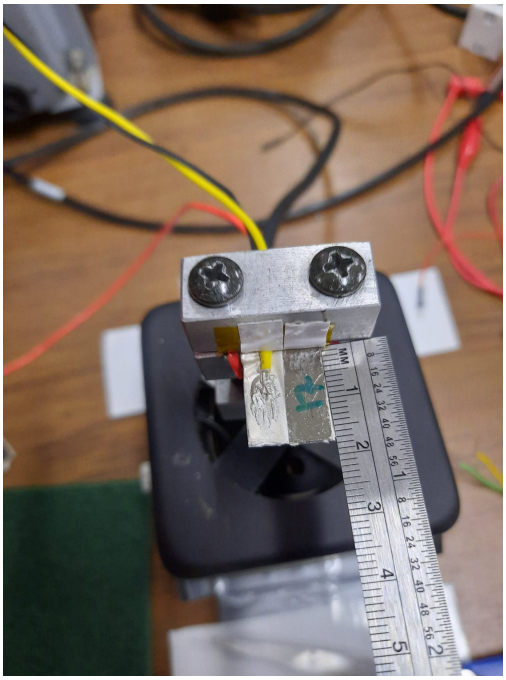

(a) ME antenna with 22 AWG silicon wire leads clamped to shaker with no padding.

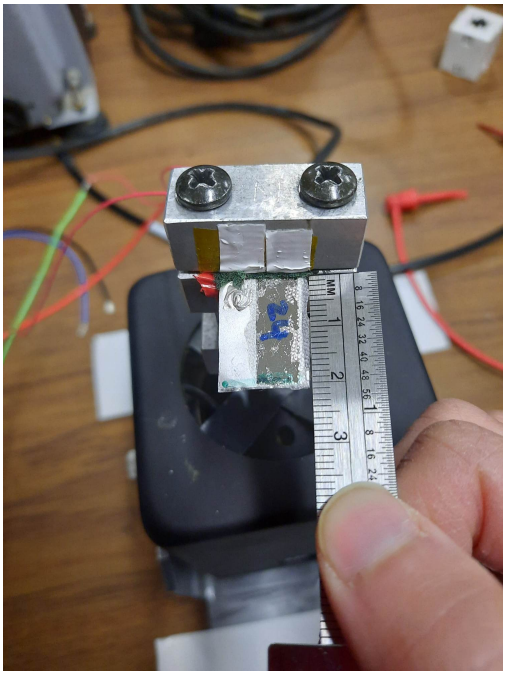

(b) ME antenna with 28 AWG wire leads clamped to shaker with padding.

Figure 5.28: Various clamping scenarios to transfer vibration to ME antenna.

surements were taken with an input vibration of approximately +/- 8 g. The gauge of wire does not have a significant effect on the voltage produced by the ME antenna from vibration, so the thinner gauge (28 AWG) is preferred because it is easier to clamp to the shaker. The voltage density varies widely between the different length antennas; there is no clear correlation between antenna length and voltage density. Further investigation with emphasis on keeping all parameters identical (wire gauge, lead placement, epoxy, shaker attachment) can help to verify whether this trend is not correlated to antenna length.

5.7 Vibration: Results

As mentioned previously, the high impedance of the PVDF is due to it being mainly capacitive, and this characteristic makes the voltage multiplier inefficient, since the intermediate stage capacitor in the multiplier forms a voltage divider with the PVDF. A full bridge rectifier is more optimal because it does not contain any stage capacitors, but care must be taken that the diodes chosen have low leakage current (TBAT54S diodes were used), since the PVDF normally outputs a low current. Figure 5.30 shows the different rectifier topologies for comparison.

The output power for two antennas with protruding lengths of 18 mm and 29 mm was measured as a function of load resistance (Fig. 5.31). As expected, the smaller ME antenna has a lower output power because there is less PVDF material to harvest the vibration and convert it to voltage. In addition, the power ratio between the 18 mm and 29 mm long antennas correlate with the area ratio between the two. The maximum power output of the 18 mm antenna is about 57 percent of that of the 29 mm antenna, while it is approximately 62 percent the size of the 29 mm one. In both cases, the maximum power point occurs at a load of around 460 kΩ to 680 kΩ. The load resistance values were swept using discrete resistors, and measurements were taken with an input vibration of approximately +/- 8 g.

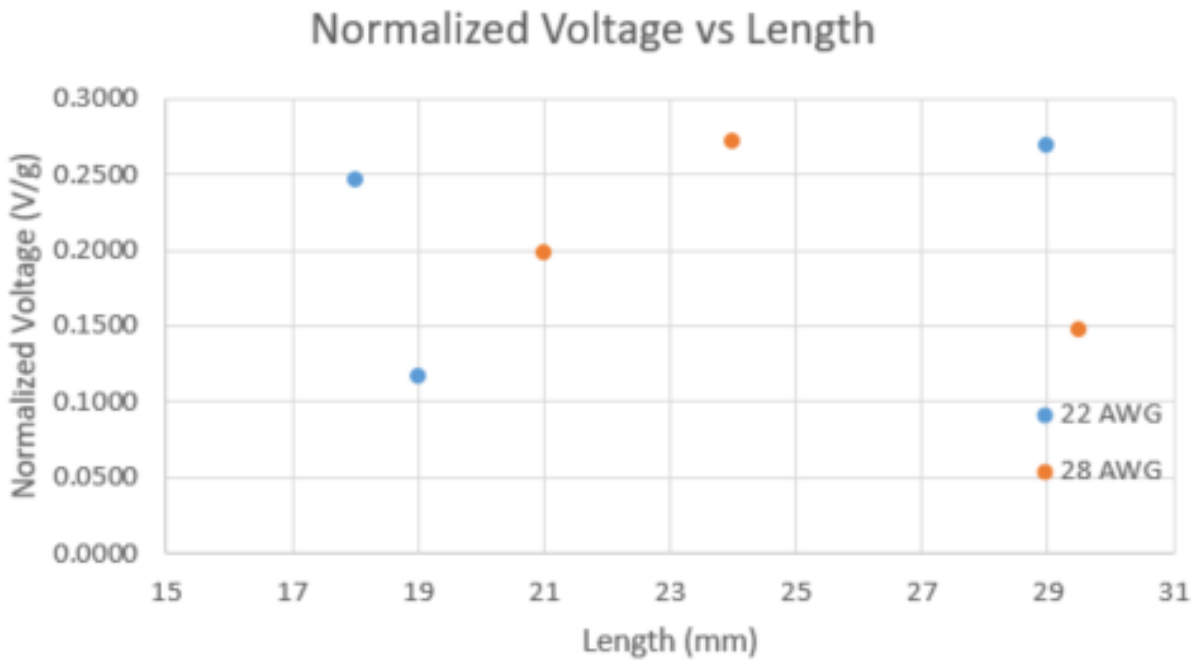

(a)

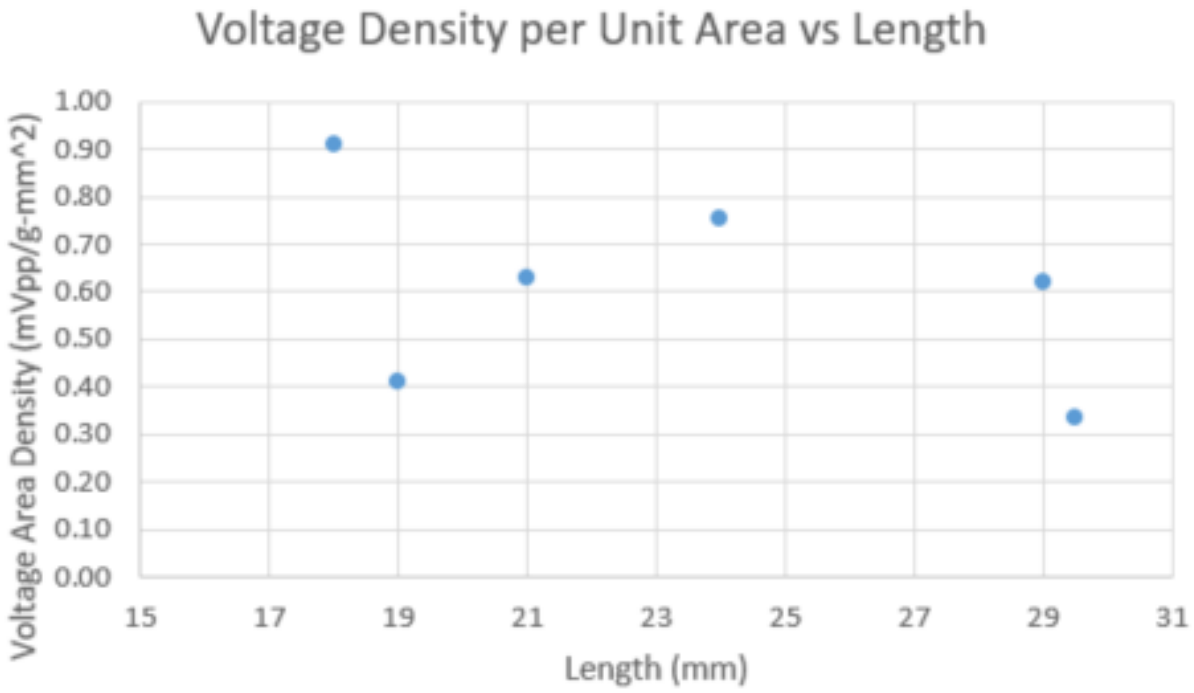

(b)

Figure 5.29: Measured normalized output voltage (a) and voltage area density (b) with respect to antenna length.

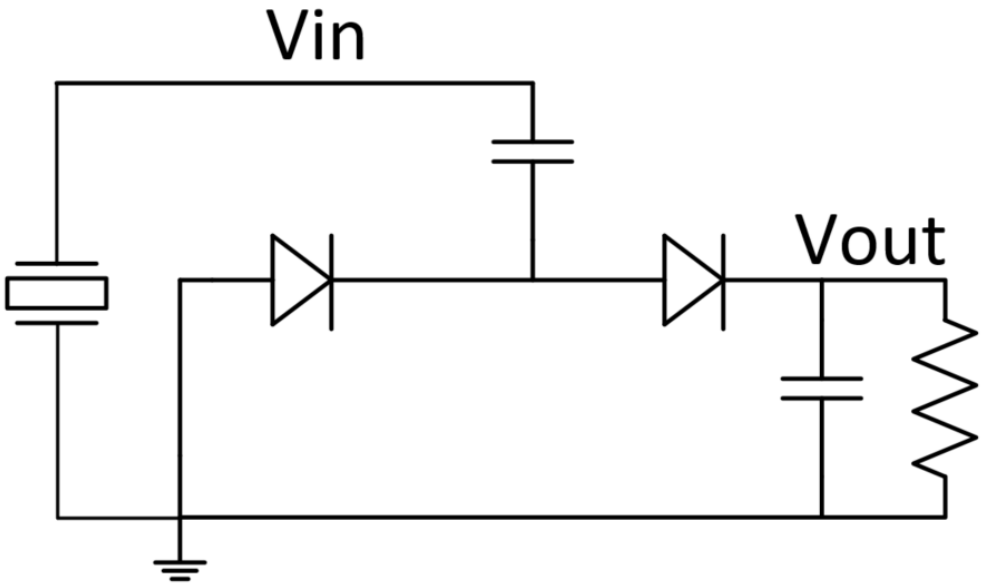

(a)

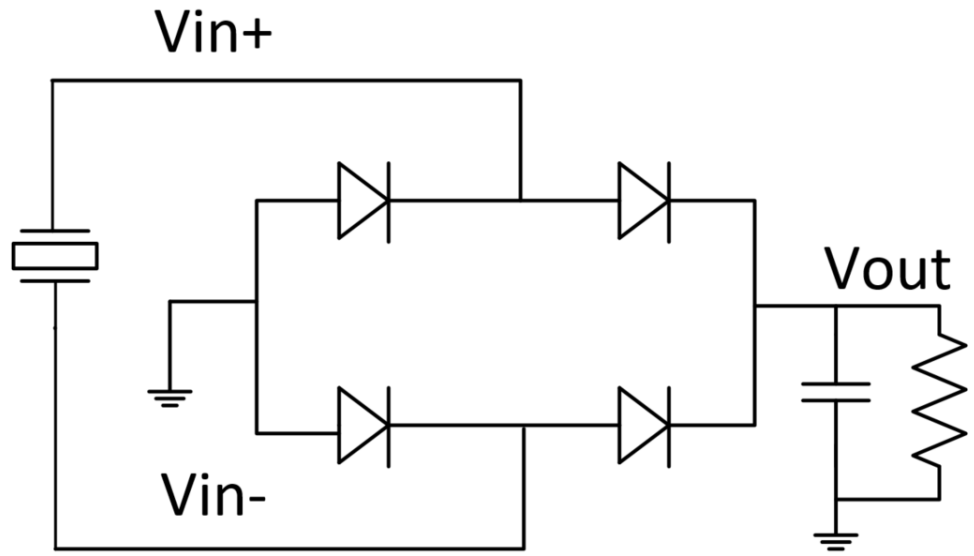

(b)

Figure 5.30: Schematic of voltage multiplier (a) and full bridge rectifier (b).

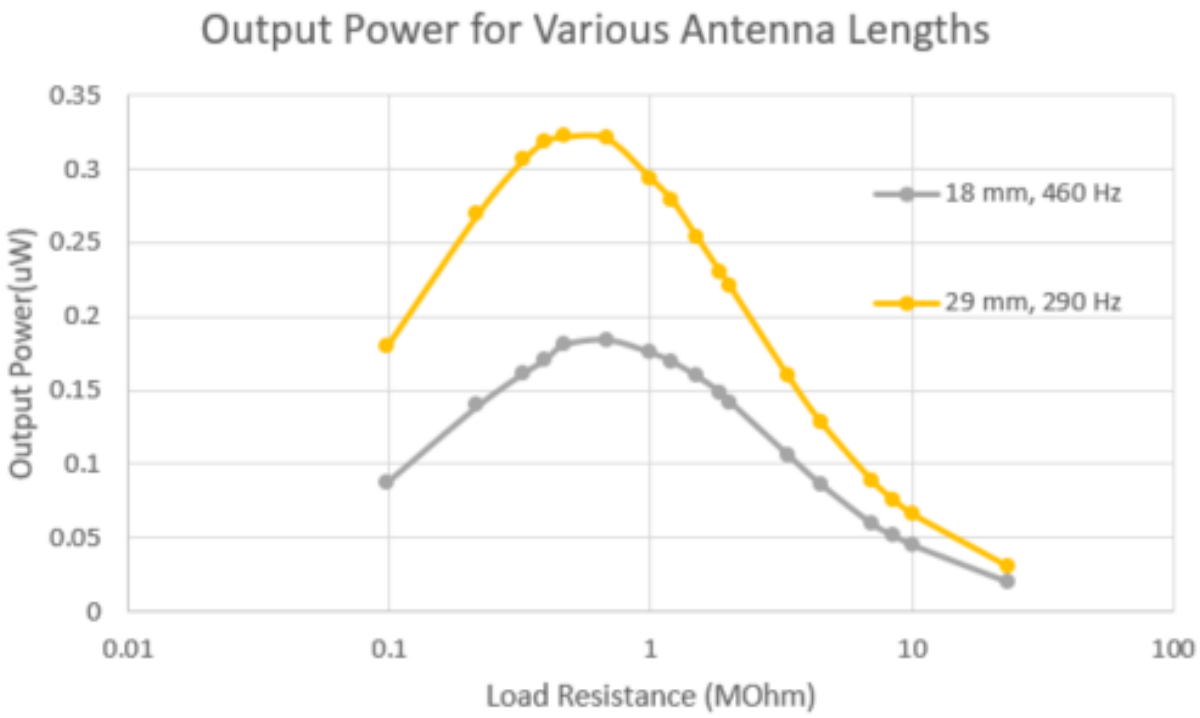

Figure 5.31: Measured output power of FBR with antennas of different lengths and and input vibration acceleration of around +/- 8 g.

Because the 30 mm antenna had the higher output power, it was used to measure the output power at various input vibration levels. The results are summarized in Fig. 5.32. At +/- 5 g of vibration, the output power of the ME antenna and full bridge rectifier decreases significantly. This can be explained by looking at the open circuit output voltage curve as a function of frequency (Fig. 5.33). The voltages measured in Fig. 5.32 are open circuit voltages, without connecting the ME antenna to the full bridge rectifier (which causes loading and a decrease of voltage even without a load resistance). At an input vibration of +/-5g, the unloaded output voltage is less than 1 V, and although the forward voltage of the TBAT54S diode is small (0.16 V for a forward current of 100 μA), the output power is still greatly decreased.

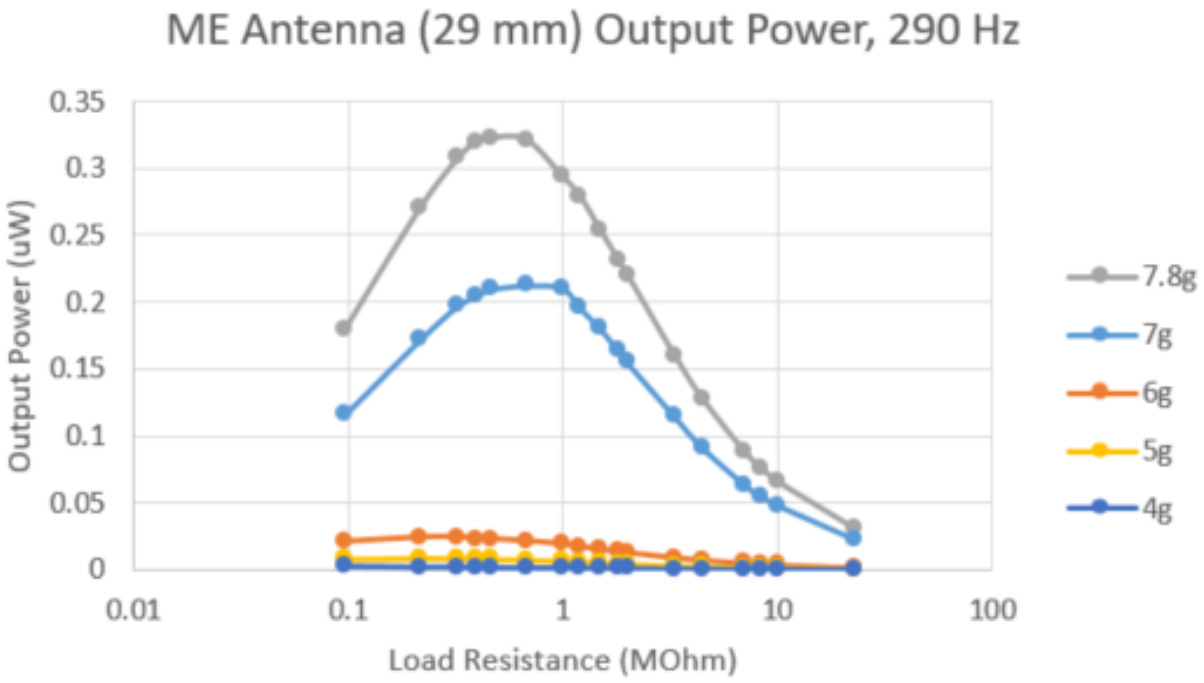

(a)

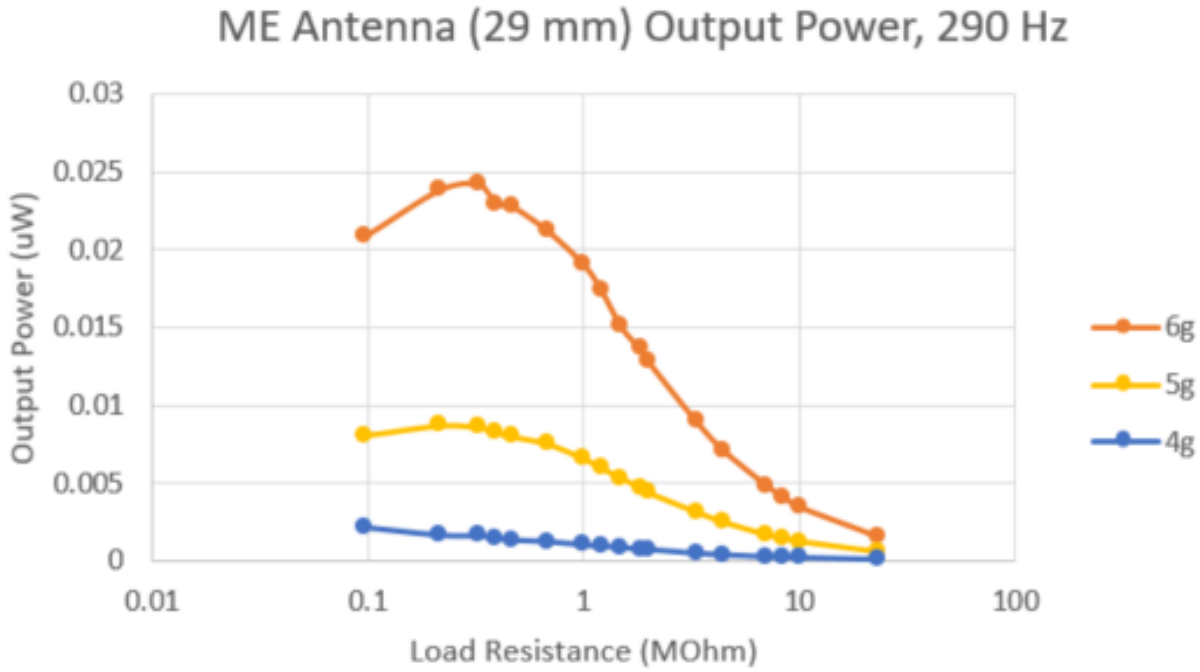

(b)

Figure 5.32: Measured output power of 29 mm ME antenna at different input vibration levels (a) and measured output power with input vibration accelerations of +/- 6 g to +/- 4 g (b).

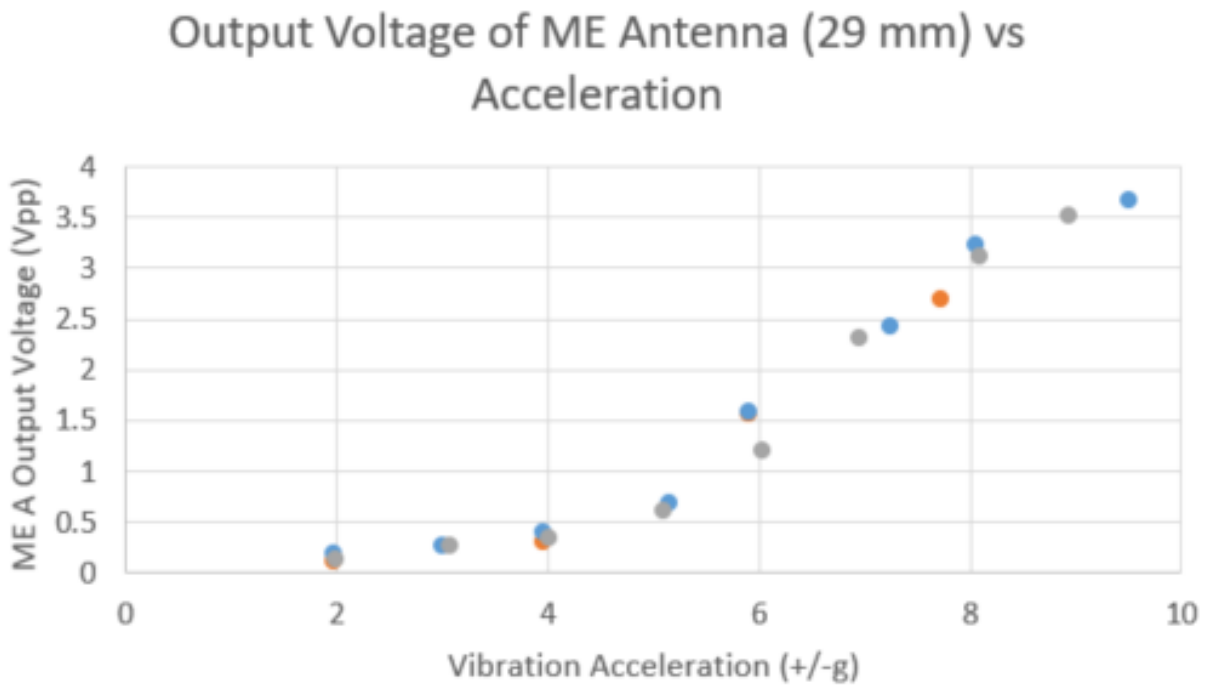

Figure 5.33: Measured output voltage of open circuit ME antenna as a function of input vibration acceleration.

5.8 Conclusion and Future Work

Comparing the output of a one stage diode rectifier with an ME antenna or coil antenna as the receiver, there are mixed results depending on which aspect of performance is more important. The power and voltage density per unit volume for the ME antenna is higher, but the coil antenna has a higher power and voltage density per unit area. A slight change in input did not significantly impact the output, so the densities can be compared for constant input current, power, or voltage between the two types of antennas. Several characteristics of the ME antenna (MPP, thickness) make it an attractive option as the receiver for low power wearable electronics. Additional investigation with the ME antenna performance in other dielectric media can determine its feasibility for implantable devices. Future work focused on decreasing the energy transfer loss between the MR and PE materials and epoxy will also increase the maximum output power possible of an ME device.

Chapter 6

Integrated Rectifier and DC-DC Converter

6.1 Introduction

As mentioned in Section 3.6, the high threshold voltage of discrete power MOSFETs degrade the DC-DC converter performance and prevent it from being a boost converter. Implementing this design with integrated MOSFETs can address this issue. The SkyWater Process Design Kit (PDK) SKY130 is an open source 130 nm process node created and sponsored by Google and SkyWater Technology Foundry to be used on Efabless's free shuttle runs called the Open MPW program [52]. An integrated rectifier design was submitted to the Efabless shuttle run in March 2022, which was called MPW-5. The design was placed in the required Caravel harness and is discussed in further detail below.

6.2 Circuit Simulation with Xschem

The rectifier and DC-DC converter designs were first created in the circuit simulator, Xschem, using devices from the SkyWater PDK [53]. The rectifier was implemented using

diode-connected NMOS devices and integrated capacitors. The load capacitor and resistor were kept consistent with what was used in the prototype described in Section 2.3, but the intermediate stage capacitors were decreased to 0.1 nF for a more compact size. Figure 6.1(a) shows the schematic for a 1-stage voltage multiplier using ideal capacitors, while Fig. 6.1(b) shows a schematic of a voltage doubler using integrated capacitors. Higher order stage Dickson rectifier schematics can be found in Appendix H. The simulated output voltages for the fully integrated rectifiers and rectifiers with ideal capacitors are compared in Fig. 6.2 for their respective number of stages. It can be seen that transitioning to an integrated capacitor with the same capacitance has a negligible effect on the output. In addition, the output voltage for the higher order stage rectifiers is consistent with the number of additional stages; the 2-stage rectifier has an output of 3.4 V, which is approximately double the output of the 1-stage rectifier (1.8 V). Likewise, the output of the 3-stage rectifier is 4.9 V, which is 2.7 times the output of the 1-stage rectifier.

In addition, the resonator-based DC-DC converter was also implemented in Xschem using SkyWater devices. The first design (Fig. 6.3 was a direct conversion of the LTSpice design shown in Fig. 3.10. Using the same timing for the NMOS switches, the simulated results (Fig. 6.4-6.6) showed that even with increased transistor sizes and increased load resistance and capacitance, the converter was not transferring the energy from the input to output as desired. The main issue was that although the output voltage was higher than the input (meaning boost conversion), it was too large at almost 10 V even before reaching steady state. According to the SkyWater specifications, the absolute maximum supply voltage at the pads of the Caravel harness is only 5 V, and the Spice model for the NMOS transistors used is valid for V_{DS} and V_{GS} in the range of 0 to 1.95 V. In addition, the resonator voltage, V_p, is much less than the input voltage when connected to the input with approximately a 1 V drop as seen in Fig. 6.5. From Fig. 6.5, it can also be seen that the previous timing sequence is not optimal, with the switches turning on and connecting the resonator to a

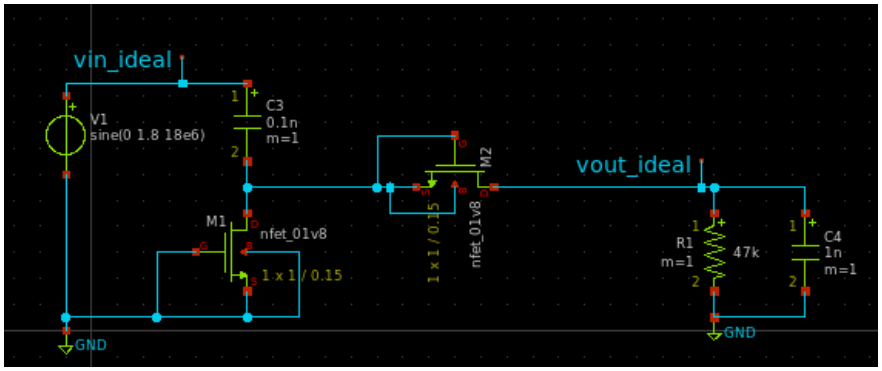

(a)

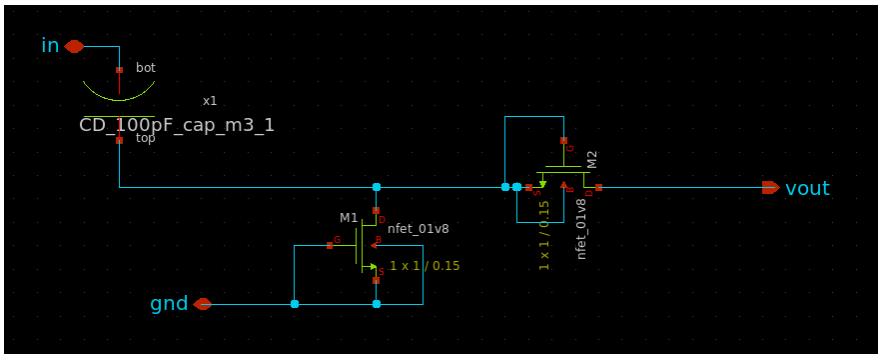

(b)

Figure 6.1: Rectifier schematic using integrated NMOS devices and ideal (a) or integrated (b) capacitors.

different potential than its present voltage. The current through the shunt branch and the RLC branch of the resonator confirms this, with high ringing in the shunt capacitor current.

Because of these problems, several changes were made to the design. First, the series combination of NMOS switches was replaced with a single PMOS switch to increase the voltage delivered to the resonator from the input. In addition, the output diode-connected NMOS was replaced with a PMOS switch. Although this introduces an additional switch timing signal, it provides better control of when to connect the output to the resonator, and using PMOS devices decreases the voltage drop across the switch. This design can be seen in Fig. 6.7. The transistor sizes were increased by using the multiplicity factor, which indicates how many transistors are in parallel. A test bench was made to verify this (Fig.

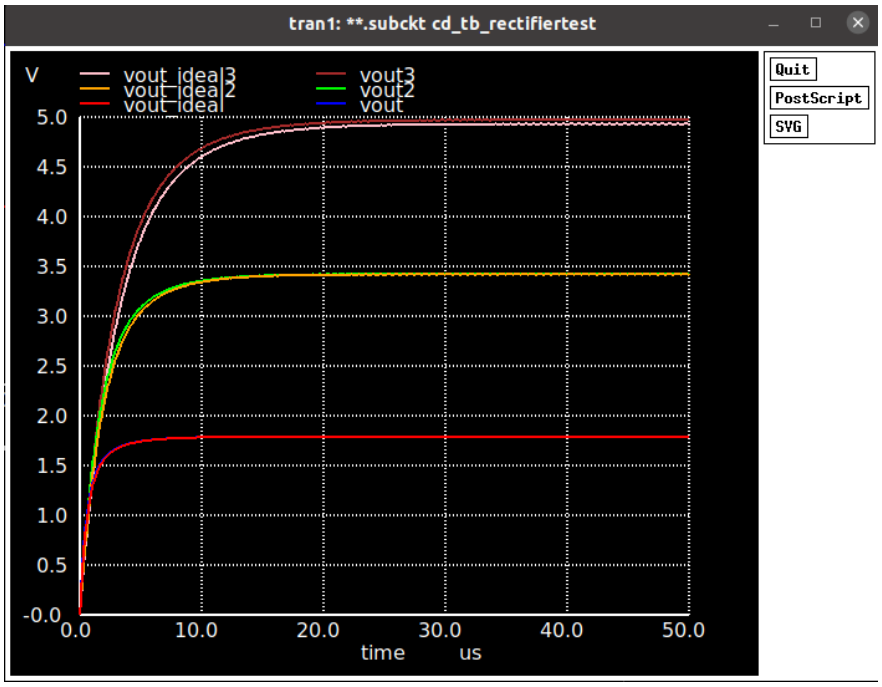

Figure 6.2: Comparison of output voltage of 1-, 2-, and 3-stage Dickson rectifiers with integrated and ideal capacitors.

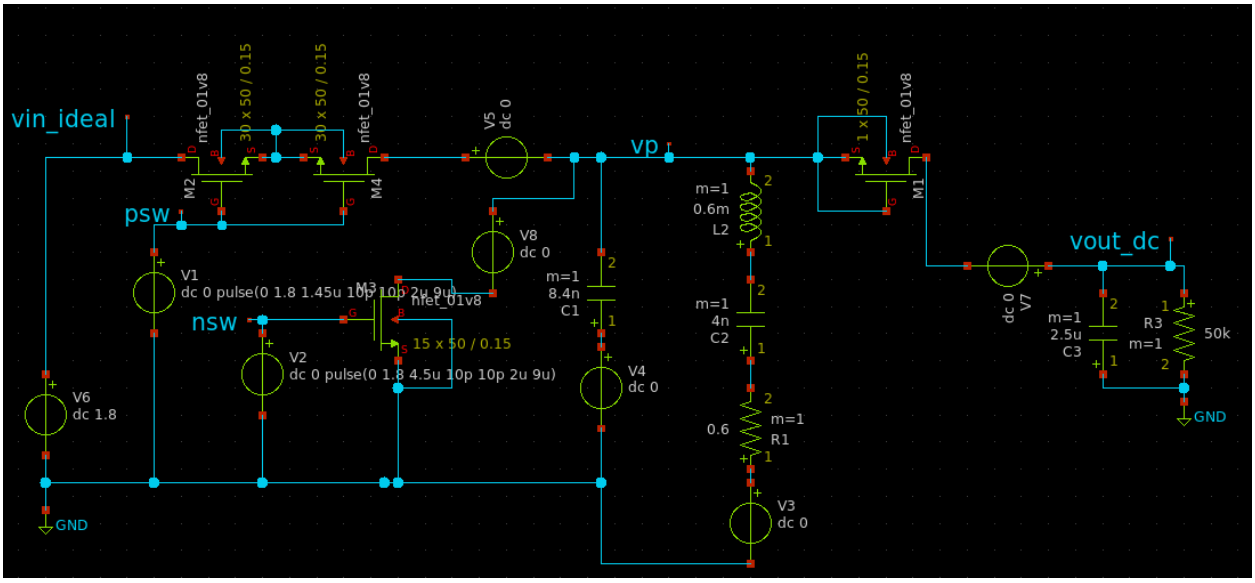

Figure 6.3: Schematic of resonator-based DC-DC converter using NMOS switches and output diode.

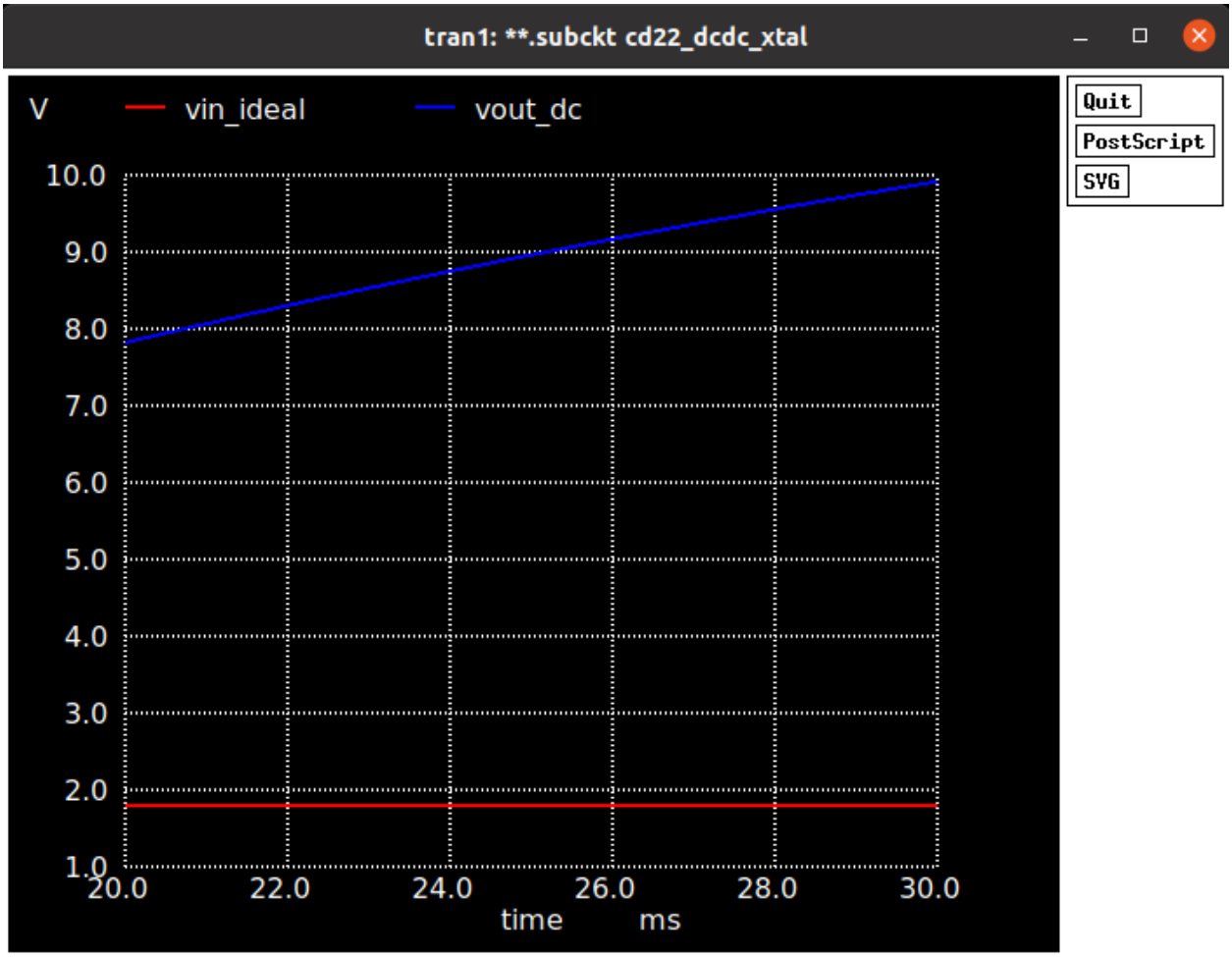

Figure 6.4: Simulated output and input voltage for integrated NMOS-based DC-DC converter.

6.8. The switching signals are supplied through an inverter chain with the fanout-of-4 (FO4) sizing topology shown in Fig. 6.9. The component 22_DCxtalFETSYM is the transistor network for the DC-DC converter implemented with transistors in parallel (Fig. 6.10(a)), and 22_DCxtalMultSYM is the transistor network using multiplicity to obtain the same sizing (Fig. 6.10(b)).

The output voltages from simulating the three schematics shown in Fig. 6.8 are compared in Fig. 6.11 with an input voltage of 1.8 V. The output voltage of 2.5 V is a boost of 1.41 times the input, which is similar to the previous LTSpice simulations which had a boost of 1.44 in Section 3.4. All output voltages were identical. The resonator voltage was also

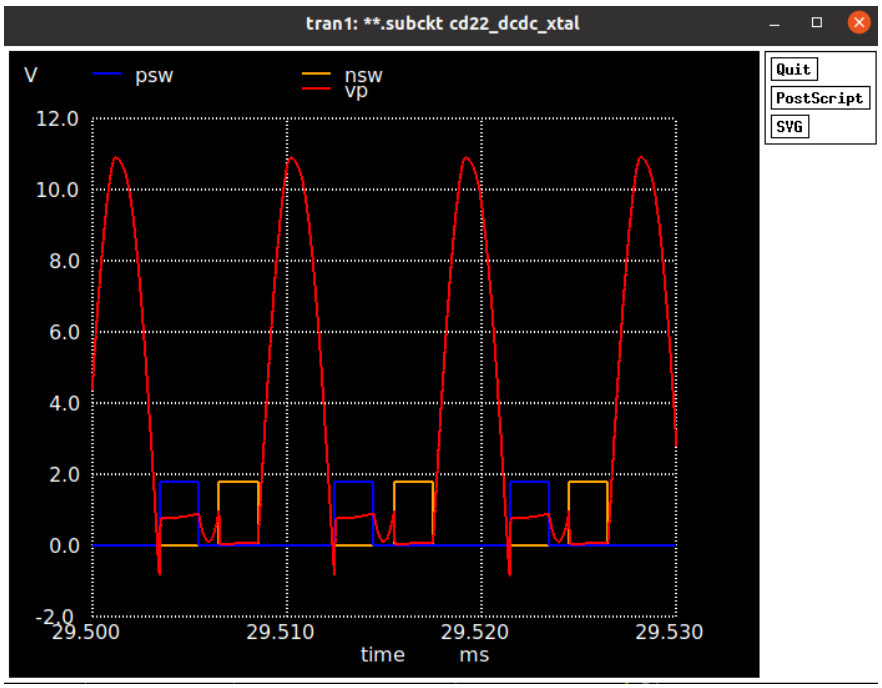

Figure 6.5: Simulated output and input voltage for NMOS-based DC-DC converter.

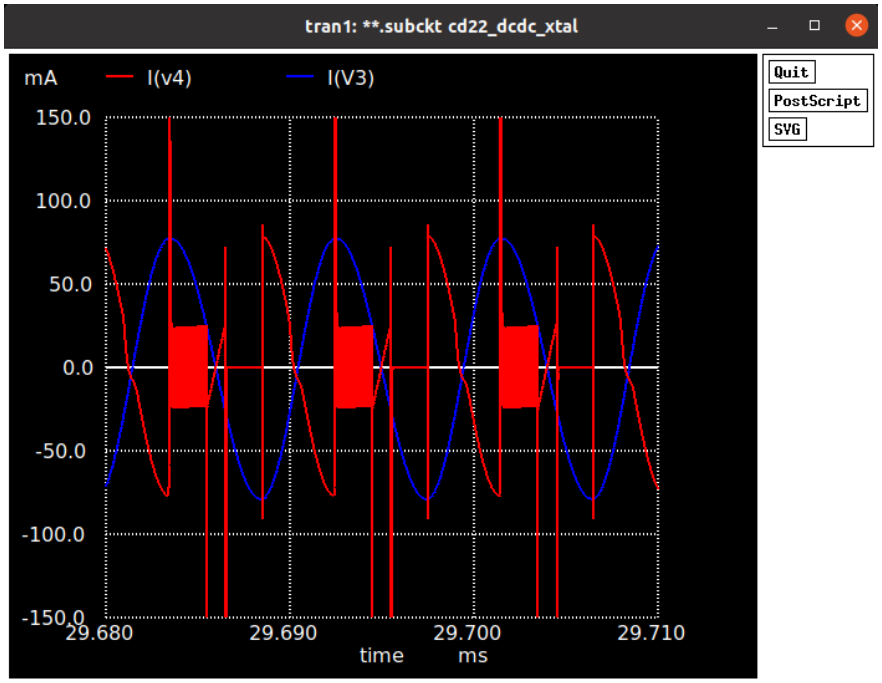

Figure 6.6: Simulated current through shunt capacitor, C1 (I(v4)), and current through RLC branch (I(v3)).

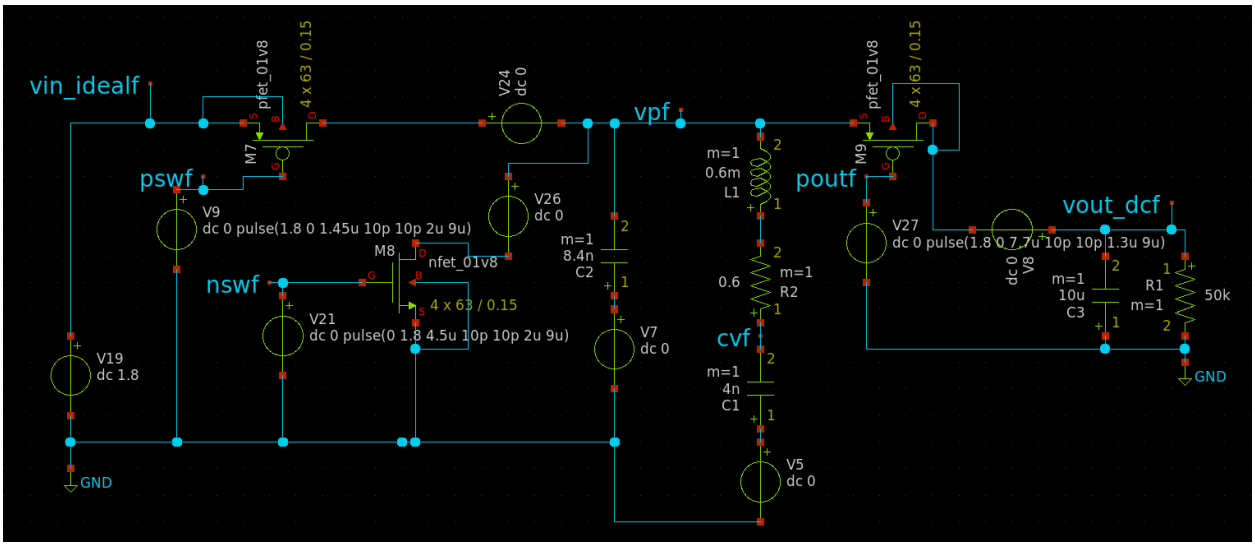

Figure 6.7: DC-DC converter using PMOS and NMOS switches.

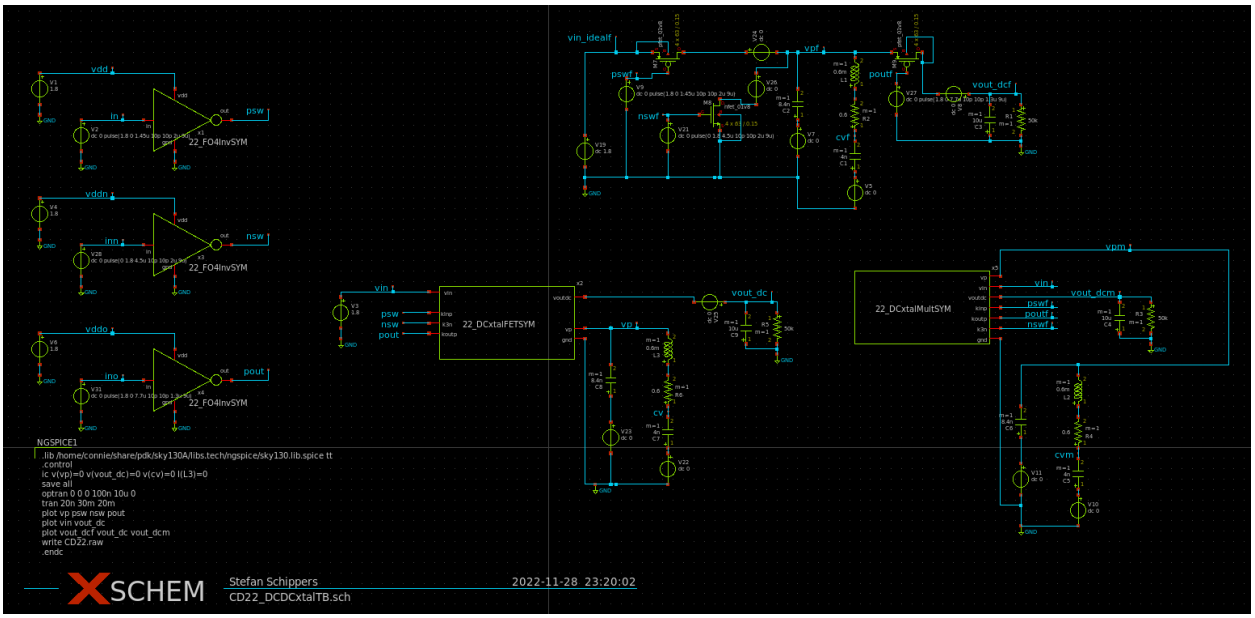

Figure 6.8: DC-DC converter simulation testbench.

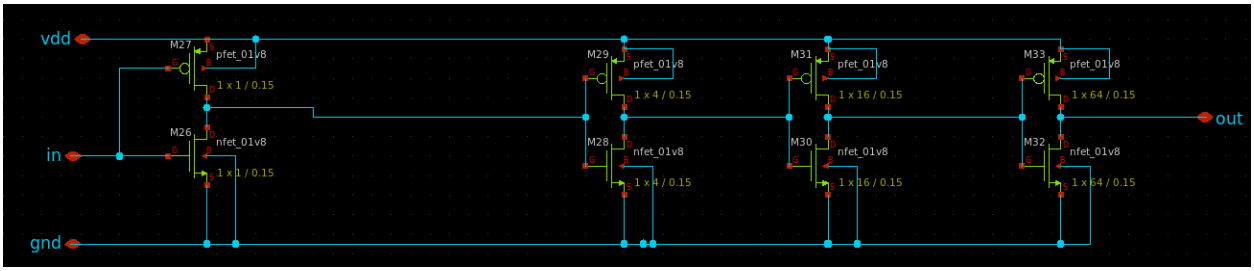

Figure 6.9: Inverter chain for driving power FETs schematic.

plotted and compared between the three different converters in Fig. 6.12. As expected from the output voltage comparison, there are negligible differences between the three topologies, meaning the FO4 inverters do not distort the timing, and the transistor configurations are equivalent. This can be verified by looking at the rising and falling edge delay of the output of the inverter (Fig. 6.13), which is 0.17 ns and 0.19 ns, respectively. Compared to the period of 9 μs, this delay is negligible. However, when comparing the resonator voltage compared to the switching sequence (Fig. 6.14), it is apparent that the design is suboptimal. The output and input switch turns on when the resonator voltage has not quite matched the respective voltage, causing a slight spike in the output case and a dip in the input case. In addition, when the NMOS switch turns on to short the resonator to ground, the resonator voltage is still at around 0.25 V, so there is some additional energy lost in this event also. However, the output performance is close enough for the same timing sequence as that in Section 3.4, so the timing of the switches was not further tuned.

6.3 Magic Layout and Netlist Simulation with Extracted Parasitics

After proving the feasibility of implementing the rectifier and resonator-based DC-DC converter in the SkyWater 130 nm process, the design Spice files were imported into the layout sofware, Magic, and the devices were routed together and simulated with layout

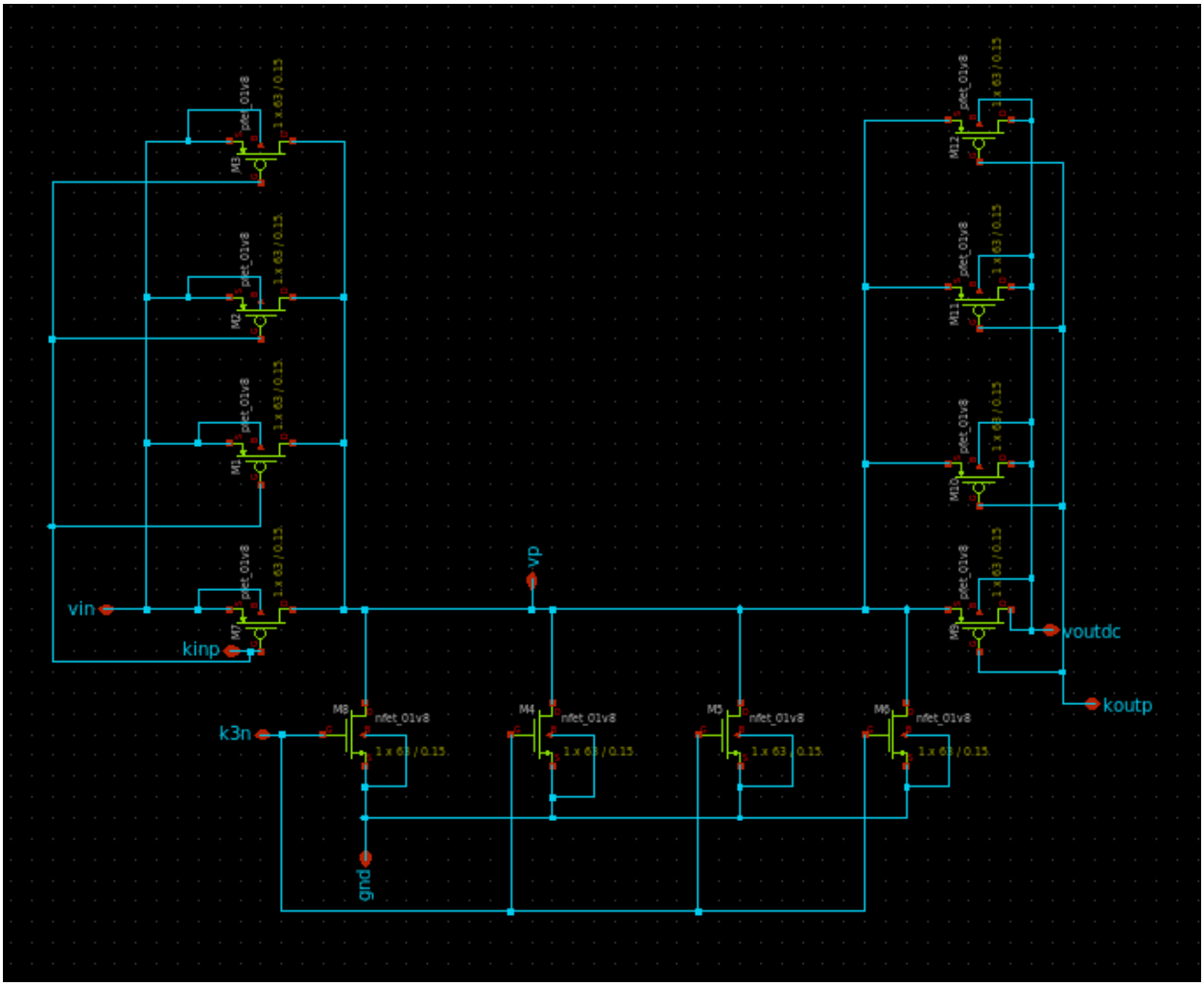

(a)

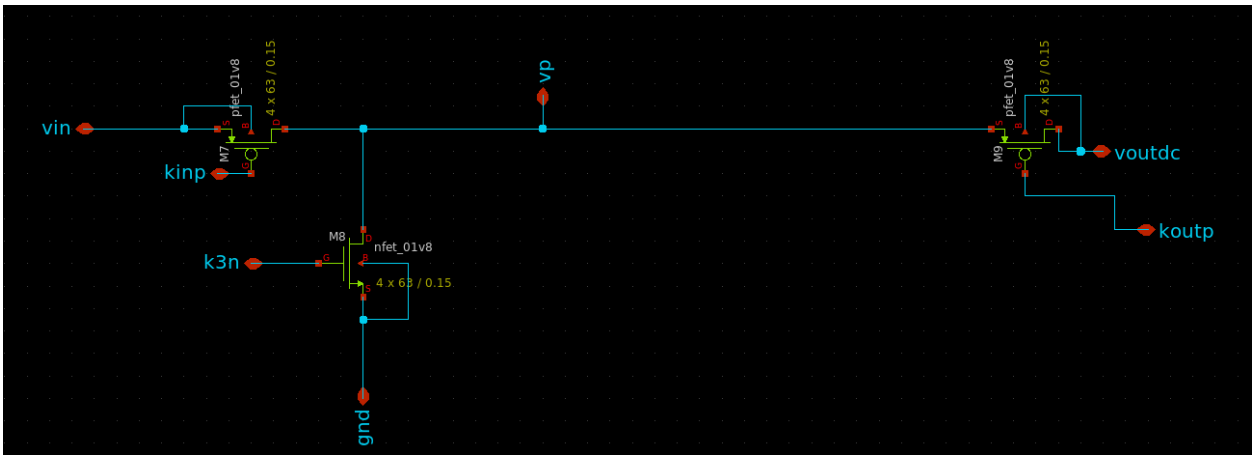

(b)

Figure 6.10: Schematic of symbol of transistor network using parallel transistors (a) or multiplicity (b).

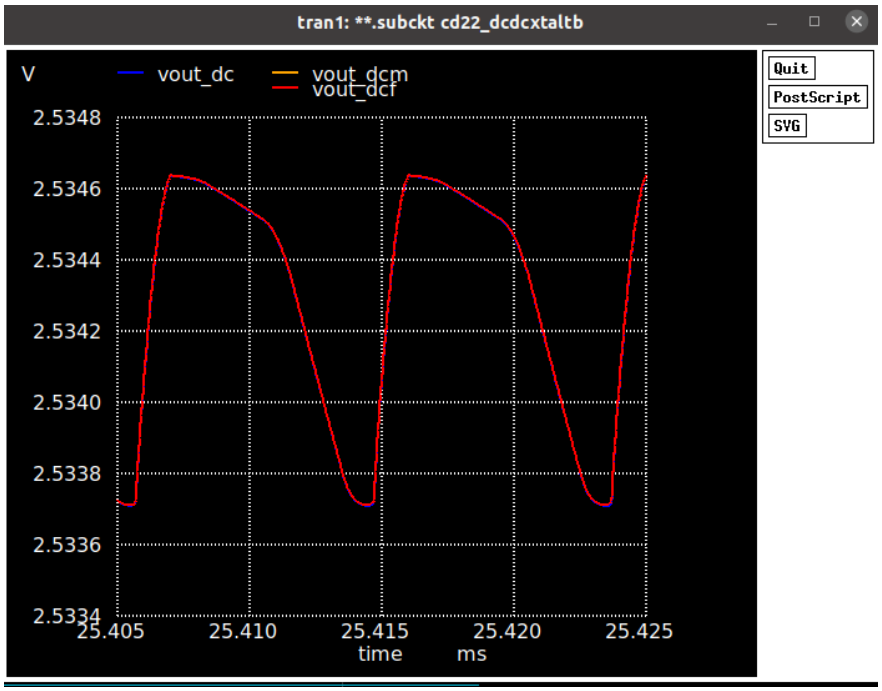

Figure 6.11: Simulated output voltage for ideal converter with no inverters (vout_dcf), converter with parallel transistors (vout_dc), and converter with transistors with multiplicity (vout_dcm).

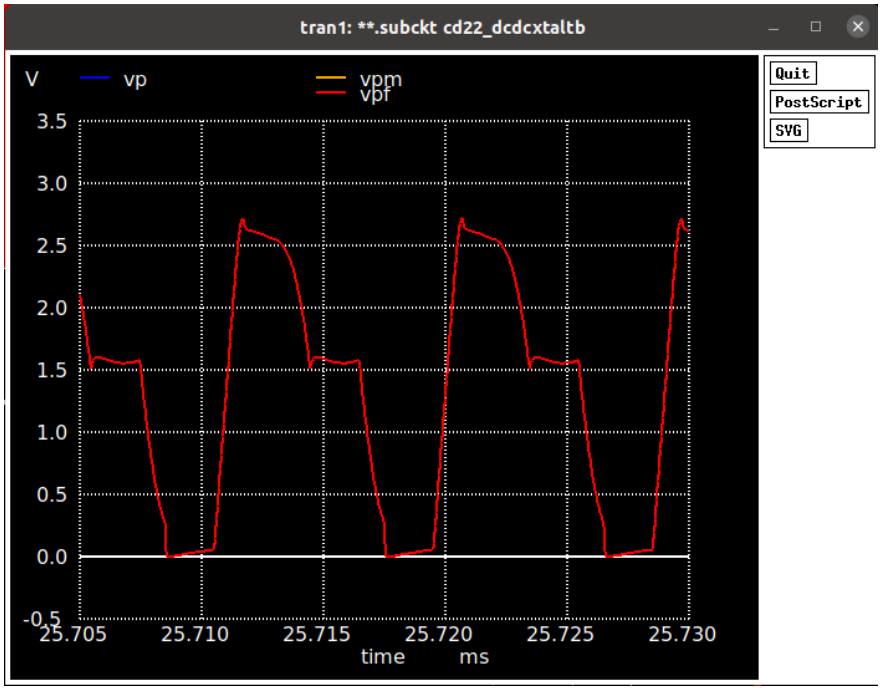

Figure 6.12: Output voltage for ideal converter with no inverters (vpf), converter with parallel transistors (vp), and converter with transistors with multiplicity (vpm).

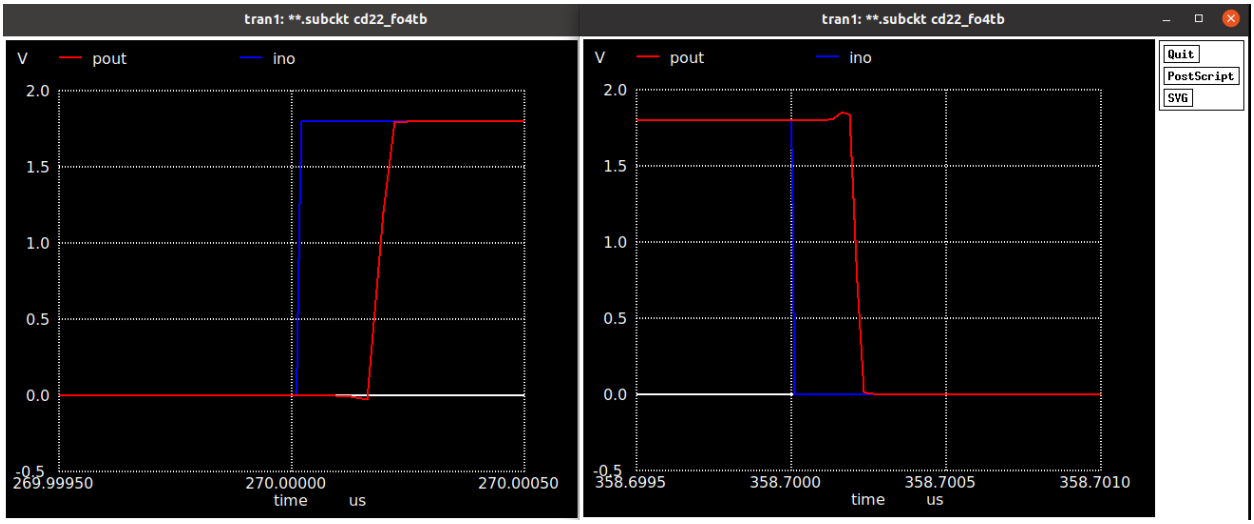

Figure 6.13: Simulated output delay of inverter on the rising and falling edge.

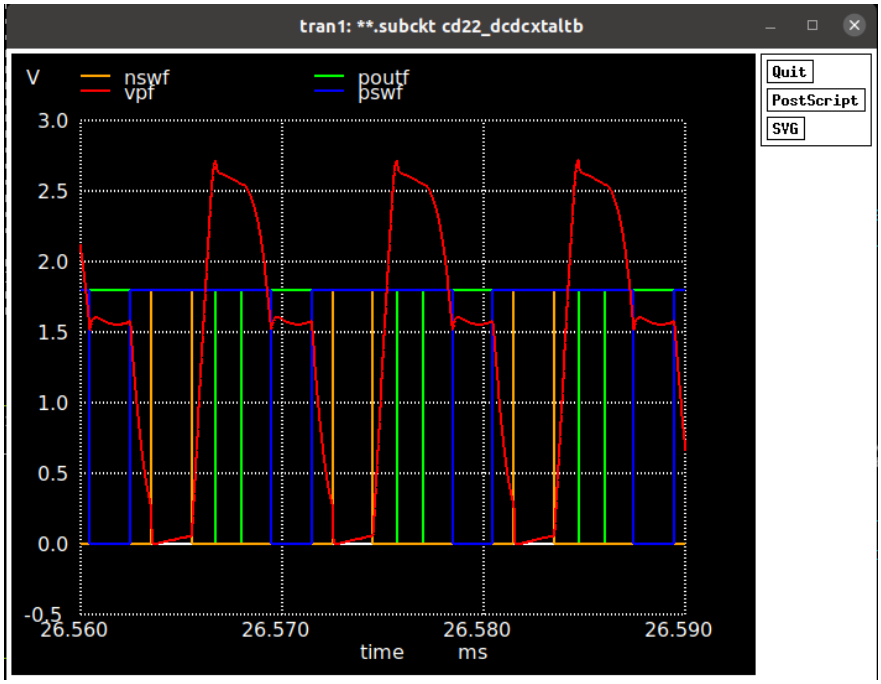

Figure 6.14: Simulated output voltage for ideal converter with no inverters (vpf), converter with parallel transistors (vp), and converter with transistors with multiplicity (vpm).

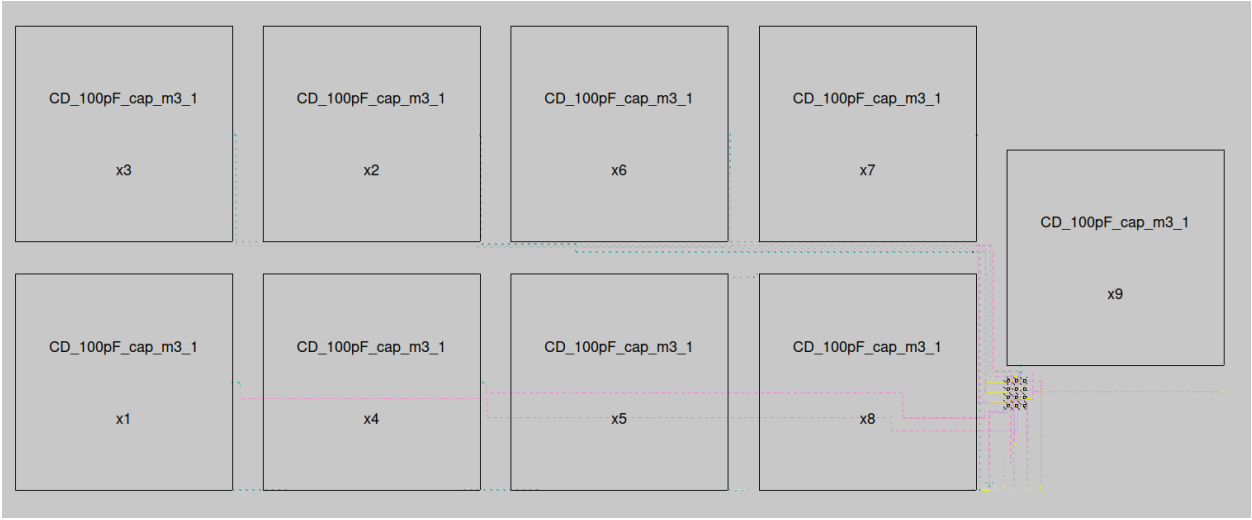

(a) Top view of rectifier layout.

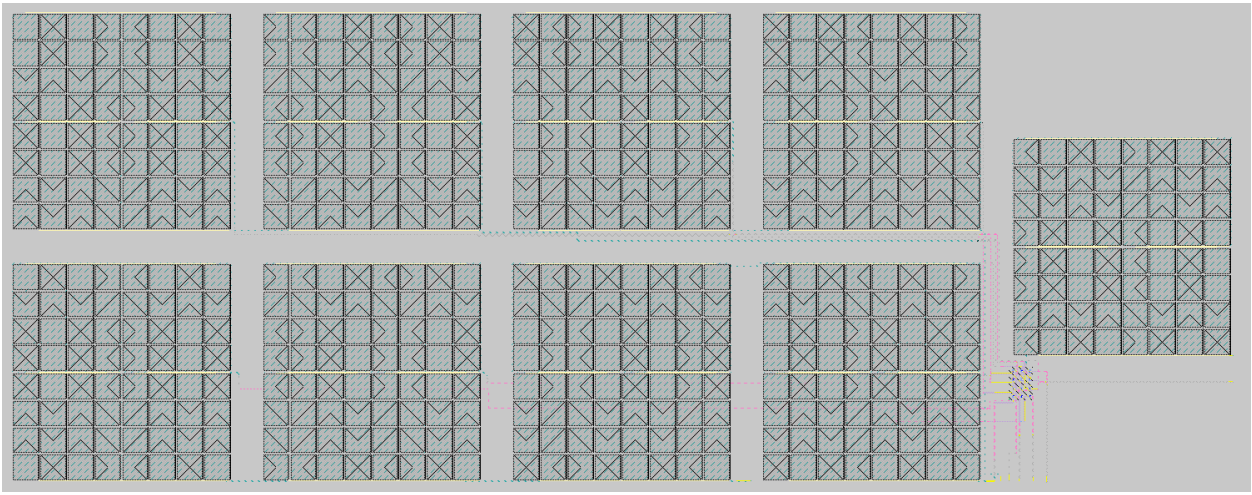

(b) Expanded view of rectifier layout.

Figure 6.15: Layout of rectifier in Magic.

parasitics. The rectifier layout can be seen in Fig. 6.15. Extracting this design with layout parasitics to a netlist allows for a post-layout simulation as shown in Fig. 6.16. Additional details about netlist extraction and Spice files can be found in Appendix I.

In addition to doing a layout of the rectifier, the transistor network and input inverters were also laid out in Magic. The DC-DC converter and FO4 inverter chain were first laid out separately as shown in Fig. 6.17 and Fig. 6.18. Their performance was also simulated

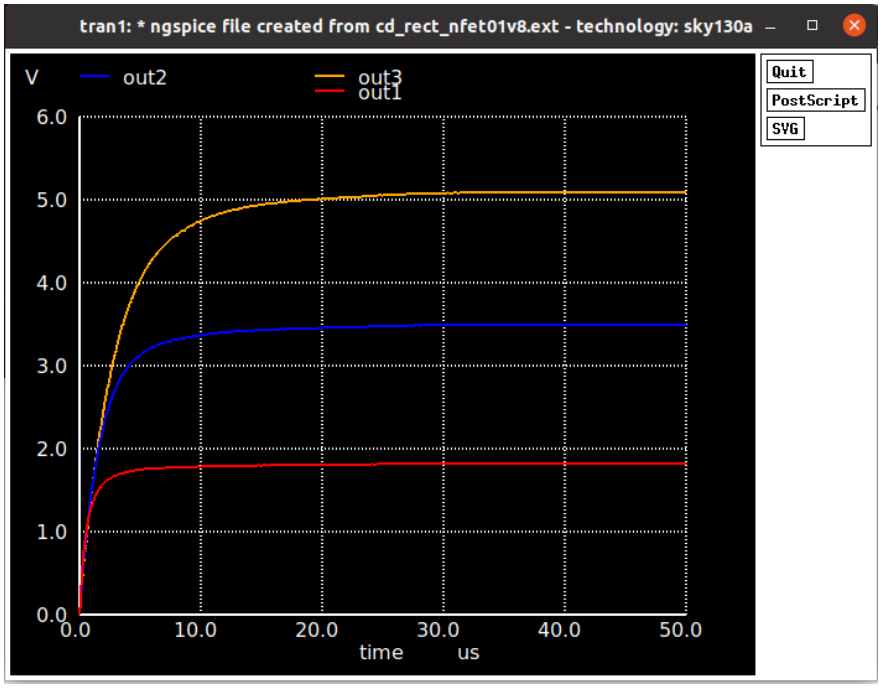

(a) Simulated output voltage of 1-, 2-, and 3-stage Dickson rectifier shown as out1, out2, out3, respectively.

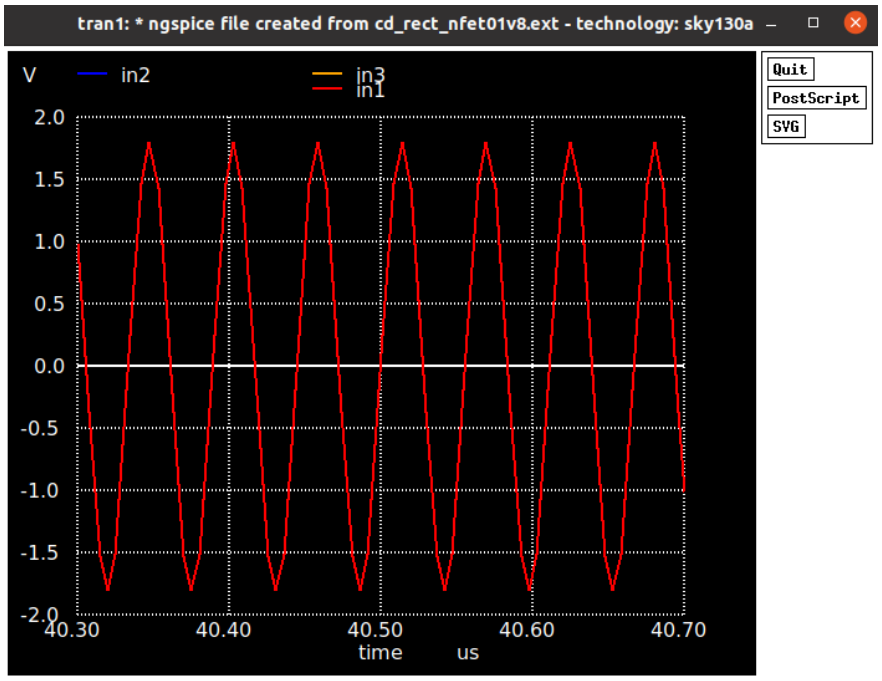

(b) Simulated input voltage of 1-, 2-, and 3-stage Dickson rectifier shown as in1, in2, and in3, respectively.

Figure 6.16: Simulated voltage waveforms of rectifier post-layout.

separately. Consistent with the Xschem simulations, the 4-stage inverter chain has negligible time delay between the output and input with a rising edge delay of 0.16 ns and a falling edge delay of 0.2 ns. Both of these delays should not effect the timing sequence in any noticeable way. Figure 6.19 shows the delay between the inverter output and input and Fig. 6.20 shows the output of the inverter and the voltage at each stage of the inverter. In addition, the transistor switches were also extracted with parasitics from the layout and simulated as a DC-DC converter with an external resonator and load. Because the resonator is a discrete component and the load will most likely be an external device that is currently modeled as a parallel combination of a capacitor and a resistor, these two components are not implemented in the converter layout. Figure 6.21(a) shows the output voltage with respect to the input voltage of 1.8, while Fig. 6.21(b) shows the ripple of the output voltage. The resonator voltage in comparison to the switching sequence is shown in Fig. 6.22. In these simulations, the pulse signals for the switches are applied directly to the transistors with no inverter buffer.

The DC-DC converter and inverter chain were combined in the same layout as shown in Fig. 6.23. Both the converter and the inverter were separately flattened in Magic, which means the hierarchy of the cells was removed, eliminating the subcircuits and creating the netlist from only the lowest level of transistors. This was done in order to prevent too many layers of cells in the topmost level of the design (the Caravel harness, see below). By removing the lowest level of subcircuits, the hierarchy will ultimately only consist of two levels of subcircuits, which will have the DC-DC converter and inverter at the lower level and the full converter and rectifier on the upper level. Again, the simulated response was observed at the output (Fig. 6.24) and the resonator voltage (Fig. 6.25), with no noticeable decline in performance. In this case, the input voltage is still 1.8 V.

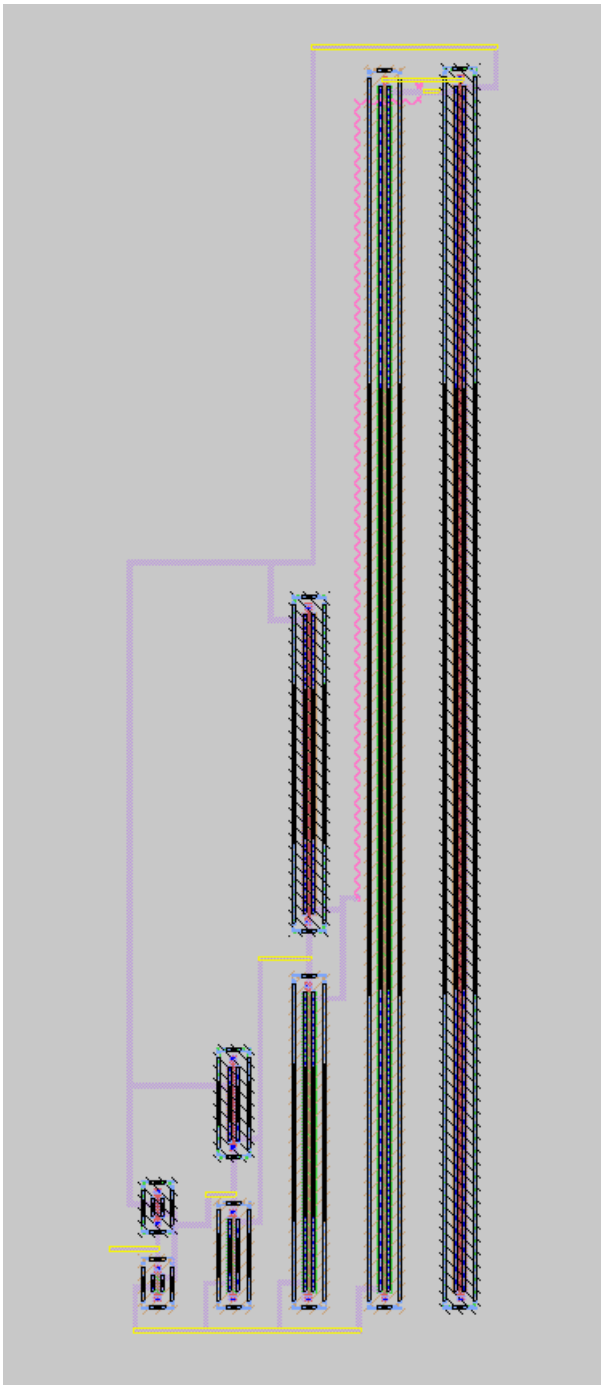

(a) Layout of transistors for inverter.

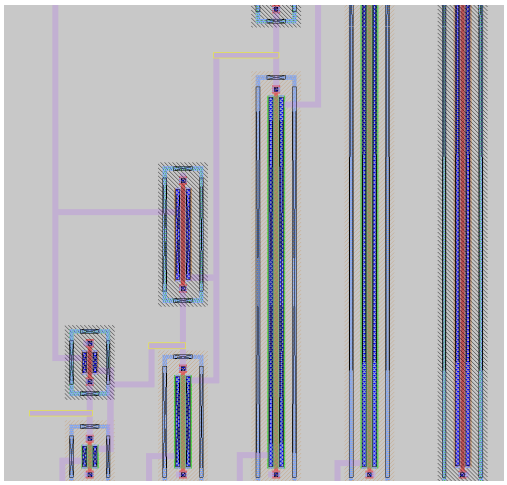

(b) Zoomed in view of transistors showing traces and transistors.

Figure 6.17: Layout of 4-stage FO4 inverter chain.

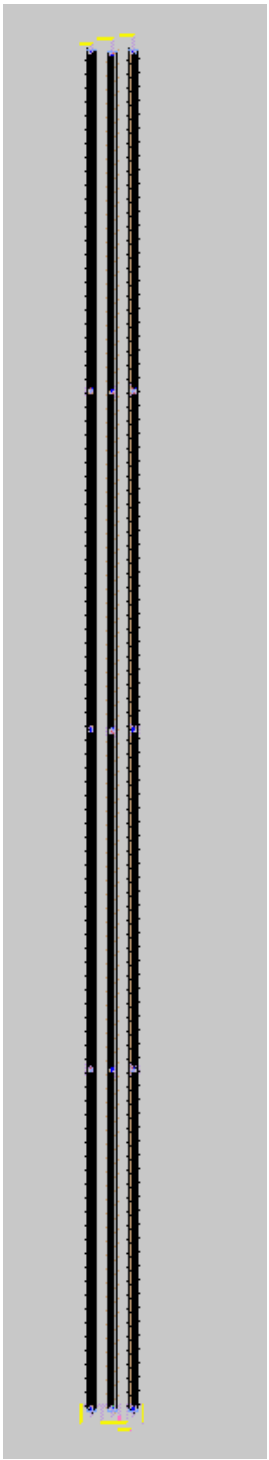

(a) Layout of power transistors for DC-DC converter.

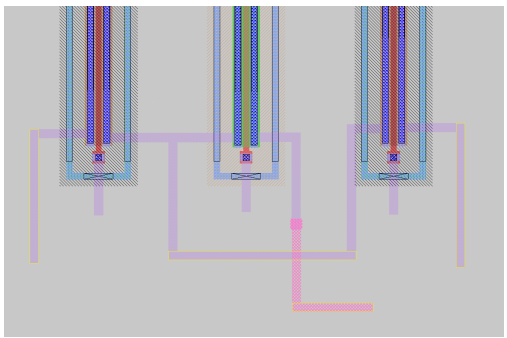

(b) Zoomed in view of power transistors showing traces and one end of transistors.

Figure 6.18: Layout of DC-DC converter.

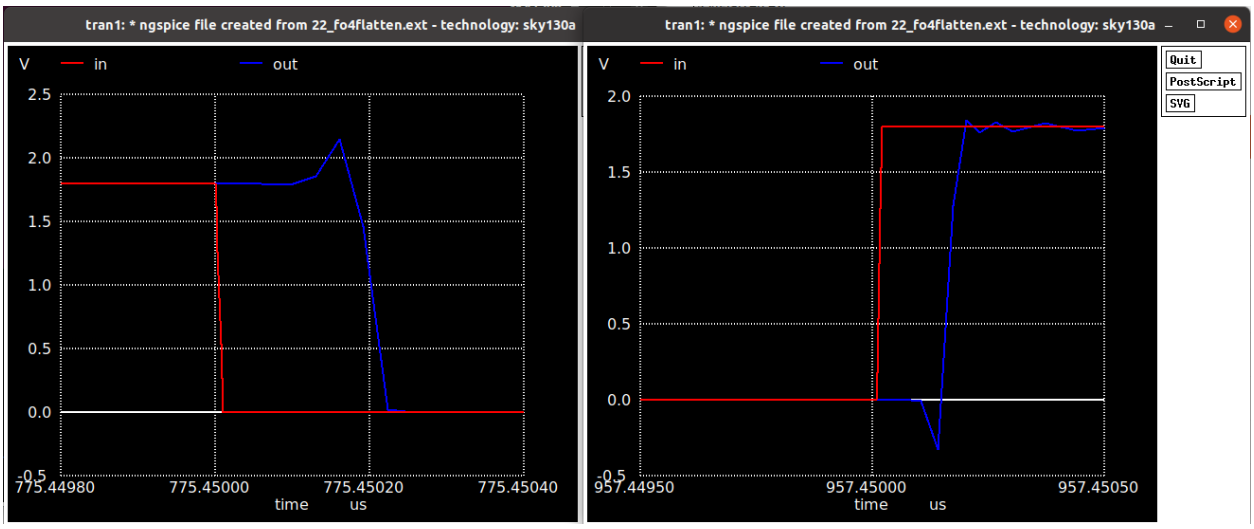

Figure 6.19: Simulated rising edge and falling edge delay of FO4 inverter chain.

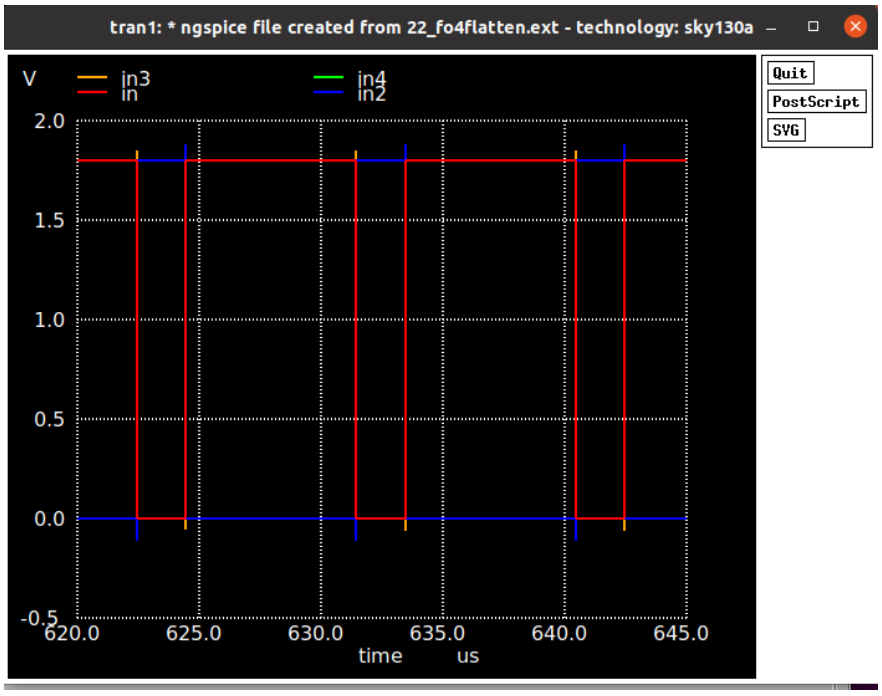

Figure 6.20: Simulated output and intermediate stage voltages of inverter chain with layout parasitics.

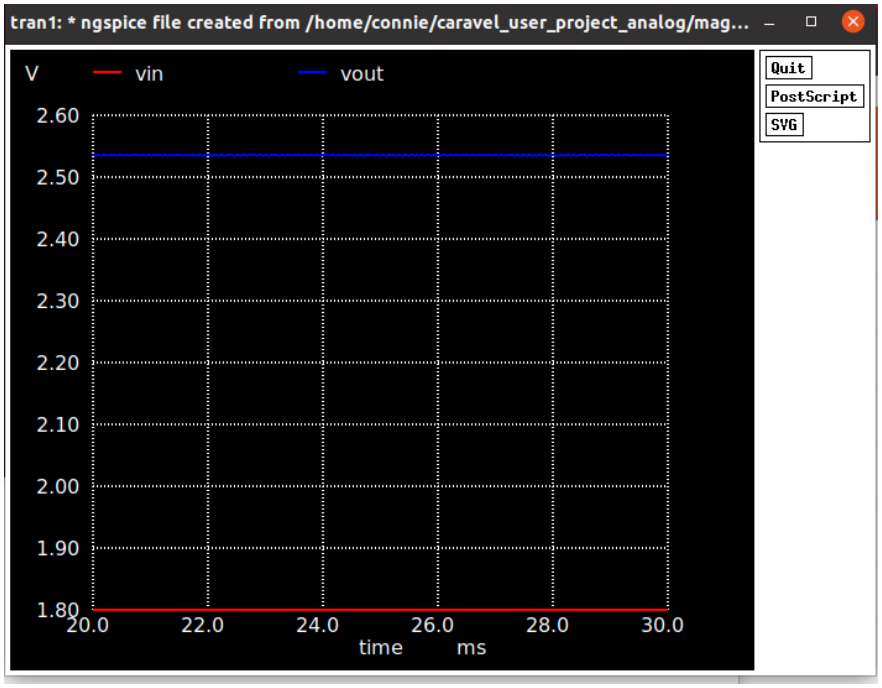

(a) Simulated output and input voltage of DC-DC converter.

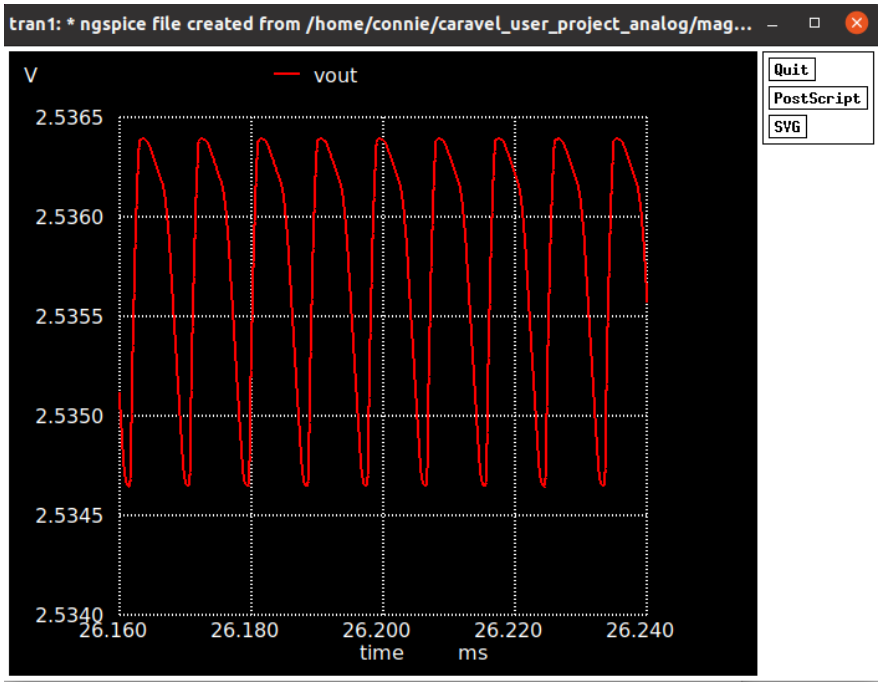

(b) Zoomed in view of simulated output voltage.

Figure 6.21: Simulated output and input voltage of DC-DC converter with extracted parasitics.

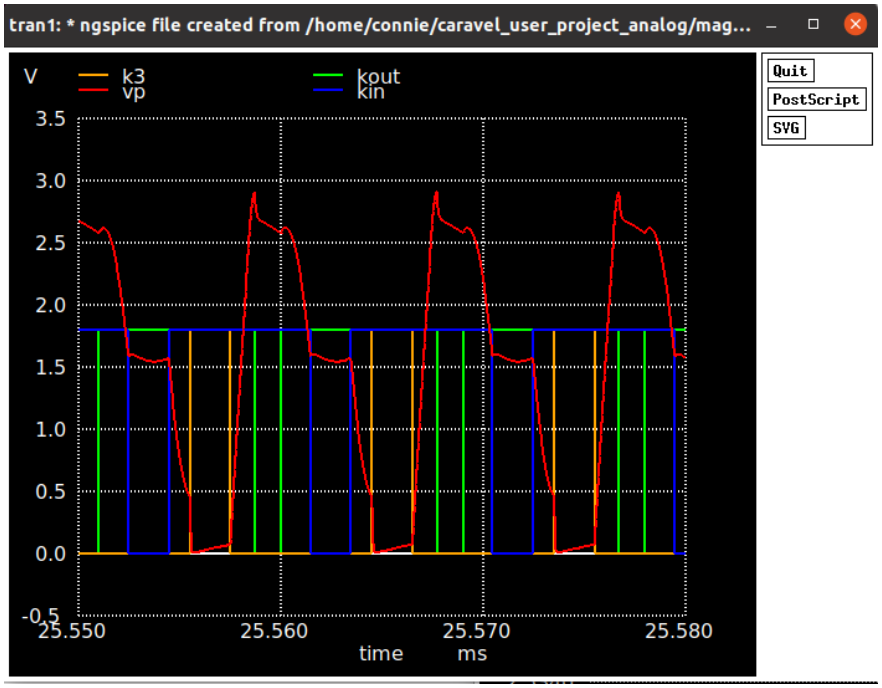

Figure 6.22: Simulated resonator voltage shown with switching sequence.

6.4 SkyWater Caravel Harness

The company, Efabless, has collaborated with Google and the SkyWater foundry to provide free shuttle runs on open-source projects using their harness, called Caravel. The harness has predefined input, output, ground, and power pads to connect to an external test fixture. The rectifier design mentioned in the previous sections was implemented on the Caravel harness and submitted for the April 2022 run. The design has since been expanded to include the DC-DC converter and inverter chain stages also. Figure 6.26(a) shows the top view of the Caravel harness layout and the placement of the rectifier and converter, while Fig. 6.26(b) shows the expanded view of the designs. In a similar fashion as before, the performance of the rectifier and converter was simulated after extracting a netlist from this layout with the trace parasitics. The full netlist can be found in Appendix I. Because of the large number of nodes due to parasitic capacitances and the increased computing power required to simulate operating at different frequencies, the rectifier and converter were run in

Table 6.1: Simulated output voltage of a 1-stage, 2-stage, and 3-stage rectifier pre- and post-layout.

Type	1-Stage (V)	2-Stage (V)	3-Stage (V)
Xschem, ideal	1.78	3.38	4.91
Xschem, integrated	1.78	3.35	4.99
Magic, standalone	1.79	3.43	5.06
Magic, Caravel	1.76	3.38	4.98

Table 6.2: Simulated resonator voltage when connected to the input ($V_{p,input}$), at maximum ($V_{p,max}$), input (V_{in}) and output voltage (V_{out}), and switching voltage (V_{sw}) of resonator-based DC-DC converter with inverter buffer chain pre-layout (Xschem) and post-layout (Xschem).

	$V_{p,in}$ (V)	$V_{p,max}$ (V)	V_{out} (V)	V_{in} (V)	V_{sw} (V)	Boost ratio
Xschem	1.56	2.70	2.53	1.80	1.80	1.41
Magic, standalone	1.56	2.88	2.53	1.80	1.80	1.41
Magic, Caravel	1.57	2.86	2.53	1.80	1.80	1.41

separate files, which had the transient analysis time parameters adapted to the appropriate frequency (18 MHz for the rectifier and 111 kHz for the converter). Figure 6.27 shows the simulated output voltage for the rectifiers with various stages and is summarized in Table 6.1. Table 6.2 summarizes the DC-DC converter performance with the SkyWater PDK.

The converter response is also simulated from the extracted netlist. Figure 6.28 shows the output voltage, while Fig. 6.29 shows the resonator voltage in comparison to the switching inputs. As before, the performance is unchanged, and it can be concluded even with trace parasitics that this layout design is sufficiently represented by the circuit schematic and meets the desired performance specification of increasing the input voltage by a factor of 1.4.

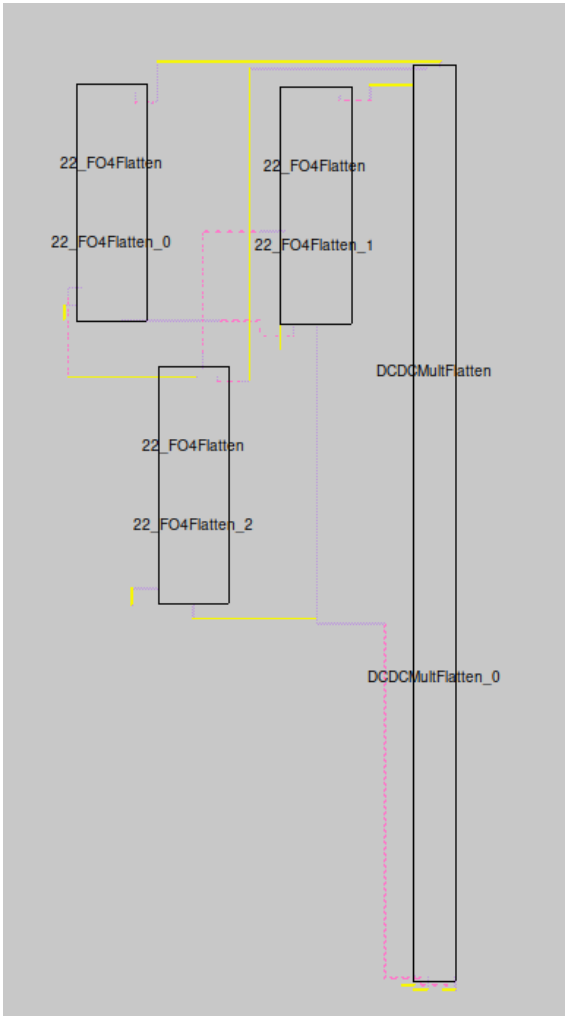

(a) Top level view of DC-DC converter driven with inverter buffers.

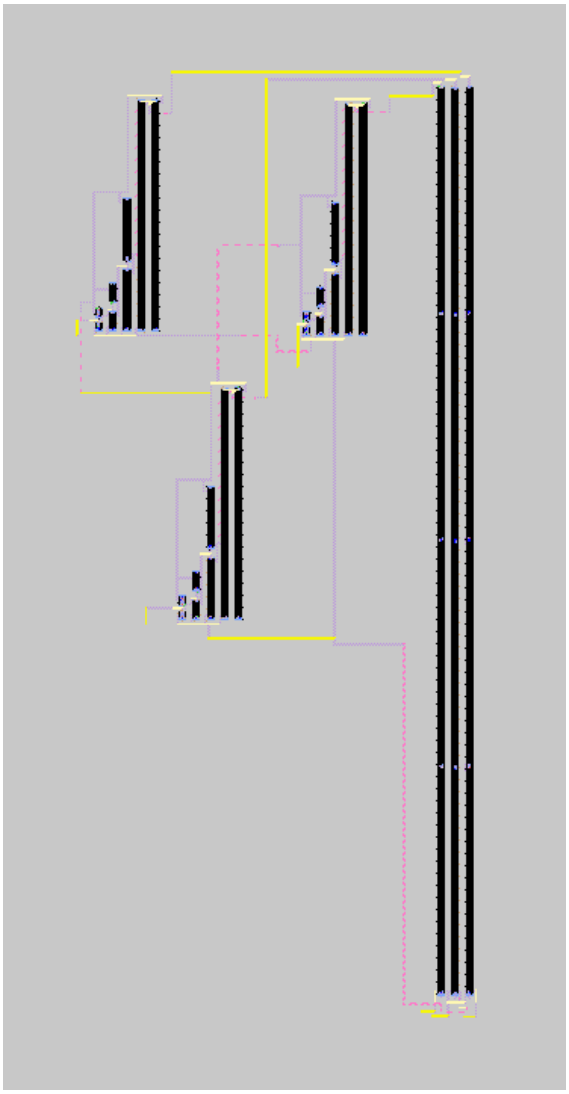

(b) Expanded view of DC-DC converter driven by inverter buffers.

Figure 6.23: Layout of DC-DC converter with inverter buffer chain.

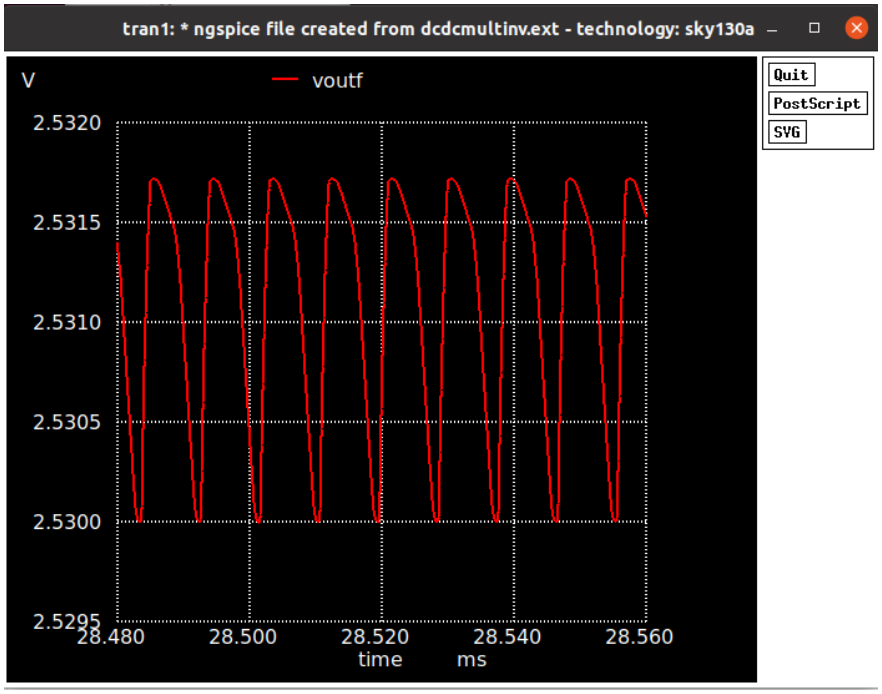

Figure 6.24: Simulated output voltage of DC-DC converter and inverter chain post-layout.

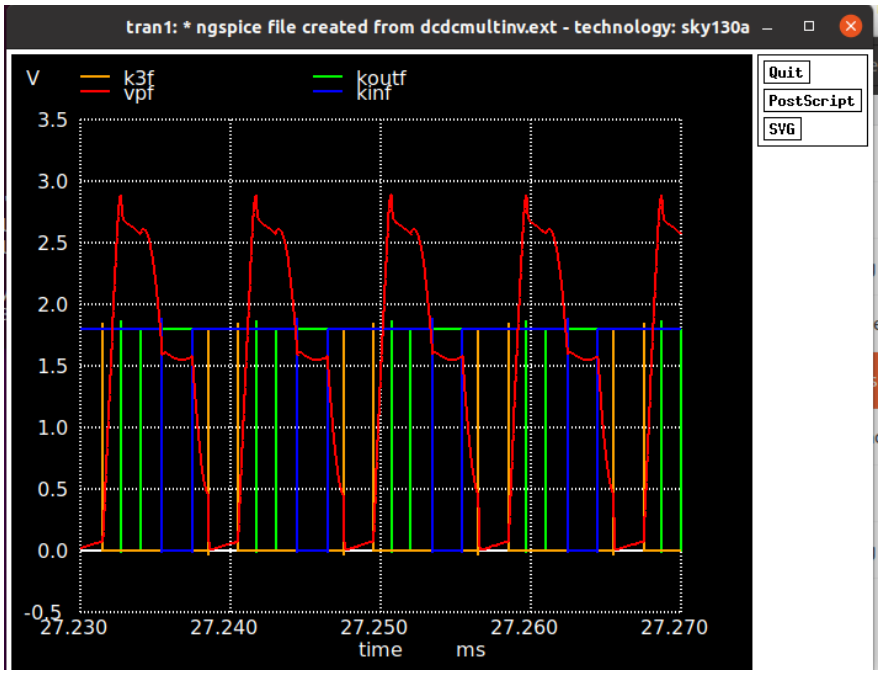

Figure 6.25: Simulated resonator voltage shown with switching sequence of DC-DC converter with inverter chain post-layout.

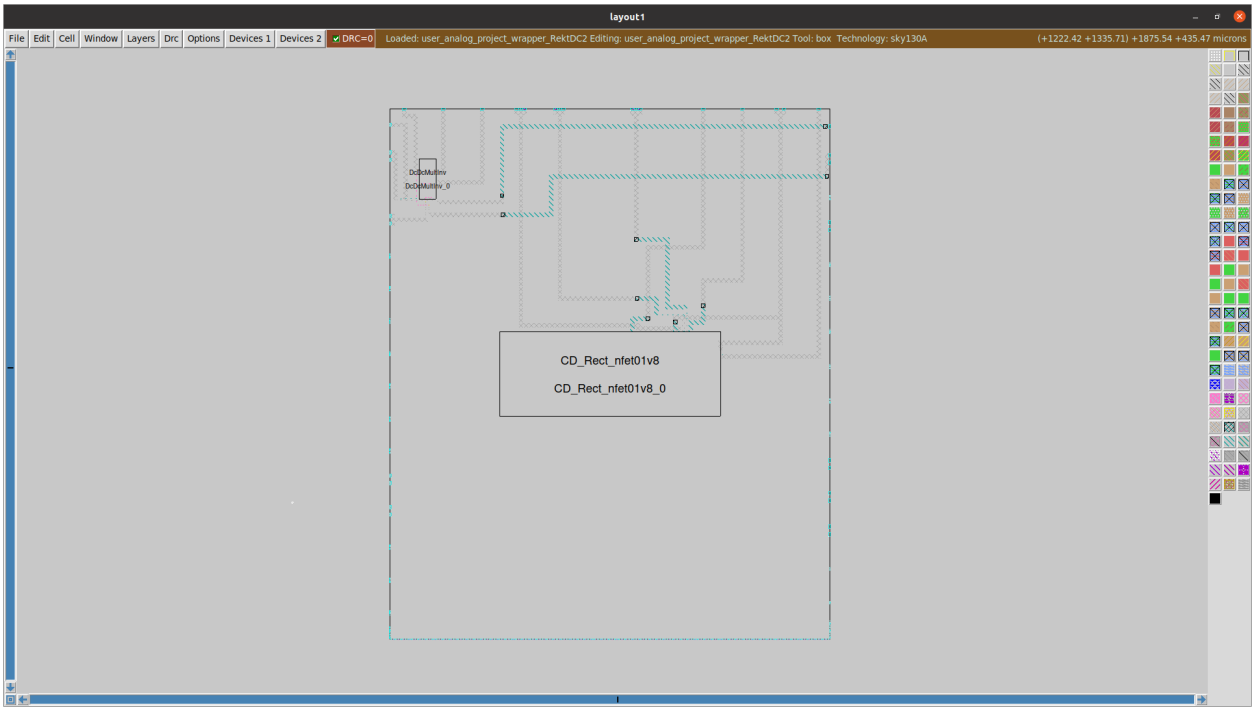

(a) Top level view of converter and rectifier in Caravel harness.

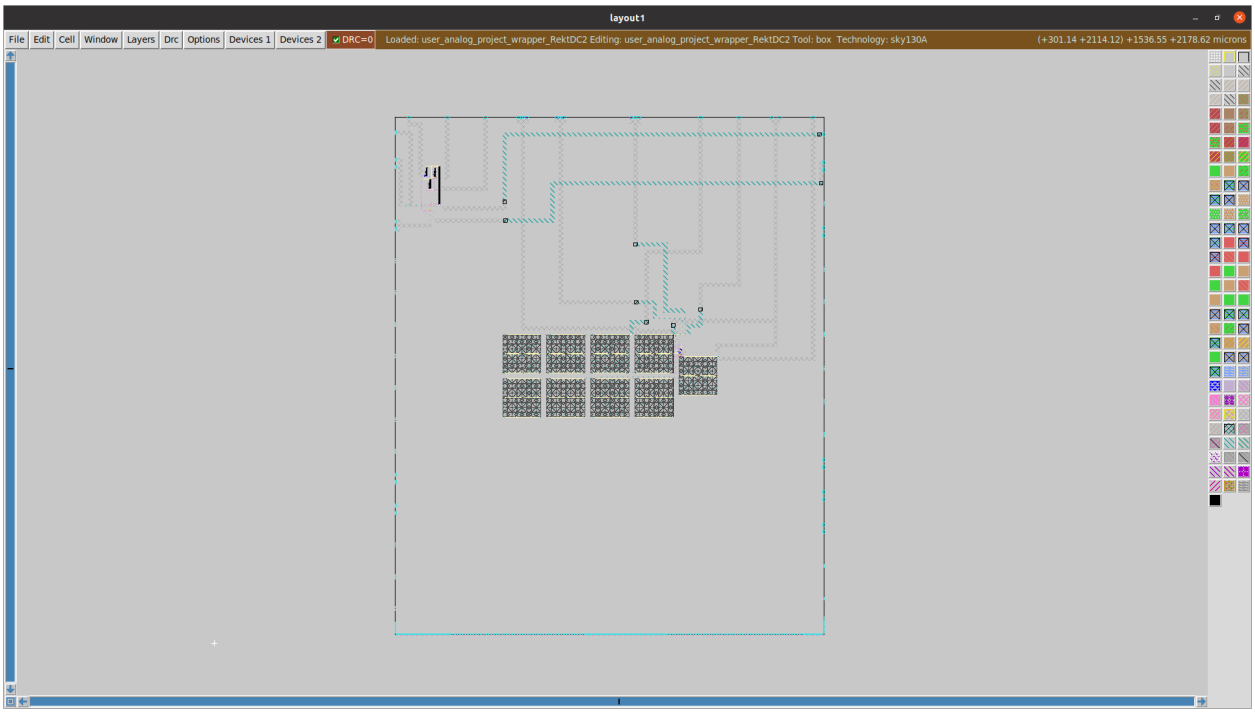

(b) Expanded view of converter and rectifier in Caravel harness.

Figure 6.26: Layout of DC-DC converter in Caravel harness.

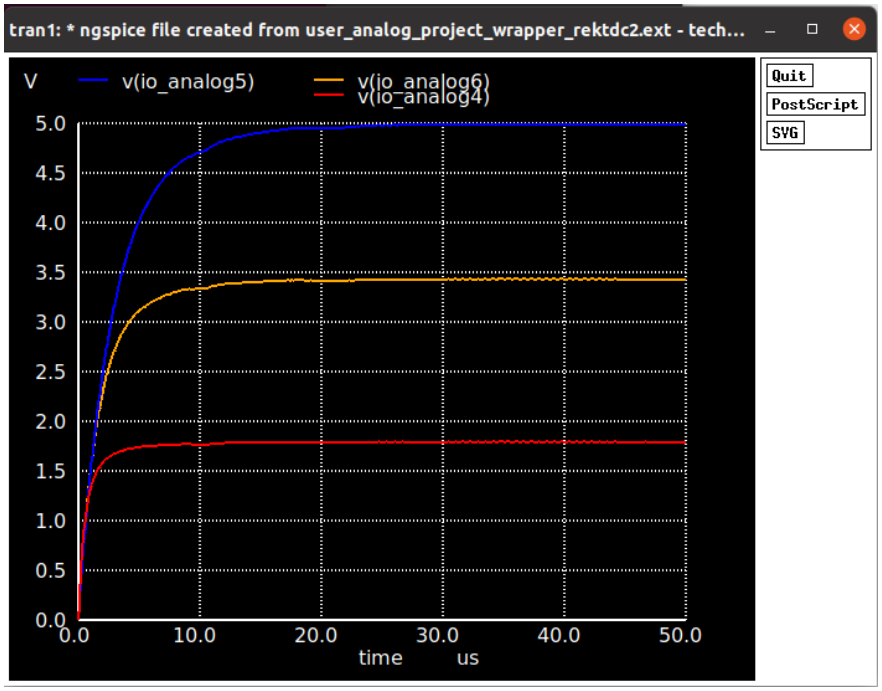

Figure 6.27: Simulated output voltage for a 1-stage (io_analog4), 2-stage (io_analog6), and 3-stage (io_analog5) rectifier in harness post-layout.

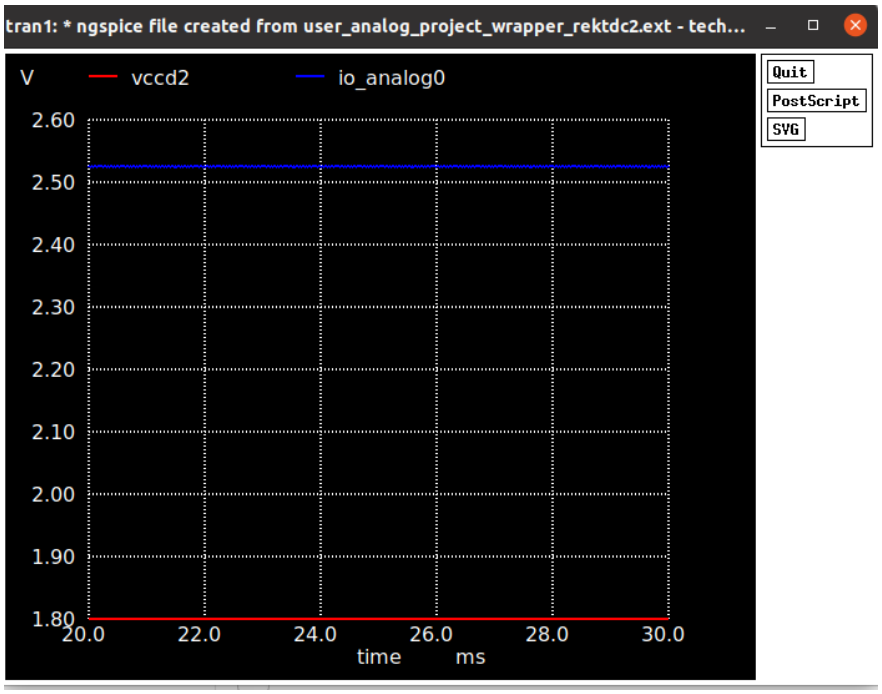

(a) Simulated output (io_analog0) and input (vccd2) voltage of DC-DC converter in Caravel harness.

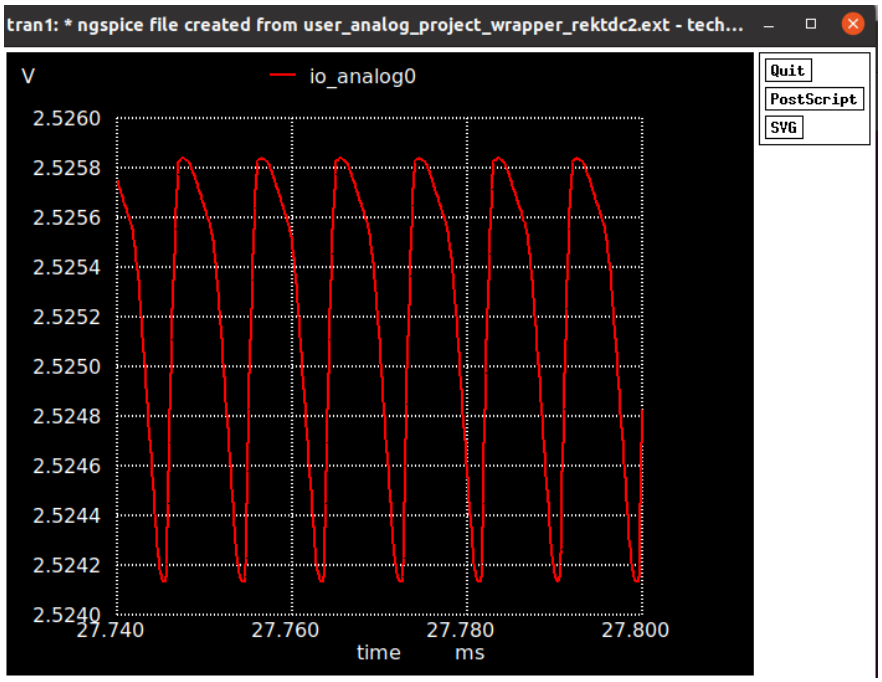

(b) Simulated output voltage ripple of DC-DC converter.

Figure 6.28: Simulated output voltage performance of DC-DC converter with parasitics in Caravel harness.

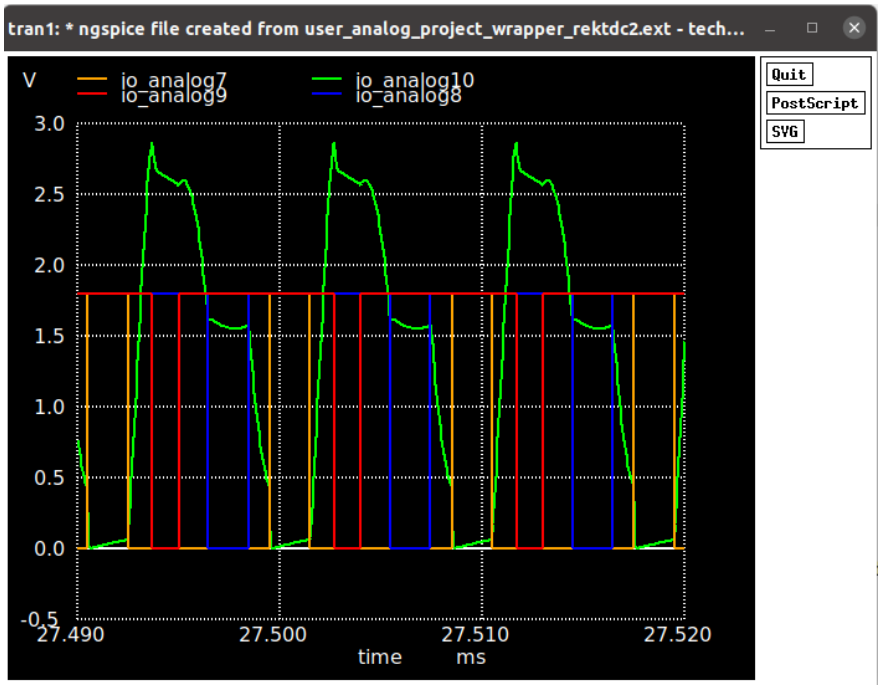

Figure 6.29: Simulated resonator voltage (io_analog10) plotted in comparison with input (io_analog8), nmos (io_analog7), and output (io_analog9) switching signals of DC-DC converter with inverter chain in Caravel harness with extracted parasitics.

Chapter 7

Conclusion and Future Work

Electromechanical resonators with high quality factors were used to passively boost the output voltage of rectifiers and DC-DC converters. In the AC domain, high-Q resonators were used at 18 MHz to improve the impedance match between a Dickson rectifier and a signal generator and produced a maximum of 30 percent higher output voltage than a rectifier matched with discrete inductors and a maximum of 8 times the output voltage of an unmatched rectifier. Additional simulations were done within the Qi standard frequency range (100 kHz-200 kHz) at 185 kHz with the goal of sharing the resonator between the rectifier and DC-DC converter.

Resonator-based DC-DC converters were implemented in simulation and had a 68 percent efficiency with a boost ratio of 1.4:1 and switching frequencies of 83 kHz and 110 kHz. This was consistent with literature and, in the absence of strict voltage regulation requirements, allows for a more compact size without the need for closed loop control circuitry. A printed circuit board prototype was also built using a ceramic resonator with a series resonant frequency of 185 kHz and discrete NMOS transistors with a switching frequency of 200 kHz. General switching signals and resonator voltage waveforms were verified, but high voltage drops in the transistors and diodes and high series resistance prevent the converter from operating successfully in the boost mode. The highest ratio of output to input voltage

achieved is 1.1:1 in simulation and 0.82:1 in the PCB prototype with a switching amplitude of 5.1 V. In simulation, this issue was addressed by using a floating driver for the input NMOS switch, which allowed a boost ratio of 1.31:1. In the PCB prototype, the main option to boost the output without a floating driver was to lower the input voltage; measurements showed that the resonator-based DC-DC converter was unable to boost input voltages larger than 100 mV. This also showed the need for an integrated design, which was explored using the SkyWater 130 nm PDK.

Combining the rectifier and converter requires a switching network which was simulated in ADS to observe its effect on the impedance match of the rectifier with the resonator. The lower frequency one with a 185 kHz resonator had slight deviations in the impedance which could be fixed with tuning, but the higher frequency operation at 18 MHz does not work with discrete NMOS transistors.

The SkyWater PDK was used to develop an integrated rectifier and resonator-based DC-DC converter. One-stage, two-stage, and three-stage rectifiers were designed using integrated capacitors and diode-connected NMOS transistors. The switches and diodes used in the DC-DC converter were also implemented using the appropriate transistors with external pad connections for the load and resonator. Both of these designs were laid out on the Caravel harness, which is the template used in Google's sponsored free tapeout program in collaboration with eFabless.

Magnetoelectric antennas and coil antennas were compared as the input antenna for a voltage doubler at 89 kHz. The ME antenna had a higher power density and voltage density per unit volume by a maximum of 1.3 times and 3.9 times, respectively, at the highest load resistance measured. Output voltage from an ME antenna-driven rectifier also had no ripple compared to a 23-31 percent ripple for a coil-driven rectifier at MPP. However, the coil antenna had an output power that was 2 orders of magnitude higher than that of the ME antenna and also had power area density that was 3.7 times higher and a voltage area

density that was 1.2 times larger than that of the ME antenna at the largest load resistance measured. In addition, the area of the ME antenna is half the size of the coil antenna, and the volume is only one tenth. So, in applications with harsh size constraints and the need for low power charging for a high impedance load such as a battery, an ME antenna can be more beneficial than a coil. The ME antenna can also harvest energy from vibration, with output power in the range of 100s of microwatts and a highest output voltage of 0.9 V for an input vibration acceleration of approximately +/- 8 g at 290 Hz.

7.1 Future Work: Rectifier and DC-DC converter

The next steps to developing the rectifier and DC-DC converter system will be testing the SkyWater 130 nm chip and implementing a switching network to share the resonator between the rectifier and DC-DC converter. A MEMS switch such as the ADGM1004 from Analog Devices can be used to decrease the effect of the switches on the matching network. If the switching scheme allows impedance matching in the megahertz range, a Fuji resonator with a radial resonant frequency in the Qi standard frequency range and with a thickness resonant frequency in the NFC range can be shared between the rectifier and DC-DC converter. For the ceramic disc resonator used in Section 3.6 (C-213), these specifications can be realized with a resonator having a diameter of 12 mm and a thickness of 0.15 mm.

7.2 Future work: Magnetoelectric Antenna

The main issue to address in the current ME antenna design would be increasing the output power of the ME antenna by looking at different rectifier topologies (such as using the full bridge rectifier for AC magnetic field input), MR or PE materials, thickness of piezoelectric sheets (which affect the overall ME coefficient), and fabrication methods to reduce the energy loss between the composite layers. Additional work with the ME antenna

to explore the placement of lead position and MR material on the PE material can also provide ways to improve ME antenna performance by increasing the transfer of vibration from the MR material to the PE material. Because of the size benefit and low output voltage ripple for the ME antenna, future work can also be done to design it into an integrated power converter for a wearable or implantable application.

Appendices

Appendix A

Rectifier Printed Circuit Board and Test Setup

Figure A.1 shows the schematic of the rectifier, its matching network, and connection to the source or antenna. Figure A.2 and Fig. A.3 show the layout and printed circuit board of the rectifier. The test setup diagram and laboratory equipment are shown in Fig. A.4.

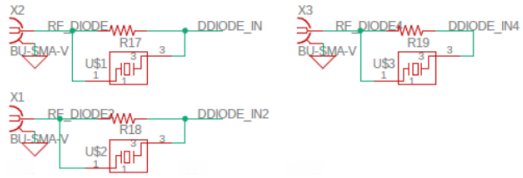

(a) Front end.

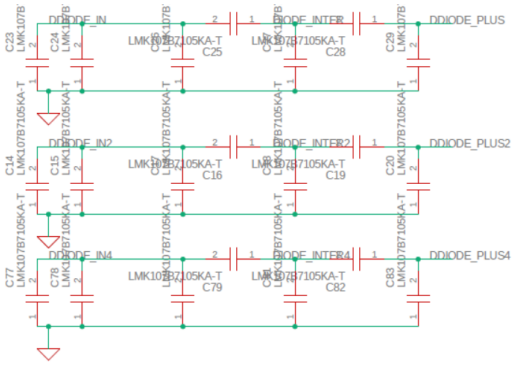

(b) Matching network.

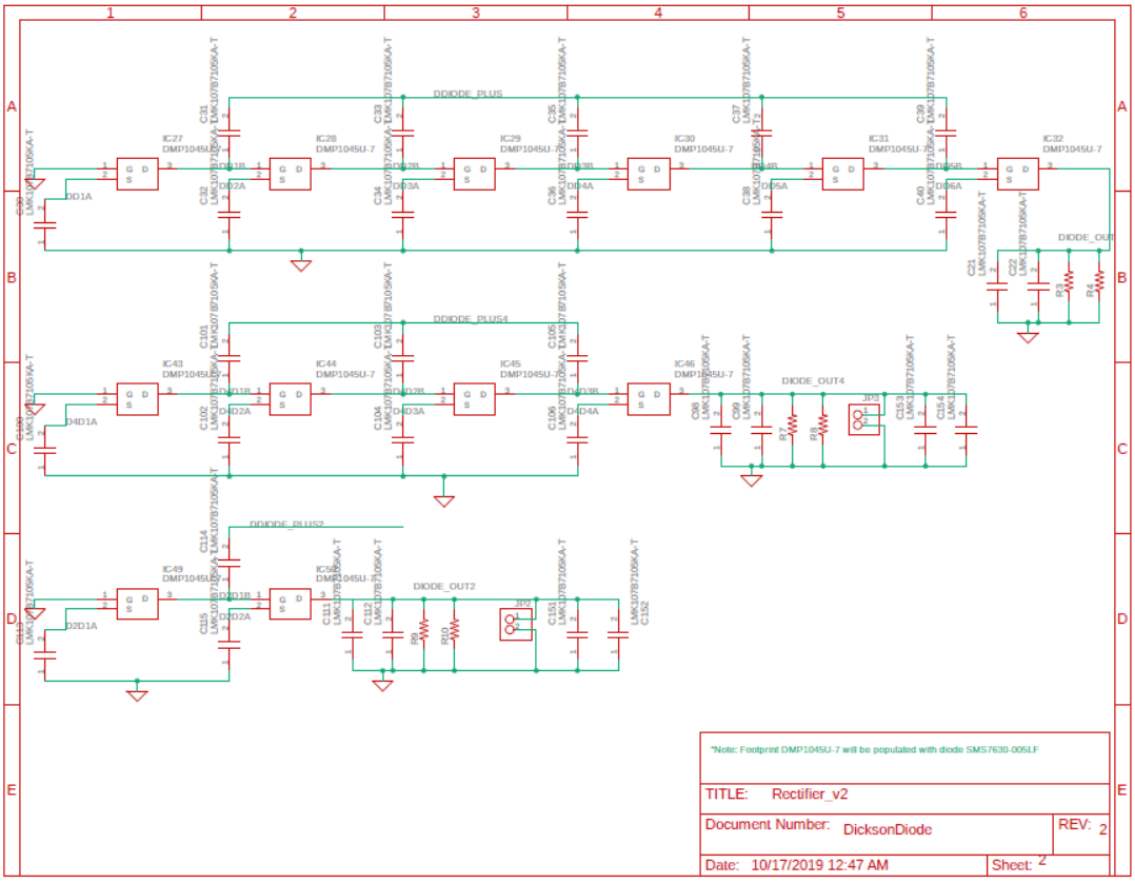

(c) 1, 2, and 3 stage diode rectifier.

Figure A.1: Schematic diagram of 1-3 stage Dickson rectifier printed circuit board (PCB).

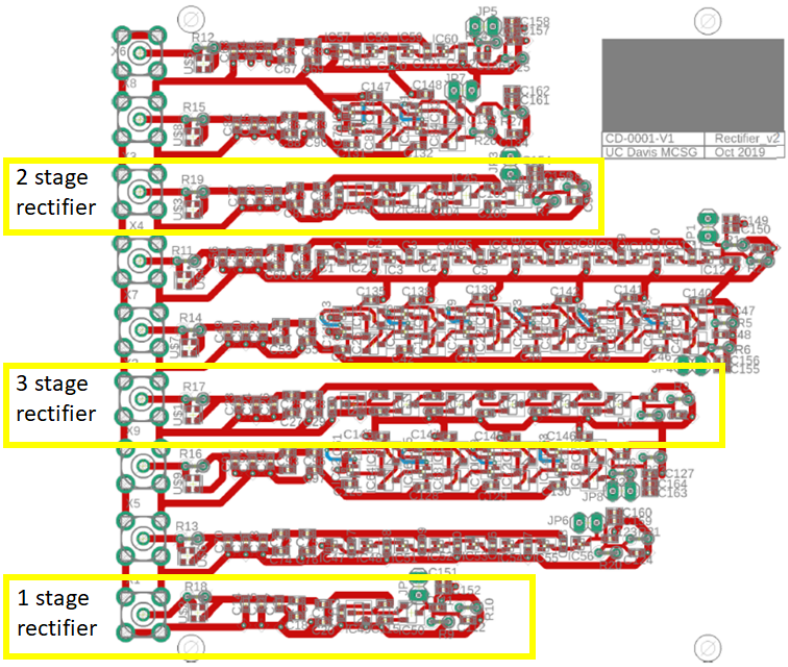

Figure A.2: PCB layout of rectifier.

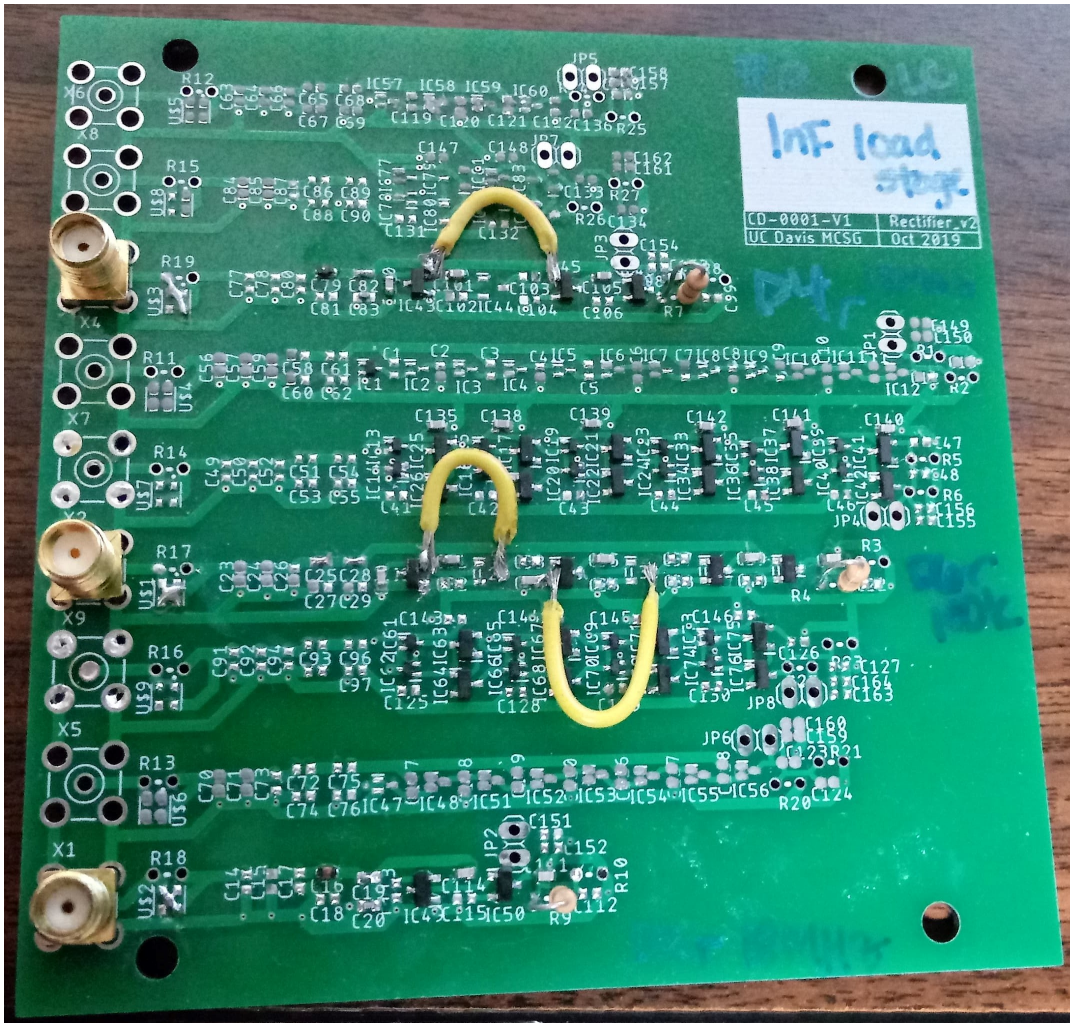

Figure A.3: Fabricated printed circuit board from JLCPCB.

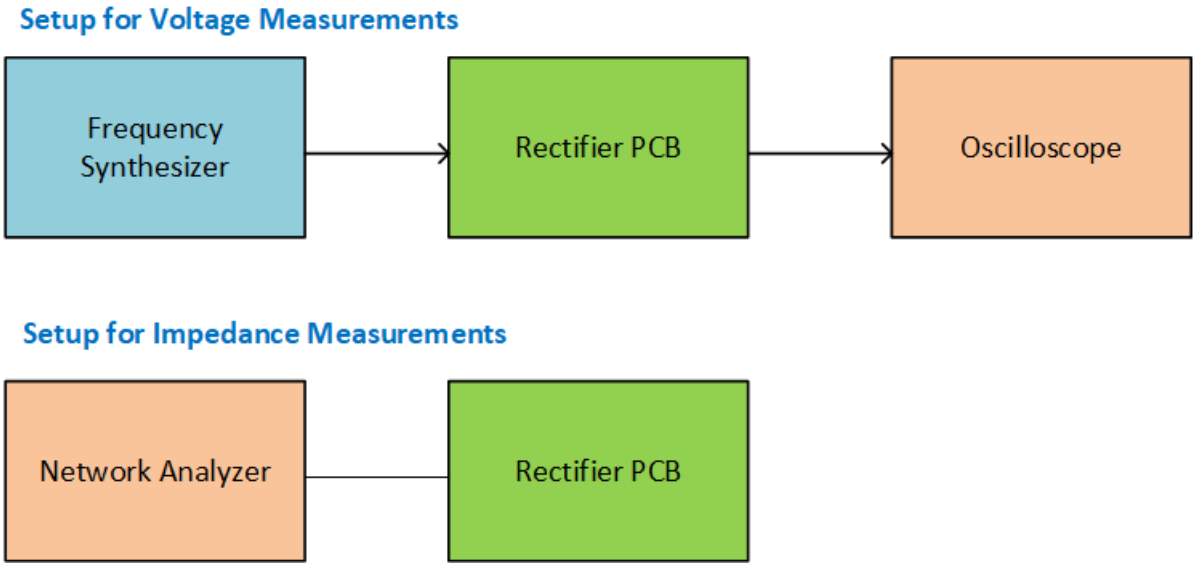

(a) Setup block diagram.

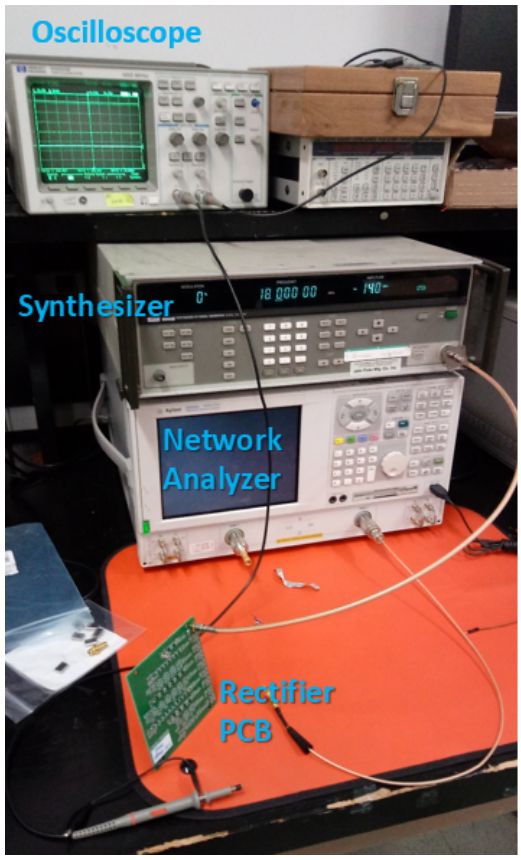

(b) Actual test setup.

Figure A.4: Test setup for rectifier.

Appendix B

ADS Rectifier Simulations

Figure B.1 shows examples of the resonator and inductor matching networks simulated in ADS for a 1-stage rectifier. Similar ones were used for the 2- and 3-stage rectifiers. Figure B.2 shows the different rectifiers used.

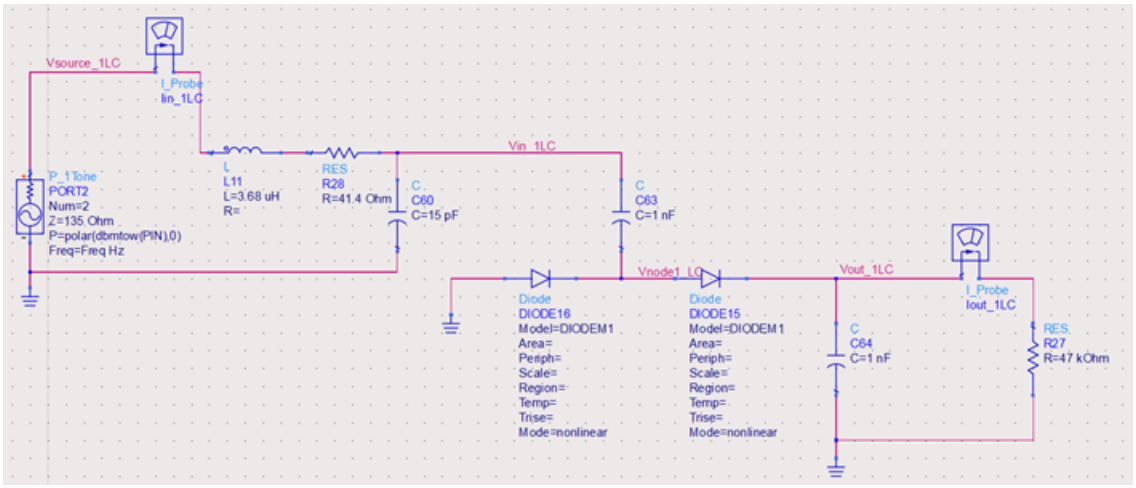

(a) Inductor-based matching network.

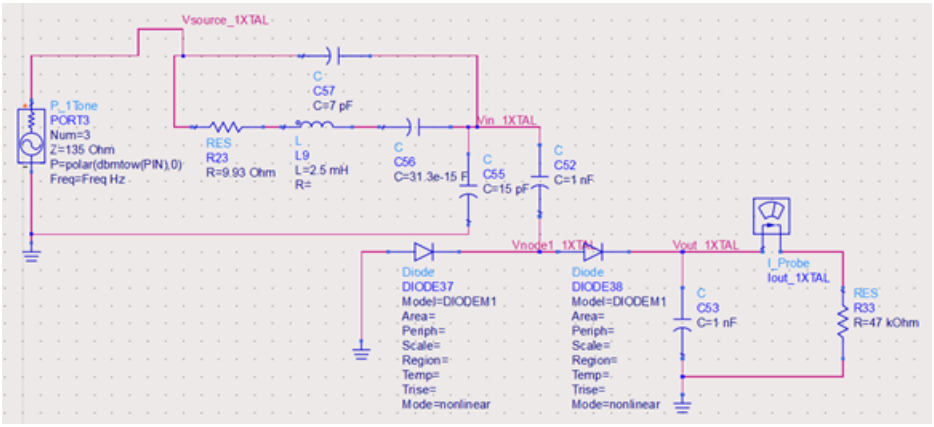

(b) Resonator-based matching network.

Figure B.1: Matching networks for a 1 stage rectifier for ADS simulation.

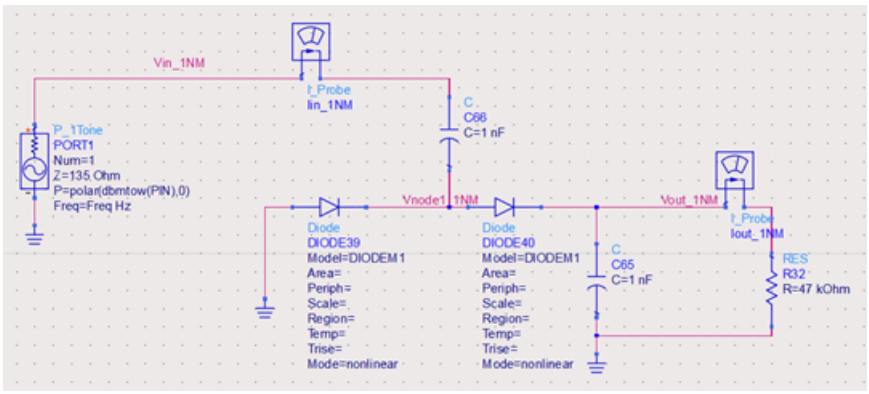

(a) 1-stage rectifier.

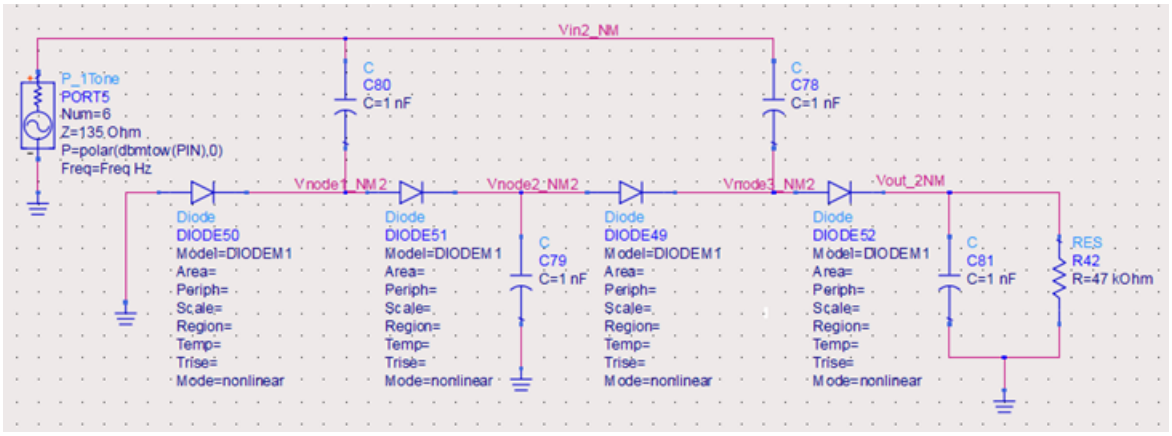

(b) 2-stage rectifier.

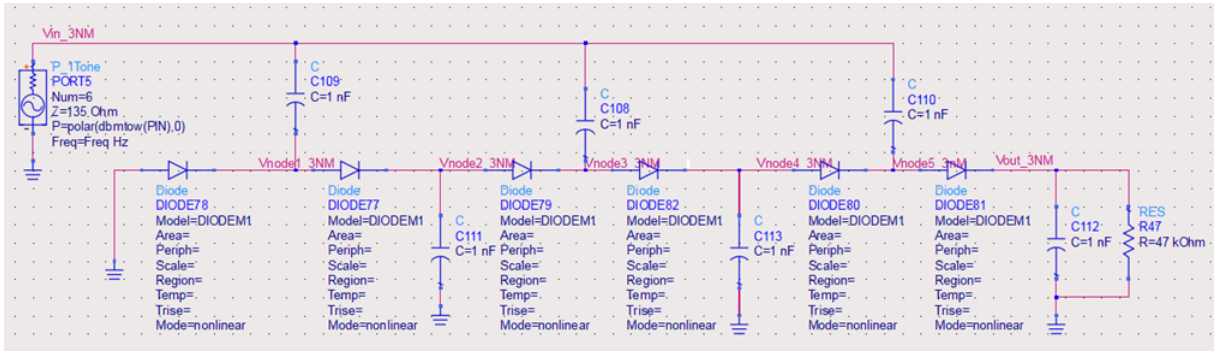

(c) 3-stage rectifier.

Figure B.2: ADS schematics of various rectifiers used.

Appendix C

DC-DC Converter LTSpice Simulations

Figure C.1 shows the ideal and off-the-shelf components used in the DC-DC converter LTSpice simulations. The efficiency calculations are shown in Fig. C.2.

```
.model MYSW SW(Ron=1 Roff=1Meg Vt=0.05)
.model IdealDiode D(Ron=1 Roff=1Meg Vfwd=0 Vrev=100)
.model SMS7630 D(Is=5e-6 Rs=20 N=1.05 Tt=1e-11
+Cjo=0.14e-12 Vj=0.34 M=0.4 Eg=0.69 Xti=2
+Fc=0.5 BV=40 Ibv=1e-4)
```

(a) Ideal switch and diode model and SMS7630 Schottky diode model.

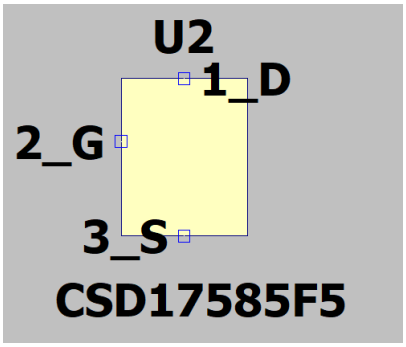

(b) Symbol for CSD1785F5 NMOS (Vt = 1.3V).

Figure C.1: Model of switches, NMOS devices, and diodes used in LTSpice simulations.

```
.meas PinXf AVG -V(Vin_SUf)*I(V1) FROM 4u TO 0.1m
.meas PoutXf AVG V(Vout_SUf)*I(R4) FROM 4u TO 0.1m
.meas EffX_f PARAM PoutXf/PinXf
```

Figure C.2: Example of efficiency calculations done in LTSpice for converter.

Appendix D

Resonator Summary

Table D.1 summarizes the specifications of the resonators used in this dissertation for the rectifier matching network and the DC-DC converter energy storage element. Several have been proposed for future work. Equation D.1 shows the equation used to calculate percent error between datasheet (expected) and measured specifications.

$$\% \; error = \left| \frac{measured - expected}{expected} \right| \times 100 \tag{D.1}$$

Table D.1: Resonators and their specifications. PZT stands for lead zirconate titanate. The 13.56 MHz resonators are proposed for future use.

P/N	ECS-180-S-1x	[26]	–	Z0.75T120-W	Z0.154T120-W	ECS-135.6-20.1X
Type	quartz crystal	Fuji C213 PZT ceramic	Fuji C213 PZT ceramic	Fuji C213 PZT ceramic	Fuji C213 PZT ceramic	quartz crystal
Freq (MHz)	18	0.08	0.103	0.185	102-200	13.56
Operating Freq (MHz)	18	0.83	0.110	0.2	13.56	13.56
Lm (mH)	2.5	1	0.6	1.039	–	–
Rm (Ω)	9.93	0.6	0.6	0.5	–	–
Cm (F)	31f	4n	4n	710p	–	–
Cp (F)	7p	8.4n	8.4n	2n	–	7p
Size (mm)	11x5x13	25x0.75	–	12x0.75	12x0.104-0.204	11x5x13
Shape	rectangle	disc	–	disc	disc	rectangle
Q	2900	800	645	2500	–	–

Appendix E

DC-DC Converter Test Setup

Figure E.1 below shows the test setup of the resonator based DC-DC converter. The HFS 9003 is supplying the switching signals. There is an additional PCB not shown in the block diagram in Section 3.6, which is the board that converts the SMA connector on the cables used with the HFS9003 stimulus system to jumper wires for connection to the DC-DC converter PCB.

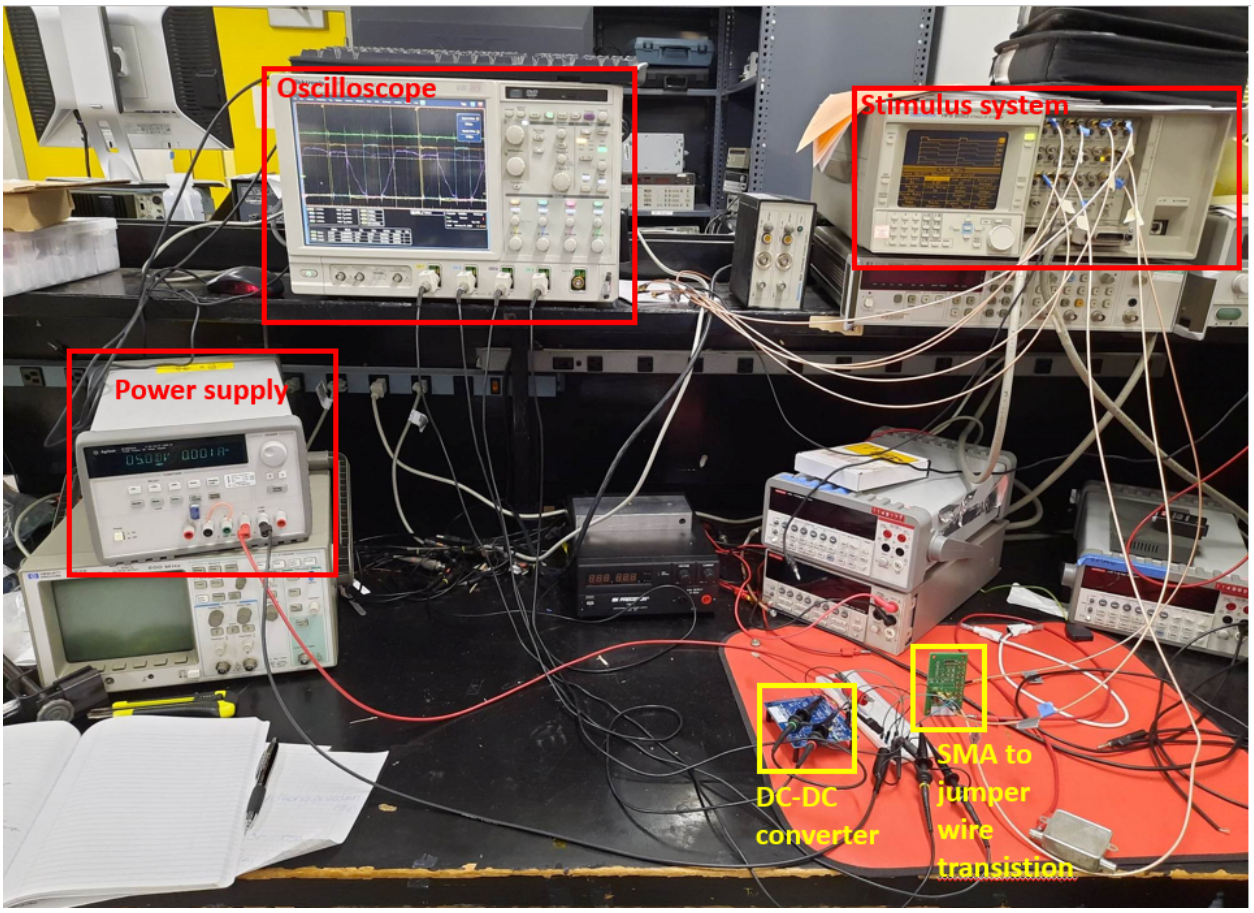

Figure E.1: Test setup for resonator-based DC-DC converter measurements.

Appendix F

ME Antenna Coupling Coefficient Parameters and Applied Stress

Reproduced from [38], C_o is the piezoelectric material capacitance (Eqn. F.1), dependent on the PE film dimensions and $\bar{\beta}_p$, which is the "effective inverse dielectric constant," defined by Eqn. F.2. These parameters can be used to calculate the magneto-elastic coupling factor, ϕ_m and C_o in Section 5.2.

$$C_o = \frac{wl}{t_p \bar{\beta}_p} \tag{F.1}$$

$$\bar{\beta}_p = \beta_p \left(1 + \frac{g_{31}^2}{s_{11}^D \beta_p}\right) \tag{F.2}$$

For a laminate structure, all layers experience the same strain, but strain is related to the stress applied through each layer's Young's modulus. Equation F.3 shows the relationship between stress (σ), Young's modulus (E), and strain (ϵ) for Material 1 and Material 2. If both materials are layers of a laminate, the strain will be the same leading to Eqn. F.4, which gives the stress in Material 1 as a function of the stress in Material 2.

$$\sigma_1 = E_1 \times \epsilon_1$$
$$\sigma_2 = E_2 \times \epsilon_2 \tag{F.3}$$

$$\sigma_1 = \frac{E_1 \sigma_2}{E_2} \tag{F.4}$$

Appendix G

Magnetoelectric Antenna Vibration Test Setup

Figure G.1 shows the test setup for measuring the ME antenna vibration response with an oscilloscope. Figure G.2 shows the myDAQ unit and buffer (not connected to the ME antenna in the photo) used when measuring the ME antenna signal with LabVIEW. The full-bridge rectifier (FBR) is also shown in closer detail.

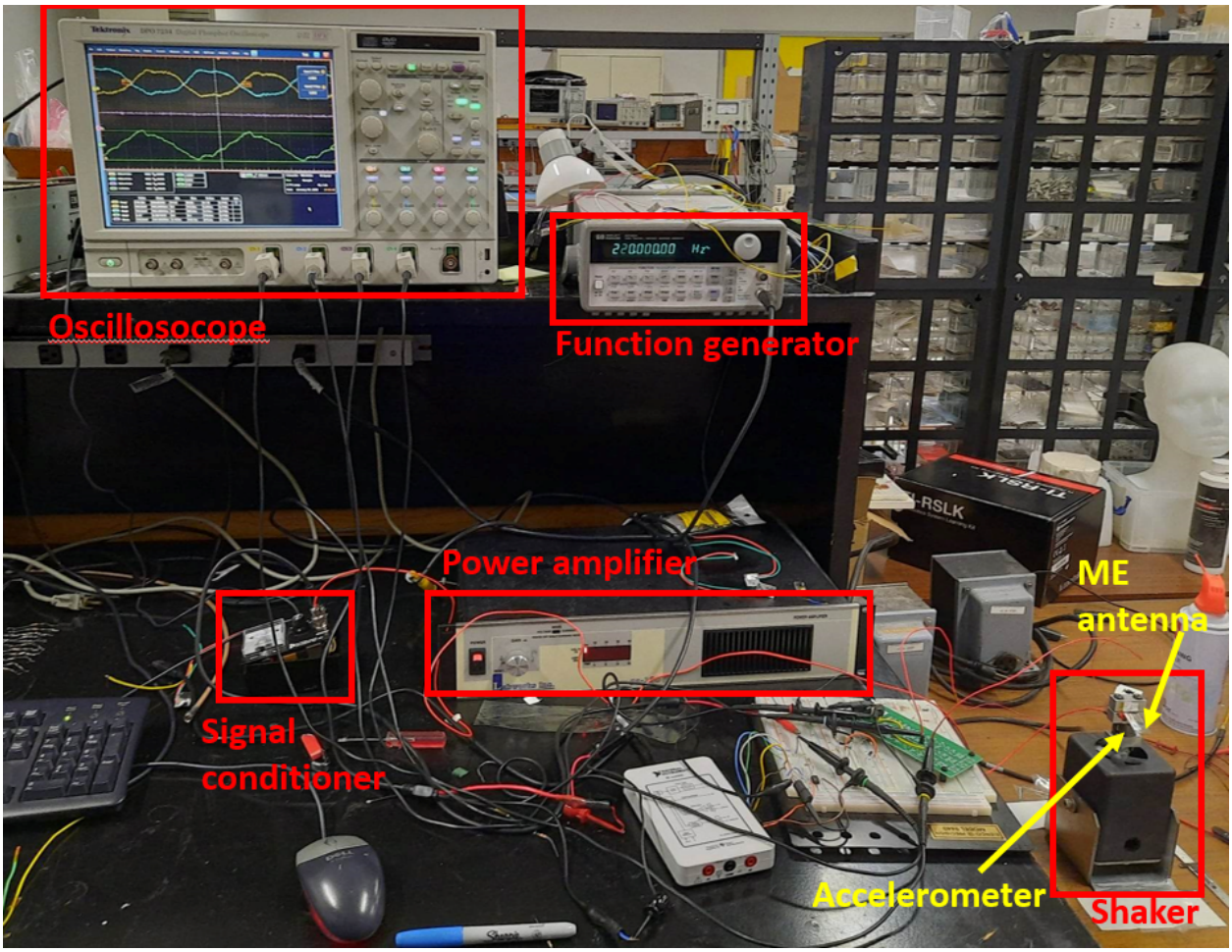

Figure G.1: Test setup to measure output power of FBR from input vibration.

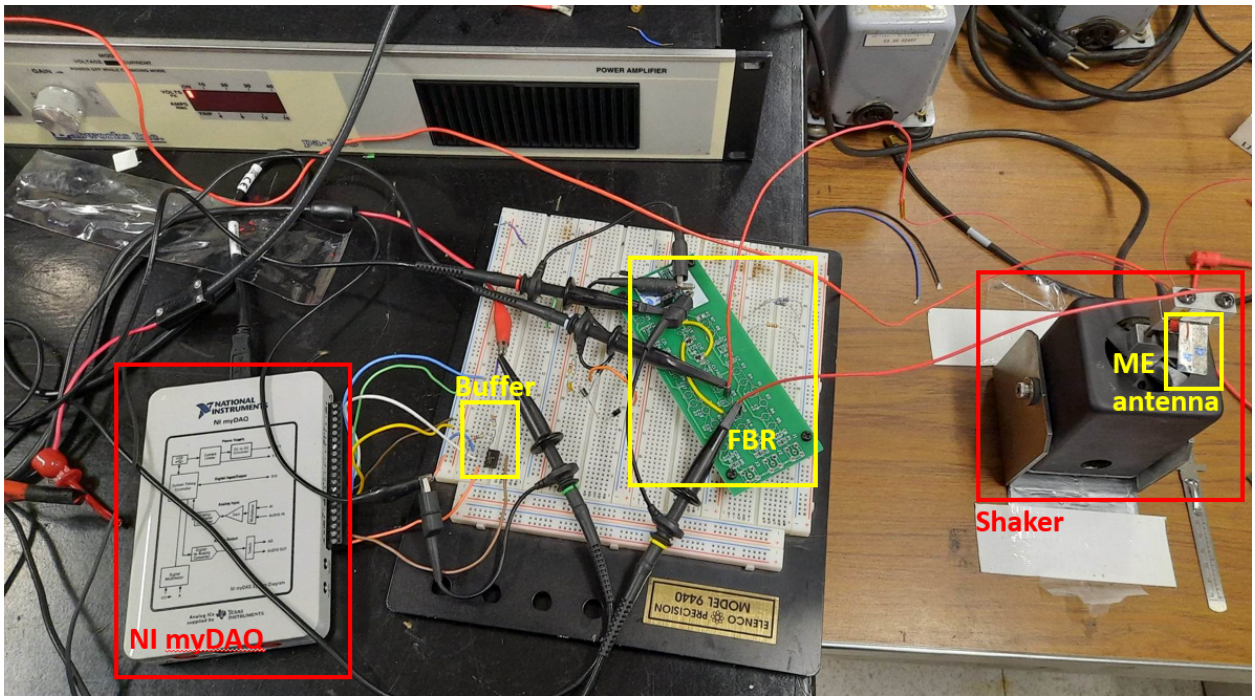

Figure G.2: NI myDAQ unit shown with buffer and shaker with ME antenna.

Appendix H

SkyWater Schematics: Xschem

A 2- and 3-stage Dickson rectifier was also implemented using the SkyWater 130 nm node PDK devices. Figure H.1 shows the 2-stage rectifier schematics with ideal and integrated capacitors, while Fig. H.2 shows the circuit diagrams for the 3-stage rectifiers. Figure H.3 shows the testbench of the fully integrated rectifier with all three rectifier topologies in the same symbol.

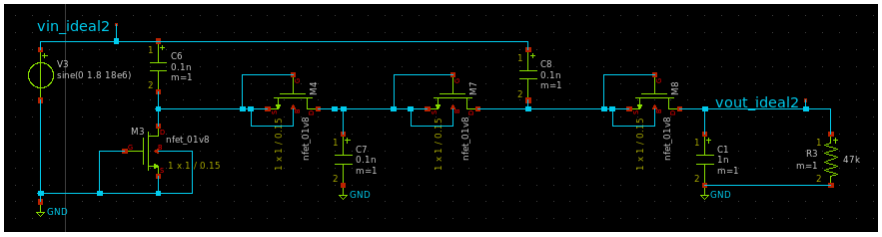

(a)

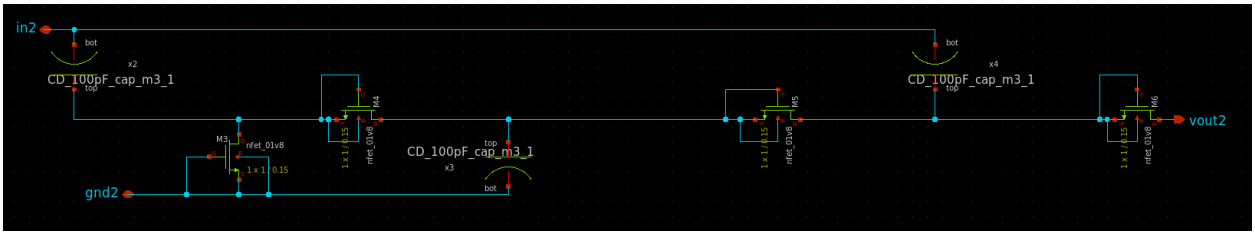

(b)

Figure H.1: Two-stage Dickson rectifier schematic using integrated NMOS devices and ideal (a) or integrated (b) capacitors.

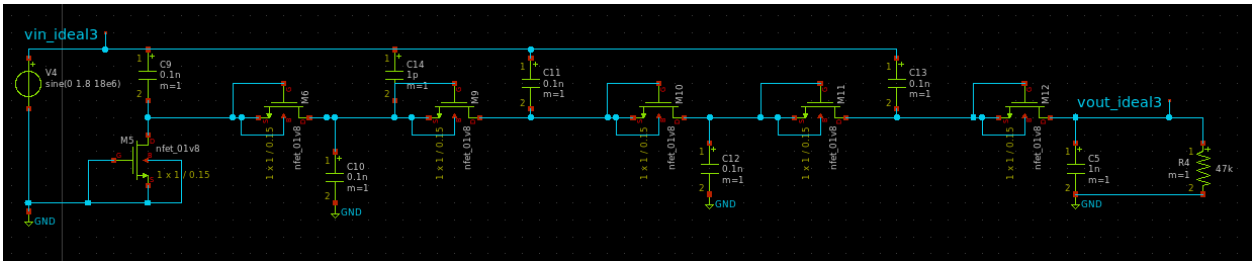

(a)

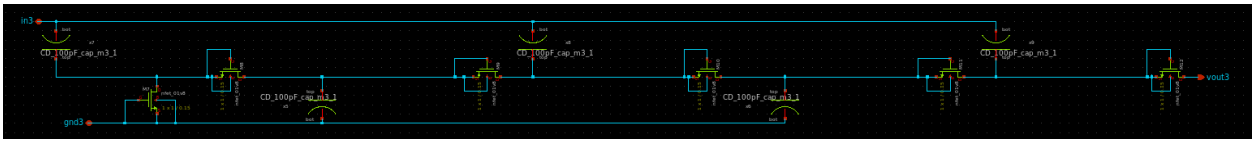

(b)

Figure H.2: Three-stage Dicskson rectifier schematic using integrated NMOS devices and ideal (a) or integrated (b) capacitors.

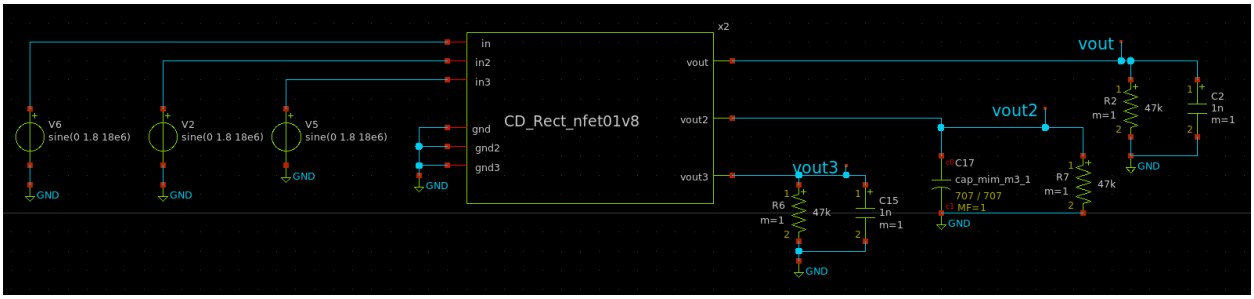

Figure H.3: Schematic symbol simulating 1-, 2-, and 3-stage Dickson rectifiers with integrated NMOS and capacitors.

Appendix I

SkyWater Spice Files: Magic

I.1 Netlist Extraction and Simulation Code

The code to extract the netlist with layout parasitics uses the following options:

```
extract all
ext2spice lvs
ext2spice cthresh 0 rthresh 0
ext2spice
```

The source code to simulate the rectifier in the Caravel harness is given below (the voltage sources and loads are not included in the extracted netlist):

```
* Rectifier
V1 io_analog1 gnd sine(0 1.8 18e6)
V2 io_analog2 gnd sine(0 1.8 18e6)
V3 io_analog3 gnd sine(0 1.8 18e6)
Rl1 io_analog4 gnd 47k m=1
Cl10 io_analog4 gnd 1n m=1
Rl2 io_analog6 gnd 47k m=1
Cl11 io_analog6 gnd 1n m=1
Rl3 io_analog5 gnd 47k m=1
Cl12 io_analog5 gnd 1n m=1
Rg gnd vssa1 0

.lib /home/connie/share/pdk/sky130A/libs.tech/ngspice/sky130.lib.spice tt

.control
set filetype=binary
*save v(io_analog0) v(io_analog10) v(io_analog7) v(io_analog8) v(io_analog9) v(vccd2) v(vccd1)
*optran 0 0 0 100n 10u 0
*tran 100n 30m 20m
```

```
**ic v(vp)=0 v(vout=0 v(cv)=0 I(L1)=0

* Rectifier
save v(io_analog1) v(io_analog2) v(io_analog3) v(io_analog4) v(io_analog5) v(io_analog6)
optran 0 0 0 100n 10u 0
tran 10n 50u
write CD22.raw
.endc
```

The source code to simulate the DC-DC converter in the Caravel harness is given below (the voltage sources, load and resonator are not included in the extracted netlist):

```
* sources
V1 io_analog8 vssa2 dc 0 pulse(1.8 0 1.45u 10p 10p 2u 9u)
V3 io_analog7 vssa2  dc 0 pulse(0 1.8 4.5u 10p 10p 2u 9u)
V2 io_analog9 vssa2 dc 0 pulse(1.8 0 7.7u 10p 10p 1.3u 9u)
V4 vccd1 vssa2 1.8
V5 vccd2 vssa2 1.8
V6 vssa2 gnd 0

* piezoelectric resonator
Cp io_analog10 vssa2 8.4n
Cs cv vssa2 4n
Ls io_analog10 rp 0.6m
Rs rp cv 0.6

* output load
Cl io_analog0 vssa2 10u
Rl io_analog0 vssa2 50k

.lib /home/connie/share/pdk/sky130A/libs.tech/ngspice/sky130.lib.spice tt

.control
set filetype=binary
save v(io_analog0) v(io_analog10) v(io_analog7) v(io_analog8) v(io_analog9) v(vccd2) v(vccd1)
optran 0 0 0 100n 10u 0
tran 100n 30m 20m
*ic v(vp)=0 v(vout=0 v(cv)=0 I(L1)=0
write CD22.raw
.endc
```

I.2 Extracted Rectifier Netlist with Parasitics

The code below is the subcircuit modeling the NMOS devices in the rectifier extracted with layout parasitics:

```
* NGSPICE file created from CD_Rect_nfet01v8.ext - technology: sky130A
```

```
.subckt sky130_fd_pr__nfet_01v8_648S5X gsb drain
X0 drain gsb gsb gsb sky130_fd_pr__nfet_01v8 ad=2.9e+11p pd=2.58e+06u as=2.9e+11p ps=2.58e+06u w=1e+06u
    l=150000u
C0 drain gsb 0.55fF
.ends
```

The code below shows the capacitor subcircuit netlist that was extracted from the rectifier layout with parasitics:

```
.subckt sky130_fd_pr__cap_mim_m3_1_CNFDQN bottom top VSUBS
X0 top bottom sky130_fd_pr__cap_mim_m3_1 l=3e+07u w=3e+07u
X1 top bottom sky130_fd_pr__cap_mim_m3_1 l=3e+07u w=3e+07u
X2 top bottom sky130_fd_pr__cap_mim_m3_1 l=3e+07u w=3e+07u
X3 top bottom sky130_fd_pr__cap_mim_m3_1 l=3e+07u w=3e+07u
X4 top bottom sky130_fd_pr__cap_mim_m3_1 l=3e+07u w=3e+07u
X5 top bottom sky130_fd_pr__cap_mim_m3_1 l=3e+07u w=3e+07u
X6 top bottom sky130_fd_pr__cap_mim_m3_1 l=3e+07u w=3e+07u
X7 top bottom sky130_fd_pr__cap_mim_m3_1 l=3e+07u w=3e+07u
X8 top bottom sky130_fd_pr__cap_mim_m3_1 l=3e+07u w=3e+07u
X9 top bottom sky130_fd_pr__cap_mim_m3_1 l=3e+07u w=3e+07u
X10 top bottom sky130_fd_pr__cap_mim_m3_1 l=3e+07u w=3e+07u
X11 top bottom sky130_fd_pr__cap_mim_m3_1 l=3e+07u w=3e+07u
X12 top bottom sky130_fd_pr__cap_mim_m3_1 l=3e+07u w=3e+07u
X13 top bottom sky130_fd_pr__cap_mim_m3_1 l=3e+07u w=3e+07u
X14 top bottom sky130_fd_pr__cap_mim_m3_1 l=3e+07u w=3e+07u
X15 top bottom sky130_fd_pr__cap_mim_m3_1 l=3e+07u w=3e+07u
C0 bottom top 1316.42fF
C1 top VSUBS 6.79fF
C2 bottom VSUBS 235.50fF
.ends

.subckt CD_100pF_cap_m3_1 bottom_p VSUBS top_p
XXC1 bottom_p top_p VSUBS sky130_fd_pr__cap_mim_m3_1_CNFDQN
XXC2 bottom_p top_p VSUBS sky130_fd_pr__cap_mim_m3_1_CNFDQN
XXC3 bottom_p top_p VSUBS sky130_fd_pr__cap_mim_m3_1_CNFDQN
XXC4 bottom_p top_p VSUBS sky130_fd_pr__cap_mim_m3_1_CNFDQN
C0 bottom_p top_p 37.72fF
C1 top_p VSUBS 47.61fF
C2 bottom_p VSUBS 940.47fF
.ends
```

The following code is the extracted netlist for the rectifier with layout parasitics:

```
XXM12 v1 out1 sky130_fd_pr__nfet_01v8_648S5X
Xx1 in3 VSUBS v3e CD_100pF_cap_m3_1
Xx2 gnd3 VSUBS v3b CD_100pF_cap_m3_1
Xx3 gnd3 VSUBS v3d CD_100pF_cap_m3_1
Xx4 in3 VSUBS v3c CD_100pF_cap_m3_1
Xx5 in3 VSUBS v3a CD_100pF_cap_m3_1
Xx6 in2 VSUBS v2c CD_100pF_cap_m3_1
Xx7 in2 VSUBS v2a CD_100pF_cap_m3_1
Xx8 gnd2 VSUBS v2b CD_100pF_cap_m3_1
Xx9 in1 VSUBS v1 CD_100pF_cap_m3_1
```

```
XXM1 gnd2 v2a sky130_fd_pr__nfet_01v8_648S5X
XXM2 v2b v2c sky130_fd_pr__nfet_01v8_648S5X
XXM3 v2a v2b sky130_fd_pr__nfet_01v8_648S5X
XXM4 v2c out2 sky130_fd_pr__nfet_01v8_648S5X
XXM5 v3d v3e sky130_fd_pr__nfet_01v8_648S5X
XXM6 v3b v3c sky130_fd_pr__nfet_01v8_648S5X
XXM7 v3a v3b sky130_fd_pr__nfet_01v8_648S5X
XXM8 gnd3 v3a sky130_fd_pr__nfet_01v8_648S5X
XXM9 v3e out3 sky130_fd_pr__nfet_01v8_648S5X
XXM10 v3c v3d sky130_fd_pr__nfet_01v8_648S5X
XXM11 gnd v1 sky130_fd_pr__nfet_01v8_648S5X
C0 v3d out1 0.10fF
C1 gnd3 v2b 0.07fF
C2 v2a v3d 0.15fF
C3 out1 v3b 0.01fF
C4 v2a v3b 0.13fF
C5 v3a v2c 0.21fF
C6 dw_239400_19600# out1 0.13fF
C7 gnd2 dw_239400_19600# 6.73fF
C8 v2a dw_239400_19600# 8.63fF
C9 v3d in2 2.07fF
C10 gnd v1 0.67fF
C11 v3b in2 5.88fF
C12 gnd3 gnd2 0.05fF
C13 v2a gnd3 0.19fF
C14 in1 v3d 0.33fF
C15 out2 v3d 0.05fF
C16 v2b v3c 5.93fF
C17 out2 v3b 0.07fF
C18 gnd3 in2 1.58fF
C19 v3e out3 0.07fF
C20 out2 dw_239400_19600# 0.45fF
C21 v3e v2b 6.17fF
C22 gnd3 out2 0.65fF
C23 gnd2 v3c 45.77fF
C24 v3a v2b 50.65fF
C25 v3c in2 0.07fF
C26 in3 v3c 41.82fF
C27 v3e gnd2 44.42fF
C28 v3a gnd2 0.23fF
C29 v2a v3a 0.14fF
C30 out2 v3c 0.16fF
C31 v3e in2 0.07fF
C32 v3e in3 83.65fF
C33 out1 v1 0.08fF
C34 v3a in2 0.14fF
C35 v3a in3 -0.06fF
C36 v3e out2 0.09fF
C37 v3d v3b 12.32fF
C38 v3a out2 0.09fF
C39 v2c v2b 0.69fF
C40 in1 v1 0.07fF
C41 dw_239400_19600# v3d 7.55fF
C42 dw_239400_19600# v3b 9.28fF
```

```
C43 gnd3 v3d 14.99fF
C44 gnd3 v3b 8.50fF
C45 gnd out1 0.14fF
C46 gnd3 dw_239400_19600# 7.31fF
C47 v2a v2c 0.15fF
C48 v2c in2 4.76fF
C49 v3d v3c 0.57fF
C50 v3b v3c 0.97fF
C51 out2 v2c 0.66fF
C52 dw_239400_19600# v3c 6.80fF
C53 v3e v3d 0.59fF
C54 gnd3 v3c 0.17fF
C55 v3a v3d 1.02fF
C56 v3a v3b 1.60fF
C57 v3e dw_239400_19600# 4.64fF
C58 gnd2 v2b 11.19fF
C59 v2a v2b 0.75fF
C60 v3d v1 0.14fF
C61 v3a dw_239400_19600# 10.51fF
C62 v3b v1 0.08fF
C63 gnd3 v3e 0.34fF
C64 v2b in2 4.29fF
C65 dw_239400_19600# v1 5.02fF
C66 v3a gnd3 4.34fF
C67 v2a gnd2 0.68fF
C68 gnd3 v1 0.00fF
C69 out2 v2b 0.90fF
C70 gnd2 in2 3.23fF
C71 v2a in2 2.36fF
C72 v3e v3c 6.20fF
C73 v3a v3c 5.95fF
C74 gnd2 out2 0.57fF
C75 gnd v3d 0.09fF
C76 v2a out2 0.75fF
C77 v2c v3d 6.78fF
C78 gnd v3b 0.02fF
C79 v2c v3b 6.17fF
C80 gnd dw_239400_19600# 6.53fF
C81 v2c dw_239400_19600# 6.23fF
C82 v3a v3e 5.95fF
C83 gnd3 v2c 1.55fF
C84 v3a v1 0.01fF
C85 v3d out3 0.01fF
C86 dw_239400_19600# out3 0.13fF
C87 gnd v3c 0.01fF
C88 dw_239400_19600# v2b 9.99fF
C89 gnd VSUBS 18.73fF
C90 dw_239400_19600# VSUBS 130.24fF $ **FLOATING
C91 out3 VSUBS -0.27fF
C92 out2 VSUBS 5.84fF
C93 v1 VSUBS 26.76fF
C94 in1 VSUBS 940.24fF
C95 v2b VSUBS 48.48fF
C96 gnd2 VSUBS 948.11fF
```

```
C97 v2a VSUBS 69.37fF
C98 in2 VSUBS 1905.95fF
C99 v2c VSUBS 82.21fF
C100 v3a VSUBS 47.64fF
C101 v3c VSUBS 173.06fF
C102 in3 VSUBS 2828.41fF
C103 v3d VSUBS 102.35fF
C104 gnd3 VSUBS 1933.04fF
C105 v3b VSUBS 117.27fF
C106 v3e VSUBS 160.18fF
C107 out1 VSUBS 13.52fF
```

I.3 Extracted DC-DC Converter Netlist with Parasitics

The code below is the extracted netlist for the inverter chain subcircuit with layout parasitics:

```
* NGSPICE file created from DcDcMultInv.ext - technology: sky130A

.subckt x22_FO4Flatten vdd w_3200_0# w_800_1600# gnd a_36_36# out w_0_800# a_2436_36#
+ in4 in3 in2 in
X0 in4 in3 vdd w_1600_4000# sky130_fd_pr__pfet_01v8 ad=4.64e+12p pd=3.258e+07u as=2.465e+13p
     ps=1.7232e+08u w=1.6e+07u l=150000u
X1 in3 in2 gnd a_36_36# sky130_fd_pr__nfet_01v8 ad=1.16e+12p pd=8.58e+06u as=2.465e+13p ps=1.7232e+08u
     w=4e+06u l=150000u
X2 out in4 gnd a_36_36# sky130_fd_pr__nfet_01v8 ad=1.856e+13p pd=1.2858e+08u as=0p ps=0u w=6.4e+07u
     l=150000u
X3 in3 in2 vdd w_800_1600# sky130_fd_pr__pfet_01v8 ad=1.16e+12p pd=8.58e+06u as=0p ps=0u w=4e+06u
     l=150000u
X4 vdd in4 out w_3200_0# sky130_fd_pr__pfet_01v8 ad=0p pd=0u as=1.856e+13p ps=1.2858e+08u w=6.4e+07u
     l=150000u
X5 in2 in gnd a_36_36# sky130_fd_pr__nfet_01v8 ad=2.9e+11p pd=2.58e+06u as=0p ps=0u w=1e+06u l=150000u
X6 in2 in vdd w_0_800# sky130_fd_pr__pfet_01v8 ad=2.9e+11p pd=2.58e+06u as=0p ps=0u w=1e+06u l=150000u
X7 in4 in3 gnd a_36_36# sky130_fd_pr__nfet_01v8 ad=4.64e+12p pd=3.258e+07u as=0p ps=0u w=1.6e+07u
     l=150000u
C0 gnd in2 0.64fF
C1 w_0_800# in2 0.32fF
C2 w_3200_0# w_1600_4000# 0.21fF
C3 gnd vdd 1.70fF
C4 in in4 0.02fF
C5 in4 w_1600_4000# 1.75fF
C6 w_0_800# vdd 0.21fF
C7 out w_800_1600# 0.02fF
C8 w_3200_0# in4 0.44fF
C9 in3 out 0.20fF
C10 gnd w_0_800# 0.03fF
C11 w_800_1600# in2 0.38fF
C12 in3 in2 0.28fF
C13 w_800_1600# vdd 0.53fF
C14 out w_1600_4000# 0.33fF
C15 in3 vdd 1.38fF
```

```
C16 w_3200_0# out 7.73fF
C17 in in2 0.22fF
C18 gnd w_800_1600# 0.12fF
C19 gnd in3 1.84fF
C20 out in4 1.58fF
C21 in3 w_0_800# 0.01fF
C22 in vdd 0.09fF
C23 vdd w_1600_4000# 1.82fF
C24 in4 in2 0.09fF
C25 w_3200_0# vdd 6.75fF
C26 gnd in 0.16fF
C27 gnd w_1600_4000# 0.29fF
C28 in w_0_800# 0.37fF
C29 in4 vdd 5.04fF
C30 gnd w_3200_0# 0.98fF
C31 in3 w_800_1600# 0.52fF
C32 gnd in4 5.41fF
C33 in4 w_0_800# 0.01fF
C34 out in2 0.02fF
C35 in3 in 0.03fF
C36 out vdd 19.82fF
C37 in3 w_1600_4000# 0.36fF
C38 in3 w_3200_0# 0.00fF
C39 vdd in2 0.39fF
C40 gnd out 19.36fF
C41 in4 w_800_1600# 0.08fF
C42 in3 in4 0.50fF
C43 out a_36_36# 8.15fF
C44 gnd a_36_36# 11.40fF
C45 in a_36_36# 0.58fF
C46 in2 a_36_36# 1.22fF
C47 in4 a_36_36# 6.90fF
C48 vdd a_36_36# 9.00fF
C49 in3 a_36_36# 2.41fF
C50 w_3200_0# a_36_36# 19.08fF
C51 w_0_800# a_36_36# 0.96fF
C52 w_800_1600# a_36_36# 1.85fF
C53 w_1600_4000# a_36_36# 5.20fF
.ends
```

The code below is the extracted netlist for the DC-DC converter subcircuit with layout parasitics:

```
.subckt DCDCMultFlatten vin kin kout vp a_836_36# gnd vout w_1600_0# k3 w_0_0#
X0 vp kin vin w_0_0# sky130_fd_pr__pfet_01v8 ad=1.4616e+14p pd=1.01264e+09u as=7.308e+13p ps=5.0632e+08u
    w=6.3e+07u l=150000u
X1 gnd k3 vp a_836_36# sky130_fd_pr__nfet_01v8 ad=7.308e+13p pd=5.0632e+08u as=7.308e+13p ps=5.0632e+08u
    w=6.3e+07u l=150000u
X2 gnd k3 vp a_836_36# sky130_fd_pr__nfet_01v8 ad=0p pd=0u as=0p ps=0u w=6.3e+07u l=150000u
X3 vp kin vin w_0_0# sky130_fd_pr__pfet_01v8 ad=0p pd=0u as=0p ps=0u w=6.3e+07u l=150000u
X4 vout kout vp w_1600_0# sky130_fd_pr__pfet_01v8 ad=7.308e+13p pd=5.0632e+08u as=0p ps=0u w=6.3e+07u
    l=150000u
X5 gnd k3 vp a_836_36# sky130_fd_pr__nfet_01v8 ad=0p pd=0u as=0p ps=0u w=6.3e+07u l=150000u
```

```
X6 vout kout vp w_1600_0# sky130_fd_pr__pfet_01v8 ad=0p pd=0u as=0p ps=0u w=6.3e+07u l=150000u
X7 vp kin vin w_0_0# sky130_fd_pr__pfet_01v8 ad=0p pd=0u as=0p ps=0u w=6.3e+07u l=150000u
X8 vout kout vp w_1600_0# sky130_fd_pr__pfet_01v8 ad=0p pd=0u as=0p ps=0u w=6.3e+07u l=150000u
X9 gnd k3 vp a_836_36# sky130_fd_pr__nfet_01v8 ad=0p pd=0u as=0p ps=0u w=6.3e+07u l=150000u
X10 vout kout vp w_1600_0# sky130_fd_pr__pfet_01v8 ad=0p pd=0u as=0p ps=0u w=6.3e+07u l=150000u
X11 vp kin vin w_0_0# sky130_fd_pr__pfet_01v8 ad=0p pd=0u as=0p ps=0u w=6.3e+07u l=150000u
C0 k3 gnd 0.35fF
C1 vp kin 0.36fF
C2 gnd kin 0.03fF
C3 vp w_0_0# 32.14fF
C4 vin w_1600_0# 0.97fF
C5 w_1600_0# kout 0.89fF
C6 gnd w_0_0# 3.62fF
C7 k3 vout 0.03fF
C8 vp gnd 80.27fF
C9 k3 vin 0.03fF
C10 vout w_0_0# 0.97fF
C11 k3 kout 0.07fF
C12 vin kin 0.32fF
C13 vp vout 76.80fF
C14 kout kin 0.04fF
C15 k3 w_1600_0# 0.02fF
C16 vout gnd 4.39fF
C17 vin w_0_0# 27.28fF
C18 w_0_0# kout 0.01fF
C19 w_1600_0# kin 0.01fF
C20 vp vin 77.21fF
C21 vp kout 0.37fF
C22 vin gnd 3.92fF
C23 w_1600_0# w_0_0# 2.99fF
C24 gnd kout 0.06fF
C25 vp w_1600_0# 31.50fF
C26 w_1600_0# gnd 4.11fF
C27 k3 kin 0.06fF
C28 vout kout 0.30fF
C29 k3 w_0_0# 0.02fF
C30 w_0_0# kin 1.04fF
C31 vp k3 0.42fF
C32 w_1600_0# vout 26.94fF
C33 vout a_836_36# 3.95fF
C34 kout a_836_36# 0.48fF
C35 gnd a_836_36# 27.30fF
C36 k3 a_836_36# 1.40fF
C37 vp a_836_36# 36.01fF
C38 vin a_836_36# 3.99fF
C39 kin a_836_36# 0.34fF
C40 w_1600_0# a_836_36# 73.54fF
C41 w_0_0# a_836_36# 73.54fF
.ends
```

The code below is the extracted netlist for the DC-DC converter with inverter buffers with layout parasitics:

```
X22_FO4Flatten_0 vinv 22_FO4Flatten_0/w_3200_0# 22_FO4Flatten_0/w_800_1600# gnd VSUBS
+ koutf 22_FO4Flatten_0/w_0_800# 22_FO4Flatten_0/a_2436_36# 22_FO4Flatten_0/in4 22_FO4Flatten_0/in3
+ 22_FO4Flatten_0/in2 koutv x22_FO4Flatten
X22_FO4Flatten_1 vinv 22_FO4Flatten_1/w_3200_0# 22_FO4Flatten_1/w_800_1600# gnd VSUBS
+ kinf 22_FO4Flatten_1/w_0_800# 22_FO4Flatten_1/a_2436_36# 22_FO4Flatten_1/in4 22_FO4Flatten_1/in3
+ 22_FO4Flatten_1/in2 kinv x22_FO4Flatten
X22_FO4Flatten_2 vinv 22_FO4Flatten_2/w_3200_0# 22_FO4Flatten_2/w_800_1600# gnd VSUBS
+ k3f 22_FO4Flatten_2/w_0_800# 22_FO4Flatten_2/a_2436_36# 22_FO4Flatten_2/in4 22_FO4Flatten_2/in3
+ 22_FO4Flatten_2/in2 k3v x22_FO4Flatten
XDCDCMultFlatten_0 vinf kinf koutf vpf VSUBS gnd voutf DCDCMultFlatten_0/w_1600_0#
+ k3f DCDCMultFlatten_0/w_0_0# DCDCMultFlatten
C0 voutf vpf 0.03fF
C1 voutf koutf 0.00fF
C2 koutf vinv 0.25fF
C3 k3f vpf 0.00fF
C4 k3f koutf 1.09fF
C5 22_FO4Flatten_1/in2 kinv 0.03fF
C6 gnd vpf 0.06fF
C7 gnd koutf 0.06fF
C8 22_FO4Flatten_0/w_0_800# 22_FO4Flatten_0/in2 0.00fF
C9 22_FO4Flatten_1/in2 22_FO4Flatten_1/w_0_800# 0.00fF
C10 voutf DCDCMultFlatten_0/w_1600_0# 0.00fF
C11 22_FO4Flatten_0/in4 gnd 0.02fF
C13 kinf vpf 0.05fF
C14 kinf koutf 0.10fF
C15 DCDCMultFlatten_0/w_0_0# vpf 0.00fF
C16 22_FO4Flatten_0/w_3200_0# vinv 0.00fF
C17 k3f vinf 0.00fF
C18 22_FO4Flatten_2/w_3200_0# vinv 0.00fF
C19 koutv vinv 0.08fF
C20 gnd vinf 0.06fF
C22 k3f 22_FO4Flatten_2/w_3200_0# 0.13fF
C23 22_FO4Flatten_1/in3 kinv 0.01fF
C24 koutv gnd 0.02fF
C25 kinf vinf 0.04fF
C26 koutf vpf 0.00fF
C27 DCDCMultFlatten_0/w_0_0# vinf 0.00fF
C28 22_FO4Flatten_2/in4 22_FO4Flatten_2/w_3200_0# 0.01fF
C29 k3f vinv 0.27fF
C30 gnd vinv 0.07fF
C31 koutv 22_FO4Flatten_0/in2 0.02fF
C32 22_FO4Flatten_0/in4 koutf 0.02fF
C33 k3f gnd 0.09fF
C35 22_FO4Flatten_2/in3 gnd 0.00fF
C37 kinf vinv 0.12fF
C38 k3f kinf 0.27fF
C39 22_FO4Flatten_0/in2 vinv 0.01fF
C40 vpf vinf 0.06fF
C41 gnd kinf 0.03fF
C42 koutf 22_FO4Flatten_0/w_3200_0# 0.13fF
C43 koutf vinf 0.00fF
C44 22_FO4Flatten_2/in4 k3f 0.02fF
C45 k3f 22_FO4Flatten_1/in4 0.02fF
C46 22_FO4Flatten_2/in4 gnd 0.01fF
```

```
C47 kinf 22_FO4Flatten_1/w_3200_0# 0.13fF
C48 22_FO4Flatten_0/w_800_1600# 22_FO4Flatten_0/in2 0.00fF
C49 22_FO4Flatten_0/in4 22_FO4Flatten_0/w_3200_0# -0.04fF
C50 22_FO4Flatten_1/in4 22_FO4Flatten_1/w_3200_0# 0.01fF
C51 gnd kinv 0.23fF
C52 22_FO4Flatten_1/in4 kinf 0.02fF
C53 DCDCMultFlatten_0/w_0_0# kinf -0.02fF
C54 vinv VSUBS 10.01fF
C55 voutf VSUBS 4.01fF
C56 gnd VSUBS 80.64fF
C57 vpf VSUBS 36.81fF
C58 vinf VSUBS 3.24fF
C59 DCDCMultFlatten_0/w_1600_0# VSUBS 73.54fF
C60 DCDCMultFlatten_0/w_0_0# VSUBS 73.54fF
C61 k3f VSUBS 9.65fF
C62 k3v VSUBS -0.62fF
C63 22_FO4Flatten_2/in2 VSUBS 1.22fF
C64 22_FO4Flatten_2/in4 VSUBS 6.90fF
C65 22_FO4Flatten_2/in3 VSUBS 2.41fF
C66 22_FO4Flatten_2/w_3200_0# VSUBS 19.08fF
C67 22_FO4Flatten_2/w_0_800# VSUBS 0.96fF
C68 22_FO4Flatten_2/w_800_1600# VSUBS 1.85fF
C69 22_FO4Flatten_2/w_1600_4000# VSUBS 5.20fF $ **FLOATING
C70 kinf VSUBS 9.12fF
C71 kinv VSUBS 1.70fF
C72 22_FO4Flatten_1/in2 VSUBS 1.21fF
C73 22_FO4Flatten_1/in4 VSUBS 6.90fF
C74 22_FO4Flatten_1/in3 VSUBS 2.41fF
C75 22_FO4Flatten_1/w_3200_0# VSUBS 19.08fF
C76 22_FO4Flatten_1/w_0_800# VSUBS 0.96fF
C77 22_FO4Flatten_1/w_800_1600# VSUBS 1.85fF
C78 22_FO4Flatten_1/w_1600_4000# VSUBS 5.20fF $ **FLOATING
C79 koutf VSUBS 9.33fF
C80 koutv VSUBS 0.64fF
C81 22_FO4Flatten_0/in2 VSUBS 1.22fF
C82 22_FO4Flatten_0/in4 VSUBS 6.90fF
C83 22_FO4Flatten_0/in3 VSUBS 2.41fF
C84 22_FO4Flatten_0/w_3200_0# VSUBS 19.08fF
C85 22_FO4Flatten_0/w_0_800# VSUBS 0.96fF
C86 22_FO4Flatten_0/w_800_1600# VSUBS 1.85fF
C87 22_FO4Flatten_0/w_1600_4000# VSUBS 5.20fF $ **FLOATING
```

References

[1] Wireless Power Consortium. "Find a product. Accessed Jan 11, 2021." (2021), [Online]. Available: https://www.wirelesspowerconsortium.com/products.

[2] A. Patil, R. Humbare, and V. Kumar, *Wireless Charging Market By Technology (Inductive, Resonant, Radio Frequency, and Others) and Industry Vertical (Electronics, Automotive, Industrial, Healthcare, and Aerospace & Defense): Global Opportunity Analysis and Industry Forecast, 2020–2027*, Allied Market Research, A01450, 2020. [Online]. Available: https://www.alliedmarketresearch.com/wireless-charging-market.

[3] *Introduction to the Power Class 0 Specification*, 2017.

[4] *The Qi Wireless Power Transfer System Power Class 0 Specification*, 2017.

[5] Electronics Tutorials. ""Mutual Inductance." Accessed Jan. 11, 2021." (2021), [Online]. Available: https://www.electronics-tutorials.ws/inductor/mutual-inductance.html.

[6] nucurrent. ""NFC Charging Development Platform." Accessed Jan. 11, 2021." (2021), [Online]. Available: https://www.nucurrent.com/nueva/nfc-charging/.

[7] nucurrent. ""NFC Wireless Charging Explained." Accessed Jan. 11, 2021." (2021), [Online]. Available: https://www.nucurrent.com/nfc-wireless-charging-explained/.

[8] NFC Forum. ""Wireless Charging (WLC) Technical Specification Version 1.0." Accessed Jan. 11, 2021." (2021), [Online]. Available: https://nfc-forum.org/product/nfc-forum-wireless-charging-wlc-candidate-technical-specification-version-1-0/.

[9] H. Lin, M. Zaeimbashi, N. Sun, *et al.*, "Nems magnetoelectric antennas for biomedical application," in *2018 IEEE International Microwave Biomedical Conference (IMBioC)*, IEEE, 2018, pp. 13–15.

[10] G. Papotto, F. Carrara, and G. Palmisano, "A 90-nm CMOS threshold-compensated RF energy harvester," *IEEE Journal of solid-state circuits*, vol. 46, no. 9, pp. 1985–1997, 2011.

[11] Z. Hameed and K. Moez, "Hybrid forward and backward threshold-compensated RF-DC power converter for RF energy harvesting," *IEEE Journal on Emerging and Selected Topics in Circuits and Systems*, vol. 4, no. 3, pp. 335–343, 2014.

[12] P. T. Theilmann, C. D. Presti, D. J. Kelly, and P. M. Asbeck, "A uW Complementary Bridge Rectifier With Near Zero Turn-on Voltage in SOS CMOS for Wireless Power Supplies," *IEEE Transactions on Circuits and Systems I: Regular Papers*, vol. 59, no. 9, pp. 2111–2124, 2012.

[13] S. H. Nguyen, N. Ellis, and R. Amirtharajah, "Powering smart jewelry using an RF energy harvesting necklace," in *2016 IEEE MTT-S International Microwave Symposium (IMS)*, IEEE, 2016, pp. 1–4.

[14] A. Nimo, J. Albesa, and L. M. Reindl, "Investigating the effects of parasitic components on wireless RF energy harvesting," in *2014 IEEE 11th International Multi-Conference on Systems, Signals & Devices (SSD14)*, IEEE, 2014, pp. 1–6.

[15] A. Nimo, D. Grgic, and L. M. Reindl, "Impedance optimization of wireless electromagnetic energy harvesters for maximum output efficiency at uW input power," in *Active and Passive Smart Structures and Integrated Systems 2012*, International Society for Optics and Photonics, vol. 8341, 2012, 83410W.

[16] S. T. Block, X. Jiang, B. Harris, *et al.*, "A 170 nW CMOS wake-up receiver with -60 dBm sensitivity using AlN high-Q piezoelectric resonators," in *2017 IEEE International Symposium on Circuits and Systems (ISCAS)*, IEEE, 2017, pp. 1–4.

[17] M. H. Straughn and C.-C. Chen, "Efficient RF energy harvesting circuitry study," in *2016 10th European Conference on Antennas and Propagation (EuCAP)*, IEEE, 2016, pp. 1–4.

[18] C. Song, Y. Huang, J. Zhou, *et al.*, "Matching network elimination in broadband rectennas for high-efficiency wireless power transfer and energy harvesting," *IEEE Transactions on Industrial Electronics*, vol. 64, no. 5, pp. 3950–3961, 2016.

[19] A. Nimo, "Efficient voltage transformation of wirelessly captured ambient electromagnetic power," Ph.D. dissertation, Dept. Microsystems Eng., Univ. of Freiburg, Freiburg im Breisgau, Germany, 2015.

[20] Changpuak. ""Quartz Crystal Filter Design." Accessed Jan 11, 2021." (2021), [Online]. Available: https://www.changpuak.ch/electronics/Quartz_Crystal_Filter_Designer_1.php.

[21] STMicroelectronics, *An MCU-based low cost non-inverting buck-boost converter for battery chargers*, AN2389, 2007. [Online]. Available: https://www.st.com/resource/en/application_note/cd00116928-an-mcubased-low-cost-noninverting-buckboost-converter-for-battery-chargers-stmicroelectronics.pdf.

[22] M. Ekhtiari, Z. Zhang, and M. A. Andersen, "State-of-the-art piezoelectric transformer-based switch mode power supplies," in *IECON 2014-40th Annual Conference of the IEEE Industrial Electronics Society*, IEEE, 2014, pp. 5072–5078.

[23] M. Day and B. Lee, "Understanding piezoelectric transformers in CCFL backlight applications," *Texas Instruments Incorporated Analog Applications Journal.*, vol. 4Q, 2002. [Online]. https://www.ti.com/lit/an/slyt107/slyt107.pdf.

[24] J. D. Boles, J. J. Piel, and D. J. Perreault, "Analysis of high-efficiency operating modes for piezoelectric resonator-based DC-DC converters," in *2020 IEEE Applied Power Electronics Conference and Exposition (APEC)*, IEEE, 2020, pp. 946–953.

[25] J. D. Boles, J. J. Piel, and D. J. Perreault, "Enumeration and Analysis of DC-DC Converter Implementations Based on Piezoelectric Resonators," in *2019 20th Workshop on Control and Modeling for Power Electronics (COMPEL)*, IEEE, 2019, pp. 1–8.

[26] B. Pollet, G. Despesse, and F. Costa, "A New Non-Isolated Low-Power Inductorless Piezoelectric DC–DC Converter," *IEEE Transactions on Power Electronics*, vol. 34, no. 11, pp. 11 002–11 013, 2019.

[27] B. Pollet, M. Touhami, G. Despesse, and F. Costa, "Effects of disc-shaped piezoelectric size reduction on resonant inductorless DC-DC converter," in *2019 20th International Conference on Solid-State Sensors, Actuators and Microsystems & Eurosensors XXXIII (TRANSDUCERS & EUROSENSORS XXXIII)*, IEEE, 2019, pp. 1423–1426.

[28] J. Moon, J. Lee, S. Kim, *et al.*, "60-V Non-Inverting Four-Mode Buck–Boost Converter With Bootstrap Sharing for Non-Switching Power Transistors," *IEEE Access*, vol. 8, pp. 208 221–208 231, 2020.

[29] W. D. Braun, Z. Tong, and J. Rivas-Davila, "Inductorless Soft Switching DC-DC Converter with an Optimized Piezoelectric Resonator," in *2020 IEEE Applied Power Electronics Conference and Exposition (APEC)*, IEEE, 2020, pp. 2272–2278.

[30] T. Nan, H. Lin, Y. Gao, *et al.*, "Acoustically actuated ultra-compact NEMS magnetoelectric antennas," *Nature communications*, vol. 8, no. 1, pp. 1–8, 2017.

[31] J. Zhai, S. Dong, Z. Xing, J. Li, and D. Viehland, "Giant magnetoelectric effect in Metglas/polyvinylidene-fluoride laminates," *Applied Physics Letters*, vol. 89, no. 8, p. 083 507, 2006.

[32] J. Kiser, P. Finkel, J. Gao, C. Dolabdjian, J. Li, and D. Viehland, "Stress reconfigurable tunable magnetoelectric resonators as magnetic sensors," *Applied Physics Letters*, vol. 102, no. 4, p. 042 909, 2013.

[33] A Lasheras, J Gutiérrez, S Reis, *et al.*, "Energy harvesting device based on a metallic glass/PVDF magnetoelectric laminated composite," *Smart Materials and Structures*, vol. 24, no. 6, p. 065 024, 2015.

[34] H. Lin, M. Zaeimbashi, N. Sun, *et al.*, "Future antenna miniaturization mechanism: Magnetoelectric antennas," in *2018 IEEE/MTT-S International Microwave Symposium-IMS*, IEEE, 2018, pp. 220–223.

[35] Samsung. ""Galaxy Watch." Accessed Sept. 27, 2020." (2021), [Online]. Available: https://www.samsung.com/global/galaxy/galaxy-watch/specs/.

[36] Apple. ""Watch." Accessed Mar. 23, 2021." (2021), [Online]. Available: https://www.apple.com/watch/.

[37] S. Dong, J.-F. Li, and D. Viehland, "Longitudinal and transverse magnetoelectric voltage coefficients of magnetostrictive/piezoelectric laminate composite: Theory," *IEEE Transactions on Ultrasonics, Ferroelectrics, and frequency control*, vol. 50, no. 10, pp. 1253–1261, 2003.

[38] T. Rupp, B. D. Truong, S. Williams, and S. Roundy, "Magnetoelectric transducer designs for use as wireless power receivers in wearable and implantable applications," *Materials*, vol. 12, no. 3, p. 512, 2019.

[39] B. D. Truong and S. Roundy, "Experimentally validated model and power optimization of a magnetoelectric wireless power transfer system in free-free configuration," *Smart Materials and Structures*, vol. 29, no. 8, p. 085 053, 2020.

[40] L. Hu, H. Wu, Q. Zhang, *et al.*, "Self-powered energy-harvesting magnetic field sensor," *Applied Physics Letters*, vol. 120, no. 4, p. 043 902, 2022.

[41] S Reis, M. Silva, N Castro, *et al.*, "Electronic optimization for an energy harvesting system based on magnetoelectric metglas/poly (vinylidene fluoride)/metglas composites," *Smart Materials and Structures*, vol. 25, no. 8, p. 085 028, 2016.

[42] A Lasheras, P. Saiz, J. Porro, I Quintana, C Polak, and A. Lopes, "Enhanced performance of magnetoelectric laminated composites by geometry engineering for high frequency applications," *Journal of Alloys and Compounds*, vol. 884, p. 161 065, 2021.

[43] Y. Shen, J. Gao, Y. Wang, P. Finkel, J. Li, and D. Viehland, "Piezomagnetic strain-dependent non-linear magnetoelectric response enhancement by flux concentration effect," *Applied Physics Letters*, vol. 102, no. 17, p. 172 904, 2013.

[44] S. Gillette, A. Geiler, D Gray, D Viehland, C Vittoria, and V. Harris, "Improved sensitivity and noise in magneto-electric magnetic field sensors by use of modulated ac magnetostriction," *IEEE Magnetics Letters*, vol. 2, pp. 2 500 104–2 500 104, 2011.

[45] S. Nguyen and R. Amirtharajah, "A hybrid rf and vibration energy harvester for wearable devices," in *2018 IEEE Applied Power Electronics Conference and Exposition (APEC)*, IEEE, 2018, pp. 1060–1064.

[46] MatWeb Material Property Data. Accessed Dec. 11, 2022. (), [Online]. Available: https://www.matweb.com/index.aspx.

[47] N. Yang, H. Wu, S. Wang, *et al.*, "Ultrasensitive flexible magnetoelectric sensor," *APL Materials*, vol. 9, no. 2, p. 021 123, 2021.

[48] C. M. Leung, X. Zhuang, J. Xu, *et al.*, "Enhanced tunability of magneto-impedance and magneto-capacitance in annealed metglas/pzt magnetoelectric composites," *AIP Advances*, vol. 8, no. 5, p. 055 803, 2018.

[49] Y. Wang, D. Gray, D. Berry, *et al.*, "An extremely low equivalent magnetic noise magnetoelectric sensor," *Advanced materials*, vol. 23, no. 35, pp. 4111–4114, 2011.

[50] J. Tatum, *6.7: Helmholtz Coils*, Physics: LibreTexts, 2022 [Online]. [Online]. Available: https://phys.libretexts.org/Bookshelves/Electricity_and_Magnetism/Electricity_and_Magnetism_(Tatum)/06%3A_The_Magnetic_Effect_of_an_Electric_Current/6.07%3A_Helmholtz_Coils.

[51] *AC Magnetic Field Generator Uses New Resonant*, Accel Instruments, 2022. [Online]. Available: https://www.accelinstruments.com/Applications/WaveformAmp/Magnetic-Field-Generator.html.

[52] *Welcome to the Efabless Open MPW Program*, Efabless, 2022. [Online]. Available: https://efabless.com/open_shuttle_program.

[53] *Skywater Open Source PDK*, GitHub, 2020. [Online]. Available: https://github.com/google/skywater-pdk.